190(3), 2022

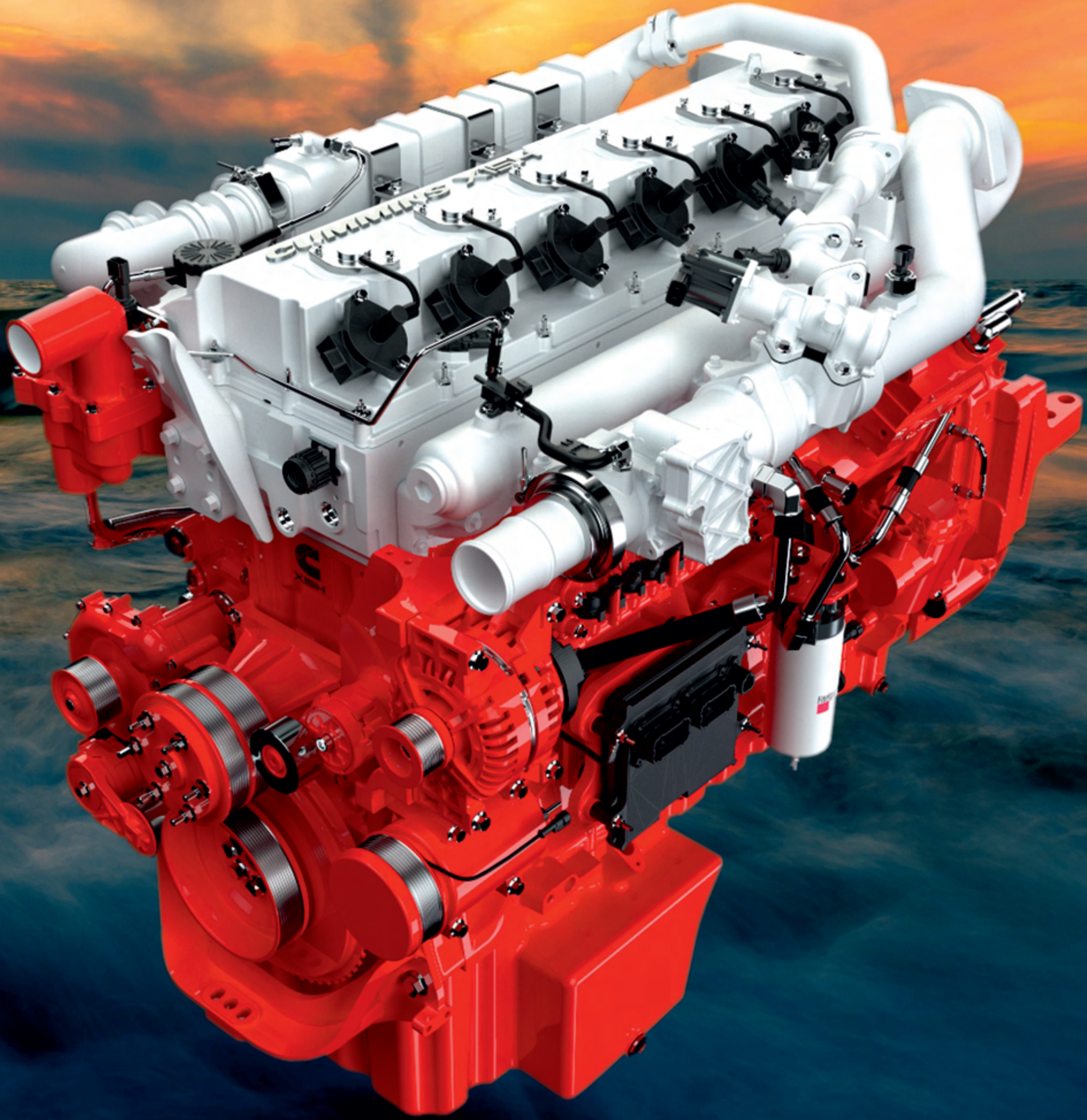

COMBUSTION ENGINES

PTNSS Supporting Members
Członkowie wspierający PTNSS

BOSMAL Automotive Research and Development Institute Ltd
Instytut Badań i Rozwoju Motoryzacji BOSMAL Sp. z o.o

Motor Transport Institute
Instytut Transportu Samochodowego

Institute of Aviation
Sieć Badawcza Łukasiewicz – Instytut Lotnictwa

Automotive Industry Institute
Sieć Badawcza Łukasiewicz – Przemysłowy Instytut Motoryzacji

Sieć Badawcza Łukasiewicz – Poznański Instytut Technologiczny

AVL List GmbH

Solaris Bus & Coach S.A.

Air Force Institute of Technology
Instytut Techniczny Wojsk Lotniczych

Military Institute of Armoured & Automotive Technology
Wojskowy Instytut Techniki Pancernej i Samochodowej

Toyota Motor Poland Ltd. Sp. z o.o.

RADWAG Balances and Scales
RADWAG Wagi Elektroniczne

MS Mechatronic Solutions Group

FOGO Sp. z o.o.

COMBUSTION ENGINES
A Scientific Magazine
2022, 190(3)
Year LXI
PL ISSN 2300-9896
PL eISSN 2658-1442

Publisher:
Polish Scientific Society of Combustion Engines
60-965 Poznan, pl. M. Skłodowskiej-Curie 5, Poland
tel.: +48 61 6475966, fax: +48 61 6652204
E-mail: sekretariat@ptnss.pl
WebSite: http://www.ptnss.pl
Papers available on-line: http://combustion-engines.eu

Scientific Board:

Krzysztof Wisłocki – chairman, Poland (*Poznan University of Technology*)
Yuzo Aoyagi – Japan (*Okayama University*)
Ewa Bardasz – USA (*National Academy of Engineering*)
Piotr Bielaczyc – Poland (*BOSMAL Automotive Research and Development Institute Ltd.*)
Zdzisław Chłopek – Poland (*Warsaw University of Technology*)
Tadeu Cordeiro de Melo – Brazil (*Petrobras*)
Jan Czerwinski – Switzerland (*CJ Consulting*)
Friedrich Dinkelacker – Germany (*Leibniz Universität Hannover*)
Hubert Friedl – Austria (*AVL*)
Barouch Giechaskiel – Italy (*European Commission, JRC Italy*)
Leslie Hill – UK (*Horiba*)
Timothy Johnson – USA (*Corning Inc.*)
Kazimierz Lejda – Poland (*Rzeszow University of Technology*)
Hans Peter Lenz – Austria (*TU Wien*)
Helmut List – Austria (*AVL*)
Toni Kinnunen – Finland (*Proventia*)
David Kittelson – USA (*University of Minnesota*)
Christopher Kolodziej – USA (*Delphi Automotive Systems*)
Hu Li – UK (*University of Leeds*)
Federico Millo – Italy (*Politecnico Torino*)
Jeffrey D. Naber – USA (*Michigan Technological University*)
Andrzej Niewczas – Poland (*Motor Transport Institute*)
Marek Orkisz – Poland (*Rzeszow University of Technology*)
Dieter Peitsch – Germany (*TU Berlin*)
Stefan Pischinger – Germany (*FEV Germany*)
Andrzej Sobiesiak – Canada (*University of Windsor*)
Stanisław Szwaja – Poland (*Częstochowa University of Technology*)
Piotr Szymański – Nederlands (*European Commission, JRC*)
Leonid Tartakovsky – Israel (*Technion – Israel Institute of Technology*)
Andrzej Teodorczyk – Poland (*Warsaw University of Technology*)
Xin Wang – China (*Beijing Institute of Technology*)
Thomas Wallner – USA (*Argonne National Laboratory*)
Michael P. Walsh – USA (*International Council on Clean Transportation*)
Mirosław Wendeker – Poland (*Lublin University of Technology*)
Piotr Wolański – Poland (*Warsaw University of Technology*)

Contents

Editorial:
Institute of Combustion Engines and Powertrains
Poznan University of Technology
60-965 Poznan, Piotrowo 3 Street
tel.: +48 61 2244505, +48 61 2244502
E-mail: papers@ptnss.pl

Publisher:

Polish Scientific Society of Combustion Engines
60-965 Poznan, pl. M. Sklodowskiej-Curie 5, Poland
tel.: +48 61 6475966, fax: +48 61 6652204
E-mail: sekretariat@ptnss.pl
WebSite: http://www.ptnss.pl

Subscriptions
Send subscription requests to the Publisher's address.
Cost of a single issue PLN 40.

Preparation for print
ARS NOVA Publishing House
60-782 Poznan, ul. Grunwaldzka 17/10A

Circulation: 100 copies

Printing and binding

Zakład Poligraficzny Moś i Łuczak, sp. j.,
Poznań, ul. Piwna 1

The journal is under
the patronage
of the Transport Committee
of the Polish Academy of Sciences

PAN
POLSKA AKADEMIA NAUK

The journal is registered and listed in the Polish
and international database

BazTech
INDEX COPERNICUS INTERNATIONAL
Crossref
EBSCO
DOAJ DIRECTORY OF OPEN ACCESS JOURNALS
POL-index Polska Baza Cytowań
SHERPA/RoMEO
ROAD DIRECTORY OF OPEN ACCESS SCHOLARLY RESOURCES

Papers published in the
Combustion Engines
quarterly receive 70 points as stated
by the Notification of the Minister of Science
and Education dated 1 December 2021.

Declaration of the original version
*The original version of the Combustion Engines journal
is the printed version.*

Cover
I – Cummins X15H – hydrogen-fueled 15-liter engine
(www.cummins.com);
background *(photo by Anas Hinde from Pexels)*
IV – 2022 BMW i4 eDrive40 – electric RWD four-door coupe
(www.paultan.org)

Article citation info:
KUTA, K., NADIMI, E., PRZYBYŁA, G. et al. Ammonia CI engine aftertreatment systems design and flow simulation. *Combustion Engines*. 2022, **190**(3), 3-10. https://doi.org/10.19206/CE-143158

Kacper KUTA
Ebrahim NADIMI
Grzegorz PRZYBYŁA
Zbigniew ŻMUDKA
Wojciech ADAMCZYK

Combustion Engines
Polish Scientific Society of Combustion Engines

Ammonia CI engine aftertreatment systems design and flow simulation

ARTICLE INFO

Received: 15 July 2021
Revised: 6 August 2021
Accepted: 18 October 2021
Available online: 22 November 2021

Investigation of exhaust emissions and ammonia flow behavior in the exhaust system incorporating with Selective Catalytic Reduction (SCR) unit is discussed. An aftertreatment system is designed to work without additional urea injection. This study is focused on obtaining optimal parameters for catalysis. Its effectiveness is considered as a function of basic parameters of exhaust gases mixture and SCR material characteristics. A 3D geometry of SCR with porous volume has been simulated using Ansys Fluent. Moreover, a 1D model of ammonia dual-fuel CI engine has been obtained. Results were focused on obtaining local temperature, velocity, and exhaust gases composition to predict optimal probes placement, pipes insulation parameters, and characteristic dimensions.

Key words: *ammonia, SCR, compression ignition engine, test rig, emissions*

1. Introduction

Ammonia can be used with diesel fuel or any other fuels in dual-fuel model, notably decreasing carbon and, in specific cases, also nitrogen-based emissions. Nevertheless, research on ammonia dual-fuel engines is still in early stage progressing, and there are only a few papers regarding ammonia as the primary fuel for ICE. Grannell et al. [1] examined mixtures of ammonia in gas phase and gasoline in a spark ignition (SI) cooperative fuel research engine. Different ammonia/gasoline ratios were utilized in knock free condition. Their test results revealed that performance of engine with a mixture of 70% ammonia and 30% gasoline by mass could be applied. Even higher ammonia to gasoline ratio was possible for supercharged operation. Reiter et al. [2] investigated a compression-ignition engine's combustion and emissions characteristics using a dual-fuel method with ammonia and diesel oil. Gaseous ammonia was sprayed into the intake system, and diesel oil was injected inside the cylinder to ignite the mixture. They examined several ammonia/diesel ratios with a small mass of diesel fuel and different mass flow of ammonia. The approved operating range was to utilize 40–60% energy provided by diesel fuel mixture with 60–40% energy from the ammonia. Moreover, their measurements show that increasing the quantity of ammonia will result in longer ignition delays. Besides, using the dual-fuel method, CO and hydrocarbons emissions were higher than using small dose of diesel fuel to obtain the same output power. In contrast, NO_x emissions were different with various ammonia/diesel mass flow. NO emission for 40% ammonia dual-fuel engine is lower than 100% diesel engine, but in 60% ammonia case, NO emission increased significantly. Their other work [3] proved that ammonia could be potentially used as an engine fuel because it has the same energy content per unit mass like a stoichiometric mixture of fossil fuels. Additionally, the results illustrated that different ammonia-diesel fuel ratios could be used to obtain the same engine torque. Furthermore, ammonia can replace as much as 95% of total energy with successful engine performance. Good fuel economy can be achieved when ammonia is applied to supply 40–80% of the total input energy. Salek et al. [4] numerically studied the effects of port injection of ammonia on performance of engine and emissions at various range of engine speeds for an ethanol/gasoline dual-fuel SI engine. They used AVL BOOST for the numerical investigation, which validated with their experiment data. Results reveal that 10% port injection of ammonia decreases the engine cylinder temperature by 50 K, which resulted in a remarkable diminution in NO_x emissions by 50% across the various engine speed. However, it imposes some unfavorable impacts on engine equivalent BSFC, CO, and HC emissions, increasing them by 3%, 30%, and 21%, respectively. Additionally, the required low octane number of fuel to prevent knock is reduced by 10% ammonia port injection, which proves that the ammonia port injection can undoubtedly impact the engine knock. Besides, port injection of ammonia raised 2% of the exhaust energy loss.

Appropriate control of combustion may reduce the amount of NO_x produced and perhaps they will not exceed the values typically occurring in diesel engines [5]. That amount of NO_x is still harmful to humans and contributes to greenhouse effect. However, DeNOx catalysts are standard element of exhaust systems and are specifically designed to reduce that pollutant. Commercial application of such catalysts begun in Japan in 1977 [6] for reducing harmful nitric oxides from exhaust gases. Some investigation was performed for obtaining optimal operating value [7] in automotive applications – both for flow profiles and temperatures distributions. Different technologies are used depending on planned application, as different catalysts offer ranges of activation energy and catalysis effectiveness. The reduction of NO to harmless N_2 occurs in presence of reductant. Injected reductant is commonly urea or another hydrogen carrier, but ammonia is sufficient for that reaction. The NH_3 concentration uniformity across the catalyst cross section has positive impact on catalysis reaction [8]. Urea-SCR is generally effective method of reducing NO_x but has three main limitations [9]: size, temperature and cell density. Size and cell density are treated in this study as given: resultant of space available in agriculture vehicle/car and producers limitation. Low temperature operation is problematic because of incomplete thermal decomposition into NH_3 and formation and decomposition of residues. First factor reduces conversion rate and the second may lead to deposits blocking SCR and reducing its lifetime [10]. A range of metal-based catalysts are considered [11] but in all cases their conversion rate in flows below 150℃ is limited and in case of urea close to impossible. One such a type, especially useful in automotive industry due to its low operating temperature, such as 523–573K range, are V_2O_5 covered catalysts [12]. Reactions in SCR are gas-solid multi-phase catalytic reactions [13] and reaction kinetics, temperature and gases composition affect them greatly. The literature provides wide spectrum of different reaction mechanisms to choose from, that are appropriate to specific cases. Obviously, crucial selection sieve is also reaction mechanism adapted. Depending on materials used, residence time (resultant of length and flow velocity) and temperature different mechanism becomes more pronounced. Among those Eley–Rideal of surface-only reaction, 2 cycle-catalysis Topsøe [13] catalysis model for standard reaction time, Ciardelli [14] or Nova [15] for low temperature NO_x reduction and Grossal for NH_4NO_3 formation are commonly used. Calculations run those mechanisms in parallel [13] or even coupled as in Mars-Van Krevelen model [15] when process is heterogynous or one of them when it's possible to select one homogenous leading mechanism.

The goal of this research is to obtain a method of optimization of NH_3-SCR process with respect to gases composition, temperature and mass flow for a given catalyzer type. Method should be computationally cost-effective as numerical optimization would require to run it multiple times for different variants, including multiple gas compositions. If such a method is obtained reduced model for real time application could be considered.

In this work measurement of fuel consumption, exhaust gases composition and temperature against the load is performed. Then collected data is fed into numerical models: 1D model of engine operation and 3D CFD model of temperature and velocity distribution. Ammonia port injection engine are modeled by 1D approach. The 3D CFD model will utilize two important simplifications: premixed mixture of exhaust gases and porous zone model.

2. Experimental Setup

2.1. Test rig and laboratory setup

The test rig setup of exhaust system had to be designed so it can be incorporated into stationary test rig and operating agricultural vehicle. This requires not only proper type of probes selected for their respective tasks but narrowly constrained positioning, too. The entirety of laboratory test bench had to fit in 780 × 700 × 1850 boundary box to maintain its maneuverability and to access all planned operating sites. It could not exceed 250 kg and should be modular to offer reassembly possibility.

Despite of its experimental character exhaust system has to be carefully insulated due to operating right next to ammonia fueling line (green pipe in the Fig. 1). This combined with limited space resulted in interest of calculating heat losses of gases before entering SCR unit and their desired temperature for optimal operation.

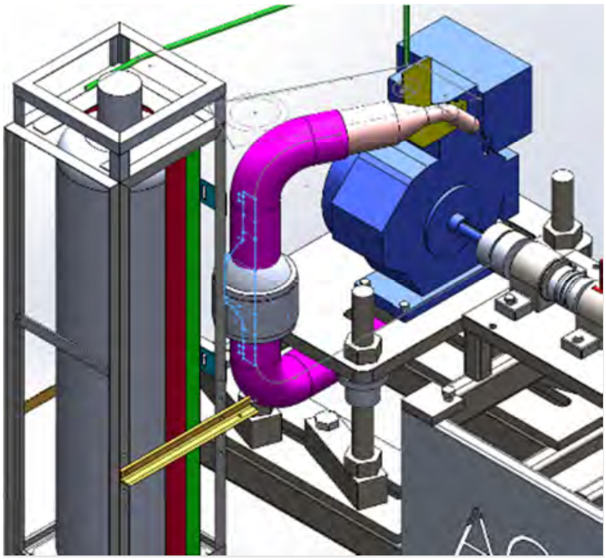

Fig. 1. Laboratory setup of design stage test rig (top) and manufactured test rig (bottom)

The measurement bases were as follows: axis of engine shaft, front plate of engine (the beginning of shaft) and mounting (bottom) plate. Those are not subdued to any (planned) changes and cooperating parts can be easily accustomed.

In case of engine shaft entire construction of laboratory stand supports easy and precise setup of angle with four degrees of freedom, and additional tilt of the table as a fifth (albeit not as precise as the four others). There are two possibilities of movement along X (along the shaft) and Y (perpendicular to shaft, parallel to table) axes: major movement realized by sliding of the dices (1 in Fig. 2) secured in position with screws (2 in Fig. 2) or minor movement allowed by slots (3 in Fig. 2) in engines bottom plate.

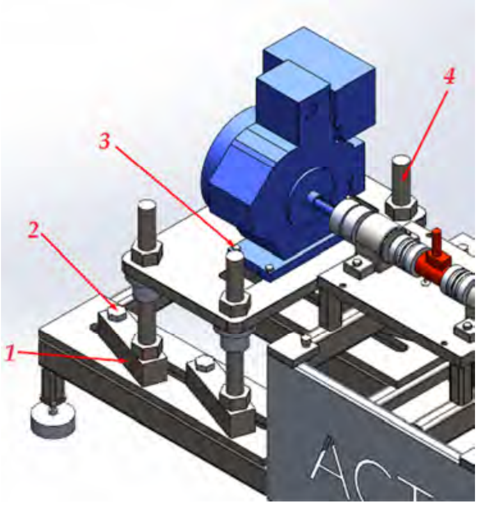

Fig. 2. Parts enabling positioning of the engine

Main movement in Z axis is resolved by four metric screws (4 in Fig. 2). They are also responsible for aforementioned tilt – or rotation with respect to either X or Y axis – if the screwing will not be uniform. Rotation with respect to Z axis is resolved by movement of the support dices or slots, exactly same as in the case of movement in X direction.

Utilizing two gas analyzers with different measuring range (this is crucial in case of CO limit) performance of agricultural vehicle with constant rollers' RPM under set of loads were tested. Tests were performed for a range of different operating cases: ignition and cold engine, subsequent tests during vehicle operation and finished when black smoke limit was reached. The fuel flow was of interest as well but it was measured with build-in sensors of vehicle.

2.2. Experimental setup and SCR structure

In this study monolithic ceramic honeycomb SCR with vanadium oxidate (V_2O_5) coating on anatase and silica (TiO_2 and SiO_2) is investigated. The 3D model was reverse engineered from commercial SCR and its main dimensions and properties of monolith are displayed in Table 1.

The SCR is installed in laboratory exhaust line as shown in the Fig. 3 and fed exhaust gases from Lifan C186F engine operating with preset conditions. Manufacturers information about engine are included in Table 2. Temperature, pressure and composition of exhaust gases are measured in sub sequent points of the exhaust. Looking from the exhaust inlet, as displayed in the Fig. 3 there is temperature 1a and lambda 2a sensors, reference pressure 4a and temperature 1b before the monolith, differential pressure 4b before and 4c after the monolith and gases composition 5a before and 5b after the SCR. In the figures are also displayed nests 3a and 3b for real time NO_x concentration and 6a and 6b for FTIR measurements but they were not used in this study. The internal geometry of the whole exhaust system is simplified for CFD modelling – the probes elements, small wedges and fillets were omitted due to their minuscule impact on fluid flow. The length of exhaust after the SCR could be reduced as well, but long pipe generally increases stability of solution reducing backflow problems.

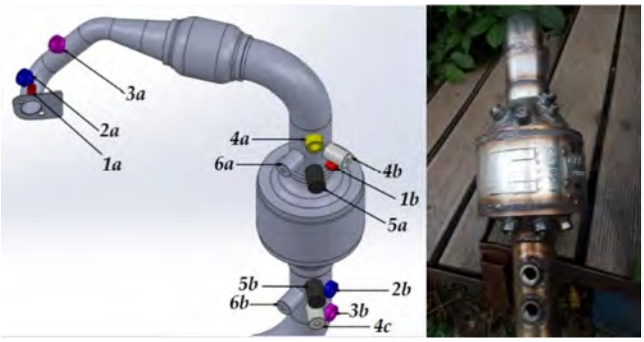

Fig. 3. Probes positions on exhaust piping modeled and final application

Table 1. SCR unit dimension and properties

Parameter	Unit	Value
Honeycomb type	–	Square opening
Coating material	–	$TiO_2.SiO_2$
Catalyst material	–	V_2O_5
Monolith diameter	mm	143.764
Monolith length	mm	76.2
Cell density	$1/cm^2$	47
Porosity	–	0.48

Table 2. Lifan C186F important values

Parameter	Unit	Value
Engine type	–	4-stroke, OHV, single cylinder, forced air
Bore × Stroke	mm × mm	86 × 70
Displacement	cm^3	406
Compression ratio	–	19:1
Maximum speed	rpm	3600
Maximum power	kW	6.8

Differences between modeling of NO_x conversion in Selective Catalytic Reduction units are stark. The approaches differ by style of geometry modeling: full geometry mesh modeling [7], single channel modeling [13] and porous zone modeling [16]. Those methods are further refined by adaptation of cyclic or symmetry boundary conditions allowing for meshing of just a fraction of geometry thus reducing computational complexity. Their limitations are derived directly from simplifications: full geometry mesh modeling offers least of them at the cost of mesh size or quality, single channel modeling ignores radial differences between channels, porous zone when exact formation zones are of no importance.

3. Numerical models

3.1. One dimensional modeling engine performance

The 1D model of single cylinder diesel engine is shown in Fig. 4. It was simulated using AVL BOOST software. This model includes the engine (E1), single cylinder (C1), Inlet (SB1) and outlet (SB2) boundary conditions, measurement points 1 and 2 (MP1, MP2), and the lines representing pipes. For this model data for setting cylinder covers the basic dimensions of the cylinder like bore, stroke, compression ratio, piston pin offset, plus information on the combustion characteristics, heat transfer, scavenging process and valve specifications for the attached pipes. Therefore, the cylinder dimensions and inlet and exhaust valves lift profiles from measurements of the engine have been used to set the 1D model. As initialization, the cylinder conditions, pressure, temperature, and gas composition at the end of the high pressure at exhaust valve opening were set. Furthermore, the initial conditions for the calculation of the cylinder have been specified.

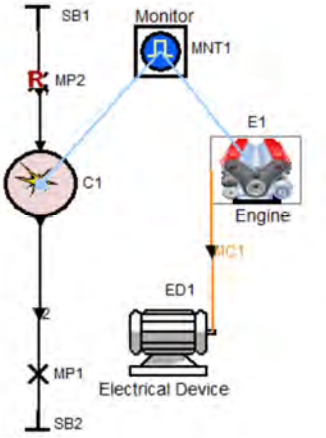

Fig. 4. One dimensional model of the engine in the AVL BOOST

The heat release rate in the cylinder was modeled by Vibe function. Vibe function is often used to approximate the heat release characteristics of the engine. Figure 5 illustrates the approximation of a heat release profile of the diesel engine by a Vibe function for different values of ’m’ shape parameter (0.4, 0.6, 0.8, and 1). Shape parameter indicates how combustion and heat release are fast. For different values of ‘m’ the Vibe diagram and burned fuel mass fraction are calculated and presented in this figure in order to obtain and validate numerical results with experimental data. However, for accurate modeling of the double peak heat release in the cylinder, since there are two peaks in the heat release diagram, the first peak due to premixed burning and the second peak due to diffusion combustion. Therefore, two Vibe functions will be specified for this study modeling. In this work, port injection of ammonia and premixed ammonia air mixture in the cylinder require to model premixed combustion, hence, premixed combustion are modeled by Vibe1. The superposition of two Vibe (Double Vibe) functions is utilized to predict the heat release rate of a diesel engine with direct injection more precisely. So, two Vibe functions are specified, the first Eq. 1 is used to model the premixed combustion and the second Eq. 2 is used to model diffusion combustion. Therefore, the combustion process in the cylinder can be modeled by the following equations, known as Vibes function:

$$x_1 = \sigma_g \left(1 - e^{-C(\emptyset_1/\emptyset_{z1})^{m_1+1}}\right) \tag{1}$$

$$x_2 = \left(1 - \sigma_g\right)\left(1 - e^{-C(\emptyset_2/\emptyset_{z2})^{m_2+1}}\right) \tag{2}$$

Double Vibe function is expressed as the sum of the first and the second part of the Vibe function:

$$x = x_1 + x_2 \tag{3}$$

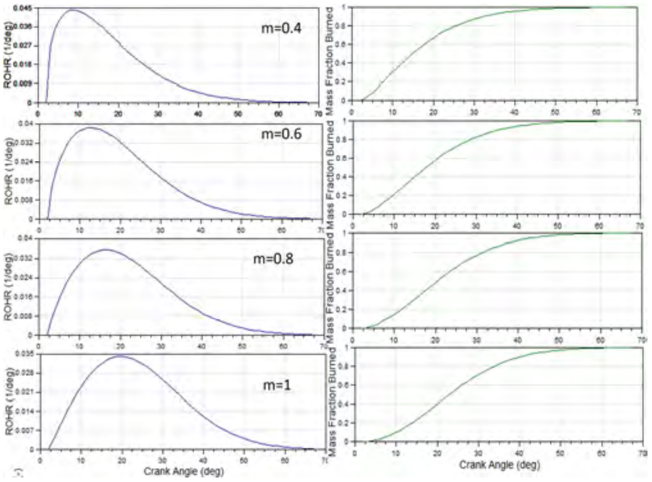

Fig. 5. First Vibe curve to model combustion and heat release in the cylinder, and influence of m (shape parameter)

3.2. 3D model of exhaust system with porous zone

Since detailed modelling of used SCR would require meshing total of 7500 channels with hydraulic diameter of around 1 mm^2 porous zone approach was chosen. Porous zone is modeled by introducing momentum sink into the standard fluid flow equations. In some approaches porous zone model can approximate turbulence, but in these calculations, flow was considered laminar due to very low hydraulic diameter of relatively long channels. To utilize this approach source term Si has to be modelled. Following experimental results from [17, 18] it can be modelled using Darcy-Forchheimer equation:

$$S_i = \frac{\Delta p}{\Delta L_i} = -\left(\frac{\mu}{\alpha} v_i + C_2 \frac{1}{2} \rho v_i^2\right) \tag{4}$$

Following pressure drop obtained from experiments [17] on similar device and operating conditions:

$$\Delta p = a v_i^2 + b v_i \tag{5}$$

Comparing equations 4 and 5 viscous and inertial resistance can be obtained as follows:

$$\frac{1}{\alpha} = \frac{b}{\mu \Delta L_i} \tag{6}$$

$$C_2 = \frac{2a}{\rho \Delta L_i} \tag{7}$$

Taking those assumptions for porous zone geometry model was prepared and meshed as seen in the Fig. 6. The volumetric fractions of subsequent species were taken from measurement results of exhaust gases as seen in the Table 3 and gaseous ammonia was added to the mixture. The viscosity was calculated.

Calculations were run in two segments: first of “cold flow” without heat exchange and second with heat exchange enabled. This method was used to decrease computing time and stabilize the solution. With used mesh and computing power first set of calculations was converged after 300 iterations. After adding heat exchange through walls, the residual values became stable after additional 200 iterations. In both cases all residuals stabilized below 0.00001 with exception of continuity residual that maintained at 0.001. For modeling mixture ideal gases with mixing law was used, and respective percentages are in Table 3.

Fig. 6. Finite element mesh consisting of 344672 elements

Table 3. Volumetric fractions of species in exhaust gases with added NH_3

Species	Unit	Value
CO	% vol	0.327
CO_2	% vol	9.22
O_2	% vol	8.52
NO	% vol	0.1167
NO_2	% vol	0.1202
NH_3	% vol	0.0069
N_2	% vol	81

4. Results and discussion

4.1. Effects of ammonia port injection

The numerical results of the one-dimensional modeling of ammonia port injection have been obtained. The double Vibe combustion model has a good prediction of heat release compering with experimental data. The diagram of the heat release rate of the engine is shown in Fig. 7, the first peak is due to premixed combustion, and the second one is due to diffusion combustion.

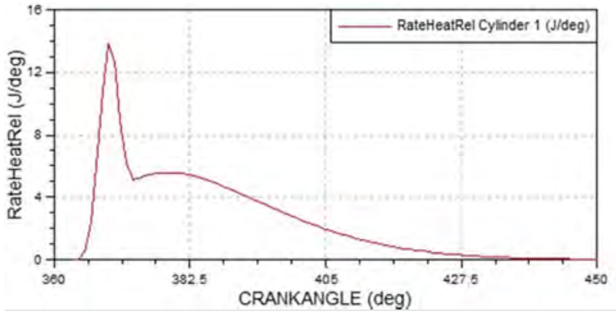

Fig. 7. Heat release rate modeled by double Vibe function for Lifan engine

Figure 8 shows the mass fraction of the selected species, the initial composition inside cylinder like CO_2, H_2O, and O_2 can be seen at 0 CA. The mass fraction of gaseous ammonia is increased during the intake stroke and then by spraying diesel and starting combustion it decreases.

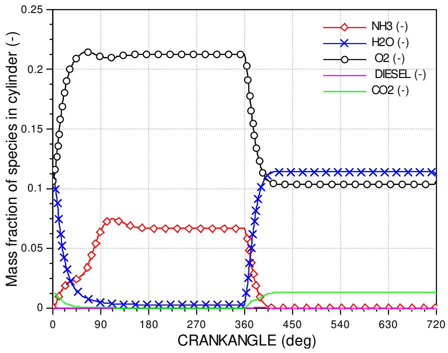

Fig. 8. Mass fraction of in-cylinder species

In-cylinder temperature and pressure diagrams are represented in Fig. 9, the numerically predicted pressure and temperature curves was calculated based on the measured in cylinder pressure. The temperature and pressure figures similar behavior to the only diesel one. The input energy supplied by ammonia for the ammonia port injection engine is equal to maximum power of the engine fueled by only diesel. 85% of input energy supplied by liquid ammonia port injection. Figure 10 illustrates exhaust emissions of the ammonia-fueled engine, NO and CO_2 emissions have been measured in the steady-state condition of 4 seconds running engine. As can be seen in this figure, emission of CO_2 less than 2% of exhaust gas.

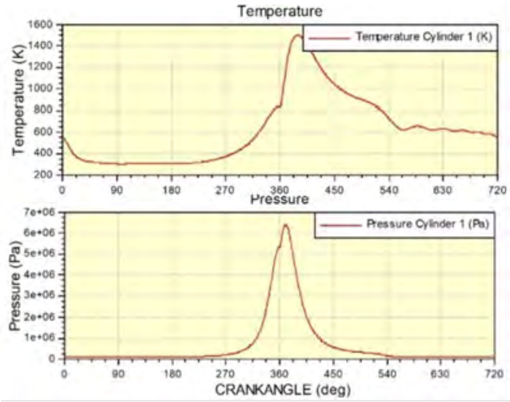

Fig. 9. In-cylinder temperature and pressure for ammonia port injection engine

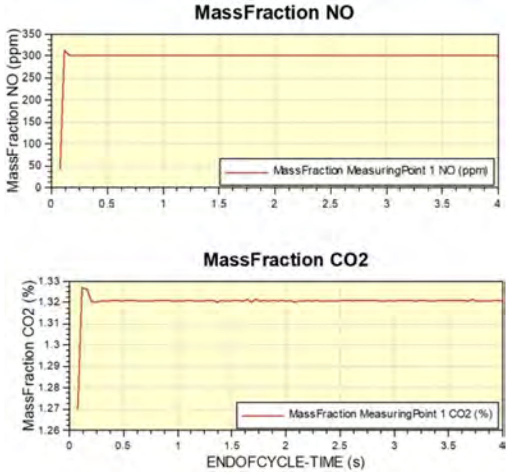

Fig. 10. Exhaust emissions of ammonia port injection in AVL BOOST

4.2. Effects of different loads on exhaust gases parameters

They can be seen in the Fig. 11. During normal operation up to load of 400 N the measured concentration of CO is kept below 6000 ppm and rises slowly symmetrically to fall of O_2. Above the first analyzer measurement range at 2500 ppm, so for loads higher than 380N up to 530 N, a rapid rise can be observed from 4000 ppm to 6500 ppm. Meanwhile the concentration of hydrocarbons and NO_x formation is on similar level as measured by first analyzer.

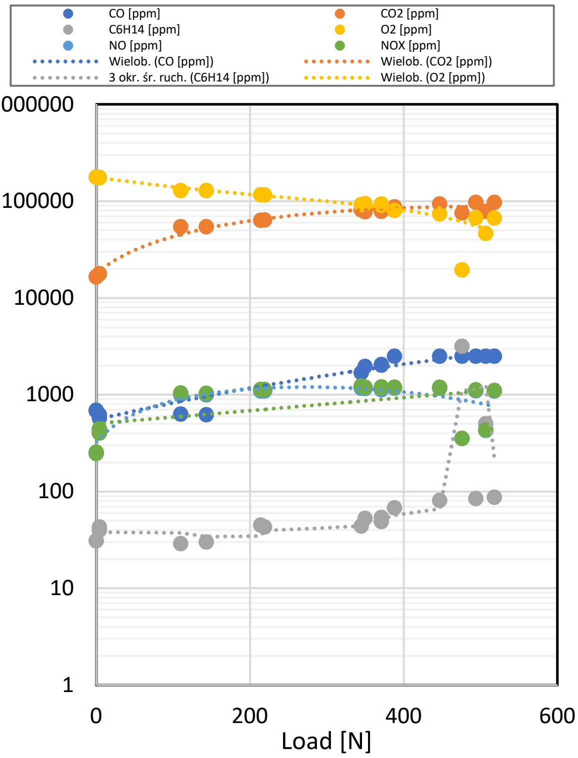

Fig. 11. Exhaust gases composition as a function of engine load during operation in 1500 rpm

Operating in 1700 rpm with similar loads proved to be less strenuous to the engine and resulted in cleaner combustion. Black smoke limit was reached as can be noticed in the Fig. 12 for the load close to 700 N. Unburned hydrocarbons concentration is shifted and rises above 600 N.

The rise of CO and HC concentration for a high load can be expected and is a result of reaching critical pressure in-cylinder that prohibits fuel from proper mixing and thus resulting in unburned mixture pushed off the engine with exhaust gas. For 1500 rpms set for this test it seems that reasonable limit of load dictated by cleaner combustion is at maximum 530 N, while 1700 rpm can operate up to 610 N.

Since exhaust gases temperature is one of the most important parameters for SCR proper operation, it was directly measured at the first element of inlet by thermocouple inserted in between two gaskets.

The temperature rise was proportional to increased load and measurements allowed to pick set of gas composition parameters to check the flow in the exhaust system. The set chosen for this are results for loads ranging from 300 to 400 N, with the average temperature of 700 K.

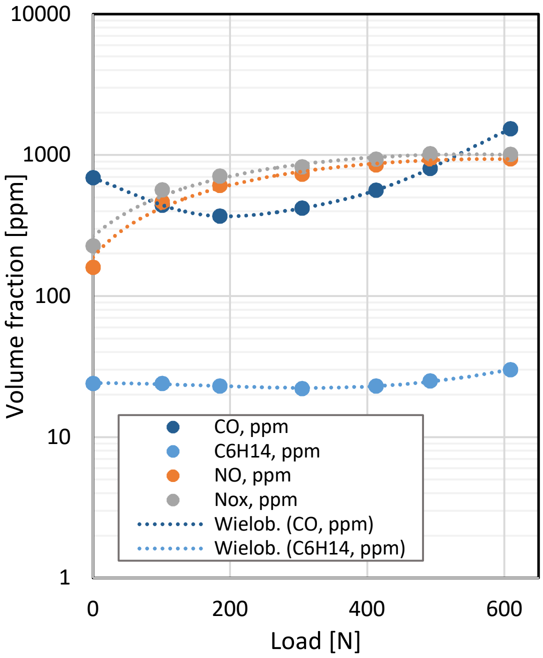

Fig. 12. Exhaust gases composition as a function of engine load during operation in 1700 rpm

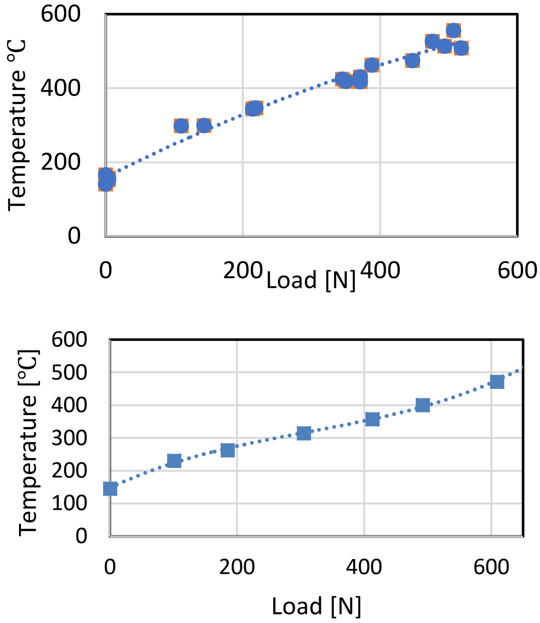

Fig. 13. Exhaust gases temperature as a function of engine load during operation in 1500 rpm and 1700 rpm

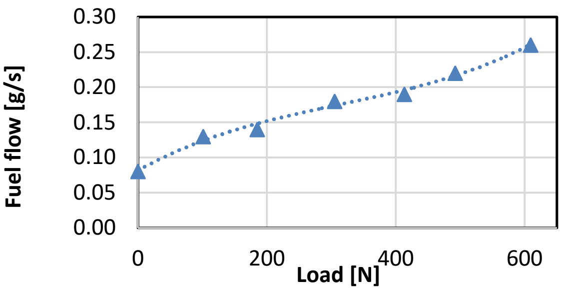

Fig. 14. Fuel flow as a function of engine load during operation in 1700 rpm

4.2. Flow through porous zone

To reliably predict and model reactions inside the SCR unit and further design exhaust system two types of results are necessary: temperature and velocity distribution. Both types of the results were 3D plotted against the exhaust shape to present estimations of exhausts gases flow velocities in Fig. 15, temperature drop along the pipe and temperature distribution in the SCR vicinity in the Fig. 16.

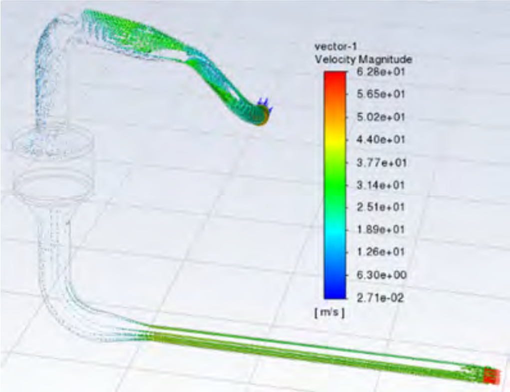

Fig. 15. Velocity profile for 0.016 kg/s mass flow and ambient pressure outlet

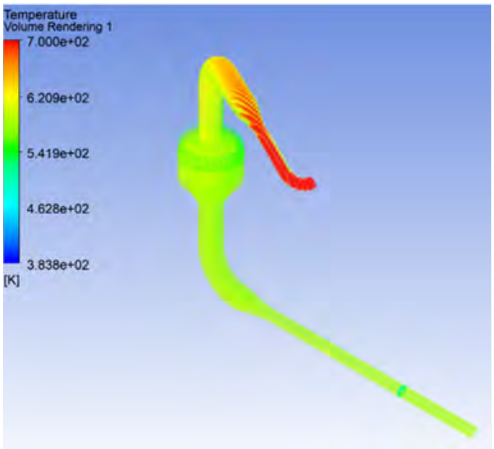

Fig. 16. Temperature distribution within the exhaust system

Substantial temperature drop that can be seen in the Fig. 16 from flow core towards outer surface of SCR proves that single channel simplification would be quite unreliable way of predicting reactions within it. Since porous zone model generally does not support non-uniform distribution of temperature between fluid and solid parts the only possibility to precisely capture it would be direct 3D model of honeycomb monolith.

Intense cooling in first element of piping, resultant of relatively high speed and temperature of fluid, is also undesirable effect that needs to be taken into account in redesign process. In case of selected inlet temperature SCR still can operate with some efficiency despite drop, but during exhaust gases measurements way lower temperatures were observed.

5. Summary and overall conclusions

This study shows methods of creating input values for catalysers reactions calculations by preparing thermodynamic parameters (especially temperature and velocity distribution) of flow entering the porous zone. The results of calculations from this paper can be further used to model reaction inside the SCR monolith – perhaps with different modelling approach to capture surface reactions of catalyst. Furthermore, 1D model of ammonia port injection CI engine has been discussed. Results shows that ammonia can used to obtain the same output power like only diesel fuel. Also, the CO_2 emission is reduced exponentially by using ammonia.

The utilised strategy of CFD modelling proved simple and reliable solution method. Step-by-step schematic of solution with cold flow calculation performed first and then performing heat exchange increased the stability of solution. Porous zone method allowed for great decrease of cells number that was necessary for proper meshing of the domain, but required experimental input and is simplification relying on negligible changes of viscosity and density of the fluid. Since that parameters changes, with relation to changing temperature in real world operation, so should change inverted permeability and inertial resistance parameters. That will be focus of future work.

The used modelling allows for parametric NH_3-SCR optimisation. Solution is stable and physically possible. Calculations allowed to select points of stable flow where probes can be inserted to compare experimental and computed results for improved quality validation. Heat loses analysis gives a foundation for system redesign.

Acknowledgements

This work was funded by Norway and Poland contract (Contract NO. NOR/POLNOR/ACTIVATE/0046/2019-00) in ACTIVATE Project.
Further information: https://ammoniaengine.org

Authors also would like to thank D. Kurzydym, Z. Żmudka and A. Klimanek [13, 14] for providing their experimental data of SCR.

Nomenclature

a	Experimental quadratic coefficient of pressure drop
b	Experimental linear coefficient of pressure drop
BSFC	brake specific fuel consumption
C	Vibe function parameter C = 6.9
C1	single cylinder
C_2	inertial resistance in porous zone
CI	compression ignition
CFD	Computational Fluid Dynamics
DI	direct injection
E1	engine
ICE	internal combustion engine
m	shape parameter of Vibe function
MP	Measurement point
SCR	selective catalytic reduction
S	body force (source term)
v_i	velocity normal to the porous face in one specific direction
x	mass fraction burned
α	permeability of the medium
$\emptyset_z$	initial and current time

$\emptyset$	angle between two Vibe functions	μ	viscosity of mixture
σ_g	duration of combustion		

Bibliography

[1] GRANNELL, S.M., ASSANIS, D.N., BOHAC, S.V. et al. The fuel mix limits and efficiency of a stoichiometric, ammonia, and gasoline dual fuelled spark ignition engine. *Journal of engineering for gas turbines and power*. 2008, **130**(4). https://doi.org/10.1115/1.2898837

[2] REITER, A.J., KONG, S.C. Combustion and emissions characteristics of compression-ignition engine using dual ammonia-diesel fuel. *Fuel*. 2011, **90**(1), 87-97. https://doi.org/10.1016/j.fuel.2010.07.055

[3] REITER, A.J., KONG, S.C. Demonstration of compression-ignition engine combustion using ammonia in reducing greenhouse gas emissions. *Energy & Fuels*. 2008, **22**(5), 2963-2971. https://doi.org/10.1021/ef800140f

[4] SALEK, F., BABAIE, M., SHAKERI, A. et al. Numerical study of engine performance and emissions for port injection of ammonia into a gasoline/ethanol dual-fuel spark ignition engine. *Applied Sciences*. 2021, **11**(4), 1441. https://doi.org/10.3390/app11041441

[5] VALERA, A. et al. Review on ammonia as a potential fuel: from synthesis to economics. *Energy Fuels*. 2021, **35**, 6964-7029. https://doi.org/10.1021/acs.energyfuels.0c03685

[6] NAKAJIMA, F., HAMADA, I. The state-of-the-art technology of NO_x control. *Catalysis Today*. 1996, **29**, 109-115. https://doi.org/10.1016/0920-5861(95)00288-X

[7] SOO-JIN, J., WOO-SEUNG, K. A numerical approach to investigate transient thermal and conversion characteristics of automotive catalytic converter, advanced converter concepts for emission control. *SAE Technical Paper* 980881. 1998. https://doi.org/10.4271/980881

[8] HUANG, H., CHEN, Y., Li, Z. et al. Analysis of deposit formation mechanism and structure optimization in urea-SCR system of diesel engine. *Fuel*. 2020, **265**, 116941. https://doi.org/10.1016/j.fuel.2019.116941

[9] KOEBEL, M., ELSENER, M., KLEEMANN, M. Urea-SCR: a promising technique to reduce NO_x emissions from automotive diesel engines. *Catalysis Today*. 2000, **59**(3-4), 335-345. https://doi.org/10.1016/S0920-5861(00)00299-6

[10] ROPPERTZ, A., FÜGER, S., KURETI, S. Investigation of urea-SCR at low temperatures. *Topics in Catalysis*. 2017, **60**, 199-203. https://doi.org/10.1007/s11244-016-0597-8

[11] DAMMA, D., ETTIREDDY P.R., REDDY, B.M. et al. A review of low temperature NH_3-SCR for removal of NO_x. *Catalysts*. 2019, **9**(4), 349. https://doi.org/10.3390/catal9040349

[12] DUMESIC, J.A., TOPSOE, N.-Y., CHEN, Y. et al. Kinetics of selective catalytic reduction of nitric oxide by ammonia over vanadia/titania. *Journal of Catalysis*. 1996, **163**, 409-417. https://doi.org/10.1006/jcat.1996.0342

[13] ZHU, Y., ZHOU, S., FENG, Y. et al. Influence of NH_4NO_3 formation on the NO_x reduction pathways over vanadium-based catalyst under diesel exhaust conditions. *Russian Journal of Physical Chemistry A*. 2018, 92, 1473-1480. https://doi.org/10.1134/S0036024418080319

[14] NOVA, I., CIARDELLI, C., TRONCONI, E. Unifying redox kinetics for standard and fast NH_3-SCR over a V_2O_5-WO_3/TiO_2 catalyst. *AIChE Journal*. 2009, **55**(6), 1514-1529. https://doi.org/10.1002/aic.11750

[15] NOVA, I. COLOMBO, M., TRONCONI, E. Kinetic modeling of dynamic aspects of the standard NH_3-SCR reaction over V_2O_5-WO_3/TiO_2 and Fe-zeolite commercial catalysts for the aftertreatment of diesel engines exhausts. *Oil & Gas Science and Technology – Revue de l IFP*. 2011, **66**(4), 681-691. https://doi.org/10.2516/ogst/2011132

[16] YAO, J. ZHONG, Z., ZHU, L. Porous medium model in computational fluid dynamics simulation of a honeycombed SCR DeNOx catalyst. *Chemical Engineering & Technology*. 2015, **38**(2), 283-290. https://doi.org/10.1002/ceat.201400127

[17] KURZYDYM, D., KLIMANEK, A., ŻMUDKA, Z. Experimental and numerical analysis of flow through catalytic converters for original part and WALKER's replacement using reverse engineering and CFD. *IOP Conferences Series: Materials Science and Engineering*. 2018, **421**, 042044. https://doi.org/10.1088/1757-899X/421/4/042044

[18] KURZYDYM, D., KLIMANEK, A., ŻMUDKA, Z. Experimental research and CFD analysis of flow parameters in a SCR system for the original part and WALKER's replacement. *Combustion Engines*. 2019, **179**(4), 12-19. https://doi.org/10.19206/CE-2019-402

Kacper Kuta, MSc. – Faculty of Energy and Environmental Engineering, Silesian University of Technology.

e-mail: *kacper.kuta@polsl.pl*

Prof. Grzegorz Przybyla, DSc., DEng. – Faculty of Energy and Environmental Engineering, Silesian University of Technology.

e-mail: *grzegorz.przybyla@polsl.pl*

Prof. Wojciech Adamczyk, DSc., DEng. – Faculty of Energy and Environmental Engineering, Silesian University of Technology.

e-mail: *wojciech.adamczyk@polsl.pl*

Ebrahim Nadimi, MSc. – Faculty of Energy and Environmental Engineering, Silesian University of Technology.

e-mail: *enaimi@polsl.pl*

Prof. Zbigniew Żmudka, DSc., DEng. – Faculty of Energy and Environmental Engineering, Silesian University of Technology.

e-mail: *zbigniew.zmudka@polsl.pl*

Article citation info:
HALLER, P., WRÓBEL, R., SIERZPUTOWSKI, G., et. al. The vehicle driver safety prediction system. *Combustion Engines*. 2022, **190**(3), 11-17. https://doi.org/10.19206/CE-142950

Piotr HALLER
Radosław WRÓBEL
Gustaw SIERZPUTOWSKI
Radostin DIMITROV
Veselin MIHAYLOW

Combustion Engines
Polish Scientific Society of Combustion Engines

The vehicle driver safety prediction system

ARTICLE INFO

Received: 14 July 2021
Revised: 6 October 2021
Accepted: 7 October 2021
Available online: 22 November 2021

The article presents analysis of road crash accidents. It presents the evolution of safety systems, starting from a description of the currently used vehicle-based systems, with particular emphasis on the prediction of the driver falling asleep. The article also proposes a proprietary system of sleep prediction based on the face detection of drivers. The detection of facial landmarks is presented as a two-step process: an algorithm finds faces in general, and then needs to localize key facial structures within the face region of interest.

Key words: *safety, system, vehicles, drowsiness, face detection*

1. The analysis of road crash accidents

1.1. General information

Each year more than 1.2 million people die in car related accidents around the world. Dying in a car accident is the most common cause of death among people aged between 15–29 years. According to statistics, roughly 90% of road traffic deaths occur in low- and middle-income countries. European roads remain the safest in the world, with a road traffic fatality rate of 9.3 per 100 000 people. The world average is 17.4 per 100 000 people, The worst results can be observed in the African Region, with a road traffic fatality rate per 100 000 of 26.6 being almost three times higher than in Europe [1].

Such a difference is caused mostly by the fact that there are older cars, worse roads, a different lifestyle, ineffective police, and a poorer society. This is why the World Health Organization make 4 main recommendations in order to reduce road traffic fatalities:

1. Legal area: countries should create and enforce laws relating to risk factors.
2. Stricter enforcement of road safety rules: the need for special social campaigns to maximize effects.
3. Paying attention to pedestrians, cyclists, and motorcyclists: roads should be built in a way that every road user can feel and be safe.
4. Car safety: even though technology in the automotive industry has become advanced, cars in poor countries usually lack even the most basic safety features.

1.2. Road accidents caused by drowsiness

Tiredness can be described as a state of fatigue caused by, among others, physical activity, insufficient sleep, or sickness. Drowsiness is described as a tendency to fall asleep. There are three stages of the process involving sleep:

1. being awake
2. non-rapid eye movement (NREM) sleep, which can be divided into:
   – stage 1: the transition from being awake to being asleep
   – stage 2: light sleep
   – stage 3: deep sleep
3. rapid eye movement (REM) sleep.

The stage of drowsiness that is most dangerous for road traffic users is stage 1 of the NREM stage. The sleepiness scale is also measured using the Karolinska sleepiness scale (KSS), the full version of which is presented in the Fig. 1. Drivers showing signs that are rated 6 or higher in the table are potentially dangerous.

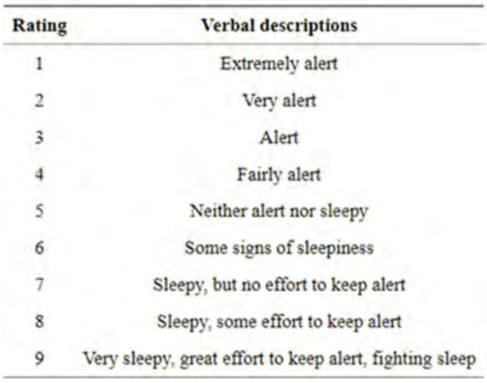

Rating	Verbal descriptions
1	Extremely alert
2	Very alert
3	Alert
4	Fairly alert
5	Neither alert nor sleepy
6	Some signs of sleepiness
7	Sleepy, but no effort to keep alert
8	Sleepy, some effort to keep alert
9	Very sleepy, great effort to keep alert, fighting sleep

Fig. 1. Karolinska sleepiness scale (KSS)

The National Highway Traffic Safety Administration, which is an organization operating in the United States, says that approximately 72 000 road traffic accidents in 2013 were caused by the drowsiness of drivers. Those accidents resulted in 44 000 injuries and 800 deaths. These numbers, however, could be underestimated, with the real number of fatalities being closer to 6000 [2].

Road accidents caused by tiredness can be more fatal. They usually occur at a higher speed, and as the driver is not vigilant, he has no possibility of braking or making other defensive maneuvers. The most common description of a road crash caused by drowsiness is an unexpected change of lane or the hitting of the car in front. Most fatigue-related accidents occur on motorways, which is due to the fact that there is almost no stimulus to the driver because of the monotonous and boring environment. Moreover, many of the activities that are usually thought to help fight sleepiness (such as increasing the radio volume, opening windows, or pointing a blowing cold air supply at the driver's face) do not actually help at all.

According to research, falling asleep rarely comes without warning, but drivers tend to ignore the early signals, such as: difficulties with concentration, heavy eyelids, yawning, and dropping of the head. A very common phenomenon is microsleep, which is described as falling asleep for more than 2, but less than 30 seconds without realizing it. The feeling the driver may have is that he thinks he was just nodding his head, even though he was really asleep.

As driver drowsiness is a common problem all over the world, there are many different ways to solve it. One quite popular and effective method is the painting of road lines in such a way that driving on them makes a very loud and unpleasant sound – so-called rumble strips. The aim of such strips is to wake up drivers if they begin to drift away from the correct lane.

To mitigate the results of highway accidents, special infrastructure is being built, e.g. crash barriers can absorb kinetic energy and keep the driver from hitting another element or an oncoming vehicle.

Car manufacturers are also trying to solve this problem, with driver fatigue detection systems becoming more and more popular.

2. Existing safety systems

2.1. Active and passive safety

Almost from the beginning of the automotive industry, car manufacturers have tried to improve their vehicles. The first recorded car accident happened in 1887, and from that date it can be said that road safety has also been important for producers.

Safety can be divided into that of active and passive. Passive safety is a set of vehicle features that attempt to minimize the effects of an accident. It can be divided into internal passive safety and external passive safety. Internal passive safety provides measures of reducing the probability of the driver or passengers being injured or killed, as well as the cargo being damaged. External passive safety concerns the safety of other road users, such as pedestrians. The most important passive safety devices are: seatbelts with proper regulation, child seats, airbags, and headrests. The following can also be seen to be important: the proper construction of the car's body, which absorbs kinetic energy in the event of a collision; proper placement of the gas tank; placing the car's battery outside of the crash zone; using safety glass; using proper door locks, which remain functional after the collision; using bendable steering shafts and a safe steering wheel: using energy-absorbing elements in the cabin; the reduction of pointy elements inside the car; and using non-flammable materials.

Active safety is a set of vehicle functions that either enable an accident to be avoided, or reduce the impact of the accident. It allows the driver to take preventive measures before an actual accident occurs. Many of the dynamic characteristics of a car can be related to active safety: the ability to reduce car slipping and drifting, the reduction of tire skids during braking, and the ability to accelerate on wet surfaces. The elements of active safety also include fog lights, good visibility, wipers, ergonomic seats, air conditioning, and an adjustable steering wheel. To improve a car's active safety, many subsystems and solutions are used in modern cars, for example:

1. Anti-lock Braking System (ABS), which prevents the wheel from blocking during intensive braking. Braking is performed in such a way that the grip of the wheels is as high as possible, with steering ability remaining intact.
2. Automatic Stability Requirement (ASR), which prevents the wheels from losing traction during acceleration. The system may use equipment provided by ABS, and also slow down the spinning of wheels due to a loss of traction.
3. Brake Assist, which is an emergency braking assistance system. If the system detects a sudden and strongly depressed brake pedal, it can automatically increase the brake fluid pressure.
4. Electronic Stability Control (ESC), which provides lateral stability. The system can take over the acceleration or braking required by the driver if it determines that the driver's actions are not correct. Corrections are usually made by braking one wheel in order to avoid actual skidding.

2.2. Visual safety systems

In 1956, during the General Motors Motorama, Buick company presented the first conceptual car with back-up cameras. Since then, the idea of a vision detection system has been developed by the automotive industry. When Toyota began offering a rear-view camera in its cars in 1997, the technology gained more and more popularity around the world.

Modern vehicles are usually equipped with not only one, but many cameras. An additional convenience for drivers is a system called Surround View. It can display a bird's eye view of the car. This is possible thanks to the many fisheye cameras mounted throughout the car.

Such cameras are used in the following safety systems:

1. Collision Avoidance System: its task is to prevent a collision or, if this is not possible, to reduce the severity of the collision. This system records images in front of the camera using radar, laser or a digital camera and, after processing the collected data, detects the possibility of an accident.
2. Pedestrian Detection System: enables the detection of pedestrians who may interfere with the car's path. The system can also be equipped with an infrared camera, which makes it easier to see pedestrians in dark surroundings.
3. Adaptive Cruise Control: a system that keeps the car at a constant distance from the car in front that is in the same lane and moving in the same direction.
4. Blind Spot Monitoring System: supports the driver by constantly monitoring the areas that are invisible to the driver. It can inform the driver if a car, which is not yet visible in the mirror, is overtaking him.
5. Lane Departure Warning System: warns the driver that the vehicle is about to leave the lane without the turn

signals being activated. More advanced versions of this system can correct the trajectory to ensure the car stays in its lane, or even autonomously keep the car centered in the lane. The driver is only asked to take control if the lane markings are insufficiently visible.

2.3. Driver tiredness detection systems in modern cars

The driver drowsiness detection system is supposed to detect the first signs of driver fatigue and warn him about the necessity to take a break. If the systems are more advanced, they can autonomously stop the car in a safe manner when it detects that the driver is nodding or falling asleep.

Almost every major car manufacturer offers a system with a similar name and mission. Depending on the manufacturer, the main principle of operation is different. The basic division includes three groups: vehicle-based measured, behavior-based measured, and physiology-based measured [3].

Vehicle-based measurement systems analyze data from multiple sensors and try to detect any anomalies, such as: a change in pressure on the brake or accelerator pedal, steering wheel movements, or lane deviations. When the analyzed value reaches a certain level, the system will alert the driver. The following can be seen as examples of such systems:

1. Steering wheel motion monitoring: the system constantly checks the steering angle sensor and measures driver fatigue. If the driver becomes sleepy, the number of minor tweaks to the steering wheel is less than when the driver is alert. This solution usually only counts small corrections ranging from 0.5° to 5°. Any wider correction can be considered a lane change rather than a course correction. The system is very sensitive when environmental issues appear. Even a minor defect in the steering system may interfere with the system measurements and give bad results. The poor condition of roads can also disrupt the proper operation of the system.
2. Standard Deviation of Lane Position: cameras mounted somewhere on the vehicle track the position of the car in the lane. If the driver is constantly changing lanes without using the turn signals, or drives between the lanes, the system assumes that the driver is sleepy and rest is advised. The system's greatest disadvantage is that it is prone to false results when environmental conditions are not good, like heavy rain, poor lane markings, snow, and poor lighting. The standard lane departure method can also be tricked into thinking that the driver is sleepy when driving under the influence of alcohol or drugs.

The driver drowsiness detection system based on behavioral measurements checks driver actions such as yawning, eye blinking, head position and the closing of eyes. Actions are recorded by a camera and then processed in order to determine if the driver should be alerted. When people get sleepy, they start to show many characteristic facial movements. These are frequent yawning, head tilting, head nodding, fast and constant blinking, and squinting. A non-invasive method of determining whether these symptoms are related to somnolence is to install a microcamera in front of the driver, to continuously monitor these behaviors, and to compare the collected data with normalized values.

The monitoring of driver tiredness may also be performed using physiological measures. There is some correlation between driver drowsiness and physiological symptoms such as electroencephalogram (EEG), electrooculogram (EoG), electromyogram (EMG), and electrocardiogram (EKG). The main benefit of this method is that it detects signs of tiredness before they affect the driver's ability to stay alert and drive safely. Nevertheless, the way this system works would require the driver to wear special equipment. It is seen to be more invasive than other solutions, so has never become popular and is not used in regular cars.

If we compare the top 20 car manufacturers, as in Table 1, it can be seen that vehicle-based behavior systems are the most common. The popularity of this solution is due to the relatively low cost of implementing such a system. It allows the reuse of existing sensors and the data collected by other subsystems. Only 3 car manufacturers offer a Driver Drowsiness Detection System based on driver behavior: BMW Attention Assistant, DS Driver Attention Monitoring System, Jaguar and Land Rover Driver Status Monitor. The brands listed are generally considered to be luxurious in some way, and therefore their customers are willing to pay extra for more advanced and sophisticated systems.

Table 1. Comparison of the top 20 car manufacturers

Company name	**System name**	**Vehicle based**	**Behavior**
Audi	Rest recommendation system	x	
BMW	Attentiveness Assistant	x	x
Citroen	Driver Attention Alert	x	
DS	DS Driver Attention Monitoring		x
Ford	Driver Alert	x	
Honda	Driver Attention Monitor	x	
Hyundai	Driver Attention Warning/Alert	x	
Jaguar/ Land Rover	Driver Condition Monitor		x
Kia	Driver Attention Warning	x	
Mazda	Driver Attention Alert	x	
Mercedes-Benz	Attention Assist	x	
GM Group	Driver Drowsiness Alert	x	
Nissan	Driver Attention Alert	x	
Renault	Fatigue Detection Warning	x	
Skoda	Fatigue Recognition Assistant	x	
Volkswagen	Driver Fatigue Detection	x	
Volvo	Driver Alert Control	x	

3. Proposal of a driver drowsiness detection system

3.1. General information

The idea of the proposed system is to use real-time video of the driver, which is captured by a camera placed in front of him. Thanks to the image processing algorithm, it detects characteristic landmarks of the face, such as the time from last stop, eye opening level, blink time, head tilt, and excessive yawning. After detecting landmarks, the system calculates factors that may lead to the driver becoming drowsy. If the system determines that the driver is drowsy, the driver will be warned on the screen and played an alarming sound. It is important that the algorithm is properly optimized, because the analysis time cannot exceed the capture time of one video frame. Moreover, to ensure good image quality, the camera in the system captures video at 30 frames per second. The results provided by the system should be clear and precise for all drivers.

Such a system can be integrated with the car's safety and infotainment system, and therefore the results of driver drowsiness can be supplemented with information about keeping the car in one line, sudden movements of the steering wheel, and irregular use of the gas and brake pedals. Moreover, the system should persistently alert the driver that he is sleepy. If the driver does not rest after several alarms, the on-screen notification and alarm should become increasingly disturbing.

3.2. Face detection systems

Face detection systems first find the driver's face, and then locate more specific points. Descriptions of a few selected examples of such programs are shown below:

1. Face detection is the computer's ability to find a human face in a processed image thanks to certain patterns that can be seen on every face. A proper face detection algorithm should be able to find multiple faces in a photo, and not just find a face among the other elements of the photo. Parameter calibration is a key element of a properly functioning system.
2. Face recognition is the computer's ability to determine whether a processed face belongs to a specific person. Due to differences in faces, the algorithms can map the facial attributes during calibration, and then look for the distinctive attributes during recognition.
3. Face analysis is the computer's ability to read certain characteristics of a depicted face. Systems based on deep learning and machine learning can determine attributes such as age, gender, and even emotions.
4. Face tracking is the computer's ability to find specific facial characteristics in each frame of a processed video. Similar to face detection, algorithms learn to find patterns on the user's face. Distinctive points of the eyes, nose, mouth and chin can be specified.

This article is about a driver detection drowsiness system that focuses on face tracking.

3.3. How the program finds a face in a picture

Each digital image is made of pixels. A set of pixels of a given color (based on the RGB model) creates an image that can be stored in memory or displayed on the user's display. Therefore, the color of each pixel is described by a tuple of three numbers. In image processing, algorithms usually handle black and white images, which is due to the fact that color information is useless in most cases. Black and white images are described in grayscale, where (0) stands for black pixels, and (255) stands for white pixels, with all numbers in between being grayish.

The face detection algorithm was created in 2001 by Paul Viola and Michael Jones. The algorithm is divided into 4 main steps:

1. Selection of Haar-like features
2. Creating an integral image
3. Running AdaBoost
4. Creating cascades of classifiers

The algorithm scans the image and, looking at smaller areas, tries to find a face by looking for attributes in each area. Since the image can contain more than one face, and also have different sizes, the algorithm must be able to scale.

The Haar-like features make use of the properties seen in every human face captured in the photo. The most prominent feature is that the eyes are usually darker than the tip of the nose. To determine the brightness of the analyzed region, the algorithm adds the pixel values of each region. The lower sum tells the algorithm that the computed region is darker than the one with the larger sum. A visual representation of Harr-like features is shown by dividing a rectangular part of the picture, and then presenting it as black and white rectangles. Examples of it are shown in Fig. 2 below.

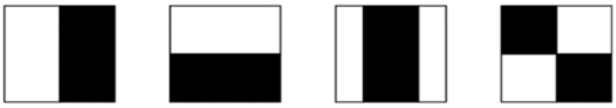

Fig. 2. Haar-like features used to detects patterns in images

Integral image (summed-area table) is an algorithm that speeds up the calculation of the sum of pixel values in a specific area. To compute the integral image, each pixel in a given area only needs to be processed once, and therefore only four numbers are needed.

With these calculated values, Adaptive Boosting (AdaBoosting) can be very useful. According to machine learning theory, a weak learner only classifies if a region contains a face slightly better than random guessing. Combining many weak learners together makes a strong learner, who is much better at finding faces. Adaptive Boosting is all about taking a plethora of weak classifiers and turning them into a strong classifier. The adaptive gain algorithm is applied to all image areas. Several areas of the image will give a higher score than others. These areas are classified as positive. For facial recognition, they are considered to include the face. Those considered not to contain a human face are classified as a minus. As the next iteration progresses, the negative elements gain more weight, and become more important for the classifier. The minus and plus areas change accordingly. After a few iterations, the classifiers are split equally, and the strong classifier is ready.

Image processing uses cascading classifiers. Cascade means that many subsequent behaviors are necessary to determine whether an image contains a face. The cascade is divided into many stages. If the first step of the cascade evaluates the region as positive, the region then moves on to further processing steps that are termed as "maybe". If either step evaluates a region as negative, the region is no longer processed and is considered to not contain a face.

3.4. Eye recognition and blinking detection

In order to detect objects on a detected face, the algorithm must use facial landmarks. The algorithm tries to find the required points on the face. Detecting facial landmarks is a two-step process. First, the algorithm finds faces in general, and then has to locate the key facial structures in the area of the face of interest. Most face landmark algorithms detect the following items: jaw, nose, left eye, right eye, left eyebrow, right eyebrow, mouth. The Dlib library used in this project to detect facial landmarks allows the location of 68 points of interest [4]. The points that are found are presented in Fig. 3.

If the classifier detects a facial landmark in an image containing a face, the result will be like in Fig. 4.

After detecting facial landmarks, it is possible to analyze whether the driver is sleepy. The clearest sign of sleepiness comes from the driver's eyes and blinking. Blink detection in this design is based on the so-called Eye Aspect Ratio (EAR). The previous algorithm is efficient enough to track 6 characteristic points for each eye. The proposed solution of using the EAR uses these 6 points for each and after simple calculations returns the aspect of the openness of the eye.

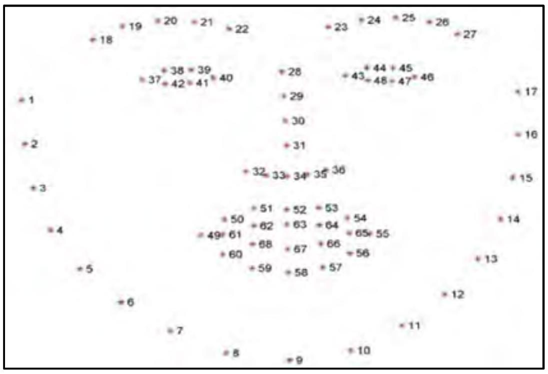

Fig. 3. Facial landmarks that are detected by the algorithm

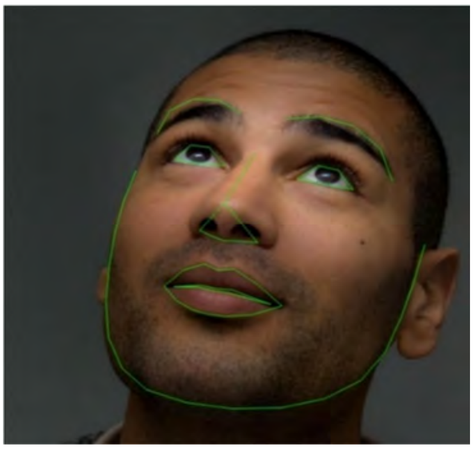

Fig. 4. Facial landmarks detected

According to research, there is a constant relationship between these points. Therefore, equation (1) can be derived in order to describe the proportions of the eye.

Equation (1) allows the distance between the vertical and horizontal landmarks of the eye to be calculated, which when properly weighted leads to the EAR. These landmarks are presented in Fig. 5.

$$\text{EAR} = \frac{\|p_2 - p_6\| + \|p_3 - p_5\|}{2 * \|p_1 - p_4\|} \tag{1}$$

When the eye is open, the proportions of the eye are almost constant. However, when the eye is closed, the number almost drops to zero. It is safe to assume that the EAR dropping below a certain threshold corresponds to the user blinking. Using the eye aspect ratio is also useful for detecting driver drowsiness. Because the proportions of the eye drop below a certain level and do not change their value for a long time, the blinks exceed the usual 100–400 ms. Over time, it can be assumed that the driver becomes drowsy.

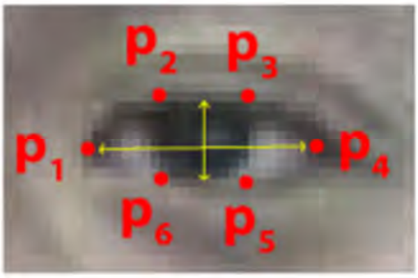

Fig. 5. Landmarks for an opened and closed eye

The algorithm used in the created driver tiredness detection systems can be divided into two stages:

1. Calibration phase: it is assumed that the driver starts the journey fully awake, and therefore the mean values of the parameters are calculated and used later as a model.
2. The system calculates the driver's drowsiness by comparing the actual values with the reference values collected during the calibration phase.

The average value of the EAR is calculated during the calibration, and if its value drops by more than 40% it is assumed that the driver is sleepy. The system calculates the blinking frequency every 10 seconds. The algorithm also records the time of a single blink. It is one of the most important parameters in determining drowsiness. Tilting of the head is also considered to be one of the factors of driver tiredness. An asymmetrical head position adds points to your overall drowsiness score.

3.5. Example of how the system works

Calibration takes place each time the system is started. This is important, as lighting conditions can vary and a different driver may be seated in the seat. In the calibration mode, the system displays research and development data, such as the number of blinks, blink duration, eye aspect ratio, face length, face position and blink frequency. The default calibration time is 60 seconds, which is enough for development purposes. In real-world situations it should be increased to at least 5 minutes for better data collecting. After calibration, all results are averaged and stored in the system’s memory for reference. It is possible to recalibrate the system in the event of a malfunction. During calibration, the user's eye and nose are highlighted, with the mean value of the EAR obtained during calibration being between 0.30 and 0.35.

After calibration, the system will start detecting driver drowsiness. The parameters obtained from the captured video frames are compared with the reference values. Each parameter is properly weighted so as not to distort the final result. The most important parameters are the time of a single blink and the proportions of the eye. These parameters can detect if a driver is sleepy or not. Closing eyes for more than one second greatly increases the effect of sleepiness. A special smile detection algorithm can lower the eye aspect threshold, as people tend to squint when smiling. Parameters such as yawning and tilting the head are weighted as less important. Paying too much attention to tilting your head can cause many false positives. Safe driving requires the driver to frequently check the mirrors, and this may cause some drivers to tilt their head slightly.

When the system remains active, with developer mode enabled, it displays all calculated information on the image. This means that it is possible to see if all the calculated information is correct. The most important parameter for the system remains the calculated fatigue value. This is the final result of the system, and ranges from 0 to 300. When the value is close to 0, the driver is considered fully alert. When the value exceeds 120, the system will consider the driver to be drowsy. Information appears on the screen and an audible alarm sounds.

An example of when the driver is alert is visible in Fig. 6, with Fig. 7 showing the driver when he is tired.

Blinks: 41
EAR: 0.32
Fatigue: 84.00
Blink duration: 0.5481
Face length: 0.8365
Blink freq: 1.0000
EAR_TRESH: 0.25
FACE POSITION: 271.0000
Menu: C – Details | Q – Quit

Fig. 6. User's interface when the driver is alert

Blinks: 10
EAR: 0.19
Fatigue: 142.54
Blink duration: 11.3161
Face length: 0.9038
Blink freq: 0.0000
EAR_TRESH: 0.25
FACE POSITION: 357.0000
Drowsiness Detected!
Menu: C – Details | Q – Quit

Fig. 7. User's interface when the driver is drowsy

In Figure 6, the fatigue level is 84 (visible in the top right corner). The proportion of the eye is high, and this is one of the main elements that has an influence on the final result. In Figure 7, the fatigue level is 142.54 (visible in the top right corner), and therefore the alarm is shown on the screen. When the fatigue detection is over, the system returns a graph of the recorded fatigue level for the entire period of activity. This allows the values recorded by the system at peak times to be better analyzed. Any anomalies, such as sudden changes in lighting or looking for upcoming traffic, which may cause different result values, are visible in the charts. When the system loses track of the driver's line of sight, the fatigue value remains constant until sight is found and tracked again.

An example of the mentioned chart can be seen in Fig. 8. The analysis of this graph may bring some conclusions about the operation of the system and its effectiveness. The first seconds of work are needed to determine the appropriate level of driver drowsiness. After about 50 seconds, the system gets a fairly consistent result, which is set to around 90. This level of tiredness is considered by the system as "being alert". Up to a peak of around 270 seconds after takeoff, there are some dips in fatigue. It gets values of around 65. This may be due to a change in lighting or wider eyes, or could actually be a real result. After the peak has caused the driver to look around, or squinttheir eyes to see traffic lights or avoid direct sunlight, the driver's fatigue level returns to its previous level and becomes stable (ranging from around 65 to 80).

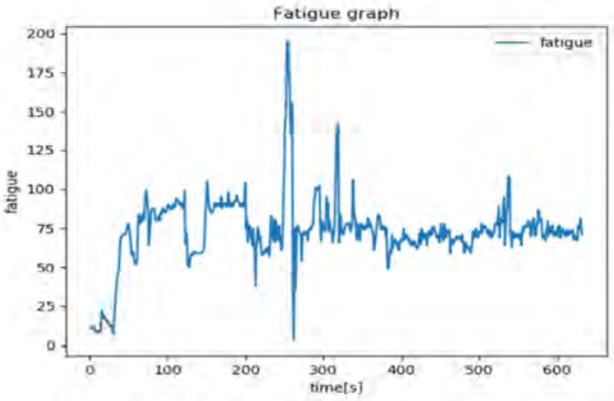

Fig. 8. Chart of the recorded fatigue level. The driver was alert

Despite the already existing systems of this type on the market, there are still many possibilities for their improvement or modification.

The experimental system mentioned in the article was built and tested at the Department of Vehicle Engineering at the Wrocław University of Technology.

Nomenclature

ABS	Anti-lock Braking System
ASR	Automatic Stability Requirement
EAR	Eye Aspect Ratio
ESC	Electronic Stability Control
KKS	Karolinska sleepiness scale
NREM	non-rapid eye movement sleep
REM	rapid eye movement sleep

Bibliography

[1] Global Status Report on Road Safety. World Health Organization, 2018. http://apps.who.int/iris/bitstream/handle/10665/277370/WHO-NMH-NVI-18.20-eng.pdf?ua=1

[2] Centers for Disease Control and Prevention. Information about drowsy driving risks. https://www.cdc.gov/features/dsdrowsydriving/index.html

[3] SAŁAPATEK, D., DYBAŁA, J., CZAPSKI, P. et al. Driver drowsiness detection systems. *Proceedings of the Institute of Vehicles.* Warsaw University of Technology. 2017, **3**(112), 41-48.

[4] PyImageSearch. Information about face elements detection. https://www.pyimagesearch.com/2017/04/10/detect-eyes-nose-lips-jaw-dlib-opencv-python

[5] LEMOV, M.R. Car Safety Wars: One Hundred Years of Technology, Politics, and Death. *Fairleigh Dickinson University Press*. 2015.

[6] ROSS, H.L. Functional safety for road vehicles. Springer 2015. https://doi.org/10.1007/978-3-319-33361-8

[7] OKA, D.K. Building Secure Cars: Assuring the Automotive Software Development Lifecycle. *Wiley*. 2021. https://doi.org/10.1002/9781119710783.ch3

[8] LOTHAR, W., SEIFFERT, U. Automotive Safety Handbook. *SAE International*. 2007. https://doi.org/10.4271/R-377

[9] AGARWAL, A., YADAV, V. Advanced integrated future vehicle telematics system concept modelling. *Global Journal of Technology & Optimization*. 2017, **8**(2), 1-6. https://doi.org/10.4172/2229-8711.1000215

Piotr Haller, MEng. – Faculty of Mechanical Engineering, Wroclaw University of Technology.
e-mail: *piotr.haller@pwr.edu.pl*

Prof. Radoslaw Wrobel, DSc., DEng. – Faculty of Mechanical Engineering, Wroclaw University of Technology.
e-mail: *radoslaw.wrobel@pwr.edu.pl*

Gustaw Sierzputowski, DEng. – Faculty of Mechanical Engineering, Wroclaw University of Technology.
e-mail: *gustaw.sierzputowski@pwr.edu.pl*

Radostin Dimitrov, DEng. – Faculty of Mechanical Engineering, Varna University of Technology.
e-mail: *r_dimitrov@tu-varna.bg*

Veselin Mihaylov, DEng. – Faculty of Mechanical Engineering, Varna University of Technology.
e-mail: *v_mihaylov@tu-varna.bg*

Article citation info:
KOZAK, M., KRYGER, T., SIEJKA, P. Environmental analysis of the traffic closure on Piotrowo and Berdychowo streets in Poznań. *Combustion Engines*. 2022, **190**(3), 18-22. https://doi.org/10.19206/CE-142593

Miłosław KOZAK
Tomasz KRYGER
Piotr SIEJKA

Combustion Engines
Polish Scientific Society of Combustion Engines

Environmental analysis of the traffic closure on Piotrowo and Berdychowo streets in Poznań

ARTICLE INFO

Received: 6 September 2021
Revised: 26 September 2021
Accepted: 26 September 2021
Available online: 5 October 2021

The article deals with the ecological assessment of the potential road investment, which is the closure of Piotrowo and Berdychowo streets within the campus of the Poznań University of Technology. The research was carried out on a simulation model of the city of Poznań with the use of PTV software. Research has shown that the closure of these streets has virtually no impact on city-wide emissions. However, the emissions deterioration takes place on a local scale, i.e. in the vicinity of the campus of the Poznań University of Technology and on most of the streets leading to it.

Key words: *road traffic simulation, environmental analysis, exhaust emissions, road infrastructure*

1. Introduction

Transport is one of the main service areas in the world, therefore great emphasis is placed on the process of its development, infrastructure reconstruction, and ensuring the safety and comfort of all road users. For many years, one of the most important aspects of transport has been the assessment of its impact on the natural environment. This assessment is possible through direct measurements of vehicle emissivity, under dynamometer or real conditions. Data on air quality is provided by measurements of concentrations of harmful compounds in the air carried out by, for example, stations of the Provincial Inspectorate for Environmental Protection. In the case of Poznań, both current data and annual reports on air quality in the Poznań agglomeration are available.

The sources of CO and HC emissions from means of transport are mainly vehicles with spark-ignition engines. The share of vehicles with spark-ignition and diesel engines in the NO_x emissions is similar, while the majority of PM emissions are due to vehicles with diesel engines [11]. Particulate matter is one of the most harmful components of engine exhaust [17]. The report of the US Environmental Protection Agency on the harmfulness of exhaust gas from diesel engines [19] showed, on the basis of several dozen independent medical studies of humans and laboratory tests on animals, that PM has carcinogenic properties and contributes in particular to the occurrence of lung cancer. The results of the works [5, 9, 13] show that the average PM emission decreases when the permitted speed of vehicles on a given section decreases. Among the hydrocarbons present in the exhaust gas, aromatic hydrocarbons, including benzene, are the most toxic [15].

It should be emphasized that the traffic conditions of vehicles, and consequently the operating conditions of their engines, largely determine the level of fuel consumption and the toxicity of exhaust gases [1, 2, 3, 7, 12, 14]. These, in turn, largely depend on the applied infrastructure solutions and road traffic control [4, 8, 18].

The assessment of the impact of transport on the environment is also possible through simulations. The basic objectives of road traffic modeling often concern environmental issues and include [10, 16]:

- construction of a displacement matrix specifying the size of the flows moving between different parts of the analyzed area (e.g. a city),
- construction of traffic maps, determination of the impact of traffic on the environment,
- identifying future transport needs,
- determining the optimal method of reconstructing road network elements,
- determining the optimal stages of the road network expansion or construction stages of a given road investment,
- support in determining the optimal route of new streets and determining their technical parameters,
- support in determining types of road intersections and their parameters along new road routes,
- determination of changes in the traffic distribution on the city's road network after the construction of a new street, intersection, shopping center, entertainment center, sports hall, petrol station, etc.

There are many programs for modeling and simulating traffic on the market, but in Poland the most popular program for modeling and forecasting traffic is VISUM, while the most popular of the traffic simulation program is VISSIM. Both programs were developed by PTV. Currently, these programs are used by municipal units, incl. in Warsaw, Kraków, Wrocław, Poznań, Gdańsk, Kielce, Katowice and Tychy, as well as consulting and design companies [6]. This type of software was also used in the research described in the article.

The object of the research was the analysis of the road section in the city of Poznań, covering the areas next to the academic campus of the Poznań University of Technology.

The thesis is based on a situational analysis of the closure of Piotrowo and Berdychowo Streets (Fig. 1) to public traffic. Currently, these streets are available to every road user, the idea of excluding them from traffic is to close the campus only to people associated with the Poznań Univer-

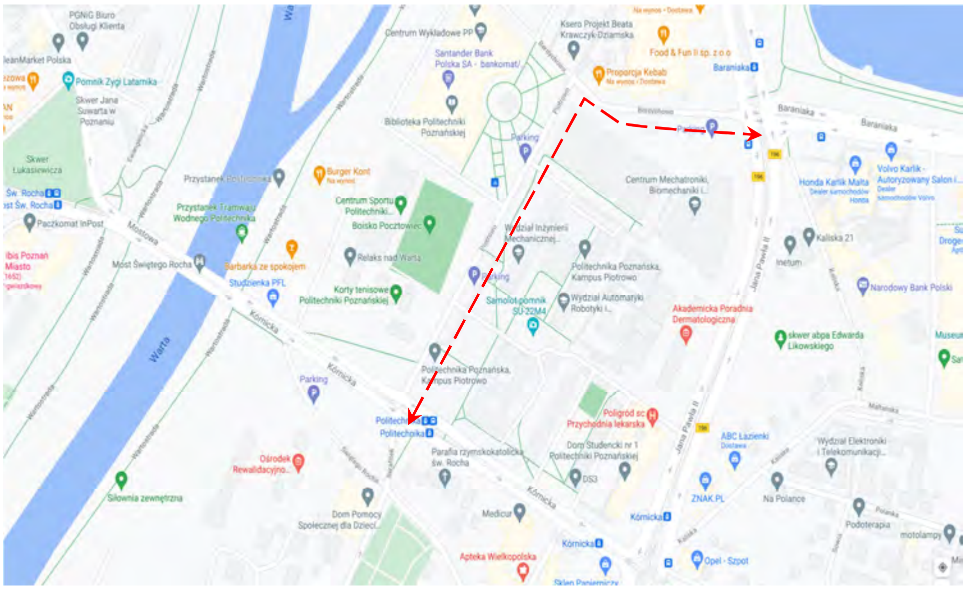

Fig. 1. Piotrowo and Berdychowo Streets in Poznań (red dotted line), the closing of which was analyzed in this article

of Technology, thus increasing the level of security and limiting third parties' access to the area intended for students and university employees. The most likely solution will be the use of barriers with the use of a card reader, the relevant certificates can only be issued to holders of employee cards or students with an electronic ID, which will allow only specific groups to move around the campus. For the sake of comparison, a simulation will be presented for both i.e. the completed initiative and the current state. On the basis of the provided analyzes, conclusions will be presented describing the impact of the investment on the level of emissions of vehicles involved in the traffic.

In order to carry out the analysis, the forecast road model for the city of Poznań was used. The program, equipped with appropriate data on traffic flows after interfering with the road network, simulated the probable loads for the remaining sections in the vicinity of the studied area. On the basis of the obtained results, a comparative analysis was performed for each of the analyzed exhaust gas components for the current state and the state after infrastructural changes. The analysis was divided into three stages due to the level of detail of the description. The first step relates to the infrastructure of the entire city. The second level focuses on a narrowed area covering the closest vicinity of the studied sections. The third stage examines in details selected adjacent road sections (Kórnicka Str., Jana Pawła II Str., Baraniaka Str., Bolesława Krzywoustego Str. and the bridge of St. Roch).

2. Results of simulation tests and their analysis

The first stage of analysis – the infrastructure of the entire city

Figures 2 and 3 show, respectively, the results of traffic simulations for the current state and after the investment in the afternoon peak conditions. Assuming the general analysis, i.e. the impact of excluding Piotrowo and Berdychowo streets for all road traffic in the city of Poznań, it can be seen that there is practically no impact on the global emission of individual exhaust gas components (Fig. 4).

Second stage of analysis – adjacent infrastructure

The next stage is based on the analysis of the infrastructure area directly adjacent to the Poznań University of Technology and streets closed to vehicle traffic. As shown in Figure 5, the exclusion of the analyzed streets causes an increase in the emission of exhaust components from vehicles participating in the traffic in this area, in particular, an increase in CO emissions can be seen.

The third stage of analysis – emissions on individual streets

In the last stage, a detailed analysis is presented, i.e. the emissions values for individual streets adjacent to the change area. The following sections and streets were taken into account:

1. Jana Pawła II Street (from Rondo Śródka do Rondo Rataje),
2. Kórnicka Street,
3. St. Roch bridge,
4. Baraniaka Street,
5. Bolesława Krzywoustego Street.

Diverse changes in emissions were obtained on individual analyzed sections (Figures 6-10). For Jana Pawła II Street (Fig. 6) a slight relative increase in emissions was obtained, mainly in terms of CO. However, it is a very busy street, hence the high absolute values of emissions. The traffic on Jana Pawła II Street is only slightly supplied by Piotrowo Street. Large – by about 50% – increases in emissions were recorded at Kórnicka Street (Fig. 7). This is due to the fact that this street mainly takes over the traffic that would normally take place along Piotrowo Street. Emission on the St. Roch bridge after the closure of ul. Piotrowo is slightly smaller (Fig. 8). This may be associated with the resignation of some travelers from traveling on this bridge and choosing alternative travel routes. We can observe a similar situation for Bolesława Krzywoustego Street (Fig. 9). Piotrowo Street is largely supplied by vehicles running along Baraniaka Str., similarly in the opposite direction, many vehicles from Piotrowo Str. drive through the intersection straight ahead, continuing along Baraniaka Str. Hence the closure of Piotrowo Street generates a significant reduction in emissions at Baraniaka Str. (Fig. 10).

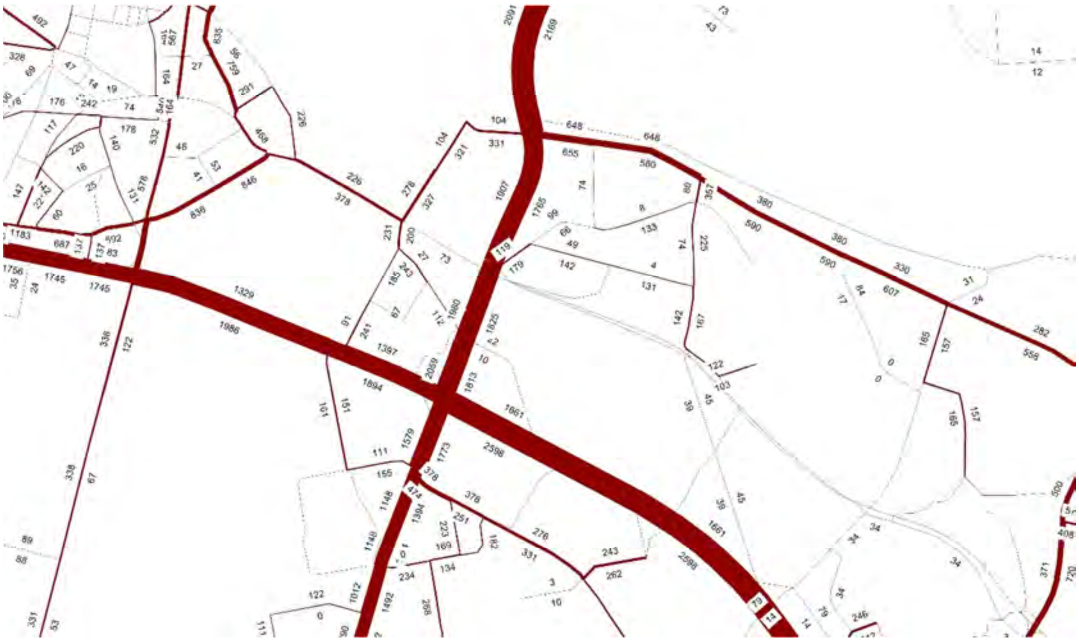

Fig. 2. Distribution of vehicle traffic in the analyzed area as it is in the afternoon peak

Fig. 3. Traffic distribution in the analyzed area in the afternoon rush hours after the closure of Piotrowo and Berdychowo streets

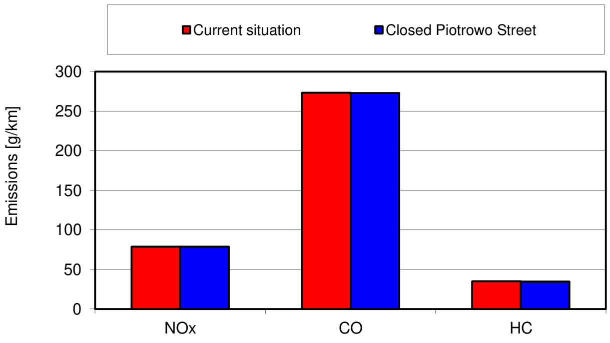

Fig. 4. Average vehicle emissions on the streets of Poznań in the afternoon rush hours

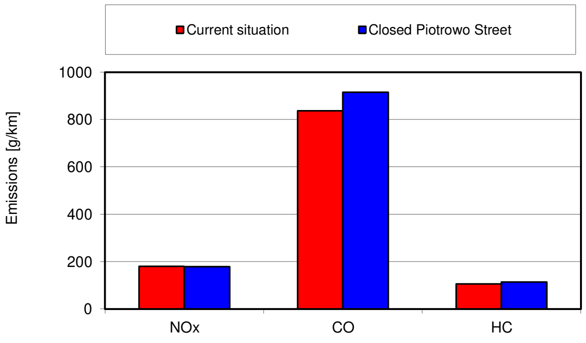

Fig. 5. Average vehicle emissions in the area directly adjacent to the Poznań University of Technology at Piotrowo Street in the afternoon rush

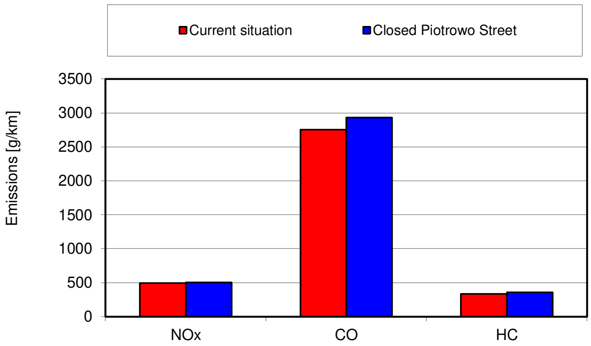

Fig. 6. Emissions of vehicles in the afternoon peak at Jana Pawła II Str.

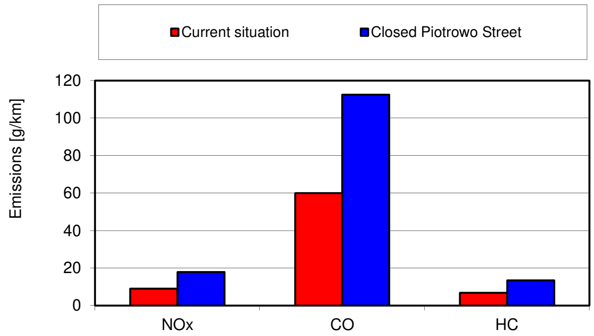

Fig. 7. Emissions of vehicles in the afternoon peak at Kórnicka Str.

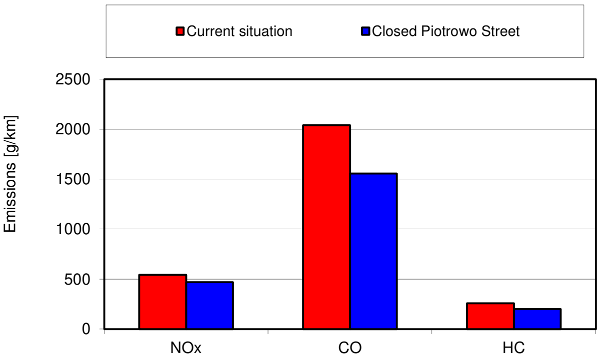

Fig. 10. Emissions of vehicles in the afternoon peak at Baraniaka Str.

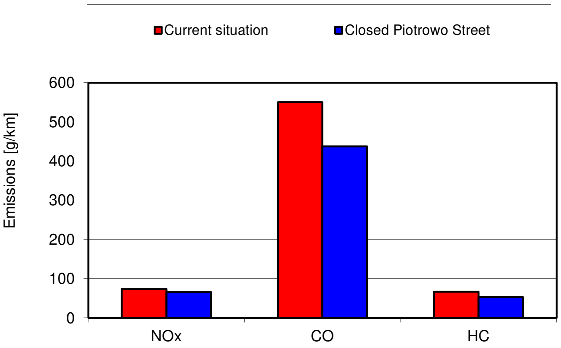

Fig. 8. Emissions of vehicles in the afternoon peak on the St. Roch bridge

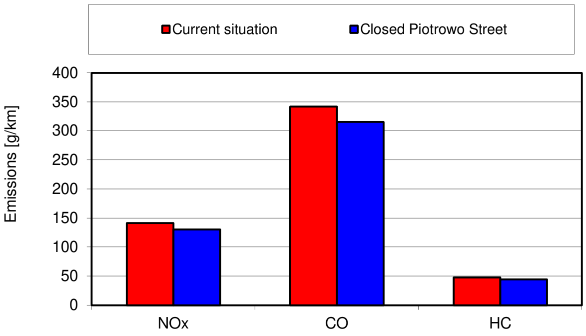

Fig. 9. Emissions of vehicles in the afternoon peak at Bolesława Krzywoustego Str.

3. Conclusions

Modeling and simulation programs are a useful tool in the environmental assessment of road investments. The accuracy of the results is influenced by many factors, starting with the selection of the simulator, the existing additional library that calculates ecological aspects, ending with the volume of collected data. The forecasted model, as the name suggests, presents only approximate values and should not be treated as a real model.

Based on the conducted research, it can be concluded that the closure of Piotrowo and Berdychowo Streets in Poznań to public traffic does not have a significant impact on the environmental situation in the entire city in terms of the exhaust emissions. On this scale, the closure of these streets generates changes in emissions at the level of at most per-milles. However, the closure of Piotrowo and Berdychowo streets has a more significant negative impact on a local scale. When analyzing the areas adjacent to the campus of the Poznań University of Technology, an increase in the exhaust emissions by several percent is observed. On some streets (Kórnicka Str.) emission increase reaches 50%. On others, however, emissions are declining. Ultimately, an unambiguous environmental assessment of this solution is difficult. It can be assumed to be neutral or slightly negative.

Bibliography

[1] BEBKIEWICZ, K., CHŁOPEK, Z., SZCZEPAŃSKI, K. et al. The influence of the properties of vehicles traffic on the total pollutant emission. *Zeszyty Naukowe Instytutu Pojazdów Politechniki Warszawskiej*. 2017, **1**.

[2] BIELACZYC, P., MERKISZ, J., PIELECHA, J. Stan cieplny silnika spalinowego a emisja związków szkodliwych. *Wydawnictwo Politechniki Poznańskiej*, Poznań 2001.

[3] CHŁOPEK, Z., LASOCKI, J. Correlation investigations into pollutant emission and the operational states of compression-ignition engines in dynamic tests. *Combustion Engines*. 2017, **169**(2), 87-92. https://doi.org/10.19206/CE-2017-215

[4] CORRIERE, F., GUERRIERI, M., TICALI, D. et al. Estimation of air pollutant emissions in flower roundabouts and in conventional roundabouts. *Archives of Civil Engineering*. 2013, **2**, 229-246. https://doi.org/10.2478/ace-2013-0012

[5] DIJKEMA, M., VAN DER ZEE, S., BRUNEKREEFT, B. et al. Air quality effects of an urban highway speed limit reduction. *Atmospheric Environment*. 2008, **42**(40), 9098-9105. https://doi.org/10.1016/j.atmosenv.2008.09.039
[6] DYBICZ, T. Modelowanie i symulacje ruchu, rys historyczny i aktualnie stosowane oprogramowanie. *Konferencja Naukowo-Techniczna SITK*. Kraków 2009.
[7] FONSECA, N., CASANOVA, J., VALDES, M. Influence of the stop/start system on CO_2 emissions of a diesel vehicle in urban traffic. *Transportation Research Part D: Transport and Environment*. 2014, **16**(2), 194-200. https://doi.org/10.1016/j.trd.2010.10.001
[8] GUERRIERI, M., CORRIERE, F., PARLA, G. et al. Reducing air pollutants through road innovative intersections. *Applied Mechanics and Materials*. 2013, **459**, 563-568. https://doi.org/10.4028/www.scientific.net/amm.459.563
[9] INT PANIS, L., BECKX, C., BROEKX, S. et al. PM, NO_x and CO_2 emission reductions from speed management policies in Europe. *Transportation Research Part D: Transport and Environment*. 2011, **18**(1), 32-37. https://doi.org/10.1016/j.tranpol.2010.05.005
[10] KOZAK, M., NIJAK, D., MERKISZ, J. Predicting exhaust emission changes resulting from local improvement of city bus traffic in Poznan. *Eighth International Conference on Urban Regeneration and Sustainability*. 3-5.12.2013. Putrajaya, Malaysia.
[11] KOZAK, M. Studium wpływu komponentów tlenowych oleju napędowego na emisję toksycznych składników spalin z silników o zapłonie samoczynnym. *Wydawnictwo Politechniki Poznańskiej*. Poznań 2013.
[12] LIJEWSKI, P., KOZAK, M., FUĆ, P. et al. Exhaust emissions generated under actual operating conditions from a hybrid vehicle and an electric one fitted with a range extender. *Transportation Research Part D: Transport and Environment*. 2020, **78**, 102183. https://doi.org/10.1016/j.trd.2019.11.012
[13] LOPEZ-APARICIO, S., GRYTHE, H., THORNE, R. Costs and benefits of implementing an environmental speed limit in a Nordic city. *Science of the Total Environment*. 2020, **720**, 137577. https://doi.org/10.1016/j.scitotenv.2020.137577
[14] MERKISZ, J., JACYNA, M., ANDRZEJEWSKI, M. et al. The influence of the driving speed on the exhaust emissions. *Combustion Engines*. 2014, **156**(1), 41-47. https://doi.org/10.19206/CE-116951
[15] National Center for Environmental Assessment. US Environmental Protection Agency: Carcinogenic Effects of Benzene – An Update. Waszyngton 1998.
[16] NIJAK, D. Środowiskowa ocena rozwiązań transportowych z wykorzystaniem symulacji ruchu drogowego. *Praca doktorska*. Wydział Inżynierii Lądowej i Transportu Politechniki Poznańskiej 2021.
[17] SCHEEPERS, P., BOS, R. Combustion of diesel fuel from a toxicological perspective. *International Archives of Occupational and Environmental Health*. 1992, **64**, 149-161. https://doi.org/10.1007/BF00380904
[18] SHANCITA, I., MASJUKI, H., KALAM, M. et al. A review on idling reduction strategies to improve fuel economy and reduce exhaust emissions of transport vehicles. *Energy Conversion and Management*. 2014, **88**, 794-807. https://doi.org/10.1016/j.enconman.2014.09.036
[19] United States Environmental Protection Agency (EPA): Health Assessment Document For Diesel Engine Exhaust. Washington 2002.

Miłosław Kozak, DSc., DEng. – Faculty of Civil and Transport Engineering, Poznan University of Technology.
e-mail: *miloslaw.kozak@put.poznan.pl*

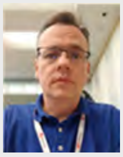

Piotr Siejka, MEng.
e-mail: *piotr_siejka@wp.pl*

Tomasz Kryger, MEng. – Wolter Koops International Logistics.
e-mail: *tomekk993@gmail.com*

Article citation info:
MARZEC, P. Tests of a SI engine powered by gaseous fuels blends of LPG + DME of various proportions with variable load. *Combustion Engines*. 2022, **190**(3), 23-26. https://doi.org/10.19206/CE-144124

Paweł MARZEC

Combustion Engines
Polish Scientific Society of Combustion Engines

Tests of a SI engine powered by gaseous fuels blends of LPG + DME of various proportions with variable load

ARTICLE INFO

Received: 19 September 2021
Revised: 15 November 2021
Accepted: 22 November 2021
Available online: 5 December 2021

The article presents the test stand and the test results of a vehicle with an SI engine, fueled by a blends of LPG and DME gaseous fuels. During the tests, a chassis dynamometer was used, which reproducibly reflected road conditions. The tests were carried out for various shares of DME in the mixture, thus determining the maximum possible share of this fuel. The measuring points have been extended with different engine loads and different rotational speeds. The analysis of the pressure inside the engine cylinder made it possible to compare the operation of the engine powered by mixtures of different proportions to the reference fuel – LPG.

Key words: *combustion process, fuel consumption, gaseous fuel blends, ignition correction, engine load*

1. Introduction

The ever-increasing demand for conventional motor fuels has also increased the interest in alternative fuels. Their market share is all the more significant, the more stringent exhaust emission standards that new car manufacturers throughout the European Union have to face. Alternative fuels, apart from the possibility of powering engines, must meet other criteria, including the two most important ones – ecological and economic assessment. The emissivity assessment is primarily influenced by the amount of harmful and toxic substances in the products of the combustion process. Their amount must be lower than that derived from the combustion of conventional fuels. The economic assessment is carried out in relation to conventional fuels and in the absence of measurable benefits for users, it is not possible to adopt such energy carriers on a wide scale of the market [1].

The current, very intensive development of alternative drives has, in a sense, verified the requirements set by lawmakers and also by the society. The pursuit of broadly understood eco-mobility began to be perceived on a larger scale. It is primarily the awareness of emissions from the entire life cycle of fuel – from its extraction, processing, distribution, to combustion products in an internal combustion engine. A similar approach applies to electric and hybrid vehicles that require external charging. Currently, the electricity used to charge these vehicles comes largely from non-renewable sources. As a result, the carbon footprint remains at a similar level as in the case of fully conventional drives. However, a significant advantage of battery powered vehicles is the fact that there is no local emission. Electric vehicles, the way of use of which is assigned to a given location, resulting from their use in urban areas, are not so burdensome for the environment. This is due to the lack of exhaust fumes and significantly lower noise. Examples of such vehicles are public transport buses or other public transport vehicles, vehicles used for the purpose of serving the urban economy or transport companies that perform the so-called last mile transport. Non-urban emissions in the case of generating electricity for EVs do not affect the deterioration of air quality in the city center, which significantly improves the quality of life of its inhabitants. However, the above benefits do not have an impact on total emissions as long as electricity is not obtained to a greater extent from renewable sources or the fuels burnt are replaced by fuels with a reduced share of coal. Another current problem of electric vehicles is energy storage. Currently available batteries often do not provide half of the vehicle's real range compared to conventionally powered vehicles. The development and use of electric vehicles also depend on the expansion of the infrastructure for charging and servicing such vehicles. Therefore, an important activity is the simultaneous development of alternative fuels. The global increase in fuel demand is related to the further development of fuels derived from renewable sources as well as from fossil sources.

2. Preparation of fuel blends

Alternative fuels also include mixtures of gaseous fuels. An example of this type of mixtures can be the mixture of LPG and DME presented in the following study. LPG, a mixture of propane and butane, is produced from crude oil in the refining process. Due to the fact that it is derived from fossil raw materials, its production, availability and scope of application are limited. The lower proportion of carbon in relation to gasoline gives about 10% lower carbon dioxide emissions.

DME is an organic chemical compound from the ether group, colorless with a characteristic odor, flammable and explosive, moderately soluble in water. It can be produced from fossil resources such as natural gas or hard coal, as well as from biomass, then it is referred to as bioDME. Currently, dimethylether is used in the energy and cosmetics industries, as well as in transport as a fuel for diesel engines, due to the high cetane number – 55 [2].

The similar physical and chemical properties of both fuels allow them to be mixed, safely stored, and used as fuel in an SI engine [3–5].

The production of mixtures on the stand included the preparation of fuel for experimental tests on a chassis dynamometer. It consisted in refueling the mixture components – LPG and DME into a common tank. First, fuel with a higher mass fraction was refueled in order to calculate the necessary mass fraction of the second fuel in the next step. The mass fraction of the second fuel (DME) differed depending on the need to obtain a specific mixture. The tank for the mixture was placed on an electronic scale with an accuracy of 1 gram. Also during the tests of the vehicle on the chassis dynamometer, the tank was placed on the scales, which made it possible to measure fuel consumption in one-minute intervals. The vehicle was powered by connecting the fuel tank to the gas reducer, using a cable for automotive gas installations. The construction of the stand is shown on the diagram (Fig. 1) and in the photo (Fig. 2).

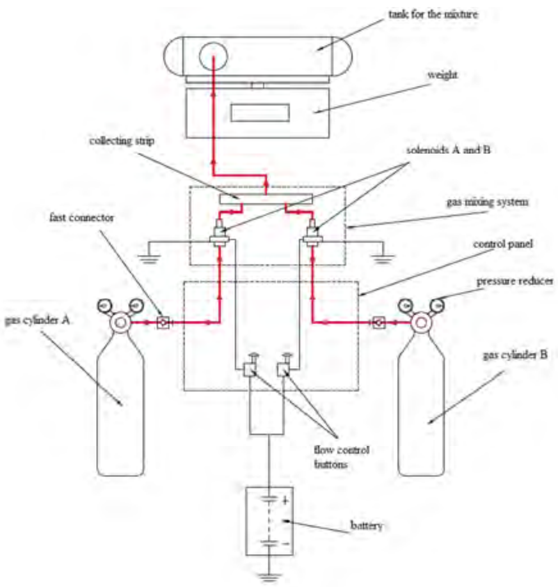

Fig. 1. Diagram of the station for the production of a gas mixture [6]

Fig. 2. Station for the production of gas blends

Based on the experience gained from the first series of tests, a stand for the production of gas mixtures was designed. The stand facilitated and shortened the time of preparing the mixture for testing. Needle valves were used for its construction, which are characterized by high accuracy during their control.

3. The object of research, research apparatus and the scope of the research carried out

The object of the research was an Opel Astra passenger car with an engine capacity of 1.6 dm^3, factory-adapted to run on unleaded petrol. The engine was equipped with an LPG gas installation. The installation does not require special adaptation to be supplied with LPG and DME mixtures, except for the possible replacement of seals, due to the possible adverse effect of DME on rubber elements.

Experimental tests were carried out on a Bosch FLA chassis dynamometer with an eddy current brake. This made it possible to measure the engine torque, power and also the speed of the vehicle. The dynamometer reflected the conditions of the vehicle moving along the road along with its resistance, additionally providing full repeatability of the measurement. The vehicle engine is equipped with the indicated pressure measurement circuit. The pressure was measured on the first cylinder using a Kistler 6121 pressure sensor which was coupled to a spark plug. The pressure sensor was connected to the charge amplifier and data acquisition system. Additionally, a marker with a photo sensor is mounted on the pulley. Thanks to it, it was possible to synchronize the position and speed signal of the crankshaft with the pressure signal.

The first stage of the research included mixtures with a DME percentage of 7, 11, 14, 17, 21%. The tests were carried out for various engine loads and selected rotational speeds. Mass measurement of fuel consumption was performed for all measurement points, the pressure indicated in 150 consecutive engine operation cycles was recorded and the exhaust gas temperature was measured in the engine exhaust manifold.

During the tests, the spark advance angle was also corrected. All measurement series were repeated three times; with factory settings and with corrections increasing the value of the spark advance angle by 3° and 6°.

Based on the analysis of the results collected at this stage of the research, an assessment of the combustion process was performed, which did not show any clear disturbances in the engine's operation. Therefore, it was decided to extend the scope of the tests to include further mixtures, where the DME percentage was 26 and 30%, respectively.

4. Development of measurement results

4.1. Fuel consumption measurement

Fuel consumption, determined by the mass method, was measured with an accuracy of 1 gram during one minute for each measuring point. The results of the measurements are presented in graphs (Fig. 3–5) for different levels of the spark advance angle.

The measurements were repeated for the changed engine controller settings, for the spark advance angle correction of 3 and 6°.

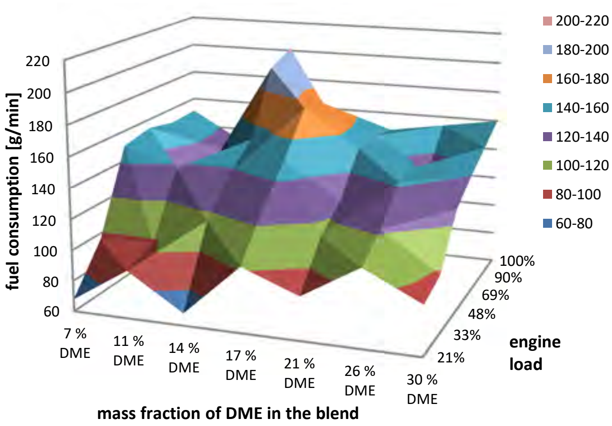

Fig. 3. Fuel consumption [g/min] depending on the percentage of DME and engine load, no correction of the spark advance angle

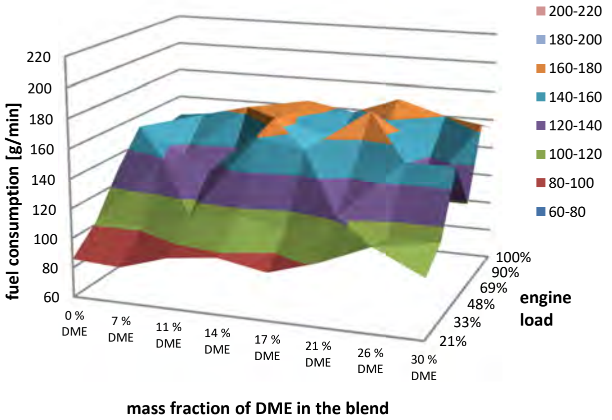

Fig. 4. Fuel consumption [g / min] depending on the percentage of DME and the engine load for the correction of the spark advance 3º

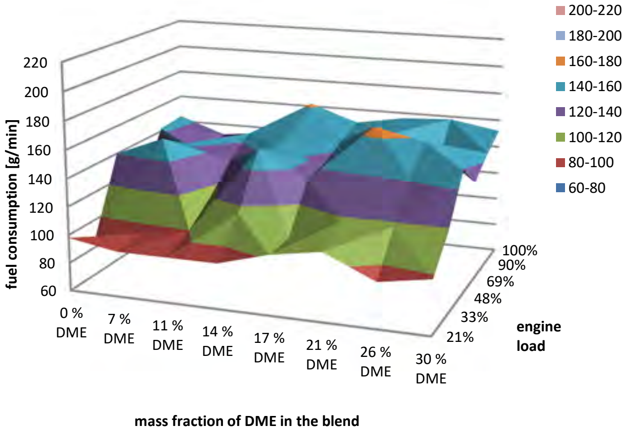

Fig. 5. Fuel consumption [g/min] depending on the percentage of DME and the engine load for the correction of the spark advance 6º

On the basis of the above charts, it can be observed that in an LPG-fueled engine, due to the slower combustion process compared to gasoline, a larger spark advance angle should be used. In the case of the mixture of LPG and DME, this relationship also occurs. For a correction by an additional 3 steps, fuel consumption decreased noticeably. Compared to the serial settings, the greatest changes were recorded for mixtures of 11 and 14% DME at partial and maximum loads. On the other hand, for the 30% mixture, the greatest differences occur at the half load of the engine. With an ignition correction of 6 degrees, an even greater benefit in fuel economy is achieved. It decreased evenly over the entire range of engine loads for all mixtures.

Fuel consumption, determined by the mass method, was measured with an accuracy of 1 gram during one minute for each measuring point. The results of the measurements are presented in graphs (Fig. 3–5) for different levels of the spark advance angle.

4.2. Changes in the combustion process

The measuring equipment described above made it possible to register the pressure inside the engine cylinder. For each measuring point, 150 engine cycles were recorded in succession. The collected data was statistically processed using the EnComAn [7] program, thus extracting a sample representative for each measurement point. Further analysis consisted in determining the boundaries of the combustion process. At this stage, the computational capabilities of the Diadem NI program were used. Using the developed model [8], on the basis of the designated sample representative of the pressure course for the recorded work cycles, the polytrope and pressure increases as a function of the crankshaft rotation angle were calculated.

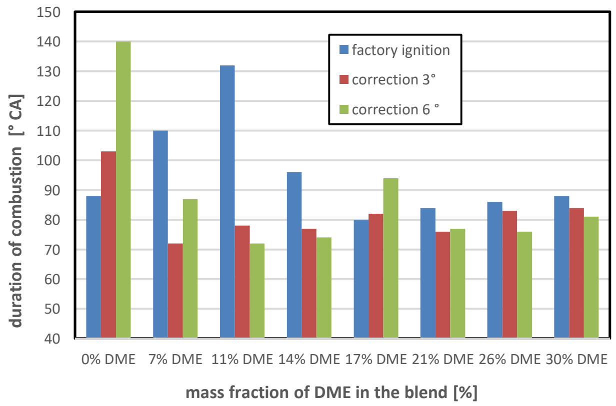

Fig. 6. Summary of the duration of combustion processes for the engine speed of 3000 rpm, fueled with LPG-DME mixtures, with the correction of the ignition angle. Engine load 33%

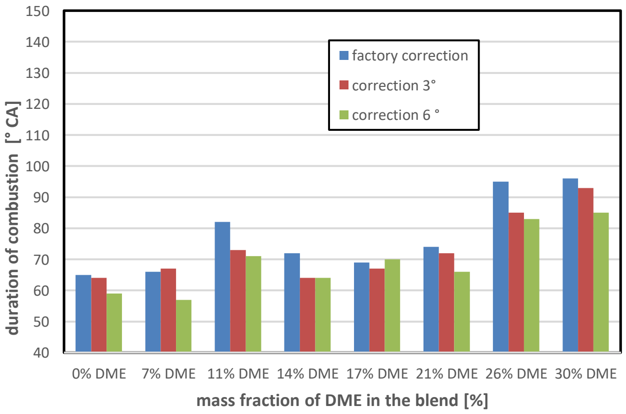

Fig. 7. Summary of the duration of combustion processes for the engine speed of 3000 rpm, fueled with LPG-DME mixtures, with the correction of the ignition angle. Engine load 69%

After determining the boundary assumptions, the combustion process in relation to the angle of rotation of the crankshaft was identified.

The results are presented by means of column charts (Fig. 6–8). The analysis of the charts made it possible to compare the length of the combustion processes for different shares of DME in the mixture for the levels used in the research. ignition timing corrections by 3 and 6 degrees, respectively, in relation to the serial settings.

The combustion period is understood as the part of the crankshaft rotation, expressed in degrees [ºCA], between the positions of the crankshaft, for which the applied thermodynamic model performs an additional energy increase, which proves the combustion process taking place.

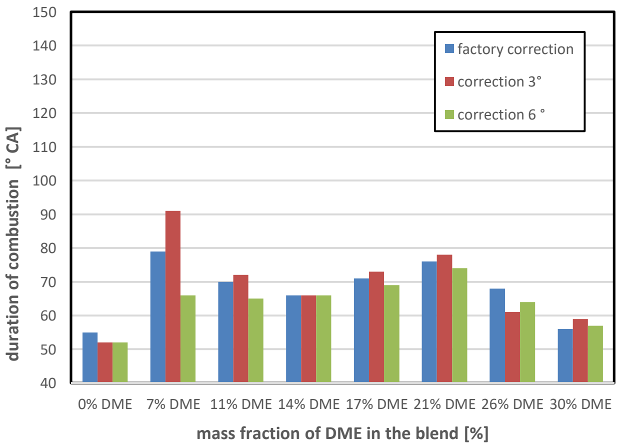

Fig. 8. Summary of the duration of combustion processes for the engine speed of 3000 rpm, fueled with LPG-DME mixtures, with the correction of the ignition angle. Engine load 100%

5. Conclusions

Based on the results of the research, the following conclusions were drawn:

- Plane graphs made it possible to compare fuel consumption for mixtures with increasing DME share as a function of engine load for serial engine settings and for two corrections
- Extending the ignition time, reducing fuel consumption, especially for engine loads above 48%
- The greatest benefits from the spark advance correction were obtained for a mixture with a mass fraction of DME 14 and 17%
- The graphs made it possible to compile representative combustion processes when fueling the engine with gaseous fuel with different DME mass fractions, for different engine loads and two additional settings of the spark advance angle
- The greater the engine load, the shorter the combustion process
- For the engine load of 69%, increasing the SA shortened the combustion process for all mixtures
- For the engine load of 69% when the engine was powered with a mixture of 26 and 30% DME, the combustion process was extended by approximately 30%
- With the engine load of 33%, the SA correction had an effect on the shortening of the combustion process, in addition to the mixtures of 100% LPG and 17% DME
- For 100% engine load, the shortest combustion process was recorded for fueling the engine with reference fuel and mixtures with the highest share of DME
- At maximum engine load, the SA correction did not have a significant effect on the duration of the combustion process for all tested mixtures

Nomenclature

DME	dimetyloeter	LPG	liquified petrolum gas
SA	spark advance	SI	spark ignition

Bibliography

[1] BRZEŻAŃSKI, M., JUDA, Z. Napędy hybrydowe, ogniwa paliwowe i paliwa alternatywne. Elektrotechnika i elektronika samochodowa. *Robert Bosch GmbH*. WKŁ Warszawa 2010.

[2] SHI, L., C, JI, WANG, S. et al. Combustion and emissions characteristics of a S.I. engine fueled with gasoline-DME blends under different spark timings. *Fuel*. 2018, **211**(1), 11-17. https://doi.org/10.1016/j.fuel.2017.09.019

[3] YOON, E.S., HAN, C. A review of sustainable energy – recent development and future prospects of dimethyl ether (DME). *Computer Aided Chemical Engineering*. 2009, **27**, 169-175. https://doi.org/10.1016/S1570-7946(09)70249-4

[4] ARCOUMANIS, C., BAE, C., CROOKES, R. et al. The potential of di-methyl ether (DME) as an alternative fuel for compression-ignition engines: A review. *Fuel*. 2008, **87**(7), 1014-1030. https://doi.org/10.1016/j.fuel.2007.06.007

[5] LEE, S., OH, S., CHOI, Y. et al. Effect of n-butane and propane on performance and emission characteristics of an SI engine operated with DME-blended LPG fuel. *Fuel*. 2011, **90**(4), 1674-1680. https://doi.org/10.1016/j.fuel.2010.11.040

[6] BYTOMSKI, D. Project of the system to preparing of fuel gas blends with a specified composition. Katowice. 2009. 57.

[7] KUBICA, G. Efektywność konwersji energii w silniku o zapłonie iskrowym zasilanym paliwami gazowymi o obniżonym udziale węgla. *Publishing House of the Institute for Sustainable Technologies-National Research Institute in Radom*, Radom 2013.

[8] NIŚCIÓR, A. Analysis of the combustion process in the stabilized working engine on the basis of indicated pressure. *Politechnika Śląska.* Katowice 2008, 53-54.

Paweł Marzec, MSc. – PhD student at Faculty of Transport and Aviation Engineering. Silesian University of Technology

e-mail: *pawelmarzec92@gmail.com*

Article citation info:
GIECHASKIEL, B., SUAREZ-BERTOA, R., MELAS, A. et al. Assessment of retrofit devices for the Horizon 2020 Cleanest Engine and Vehicle Retrofit Prizes. *Combustion Engines*. 2022, **190**(3), 27-34. https://doi.org/10.19206/CE-147158

Barouch GIECHASKIEL
Ricardo SUAREZ-BERTOA
Anastasios MELAS
Tommaso SELLERI
Maurizio MAGGIORE

Combustion Engines
Polish Scientific Society of Combustion Engines

Assessment of retrofit devices for the Horizon 2020 Cleanest Engine and Vehicle Retrofit Prizes

ARTICLE INFO

Received: 21 January 2022
Revised: 1 March 2022
Accepted: 5 March 2022
Available online: 13 March 2022

The Horizon 2020 prizes aimed at the development of retrofit and engines that would reduce pollution. The Retrofit prize had a winner, while the Engine prize not. In this paper we present the innovations that were tested at the Joint Research Centre (JRC) of the European Commission, and not awarded. One was a "condensation" aftertreatment device, two were devices inserted in the fuel supply system, and one a selective catalytic reduction (SCR) for NO_x system. The testing of the "condensation" aftertreatment device showed that it could not withstand the high exhaust gas temperatures. The results of the two fuel systems showed that they could not control efficiently the NO_x emissions. The reductions of the pollutants were neglible for the levels that the prizes were aiming. The SCR system did not achieve any significant reduction of NO_x, probably due to a malfunction of the device.

Key words: *retrofit, fuel supply innovation, SCR, Horizon 2020 prizes*

1. Introduction

Horizon 2020 competitions included two prizes: (i) the engine retrofit [1] (ii) the cleanest engine [2]. The Retrofit prize aimed at reducing the road transport pollution by spurring the development of retrofittable technology (i.e. additional devices and/or modification) applicable to Diesel engines focusing on Euro 5 vehicles (sold up to mid 2015) and Euro 6b (sold up to mid 2018), which will be on the road for many years. The purpose of the Engine prize was to stimulate the development of next generation engines and powertrain technologies using conventional fuels. This should reduce emissions of pollutants in real driving conditions to the lowest level possible in order to improve air quality in European cities, while at the same time delivering better fuel economy and lower CO_2 emissions. The assessment was done both in the laboratory and on the road requiring some of the most dangerous pollutants, NO_x and particulate matter, to be at very low levels, while limiting other pollutants and greenhouse gases. Additionally, vehicle fuel efficiency and retrofitting costs, durability, maintenance and usability, safety, drivability, and noise were considered in the prize criteria.

The innovation (engine or retrofit) had to be installed for testing purposes on a top sales C-class compact vehicle (but limited to hatchback and three volumes family car bodies). Hybrids (electric, compressed gases, hydraulic etc.), plug-in hybrids and in general systems using large energy storage capability beyond the main fuel were not admissible. A maximum volume of 50 liters of trunk space could be taken in the donor vehicle for the purpose of installing the device. For the purpose of this prize, only Diesel or gasoline and their commercial low blends were allowed.

Table 1 outlines the thresholds which had to be met prior to submitting the application. Participants conducted the tests at independent laboratories and the emissions had to be below the threshold values, before further assessment at the Joint Research Centre (JRC). Only regulated pollutants had to be presented. The same criteria were applicable as Not-To-Exceed (NTE) values for real driving tests (including altitude, use of auxiliaries testing, cold start and regenerations):

$$\text{On-road NTE limit} = \text{Laboratory limit} \times \text{CF} \qquad (1)$$

where CF is the conformity factor (= 1.2 defined in the rules) to take into account the measurement uncertainty of portable emissions measurement system (PEMS).

The prototype vehicles (with the engine or retrofit installed, activated and not) were then tested at JRC. The award criteria were based on scoring depending on how low were the emissions below the threshold (or the reduction for the retrofit devices). Details can be found in the rules of the prizes.

Table 1. Threshold values for the initial testing by the applicant

Criteria	Engine	Retrofit
NO_x (mg/km)	60	180
PM (mg/km)	1.0	4.5
$PN_{10}\times10^{11}$ (p/km)	6.0	6.0
THC (mg/km)	60	–
CO (mg/km)	400	500
Fuel consumption (FC) (dm^3/100 km)	5.0	< +10% [1]
NH_3 (mg/km)	30	–
N_2O (mg/km)	15	–
CH_2O (mg/km)	10	–

[1] compared to the baseline

The Retrofit contest was launched in April 2016 and the deadline for the submissions was June 2017 (September 2017 for the retrofitted vehicle). The evaluation was done until March 2018. The prize was awarded in April 2018. The results were published elsewhere [2–4].

The cleanest Engine contest was launched in April 2016 and the deadline for the submissions was August 2019. The evaluation was foreseen from September 2019 until March

2020. Due to the COVID-19, the evaluation was finalized in November 2020. The prize was not awarded because no prototype met the minimum thresholds of the competition. No submission incorporated a completely new engine, but only retrofitted technology.

In this paper the results of the prototype vehicles with the retrofits installed will be given, apart from the winner of the Retrofit prize, whose results were reported [3, 4]. Both JRC's and applicants' results are given, whenever available.

2. Experimental methods

2.1. Laboratory testing

The vehicles were tested at the Vehicle Emission Laboratory (VELA 2) of the European Commission Joint Research Centre (JRC), in Ispra, Italy. The climatic test cell temperature was kept at 25°C (with relative humidity 50%) or 7°C (with relative humidity of 50%) depending on the test cycle (details will follow). The dyno settings were defined in the prize rules based on the default values given in Regulation 83 using the vehicle weight. Market Diesel fuel (B7) was used for all tests for all vehicles. The 2-axle dyno was set with the appropriate dyno coefficients with the rear wheels "following" speed mode.

Measurements from the diluted gas in the full dilution tunnel with constant volume sampler (CVS) and the bags were made simultaneously. The bag results are reported here. The bag results were within 10% from those of real-time analyzers at the dilution tunnel. The gas analyzers were Horiba MEXA 7000 series with non-dispersive infrared (NDIR) analyzers for CO_2 and CO, chemiluminescence detector (CLD) for NO_x and flame ionization detector (FID) for hydrocarbons (THC). The particle number (PN) system connected at the full dilution tunnel was an AVL APC 489 with a 10 nm condensation particle counter (CPC).

Additional pollutants, including ammonia (NH_3), nitrous oxide (N_2O) and formaldehyde (CH_2O) were measured with a Fourier transform infrared (FTIR) spectrometer connected to the vehicle tailpipe, using a heated polytetrafluoroethylene sampling line (191°C). The FTIR spectrometer was the AVL Sesam including a Nicolet Antaris IGS Analyser (Thermo Electron Scientific Instruments LLC, Madison, WI, USA) with a Michelson interferometer (spectral resolution: 0.5 cm^{-1}, spectral range: 600–3500 cm^{-1}), a multipath gas cell of 2 m of optical path, a downstream sampling pump (6.5 lpm flowrate). The acquisition frequency was 1 Hz while the working pressure 860 hPa.

According to the prize rules, three cycles had to be driven in the following order:

(1) New European Driving Cycle (NEDC) with cold engine (soaked > 6 h) at 7°C,
(2) Worldwide harmonized light-duty vehicles test cycle (WLTC) with warm engine (soaked < 2 h) at 7°C,
(3) Common Artemis Driving Cycle (CADC) at 25°C (soaked > 2 h).

Due to the issues that will be described for each vehicle, this order was not always strictly followed.

2.5. On-road testing

Three routes were followed using a real-driving emissions (RDE) compliant portable emissions measurement system (PEMS) (Horiba OBS-ONE) or a portable FTIR (PEMSLAB, Certam-Addair).

The OBS measures CO_2 and CO with heated NDIR, NO_x with heated CLD and PN with a 23 nm CPC downstream of a catalytic stripper.

The portable FTIR, PEMSLAB from Certam, has a cell with an internal volume of 200 cm^3 with fixed optical path of 2 m and windows of BaF_2. The cell is operated at atmospheric pressure and heated at 180°C. Spectra are recorded by a mercury cadmium telluride (MCT) thermoelectrically (Peltier) cooled detector. The spectral range is 900–4200 cm^{-1} with a spectral resolution of 8 cm^{-1}.

Two routes (ESP and LAB) complied with the trip requirements defined in the RDE regulation were carried out in the morning with cold engine. The third route (SAC) represented hilly driving and was not RDE compliant and was conducted in the afternoon. The vehicle 12 V battery was left to charge before each test.

3. Results of Retrofit #1

3.1. General

Retrofit name: 3G exhaust system.

Owner: Galiboff Plastik Kompozit Ekstrüzyon Teknolojileri Ltd., Meric Ltd., Darıca Sanayi Sitesi, E Blok No:38, Darıca/kocaeli, Turkey

Web-site: http://www.galiboff.com/

Innovation according to the applicant: The exhaust system turns water vapor to liquid and mixes all emitted gases with water. Gases which react with water leave from the central pipe to the atmosphere as liquids. Gases that do not mix with water leave from the upper pipe, which may be connected to the intake air. This prototype upper pipe had no connection to the intake air at the prototype that was delivered to JRC.

Donor vehicle: The donor vehicle was a Seat Leon 1.9 TDI (81 kW), model year May 2004 (Euro 4), with mileage 135127 km.

3.2. Test protocol

The dyno values were: $m = 1470$ kg, $f_0 = 7.4$ N, $f_2 = 0.0502$ $N/(km/h)^2$. During the first NEDC test at 25°C (30/9/2019) the vehicle showed a malfunction. The car could not accelerate more than 100 km/h and the cycle was not compliant. The test campaign was suspended. The applicant was authorized to work on the car to fix the problem (7/10/2019 and 8/10/2019). The car was again installed in the cell (8/10/2019). The car was preconditioned at 120 km/h and then 3×EUDC (as foreseen by the regulation). Later that day (soak 6 h) a cold NEDC at 25°C was run. The results (Table 2) were above the threshold limits. Note that the prototype vehicle was delivered for the Engine prize, so it was assessed using the Engine limits. Nevertheless, it would have failed also the retrofit limits.

When the transfer line (i.e., the tube connecting the vehicle to the dilution tunnel) was disconnected, solid burned materials were found in the tailpipe with dimensions reaching 2.5 cm. It is probable that they originated from the filter filaments and material which fused at high temperatures. Also, the filters of the critical orifices of the CVS were inspected and were found contaminated. Due to these reasons, the campaign on the vehicle was terminated.

Table 2. Summary of results. F = Fail, P = Pass based on the Engine limits because the prototype vehicle was delivered for the Engine prize (Table 1)

Criteria	Limit	NEDC	3×EUDC	NEDC	
	Lab	25°C	Hot 25°C	25°C	
CO_2 (g/km)	–	164	140	161	
NO_x (mg/km)	60	1154	615	646	F
$PN_{10}\times10^{11}$ (p/km)	6	–	549	209	F
THC (mg/km)	–	247	166	152	F
CO (mg/km)	400	605	529	622	F
FC (dm^3/100 km)	5.0	6.3	5.4	6.2	F
NH_3 (mg/km)	30	–	–	0.3	P
N_2O (mg/km)	15	–	–	6.7	P
CH_2O (mg/km)	10	–	–	23.4	F

4. Results of Retrofit #2

4.1. General

Retrofit name: FuelWell 4D PC.

Main applicant: Katalitprylad, LLC TH “GlobalExim”, Belorusskaya 26, Kiev, 04050, Ukraine.

Testing laboratory: Instytut Transportu Samochodowego (Motor Transport Institute), ul. Jagiellonska 80, 03-301, Warszawa, Poland

Web-site: www.https://fuel-well.com

Innovation according to the applicant: FuelWell is installed in the fuel system of the Diesel engine. In the first chamber selective purification of Diesel fuel from sulphur compounds and resins is carried out, by catalytic treatment with granular catalyst and saturation of fuel at the molecular level of salts of alloying metals, which in the cylinder create a dopant effect (increase compression in cylinder). In the second chamber, the fuel is subject to activation, homogenization and fine purification. Complex fuel treatment increases the completeness of its combustion, which reduces the real fuel consumption and release of harmful gases. The weight is approximately 0.85 kg.

Donor vehicle: The donor vehicle was a Peugeot 308 1.6 Blue HDi (88 kW), model year June 2017 (Euro 6b), with mileage 20177 km.

4.2. Test protocol

The tests were done with two dyno settings: m=1250 kg, f_0 = 6.8 N, f_2 = 0.046 N/(km/h)^2 to match the applicant’s tests, and with the dyno values foreseen at the prize: m = 1470 kg, f_0 = 7.4 N, f_2 = 0.0502 N/(km/h)^2. Unless otherwise specified, the m = 1470 kg settings were applied.

The tests were conducted in the following order:

- 1/10/2019: NEDC cold 25°C
- 2/10/2019: NEDC cold 7°C
- 3/10/2019: NEDC cold 7°C, WLTC hot 7°C, CADC cold 25°C
- 4/10/2019: CADC cold 25°C
- 7/10/2019: 3×EUDC, NEDC cold 25°C (m = 1250 kg)
- 8/10/2019: 3×EUDC, NEDC cold 25°C (m = 1250 kg)

Tests with the retrofitted activated or not:

- 15/3/2021: WLTC hot 23°C preconditioning (activated)
- 16/3/2021: WLTC cold 23°C (activated)
- 17/3/2021: WLTC cold 23°C (activated)
- Retrofit deactivation and conditioning for 160 km.
- 24/3/2021: WLTC hot 23°C preconditioning (not-activated)
- 25/3/2021: WLTC cold 23°C (not-activated)
- Further conditioning for 150 km (not-activated)
- 7/4/2021: WLTC cold 23°C (not-activated)
- 8/4/2021: WLTC cold 23°C (not-activated)

4.3. Lab results

Table 3 summarizes the cold NEDC at 25°C results reported by the contestant, and those measured by JRC matching the settings (m = 1250 kg) and with the prize settings (1470 kg).

Based on the contestant’s results, in general, the NO_x were slightly higher than the threshold, but the other pollutants below. The device showed a small to negligible improvement of the emissions.

There is relatively good agreement between reported and measured by JRC values (except PN, which was still below the threshold), so it was decided to continue with the testing, using the official dyno coefficients.

Table 3. Comparison of emissions reported by contestant and measured by JRC using the same setting for cold start NEDC at 25°C. The same cycle with the prize dyno coefficients is also given. F = Fail, P = Pass based on the Engine limits because the prototype vehicle was delivered for the Engine prize (Table 1). Lim.=Limits

Criteria	Lim.	NEDC	NEDC	NEDC	NEDC	
Inertia (kg)		1250	1250	1250	1470	
Testing lab		applic.	applic.	JRC	JRC	
Retrofit		w/o	with	with	with	
CO_2 (g/km)	–	113.5	116.9	109–110	127	
NO_x (mg/km)	60	69.0	65.8	102–130	256	F
$PN_{10}\times10^{11}$ (#/km)	6.0	–	0.09	1.8–1.9		P
THC (mg/km)	60	12.0	12.1	12–16	31	P
CO (mg/km)	400	200.9	232.3	282–368	351	P
FC (dm^3/100 km)	5	4.32	4.45	4.20	4.8	P

Table 4 summarizes the results of the official cycles. The vehicle failed NO_x and CO, and the fuel consumption was above the threshold at one test. The prototype would also have failed the Retrofit prize NO_x limits.

It should be noted that the same model but Euro 6d-temp fulfilled the Euro 6 limits at the cold and hot start WLTCs at 23°C and 10°C [5] (i.e. NO_x < 80 mg/km). On the other hand, the Euro 5b version emitted 300 mg/km (NEDC cold 7°C), 450 mg/km (WLTC hot 7°C), and 850 mg/km (CADC 25°C) NO_x [3].

Table 4. Emissions measured by JRC for the cycles prescribed in the prize rules. F = Fail, P = Pass based on the Engine limits because the prototype vehicle was delivered for the Engine prize (Table 1). Lim. = Limits

Criteria	Lim.	NEDC	WLTC	CADC	
	Lab	7°C	Hot 7°C	25°C	
CO_2 (g/km)	–	125–127	130	154–155	–
NO_x (mg/km)	60	513–519	167–220	497–808	F
$PN_{10}\times10^{11}$ (#/km)	6.0	0.6–1.0	0.8–1.2	1.5–1.6	P
THC (mg/km)	60	21–25	2-3	2	P
CO (mg/km)	400	685–708	68-84	88–89	F
FC (dm^3/100 km)	5	4.8–4.9	4.95	5.9	F
NH_3 (mg/km)	30	0.5	41.0	47.5	F
N_2O (mg/km)	15	10.8	5.2	4.0	P
CH_2O (mg/km)	10	16.9	0.8	1.3	F

The WLTC results with the retrofit activated or not are summarized in Table 5, plotted also in Fig. 1. There is no significant reduction of the emissions. Any reduction is within the experimental uncertainty and the repeatability of the vehicle.

Table 5. Emissions measured by JRC for the cycles prescribed in the prize rules. F = Fail, P = Pass based on the Engine limits because the prototype vehicle was delivered for the Engine prize (Table 1). Lim. = Limits

Criteria	Lim.	WLTC	WLTC	Diff	
	Lab	23°C	23°C	–	
Retrofit		Not-active	Active	–	
CO_2 (g/km)	–	131.5	134.4	+2%	–
NO_x (mg/km)	180	455	432	–5%	F
$PN_{10}\times10^{11}$ (#/km)	6.0	1.76	1.58	–10%	P
THC (mg/km)	–	0.5	0.5	–	P
CO (mg/km)	500	122	84	–31%	F
FC (dm^3/100 km)	+10%	–	–	+2.2%	P

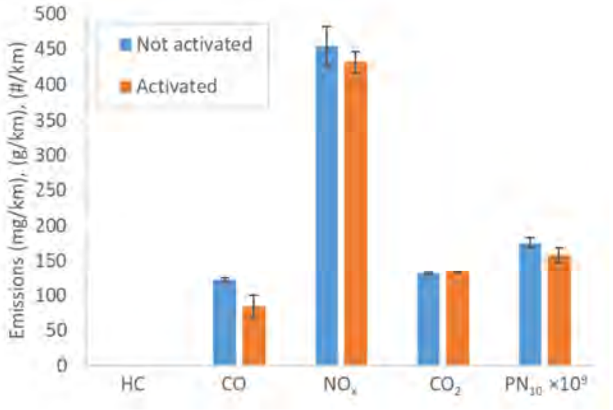

Fig. 1. Comparison of cold WLTC at 23°C emissions with the retrofitted activated or not. Error bars show max-min of 2–3 repetitions

4.4. RDE results

The on-road tests were conducted with a PEMS (Horiba OBS-ONE) for two trips and a portable FTIR (Certam-AddAir) for another two trips.

ESP and LAB were RDE compliant tests, while SAC was an altitude test. The vehicle did not pass the NO_x limit in any of the driven routes, and also the fuel consumption was higher than the threshold (Table 6). Similar conclusions would be drawn comparing with the Retrofit prize limits.

It should be added that the Euro 6d-temp version of the specific model fulfilled the Euro 6 on-road NO_x limits (emissions around 80 mg/km) [5].

Table 6. On-road emissions. F = Fail, P = Pass based on the Engine limits because the prototype vehicle was delivered for the Engine prize (Table 1). Lim. = Limits

Criteria	Lim.	ESP	SAC	LAB	SAC	
	RDE	PEMS	PEMS	FTIR	FTIR	
$T_{amb,mean}$ (°C)		14	19	14	12	
$Altitude_{max}$ (m)		300	1080	400	1080	
CO_2 (g/km)	–	148	138	132	122	
NO_x (mg/km)	72	372	357	378	178	F
$PN_{23}\times10^{11}$ (#/km)	7.2	2.5	1.7	1.8	3.9	P
CO (mg/km)	480	720	153	93	119	F
FC (dm^3/100 km)	6.0	5.4	5.1	4.9	4.6	P
NH_3 (mg/km)	36	–	–	15	1.0	P
N_2O (mg/km)	18	–	–	1.9	3.7	P
CH_2O (mg/km)	12	–	–	4.1	2.2	P

5. Results of Retrofit #3

5.1. General

Retrofit name: E.R.De.I.D.E. (Emissions Reduction Device In Diesel Engines).

Main applicant: Ve.S.T.A. s.r.l., via Burago, Ornago, Italy.

Testing laboratory: M.T.M. srl and BRC srl, part of the Westport Group Fuel Systems, with laboratories in Cherasco (Cuneo), Strada Provinciale 58, no. 11, Italy.

Web-site: www.vesta-corporate.com

Innovation according to the applicant: ERDeIDE (Emission Reduction in Diesel Engines) is a technological evolution of an earlier prototype engineered by Ve.S.T.A. srl, called Droptek. ERDeIDE is a static device to be installed downstream of the low pressure pump and before the high pressure injection systems, and it is powered by the vehicle battery at 12 V: ERDeIDE is inserted into the fuel supply circuit and applies a combination of physical effects (predetermined temperature and magnetic field) to the fuel. The applicant proposes that the combination equilibrium of the parameters, applied for at least some time, influence, with a medium-lasting effect, the molecular magnetic moment of hydrocarbons, their conformations, and angular and torsional tensions. The method is considered to affect especially the aromatic compounds. The weight is approximately 2.5 kg.

Donor vehicle: Peugeot 308 1.6 HDI Euro 5b Diesel, with engine capacity of 1560 cm^3 and a power output of 68 kW, 6 gears manual transmission, exhaust gas recirculation, Diesel oxidation catalyst and particulate filter. Model year Feb 2015, with mileage 58300 km (at JRC).

5.2. Test protocol

The car was driven to JRC with full tank with market fuel. All tests were conducted with the fuel in the tank. The dyno settings of the testing laboratory (MTM, BRC) were: $m = 1360$ kg, $f_0 = 7.1$ N, $f_2 = 0.0481$ $N/(km/h)^2$. The dyno settings of JRC were: $m = 1250$ kg, $f_0 = 6.8$ N, $f_2 = 0.0460$ $N/(km/h)^2$. The sequence of the tests conducted is presented below.

- 18/12/2017: NEDC cold 7°C, WLTC hot 7°C (with retrofit)
- 19/12/2017: NEDC cold 7°C, WLTC hot 7°C (without retrofit)
- 21/12/2017: NEDC cold 7°C (with retrofit)

The 12V battery was fully charged at the beginning of the day (cold NEDC). The first cold NEDC with the retrofit on the 18th had high emissions, probably because it was the first test after many weeks parked outside, so it was repeated on the 21st. The first test of the 18th was not considered in the analysis below. Due to the high NO_x emissions it was decided not to test the CADC.

5.3. Results

The JRC and the ERDeIDE reported results are not directly comparable because different dyno coefficients were applied. Nonetheless, the trends for the effectiveness of the retrofit should be comparable.

The JRC results showed a slight increase of the CO_2 with the retrofit (2 g/km), while the applicant's results showed a slight decrease (Fig. 2). The differences of the CO_2 emissions are < 2 g/km for both complete test cycles (NEDC and WLTC) (Fig. 2) and their urban parts (UDC and Low part of WLTC respectively) (figure not shown). The small differences fall within the experimental uncertainty and the repeatability of the measurements and differences in the gear shift strategy at the two labs. Thus the

CO_2 penalty or benefit cannot be considered to be substantial with the present data.

The JRC results showed a slight increase of the NO_x emissions, while the applicant's results showed a slight decrease when the retrofit was activated (Fig. 3). However, the changes were within experimental uncertainties in both cases. Similar conclusions can be drawn for both the complete cycles and their urban parts. The emission levels were much higher than 180 mg/km (threshold value) for both the JRC and delivered results for both the complete cycles and their urban parts.

The PN_{10} emissions slightly decreased with the activation of the retrofit (Fig. 4), however the decrease is within the experimental uncertainty. For example, the PN emissions of the first NEDC conducted at JRC without preconditioning with the retrofit were higher than without the retrofit (data not shown).

The N_2O emissions were low and practically unaffected by the retrofit (Fig. 5). The NH_3 emissions were very low and at the detection limit of the instrument.

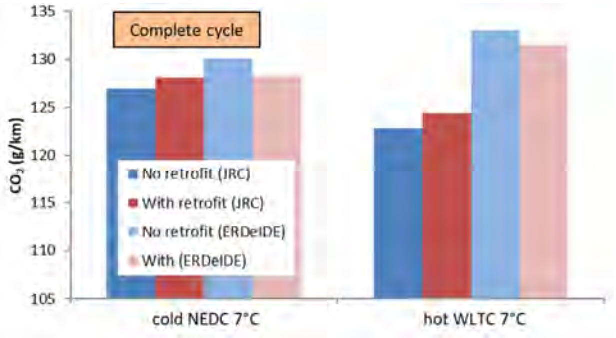

Fig. 2. CO_2 results for the complete cycles

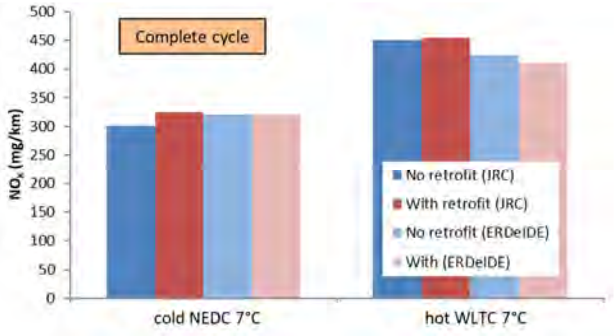

Fig. 3. NO_x results for the complete cycles

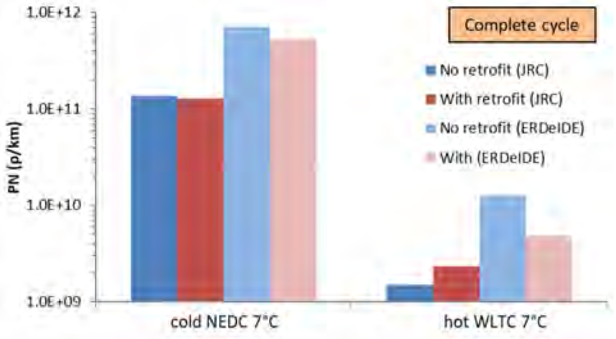

Fig. 4. PN results for the complete cycles

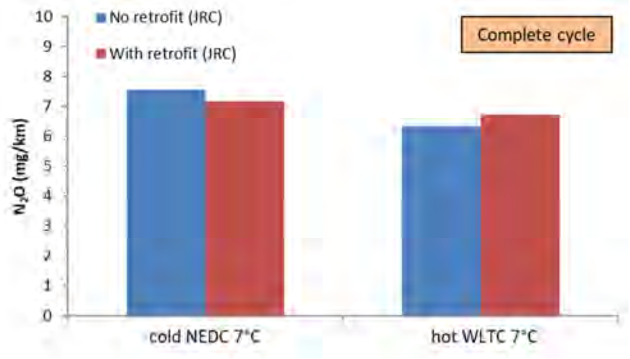

Fig. 5. N_2O results for the complete cycles

The reported (and verified by JRC) NO_x emissions of the car (Table 7) were above the thresholds (see Table 1), thus the retrofit does not fulfil the requirements of the rules of contest. Comparison of with and without retrofit did not show any significant improvement for the pollutants of interest for this competition. The retrofit was not further evaluated.

Table 7. Emissions as reported by ERDeIDE for the cycles prescribed in the prize rules. F = Fail, P = Pass. Lim. = Limits

Criteria	Lim.	NEDC	WLTC	CADC	
	Lab	7°C	Hot 7°C	25°C	
CO_2 (g/km)	–	128.3	131.5	151.4	–
NO_x (mg/km)	180	320	410	819	F
PM (mg/km)	4.5	0.51	0.14	0.22	P
$PN_{10}\times10^{11}$ (#/km)	6.0	5.2	0.05	1.5	P
CO (mg/km)	500	746	50	58	–
FC (dm^3/100 km)	+10%	–1.4%	–1.1%	+0.5%	P

6. Results of Retrofit #4

6.1. General

Retrofit name: Dr. Pley

Main applicant: Dr. Pley GmbH, Regnitzstraße 18b, D-96052, Bamberg, Germany

Testing laboratory: FAKT GmbH, Grüntenstraße 3–5
D-87751 Heimertingen, Germany

Web-site: www.dr-pley.com

Innovation according to the applicant: It is a Selective Catalytic Reduction (SCR) system with an electronic control unit that controls all actors and sensors that are required for the SCR system. Different parameters can be used (e.g. NO_x sensor signals, engine parameters, etc.) for the Diesel Exhaust Fluid (DEF) supply to the SCR system. A new SCR with a much lower light-off-temperature than what available in the market has been developed. Using these new SCR catalysts in combination with a DEF hydrolysis reactor, the ammonia injection temperature can be lowered to 130°C. Based on the measured NO_x, the device adjusts the operational parameters. The weight is approximately 15 kg (plus DEF).

Donor vehicle: Audi A3 Sportback 2.0 TDI with 110 kW power and 1968 cm^3 engine displacement. Automatic transmission, exhaust gas recirculation, Diesel oxidation catalyst and particulate filter. Model year Sept 2013 (Euro 5b), with mileage 80000 km (at JRC).

6.2. Test protocol

The dyno settings of both the testing laboratory (FAKT) and JRC were: m = 1470 kg, f_0 = 7.4 N, f_2 = 0.0502 $N/(km/h)^2$. Many tests were conducted, but due to the issues described below only some indicative results will be presented.

Due to issues at FAKT or different vehicle conditioning, the only tests close to the rules (and comparable with JRC's are those with the retrofit). The first JRC results were not in good agreement with the applicant's results. After an on-site inspection of the system (29/11/2017) the contestant found that a marten had cut the purge air pipe as well as parts of the insulation of the NH_3 transfer pipe. Due to lack of purge air, a sealing was damaged by overheating. This led to a leakage of NH_3 out of the hydrolysis reactor. However, even with damaged insulation of the transfer pipe, there was not deposit inside the transfer pipe. The contestant replaced the broken pipe and quick-fixed the broken sealing with high temperature silicone (repair 1). A few more tests were repeated.

This intervention did not improve the results, so it was decided to permit the contestant to take the car (8/1/2018) and repair it on his own premises (repair 2). The investigation showed that the leakage which was fixed on-site with silicone did not work. There was a lack of purge air resulting in a blockage of the ammonia transfer pipe and a release of DEF at the rupture of the purge air pipe. Analysis of stored device data showed that the operation of the SCR system was prevented by the retrofit control unit due to the detected failure of the purge air supply. The DEF hydrolysis reactor was replaced at Dr. Pley's premises in the end.

The tests were repeated at the beginning of January. The results after this repair did not show any improvement. According to the contestant it happened probably due to a bug in the software. The software was fixed on-site (repair 3). All SCR system components were checked by the contestant and there was no problem or leakage. The DEF consumption was in the expected range as well. Only one "official" test was conducted (NEDC cold at 7°C) and there was no difference from the previous so the rest tests were not conducted. An overview of the NO_x results in the laboratory and on the road are summarized in Fig. 6 and Fig. 7 respectively.

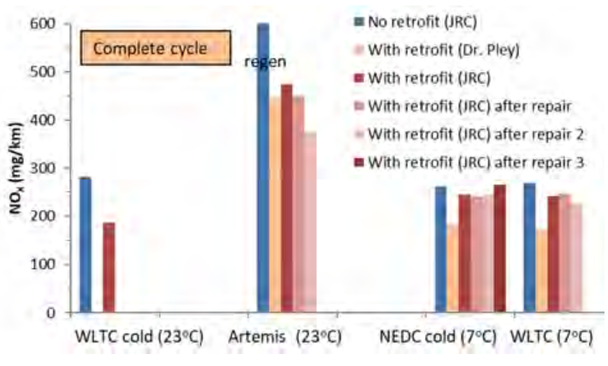

Fig. 6. NO_x results for the complete cycles. "Regen" means that regeneration took place

Table 8 summarizes the results with the retrofit installed, as reported by the applicant. Table 9 gives the same tests as measured at JRC. Although the differences were not big, the results were below and above the NO_x threshold of 180 mg/km at the two laboratories for many cycles. Based on the JRC results and the not so clear reduction of the emissions, the retrofit was not further evaluated.

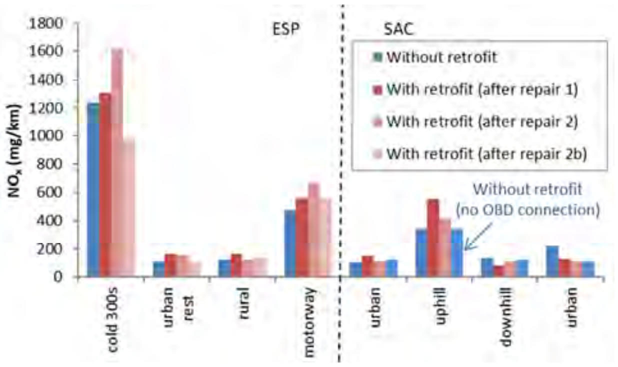

Fig. 7. NO_x results for the on-road tests

Table 8. Summary of retrofit results (as reported by Dr. Pley). F = Fail, P = Pass based on the Retrofit limits because the prototype vehicle was delivered for the Retrofit prize (Table 1). For the lab tests the average of the three cycles was considered as pass/fail criterion. Lim. = Limits

Criteria	Lim.	NEDC	WLTC	CADC	RDE	
	Lab	7°C	Hot 7°C	25°C	–	
NO_x (mg/km)	180	183	172	447	88	F
$PN_{23}\times10^{11}$ (#/km)	6.0	0.3	0.5	0.0	0.2	P
CO (mg/km)	500	113	122	10	10	P
FC (dm^3/100 km)	10%	+22%	–1%	+3%	–	P

Table 9. Summary of retrofit results (as measured at JRC). F = Fail, P = Pass based on the Retrofit limits because the prototype vehicle was delivered for the Retrofit prize (Table 1). For the lab tests the average of the three cycles was considered as pass/fail criterion. Lim. = Limits

Criteria	Lim.	NEDC	WLTC	CADC	RDE	
	Lab	7°C	Hot 7°C	25°C	–	
NO_x (mg/km)	180	246	243	476	179	F
$PN_{10}\times10^{11}$ (#/km)	6	0.4	0.5	0.1	–	P
CO (mg/km)	500	179	25	10	16	P
FC (dm^3/100 km)	10%	+0.1%	+6.7%	–	+9%	P

6. Conclusions

The Horizon prize for clean future vehicles called for innovations (engines, aftertreatment, and retrofit devices) that would result in very low tailpipe emissions and low fuel consumption. Popular devices that claim benefits on fuel economy and exhaust emissions include devices that turn water into fuel, fuel line devices that heat, magnetize, ionize irradiate or add metals, and mixture enhancers that improve the air-fuel mix prior to combustion. So far there is no strong scientific evidence on their efficiency. On the other hand, NO_x abatement devices have a strong potential [6, 7].

This paper summarized the JRC results of the submitted vehicles for the prizes. The first innovation was an aftertreatment device based on exhaust gas condensation. The concept has been used for e.g. army applications to recover the water from the exhaust gas [8]. In our tests the emissions remained very high and the testing stopped due to contamination issues of the laboratory facilities. The specific aftertreatment device, in addition to backpressure issues, did not use appropriate material to withstand high exhaust gas temperatures. The second innovation, a fuel purification system, did not result in meeting the threshold emission levels, especially for NO_x. The reactions of the fuel with the catalyst of the device are not clear, but if any, there was no obvious effect. The third innovation, a fuel magnetic device, also did not achieve the NO_x threshold emission levels. The concept of using magnetic field to reduce emissions has been reported in the literature [9, 10]. If this is happening and how the emissions are affected is not clear, but at our testing the results were not promising. A system that applied voltage at a copper coil, [11], similar to the fuel magnetic device of our study, concluded that it was possible to notice a particulate reduction. The explanation was that the copper leached in the fuel catalytically aided the combustion, but the effect was noticeable only when the fuel was in the tank for some time. The testing at JRC showed that the two fuel systems had very small reduction potential of the emissions to be meaningful for circulation of vehicles in cities. The fourth innovation was a Selective Catalytic Reduction (SCR) for NO_x system. The measurements at JRC did not show the expected NO_x reduction potential [3, 12], probably due to some issues of the device at the prototype vehicle. The system, along with others, is tested under the "Testing Retrofit Technologies" project of DG-GROW of the European Commission [13].

Concluding the results of this study showed a limited potential of the fuel line retrofit devices. Urea (ammonia) based systems, which seem the only promising technologies [14] need case by case assessment [15]. The durability of such systems should also be assessed [16].

Acknowledgements

The authors would like to thank the laboratory staff.

Nomenclature

CADC	common Artemis driving cycle
CF	conformity factor
CLD	chemiluminescence detector
CVS	constant volume sampler
DEF	diesel exhaust fluid
ESP	RDE compliant route
EUDC	extra urban driving cycle
FC	fuel consumption
FID	flame ionization detector
FTIR	Fourier transform infrared
JRC	Joint Research Centre
LAB	RDE compliant route
MCT	mercury cadmium telluride
NDIR	non-dispersive infrared
NEDC	new European driving cycle
NTE	not-to-exceed
PEMS	portable emissions measurement system
PM	particulate matter mass
PN	particle number
RDE	real driving emissions
SAC	RDE non-compliant route
SCR	selective catalytic reduction for NO_x
UDC	urban driving cycle
VELA	vehicle emission laboratory
WLTC	worldwide harmonized light-duty vehicles test cycle

Bibliography

[1] EUROPEAN COMMISSION. Horizon prize for the cleanest engine retrofit. Available online (last accessed on 18 Jan 2022). https://ec.europa.eu/info/research-and-innovation/funding/funding-opportunities/prizes/horizon-prizes/engine-retrofit_en

[2] EUROPEAN COMMISSION. Horizon prize for the cleanest engine of the future. Available online (last accessed on 18 Jan 2022). https://ec.europa.eu/info/research-and-innovation/funding/funding-opportunities/prizes/horizon-prizes/cleanest-engine-future_en

[3] GIECHASKIEL, B., SUAREZ-BERTOA, R., LAHDE, T. et al. Evaluation of NO_x emissions of a retrofitted Euro 5 passenger car for the Horizon prize "Engine retrofit". *Environmental Research.* 2018, **166**, 298-309. https://doi.org/10.1016/j.envres.2018.06.006

[4] GIECHASKIEL, B., SUAREZ-BERTOA, R., LAHDE, T. et al. Emissions of a Euro 6b Diesel passenger car retrofitted with a solid ammonia reduction system. *Atmosphere.* 2019, **10**, 180. https://doi.org/10.3390/atmos10040180

[5] FONTARAS, G., PAVLOVIC, J., CARRIERO, M. et al. Joint Research Centre 2018 light-duty vehicles emissions testing. Contribution to the EU market surveillance: testing protocols and vehicle emissions performance EUR29897 EN, *Publications Office of the European Union*, Luxembourg, 2019. https://doi.org/10.2760/289100, JRC117625

[6] MAUNULA, T. Combination of LNT and SCR for NO_x reduction in passenger car applications. *Combustion Engines*. 2014, **157**(2), 60-67. https://doi.org/10.19206/CE-116945

[7] WITTKA, T., HOLDERBAUM, B. Potentials for NO_x and CO_2 reduction of combined NSC + passive SCR system in Diesel passenger car application. *Combustion Engines.* 2014, **157**(2), 68-76. https://doi.org/10.19206/CE-116946

[8] BARROS, S., ATKINSON, W., PIDURU, N. Extraction of liquid water from the exhaust of a diesel engine. *SAE Technical Paper.* 2015. 2015-01-2806. https://doi.org/10.4271/2015-01-2806

[9] OOMMEN, L.P., KUMAR, G.N. A study on the effect of magnetic field on the properties and combustion of hydrocarbon fuels. *International Journal of Mechanical and Production Engineering Research and Development.* 2019, **9**(3), 89-98.

[10] NOTTI, E., SALA, A. Fuel saving and emission reduction in fisheries: Results of the experimentation of a new magnetic device onboard fishing vessel. 2014 Oceans – St. John's, 2014, 1-5. https://doi.org/10.1109/OCEANS.2014.7003183

[11] LA ROCCA, A., FERRANTE, A., HAFFNER-STATON, E. et al. Investigating the impact of copper leaching on combustion characteristics and particulate emissions in HPCR diesel engines, *Fuel.* 2020, **263**, 116719, https://doi.org/10.1016/j.fuel.2019.116719

[12] JAWORSKI, P., JAROSIŃSKI, S., CORTES CAPETILLO, A. et al. SCR systems for NO_x reduction in heavy and light duty vehicles. *Combustion Engines*. 2016, **164**(1), 32-36. https://doi.org/10.19206/CE-116486

[13] TESTING RETROFIT TECHNOLOGIES, https://retrofit4emissions.eu/

[14] TRIANTAFYLLOPOULOS, G., KATSAOUNIS, D., KARAMITROS, D. et al. Experimental assessment of the potential to decrease diesel NO_x emissions beyond minimum requirements for Euro 6 Real Drive Emissions (RDE) compliance. *Science of The Total Environment*. 2018, **618**, 1400-1407. https://doi.org/10.1016/j.scitotenv.2017.09.274

[15] CZERWINSKI, J., MAYER, A., HEEB, N. Quality test procedures & emissions with DPF+SCR systems. *Energy Power*. 2014, **4**(1A), 11-31. https://doi.org/10.5923/s.ep.201401.02

[16] DZIDA, J., BRZEŻAŃSKI, M. An analysis of SCR reactor deactivation impact on NO_x emissions from a compression ignition engine. *Combustion Engines*. 2019, **178**(3), 208-212. https://doi.org/10.19206/CE-2019-336

Barouch Giechaskiel, DEng. – European Commission, Joint Research Centre, Ispra, Italy.
e-mail: *barouch.giechaskiel@ec.europa.eu*

Ricardo Suarez-Bertoa, DEng. – European Commission, Joint Research Centre, Ispra, Italy.
e-mail: *ricardo.suarez-bertoa@ec.europa.eu*

Anastasios Melas, DEng. – European Commission, Joint Research Centre, Ispra, Italy.
e-mail: *anastasios.melas@ec.europa.eu*

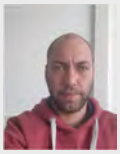

Tommaso Selleri, DEng. – European Commission, Joint Research Centre, Ispra, Italy.
e-mail: *tommaso.selleri@ec.europa.eu*

Maurizio Maggiore, Deng. – European Commission, DG-RTD, Brussels, Belgium
e-mail: *maurizio.maggiore@ec.europa.eu*

Article citation info:
MAMALA, J., GRABA, M., BIENIEK, A. et al. Evaluation of energy consumption in the acceleration process of a passenger car. *Combustion Engines*. 2022, **190**(3), 35-44. https://doi.org/10.19206/CE-142553

Jarosław MAMALA
Mariusz GRABA
Andrzej BIENIEK
Krzysztof PRAŻNOWSKI
Krystian HENNEK
Szymon KOŁODZIEJ
Bartosz MAZUREK
Maciej SPROCH

Combustion Engines
Polish Scientific Society of Combustion Engines

Evaluation of energy consumption in the acceleration process of a passenger car

ARTICLE INFO

Received: 30 August 2021
Revised: 12 September 2021
Accepted: 23 September 2021
Available online: 5 December 2021

The analysis of the vehicle acceleration process is a current topic based on the aspects related to the general characteristics of the car, its parameters, design, drive unit performance, and the influence of external factors. However, the ability to accelerate is essential from the point of view of the active safety of the car. Often the dynamic parameters are determined on the basis of the car acceleration test carried out on a level road with good surface in terms of the acceleration time is not reliable and the credibility of such results depends on many factors. Therefore in the article, the authors assessed the dynamic and energy parameters of the car motion, in which the intensity of acceleration of the car with different intensities was examined. The acceleration intensity test was carried out from the set initial speed of the car of 45 km/h to the final speed of 120 km/h at a constant gear ratio, and the set intensity of the acceleration process resulted from the constant throttle with a constant deflection of the accelerator pedal. Acceleration was carried out in two variants, the first for a normal internal combustion engine and the second for the same engine but additionally equipped with a short-term boost system. In this way, it influences the increase in power and energy in the car drive system, changing its acceleration intensity. Variable car acceleration intensity was obtained in the range from 0.12 to 1.37 m/s^2, and energy consumption at the level of 0.4 to 1.2 MJ in the distance of 1/4 mile. The article proposes a combination of energy parameters and engine power in order to assess the acceleration dynamics, for this purpose, the specific energy consumption of the car was determined, ranging from 0.35 to 2.0 J/(kg·m), which was related to the engine power, denoting it with the dynamics index. The study focuses on the assessment of the relationship between the specific energy consumption and acceleration of passenger cars in the available powertrain system using a new dynamics index. The proposed dynamics index combines the energy and dynamic parameters of the car to be able to objectively quantify the acceleration process.

Key words: *acceleration, energy consumption, vehicle dynamic, dynamic index*

1. Vehicle acceleration profile and average driving force

The acceleration process, regardless of whether it is from a resting state or from a specific initial speed to the set travel speed, is the most energy-consuming phase of motion. Because, even with moderate acceleration, the increase in consumption energy related to fuel consumption significantly exceeds the energy required to overcome the basic motion resistance, and is related to the existence of a fictitious driving force associated with the car inertia depending of total mass. In the thesis [1] the authors analyzes the effects of driving style and vehicle performance on the real-world fuel consumption of conventional vehicles. The authors analyzed that the driving aggressiveness has a important factor of fuel consumption of a vehicle. The work [2] presents a methodology for classifying road traffic energy efficiency. The indicators defined discriminate the impact of the road vertical and horizontal alignments upon energy consumption, disclosing the improvement potential of the road as a function of the traffic origin-destination matrix. On the other hand, the work [3] analyzes the emission of harmful substances into the natural environment depending on the given vehicle speed profile. It has been shown that for the dynamic profiles of the amount of emission they slightly exceed the values given in the approval cycles, and for the profiles with reduced dynamics, the emission values are lower than those obtained in the approval cycle. On the other hand, in [4], a modified four-stroke internal combustion engine was tested, in which the compression ratio was increased. This modification contributed to an improvement in engine power and overall efficiency among others was observed in the tested areas of the characteristics. In the work [5] the authors have undertaken an study into the potential to vary the power output of a powertrain system by application of the digital simulation designed with the purpose of improving the power output of powertrain system in a passenger car comprising a multi-ratio mechanical gearbox. Therefore, depending on the driver's actions and external conditions, the acceleration process is characterized by different values of both total distance-related and specific energy consumption.

In the case of the acceleration process on a horizontal road with a certain intensity, the energy needed to accelerate the car is balanced by the sum of the energy expenditure lost to overcome the rolling and air resistance, as well as the inertia of the car [6, 7]. The study [8] analyses the effect of acceleration intensity on energy consumption and drive efficiency during a road test for a passenger vehicle. The authors assessed also the relationship between the average acceleration for the speed gaining phase and unit energy consumption, where the acceleration increment by 0.1 m/s^2 causes a proportional increment in unit total energy consumption by about 0.15 J·(kg·m)$^{-1}$, regardless of the acceleration intensity. On the other hand, Kropiwnicki et al. In their work [9] analyzed the regenerative braking process for urban traffic conditions. A model was also presented that allows to calculate the amount of energy available from the braking process depending on the proposed variables characterizing the conditions of vehicle traffic. The energy intensity of motion on a horizontal road after the transformation can be expressed by Eq. (1):

$$E_M = E_R + E_A + E_I \tag{1}$$

with the components of the energy balance being recorded by Equations (2)–(5):

- motion energy consumption for the speed gaining phase

$$E_M = \int_{t_s}^{t_e} D_F \, v \, dt \tag{2}$$

- the energy expenditure to overcome rolling resistance

$$E_R = mgc_R \int_{t_s}^{t_e} v \, dt \tag{3}$$

- the energy expenditure to overcome air resistance

$$E_A = \rho/2 c_x A \int_{t_s}^{t_e} v^3 \, dt \tag{4}$$

- the energy expenditure to overcome inertia resistance is directly proportional to the increase in kinetic energy of the car

$$E_I = \frac{m\delta(V_e^2 - V_s^2)}{2} \tag{5}$$

In a number of studies, the energy expedited throughout the entire process of the car drive, not only in the acceleration phase, is applied to describe the energy consumption of movement (E_M). The authors of the article [10] defines on the possibility of reduction CO_2 of the internal combustion engine and presents the analysis based on originally conducted studies. The increase in overall engine efficiency is sought after by all engineers dealing with engine construction, one of the major ways to reduce CO_2 emissions is to increase the compression ratio. In turn Bo Hu et al. in their work [11] claim that the engine downsizing is a proven approach for achieving a superior fuel efficiency. It is conventionally achieved by reducing the swept volume of the engine and by employing some means of increasing the specific output to achieve the desired installed engine power, usually in the form of an exhaust-driven turbocharger. The article [12] presents the trend of car manufacturers related to the downsizing process of engines and the use of supercharging systems mainly for economic reasons. In turn, the authors of [13] indicate the possibilities of fuel savings through the use of an appropriate style of driving, such as the so-called "pulse and glide" (PnG). In their work, they analyse the savings resulting from the driving style for a traditional vehicle with an ICE engine and for a HEV vehicle. Savings resulting from the driving style can reach even several dozen percent. Mamala et al. in their work [4] claims that one of the ways to improve the efficiency of an IC engine is to raise its compression ratio (CR). However, high CR in spark ignition engines can be the reason of engine knock in high load and crankshaft rotation speed conditions. Therefore it would be favorable, that high CR would be obtained in low load, and low CR in high load conditions. These results and findings led the authors to build the variable Effective Compression Ratio (eVCR) system. A 4-stroke single cylinder engine was equipped with an electric actuator and its control system, allowing valvetrain-independent intake valve action. The authors of the study [5] have undertaken an study into the potential to vary the power output of a powertrain system by application of the digital simulation-control designed with the purpose of improving the power output of powertrain system in a passenger car comprising a multi-ratio mechanical gearbox.

Taking into account this assumption, it can be utilized to substitute the equation in (2) to the account for total energy consumption relative to movement (E_T) resulting from fuel use:

$$E_T = \mathrm{SFC} \cdot S_F \tag{6}$$

For the case when we consider only the acceleration phase marked by constant conditions, the total energy intensity of motion is given by the product of the mean force and the distance traveled throughout the process of acceleration (7).

The difference in energy consumption resulting from the fuel consumption and the energy delivered to the wheels results from the efficiency of the entire powertrain system, which is given with the expression (8).

$$E_T = \frac{E_M}{\eta_P} = \frac{D_F \cdot L}{\eta_P} \tag{7}$$

It should be noted that the value of a car's mean acceleration during the acceleration phase up to a certain target speed depends exclusively on the implemented speed profile that determines the distance travelled, causing a slight variation in the kinetic energy gain within one gear. The mean acceleration in the acceleration phase depends on the reserve of the driving force and this depends on the gear ratio, i.e., the transmission ratio in powertrain, which will be analyzed in the next chapter.

After the above assumption is applied in the equations (1) and (7), we can express the total distance-related energy consumption in the form

$$\Psi_T = \frac{E_T}{L} \tag{8}$$

which includes the total of the energy expenditure as well as the efficiency of the powertrain per one meter of the distance traveled by a car.

Given a constant speed, the total distance-related energy consumption is physically equal to the driving force, which also accounts for the term to express the inertia force proportional to the mass and acceleration of the car. Therefore, when we apply the assumption made in eq. (9), the indicator of the movement energy quality of the car, we can develop a parameter that expresses the total specific energy consumption, expressed as the ratio of energy expenditure to the product of mass and distance

$$Q_E = \frac{E_T}{m \cdot L} \tag{9}$$

On a horizontal road, the total specific energy consumption, similarly to eq. (9), is made up by the total of three basic energy terms, of which the first two (eq. (2)) account for the energy losses of basic movement resistance, and the third represents the ratio of kinetic energy to the product of mass and distance traveled. Thus, in physical terms, the average acceleration resulting from the energy parameters of the car.

2. Research methodology and test object

The article addresses two issues:

The first one: presents the issues of energy consumption assessment in the acceleration process – by introducing the dynamics index.

The second point: presents a system for changing the dynamics of a vehicle in the acceleration process for an internal combustion engine.

For the driver, good dynamic properties of the car are important in the acceleration process. An unsolved problem is the lack of driving force in the acceleration process, which concerns not only the internal combustion engine but also the entire drive system or the way it is controlled by the driver. This problem is also not solved in the case of electric drive systems.

Hence, it is an attempt to use a short-term boost system in an internal combustion engine to improve the car's dynamic properties. It is a response to turbocharging systems with an engine and a generator between the turbine and the compressor. The method of short-term recharging proposed in the work is a simple system in application on an internal combustion engine and requires a minimum of changes. An internal combustion engine with a factory turbocharging system was selected for the tests, for which an additional compressed air supply system was modified and introduced. During the research, the main emphasis was on the dynamics of the car in terms of energy, based on a specific dynamics index. The dynamics index was checked by using a short-term boost system which temporarily increased the power of the internal combustion engine. The basic assumption of the research is to use the same car (same weight) but with a different available power in the drive system. The increase in the power of the combustion engine and the increase in the dynamics of the car is compensated by the proportionally increase in its dynamics index. This made it possible to check the sensitivity of the dynamics index, combining energy and traction parameters.

The use of air charging is one of the methods that allows for obtaining a greater torque from the powertrain during the car’s rapid acceleration. The referenced papers [14–17] feature many such air charging systems, starting with air supercharger systems (e.g., mechanically driven compressor and turbocharger) or high-storage systems (e.g., nitrogen monoxide charging). The work [18] is devoted to the analysis of E-tronic systems (control) of superchargers in order to eliminate the Turbo Leg phenomenon. The paper [19] discusses investigations into improving the full-load and transient performance of the Ultraboost extreme downsizing engine by the application of the SuperGen variable-speed centrifugal supercharger. The improvement in full-load performance in the area where the turbocharger cannot generate the required boost by itself is reported. The transient response of the combined system at low engine speed is also presented, together with part-load fuel economy data at several engine speed and load points. On the other hand, in [20] an innovative solution was proposed for the routing of engine exhaust gases, which resulted in a reduction of the exhaust stroke resistance. The proposed method leads to a 5% fuel economy and provides an improvement in engine performance without significant engine modifications.

Despite their common use in combustion engine supply, the aforementioned systems are characterised by a series of limitations and flaws. One of the major flaws of turbochargers is the adaptation of the compression performance to the engine’s rotational speed (excess air at high engine rotational speeds) and the so-called turbocharger lag effect. Therefore, research on new air supercharger structures can be divided into three categories with the following characteristics:

- variable supercharger specification,
- combined systems,
- combining superchargers into assemblies.

The use of a turbocharger, despite substantially improving the torque parameters, is not without flaws either and does not solve the problem of lacking a turbocharger. The lacking turbocharger is the reason for deficiencies in the driving force. When the demand for torque rapidly increases at the crankshaft’s low rotational speed, the insufficient turbine fuelling prevents the compressor from supplying sufficient air quantity to meet the condition related to the excess air ratio $\lambda = 1$. The delay in the powertrain’s reaction to the driving force demand and as well as the phenomenon of a gas connection in the intake manifold of the turbocharger system is the subject of research of many scientists [21, 22]. Despite the flaw, this solution is most often used by engine manufacturers, however, new solutions feature a complex structure. The detailed schematic of the short-term compressed air supercharging system upstream of the turbocharger assembly is presented in Fig. 1.

The application of the short-term supercharging directly into the turbocharger’s assembly in the quantity required to overcome the resistance of gas flow through the compressor will enable a vacuum less engine supercharging with air required to accelerate it. This solution is based on a classic turbocharger assembly, in which the turbine was modified by placing an expansion nozzle supplying compressed air directly to the turbine’s blades. This substantially improves the increase in the turbine’s rotational speed in the conditions of its reduced performance. The adoption of these assumptions should have a positive impact on the car’s acceleration dynamics.

The bench testing, conducted on the MAHA MSR 500 4×4 chassis dynamometer, utilised a passenger car with a spark ignition engine with an indirect multipoint fuel injection and a turbocharger system, with the displacement of 1,781 cm^3 and a maximum power of 110 kW at 5,700 rpm and a torque of 210 Nm at 1,750 rpm, equipped with an electronically-controlled throttle. The power transmission system is equipped with a manual five-speed gearbox. The car’s maximum speed amounted to 223 km/h. The test car with elements of the modified turbocharging system is shown in Figs 2a, 2b.

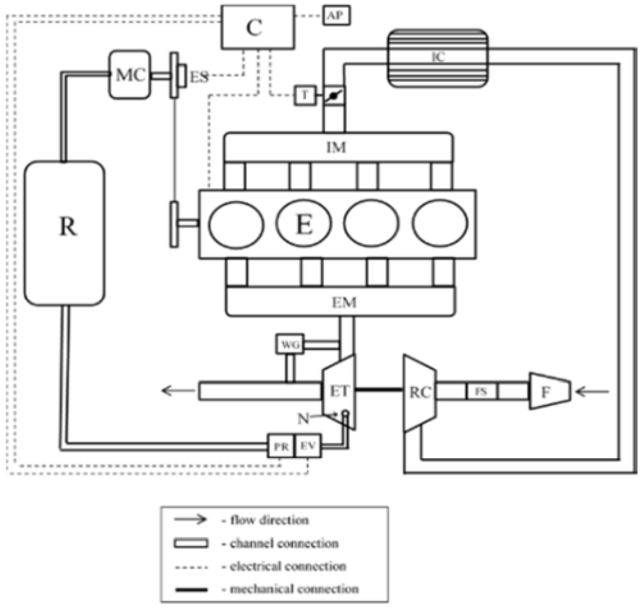

Fig. 1. Short-term compressed air supercharging system downstream of the turbocharger assembly: E – engine, EM – exhaust manifold, WG – west gate, ET – exhaust turbine, PR – pressure regulator, T – throttle, EC – electromagnetic clutch, F – air filter, RC – radial compressor, IC – intercooler, IM – intake manifold, C – controller, AP – accelerator/throttle pedal, R – reservoir, FS – mass airflow sensor, EV – valve, MC – mechanical compressor, N – nozzle

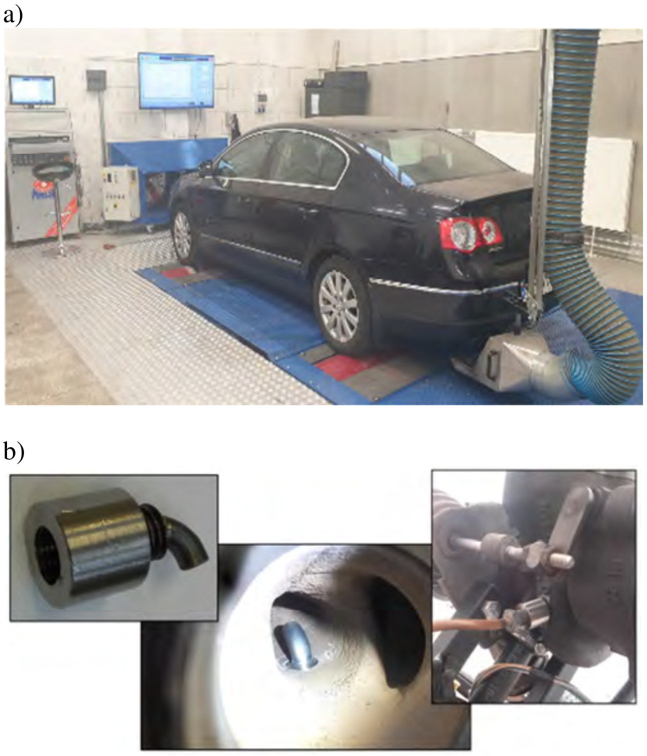

Fig. 2. Test car with a modified supercharging system: a) test vehicle, b) turbocharger assembly's

The test setup comprised an autonomous control and measurement system in the LabView environment, which resulted as an integrated application that enables controlling and recording of powertrain operating parameters during the repeatability of the flexibility test and observing of the acceleration process. To record the kinematic parameters of a passenger car in motion, a measurement system called PAAF II (Power Acceleration and Force) developed in the Department of Vehicles at the Opole University of Technology was used, which was programmed in the LabView environment. For the purposes of measurements, this software has been supplemented with a control module for the control of the additional power increase of the powertrain. It enables the recording of kinematic parameters with time from the following systems:

- from the OBDII on-board diagnostic system recording, among other parameters: engine speed, throttle position, intake manifold pressure, engine load, fuel consumption, vehicle speed,
- from additional direct devices using a measurement module: recording speed, distance by means of the Corrsys Datron L-350 optical head, throttle position, accelerator pedal, position and consumed fuel from the Flowtronic system,
- from the on-board data transmission network-based CAN BUS: standard recording engine speed, wheel acceleration, distance travelled, gear number, driver's control pedal status, and fuel consumption,
- from the supercharging system among other parameters: charging pressure.

The bench testing was conducted to obtain a detailed image about the impact of the short-term compressed air supercharging directly onto the turbine's blades via an expansion nozzle, the end of which is connected to the intake channel of the engine's exhaust manifold. The air was fed from the storage tank at the pressure of 0.9 MPa directly to the turbine blades during car acceleration on a chassis dynamometer. The air supercharging time amounted to 10 s, with an average air flow of about 62 dm^3/s. Different tank pressures and flows were tested in the study, but the results presented below refer to these settings. The tests were carried out to identify the total energy consumption, in the process of acceleration with the use of the active identification method, by observing the parameters of the powertrain operation in dynamic conditions. Therefore, the subject of further considerations is the analysis of the process of passenger car acceleration from a fixed initial speed, on a horizontal road, to a fixed final speed. The final value of the car's speed results from the balance of energy in the powertrain with the energy of motion resistance or the assumed final speed of 120 km/h achieved by the car. The intensity of the acceleration process was regulated by a constant depression of the accelerator pedal, corresponding to a throttle position in the intake manifold of 20%, 25%, 30%, 35%, 40%, 45%, 50%, 70%, and 100% of the range during the test on distance ¼ mile. The acceleration process was carried out on constants transmission ratios in the powertrain.

3. Test results

The flexibility test carried out during the acceleration process of the car over a quarter of a mile was analysed for the mean values of kinematic and energy parameters were determined (Fig. 3).

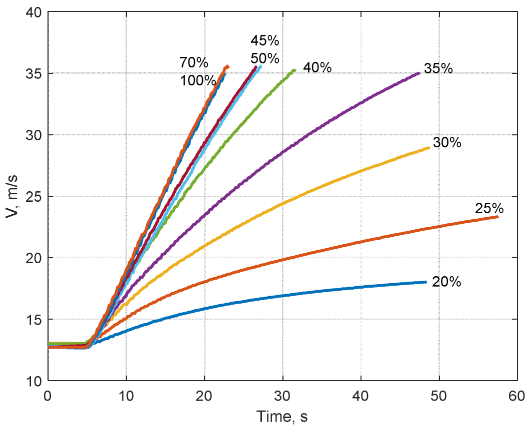

Fig. 3. Courses of linear speed car in the flexibility test during acceleration of a constant transmission on the test bench for constant throttle positions

For the throttle positions equal to 20%, 30%, and 35%, resulting from the most frequent driving operating conditions in particular for economic driving, the test was realized up to the maximum speed that can be gained for a given throttle position, because the driving force in the powertrain system, in accordance with the equation (1) was not sufficient to reach the desired speed. The value of the force results from the quotient of the efficiency of the powertrain, i.e., the energy delivered to the powertrain in relation to the length of the road taken for acceleration. Due to the different dynamics of the flexibility test, the value of the speed achieved over the distance of ¼ mile is variable. The averaged kinematic parameters recorded during the acceleration process in the ¼ mile elasticity test are summarized in Table 1.

Table 1. List of dynamic and energy parameters for the acceleration process in ¼ mil

TP [%]	a_{sf}	Time [s]	L [m]	a_{max} [m/s^2]	P_{mean} [kW]	Q_{mean} [$dm^3/100$ km]
20	0.11	25.9	401.2	0.25	4.53	6.93
25	0.17	23.5	401.5	0.41	7.73	7.86
30	0.34	23.5	401.8	0.67	10.34	9.71
35	0.51	19.7	400.8	0.83	18.99	12.29
40	0.85	18.4	401.4	1.13	26.32	15.58
45	1.06	17.6	402.8	1.18	32.67	18.26
50	1.08	17.6	401.4	1.23	33.13	18.66
70	1.30	16.8	400.5	1.36	40.57	22.88
100	1.31	16.7	400.8	1.37	40.96	22.92

4. Evaluation of the energy consumptions in acceleration process of a passenger car

The results of fuel consumption versus time recorded during the test of car acceleration elasticity with different throttle positions were compared to the mean acceleration values and subsequently to the fuel consumption [$dm^3/100$ km] (Fig. 4). The fuel consumption related to the cases marked by small values of acceleration is constant and independent of acceleration, however, for the maximum intensity of acceleration, this value varies within a wide range. It can be generalized that the low acceleration up to the value of the mean acceleration of 0.8 m/s^2 does not generate significant variations in fuel consumption. Above this value, the consumption increases significantly.

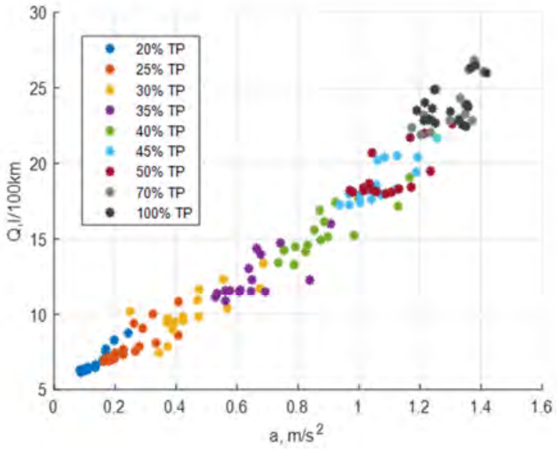

Fig. 4. Variations in distance-related fuel consumption in the acceleration elasticity test of a vehicle with constant transmission on dynamometer for constant throttle positions

In terms of the mean values resulting from the car acceleration elasticity test, the mean values are directly proportional to both fuel consumption and distance-related fuel consumption. It is difficult to relate these values to the dynamics resulting from the varied available energy in the drive system, which is indicated by the total energy consumption of car movement and is presented in Table 2.

Table 2. List of energy parameters for the acceleration process in ¼ mile test

TP [%]	Ge_{mean} [g/s]	Q_{min} [dm^3/km]	Q_{max} [$dm^3/100$ km]	E_T [MJ]	Q_E [J/(kg·m)]
20	0.780	6.28	7.96	0.441	0.355
25	0.967	6.89	9.63	0.496	0.519
30	1.219	7.41	11.71	0.550	0.688
35	1.795	11.38	15.20	0.720	1.061
40	2.446	14.24	17.16	0.888	1.404
45	3.017	17.25	19.41	1.024	1.664
50	3.088	17.98	19.62	1.033	1.691
70	4.005	22.04	23.89	1.232	2.003
100	4.056	21.48	24.03	1.224	2.008

The registered differences in terms of the total energy consumption of the investigated car can be related to its mass. Hence, in accordance with the definition derived from equation (6), the cumulative energy consumption over the entire process of acceleration that is related to mass and distance and is expressed in the physical sense by the measure expressed by m/s^2, that is, the value of the mean acceleration accompanying power supply to the wheels.

5. Evaluation of the acceleration process of a passenger car

The effect of the additional air charging of the turbocharger unit was measured on a chassis dynamometer in the form of an increase in the driving force during car acceleration from its initial speed, with a constant throttle position (Fig. 5). According to the literature data [23, 24] as well as the information presented in the introduction, a higher increase in driving force at partial throttle opening was achieved. The increase varies depending on the throttle opening.

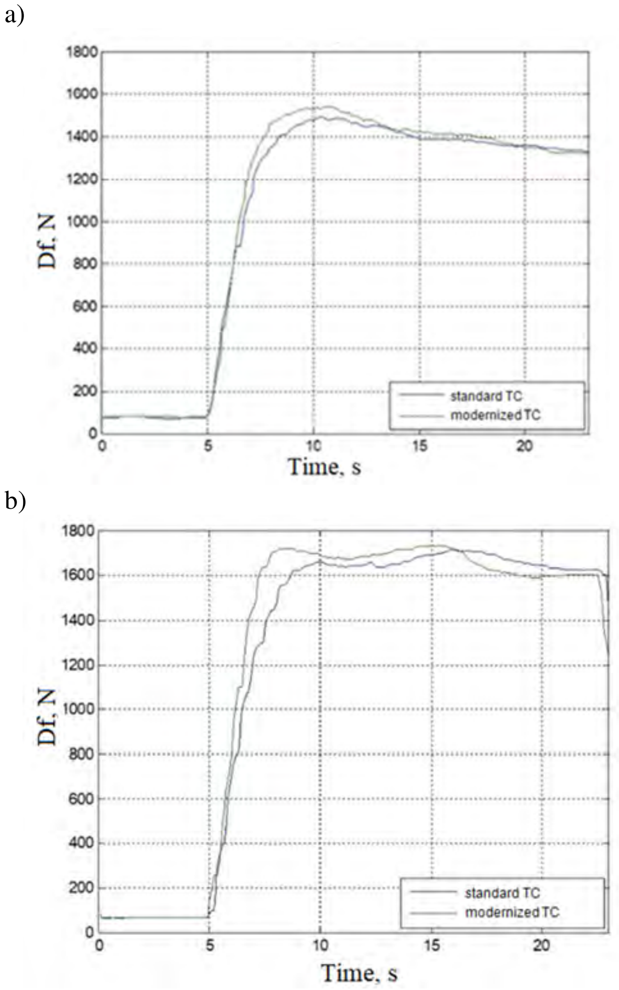

Fig. 5. Comparison of the driving forces (Df) during acceleration with and without the supercharger system for different throttle positions

The obtained higher driving force values improved the acceleration, especially in the first acceleration phase. The engine test bench was used to conduct tests of car acceleration after rapid throttle opening from its initial position of 7% to the end position during a constant transmission ratio. The initial throttle opening angle corresponded to the car's linear speed of 45 km/h, while the end throttle opening angle derived from the force balance or the measurement was interrupted after achieving the end speed of 125 km/h, which is presented in Fig. 5.

In order to analyze the sensitivity of the car dynamics related to the increase in powertrain output power, the tests were repeated for the tested car with the activated system that increases the instantaneous power in the powertrain by increasing the engine power. The comparisons of the powertrain performance during the flexibility test with different throttle openings are presented in Fig. 6.

Table 3 shows the increase in engine power with a constant position of the acceleration pedal in the boost process. The relative increase in engine power during recharging ranges from 5.7 to 12.4%. The best effect was achieved with the accelerator pedal 45%. The smallest increase in power was achieved at full engine load.

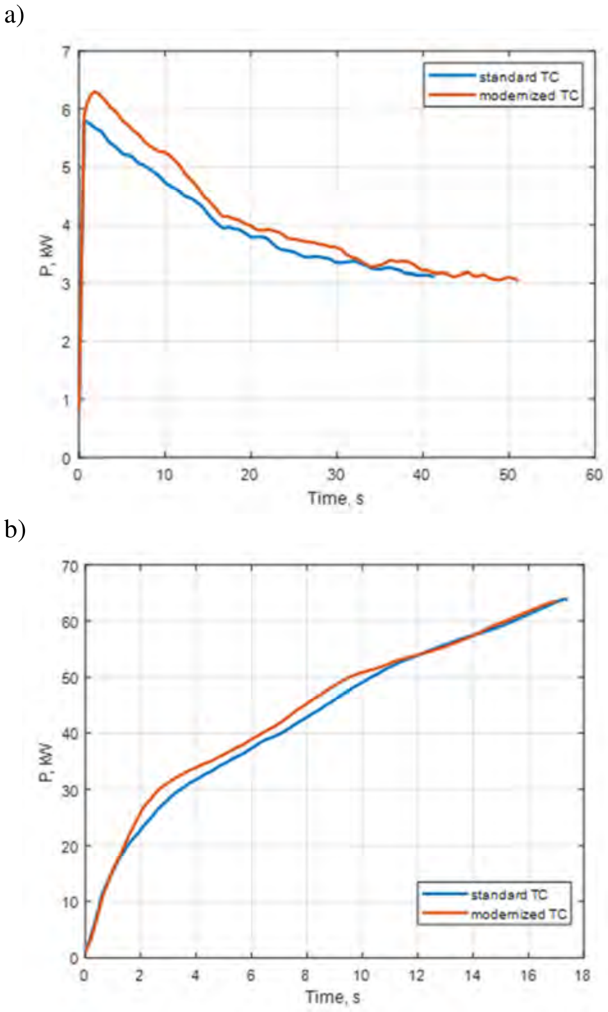

Fig. 6. Comparison of the powertrain output in the car acceleration elasticity test for a car with step-gear transmission on a dynamometer for throttle positions: a) 20 %, b) 100 %

Table 3. Increase in the engine power for a constant position of the accelerator pedal

Accelerator position, %								
20	25	30	35	40	45	50	70	100
Relative power gain during supercharging, %								
7.8	6.3	6.2	8.2	8.2	12.4	8.1	9.5	5.7

During the supercharging, a temporary increase in fuel consumption was observed (Fig. 7), which is the result of the increased amount of air flowing in the engine cylinder. It is tantamount to the increase in engine power, and Fig. 7 shows the fuel consumption for the reduced positions of the accelerator pedal, i.e., the minimum and mass of the car acceleration.

The modifications to the turbocharger assemblies in the form of short-term supercharger system allowed for achieving the linear speed within a shorter time. After the short-term charging is completed, the injected fuel dose to the engine drops sharply, which is shown in Fig. 7. This may be due to the fuel dose correction based on too high oxygen content in the exhaust gas caused by compressed air charging. It was possible to observe the following dependencies: the smaller the throttle opening angle during acceleration, the greater the importance of the short-term supercharger system are shown in Fig. 8.

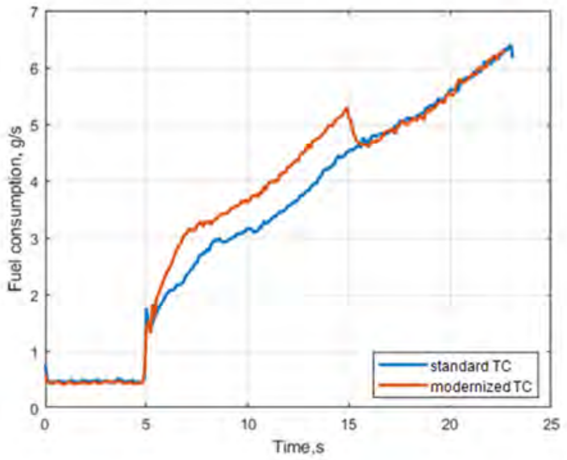

Fig. 7. Fuel consumption in the car acceleration elasticity test on a dynamometer for throttle positions 100 %

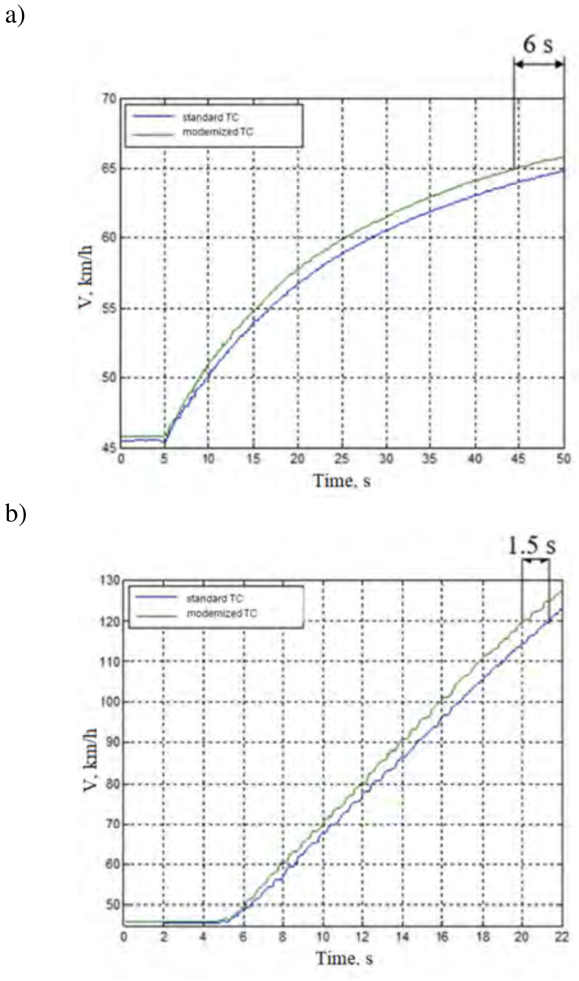

Fig. 8. Comparison of the driving forces during acceleration with and without the supercharger system for different throttle positions: a) 20%, b) 100%

For the final throttle position of 20% (Fig. 8a), achieving the final linear speed of 65 km/h took 45 s in the case of the traditional engine with a supercharger system and 6 s less in the case of an engine utilising the supercharging. Similarly, for the throttle position of 100% (Fig. 8b), the time was shorter by 1.5 s.

The presented graphs of the speed increase of the car in the flexibility test depend on the energy consumption and dynamics of the car and are directly related to the power output of the drive system, so they are difficult to compare [8, 25, 26]. In order to assess the car acceleration processes in the flexibility test, the specific energy consumption of the car was compared to the power of the drive unit. An additional index of the energy quality of the acceleration of the car was obtained according to eq. (10).

$$I_D = \frac{P}{Q_E} \qquad (10)$$

The introduced dynamics index is a universal measure, which in its properties is related to power, mass, and distance traveled, which in this way combines energy parameters with dynamics. The applied dynamics index demonstrates in the physical sense the time 1 s needed for the acceleration of a passenger car weighing 1 kg over a distance of 1 m, combining the basic kinematic properties of its movement. These quantities are known and have long been used in the automotive industry.

The achieved in the supercharging process increased engine power affects the acceleration time, but these changes are insignificant in relation to the introduced acceleration dynamics index (Fig. 9). In the case of the position of the acceleration pedal of 20% (for a low intensity of car acceleration), these differences are minimal and amount finally to 12.74 kg·m/s with the fuel consumption of 6.94 dm^3/100 km. For a full deflection of the accelerator pedal of 100%, the maximum intensity of acceleration of the car, the index increases to the value of 20.24 kg·m/s with a much greater increase in fuel consumption depending on the traveled distance 22.93 dm^3/100 km.

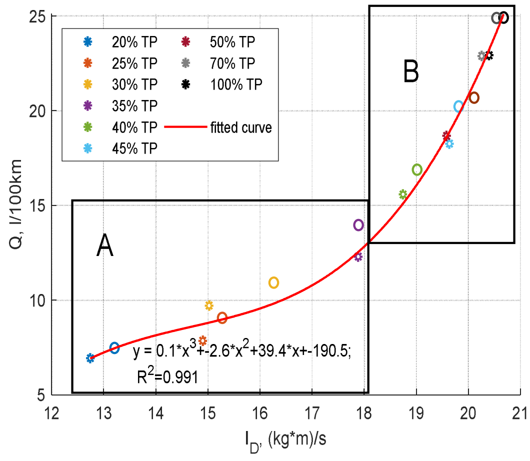

Fig. 9. Index of acceleration dynamics for throttle positions

The car acceleration energy quality indicator corresponds to the kinematic parameters of the car. Using the motion dynamics index (I_D) as in Fig. 9, two areas can be determined. Area A is the area of moderate car acceleration intensity up to 0.8 m/s^2 for the acceleration pedal value up to 45%. This is an area where the energy consumption of traffic is of great importance, related to the parameters of the car and the acceleration profile. Area B is the area assigned to engine power where the increase in acceleration intensity is due to the increase in engine power. With higher car acceleration intensity, the dynamics index (I_D) increases, which is consistent with physics due to the higher energy expenditure (Fig. 9) and the fuel consumption increases significantly. For the presented dynamics index, the instantaneous increase in engine power and acceleration intensity is compensated by the specific energy consumption of the car and the index is comparable.

6. Conclusion

In conclusion, it should be emphasized that the analysis of car acceleration processes is a complex process. A direct comparison based on the acceleration time is unreliable. As the research result has shown, of a temporary increase in the power of the combustion engine by approx. 5s, different acceleration times were achieved for the same drive system with constant control parameters (for example as constant throttle positions). The time reduction is a consequence of the increase in fuel consumption and thus the specific energy consumption of the car. However, the reference to the power in the drive system results in a comparable dynamics index of the car's acceleration. The dynamics index in its properties is related to the parameters of movement (time, speed), the design parameters of the car (mass, coefficient of aerodynamic drag) as well as the parameters of the drive system (engine power).

At the same time, the presented in the paper solution supports the car acceleration process using short-term engine supercharging with compressed air is an effective method of improving the car acceleration intensity. The use of short-term turbocharger boost using compressed air gives much greater benefits in the event of partial throttle opening, resulting in a 13.3% reduction in acceleration time, which is especially important in city traffic. As the results show, a short-term increase in fuel consumption does not affect the total specific energy consumption of the car. Similar work leading group Jaguar Land Rover Ltd in 2016 in Great Britain, GB, who reported Patent No. GB1612798.7A, charging system for air turbine blades to increase efficiency and solve the problem of "turbo lag" [27].

The article presents an assessment of the acceleration process of a passenger car equipped with an internal combustion engine, in which it is possible to increase the instantaneous power. The presented dynamics index characterizes the car acceleration process and combines the dynamic and energetic parameters of this process. Such a combination allows for meaningful comparisons of the acceleration process. In further research, using the dynamics index, it is intended to compare the acceleration process with a hybrid drive system, where the total increase in power in the drive system is much greater. In addition, the process of the temporary increase in power by the internal combustion engine must be compatible with the control of the gear ratio in the drive system [24]. Then we can achieve better work results with lower energy consumption, the acceleration process, but this also requires further work.

Nomenclature

Ψ_T	distance-related energy consumption [kJ/m]
Q_E	total specific energy consumption [kJ/m·kg^{-1}]
a	acceleration [m/s^2]
A	frontal surface of the vehicle [m^2]
AP	accelerator/throttle pedal
a_{sf}	slope factor
C	controller
C_R	rolling resistance coefficient
C_x	drag coefficient
D_F	mean acceleration force [N]
DMC	deviation from the mean confidence data
E	engine
E_A	energy of air resistance [kJ]
EC	electromagnetic clutch,
E_H	energy of gradient resistance [kJ]
E_I	energy of inertia [kJ]
EM	exhaust manifold
E_M	energy of motion [kJ]
E_R	energy of rolling resistance [kJ]
ET	exhaust turbine
E_T	total energy consumption [MJ]
EV	valve
F	air filter
FC	Fuel consumption in test [g]
F_D	driving force in the phase when power is supplied to the wheels [N]
F_{PT}	driving force [N]
FS	mass airflow sensor
g	gravitational acceleration [m/s^2]
Ge	fuel consumption [g/s]
IC	intercooler
I_D	Dynamic Index [kg·m/s]
IM	intake manifold
L	distance [m]
m	mass [kg]
MC	mechanical compressor
N	nozzle
P	power [kW]
P_{mean}	mean power [kW]
PR	pressure regulator
Q	distance-related fuel consumption [dm^3/100 km]
R	reservoir
RC	radial compressor
S_F	calorific value [MJ/kg]
SFC	specific fuel consumption [g/kWh]
SI	Spark Ignition engine
T	throttle
TC	turbocharger
t_e	end time [s]
TP	throttle position [%]
t_s	start time [s]
v	instantaneous speed of the vehicle [m/s]

V	speed profile [m/s], [km/h]
V_e	end speed [m/s]
V_{max}	highest vehicle speed [m/s]
V_s	start speed [m/s]
WG	west gate
η	efficiency
η_P	total powertrain efficiency
ρ	air density [kg/m^3]
δ	rotating mass coefficient
$_{max}$	maximum value of a parameter
$_{min}$	minimum value of a parameter
$_{mean}$	mean value of a parameter

Bibliography

[1] BERRY, M. The effect of driving style and vehicle performance on the real-world fuel consumption of US Light-Duty Vehicles. *Massachusetts Institute of Technology*. 2010. https://web.mit.edu/sloan-auto-lab/research/beforeh2/files/IreneBerry_Thesis_February2010.pdf

[2] FERREIRA, H., RODRIGUES, C.M., PINHO, C. Impact of road geometry on vehicle energy consumption and CO_2 emissions: An energy-efficiency rating methodology. *Energies*. 2020, **13**(1), 119. https://doi.org/10.3390/en13010119

[3] FONTARAS, G., FRANCO, V., DILARA, P. et al. Development and review of Euro 5 passenger car emission factors based on experimental results over various driving cycles. *Science of The Total Environment*. 2014, **468-469**, 1034-1042. https://doi.org/10.1016/j.scitotenv.2013.09.043

[4] MAMALA, J. GRABA, M. PRAZNOWSKI, K. et al. Control of the effective pressure in the cylinder of a Spark-Ignition engine by electromagnetic valve actuator. *SAE Technical Paper* 2019-01-1201. 2019. https://doi.org/10.4271/2019-01-1201

[5] PRAŻNOWSKI, K., MAMALA, J., BIENIEK, A. Potential application of power output control in the powertrain of a passenger car. *IOP Conference Series: Materials Science and Engineering*. 2018, **421**(2), 1-10. https://doi.org/10.1088/1757-899X/421/2/022027

[6] RILL, G. Road Vehicle Dynamics: Fundamentals and Modeling – 1st Edition. *CRC Press.* 2011. https://www.routledge.com/Road-Vehicle-Dynamics-Fundamentals-and-Modeling/Rill/p/book/9781439838983 (accessed on 11.06.2021).

[7] GILLESPIE, T.D. Fundamentals of vehicle dynamics. *SAE International*. Warrendale 1992.

[8] GRABA, M., MAMALA, J., BIENIEK, A. et al. Impact of the acceleration intensity of a passenger car in a road test on energy consumption. *Energy*. 2021, **226**, 120429. https://doi.org/10.1016/j.energy.2021.120429

[9] KROPIWNICKI, J., FURMANEK, M. Analysis of the regenerative braking process for the urban traffic conditions, *Combustion Engines*. 2019, **178**(3), 203-207. https://doi.org/10.19206/ce-2019-335

[10] DRABIK, D., MAMALA, J., ŚMIEJA, M. et al. Possibility of reducing CO_2 emissions from internal combustion engines. *E3S Web of Conferences. International Conference Energy, Environment and Material Systems*. 2017, **19**, 1-4. https://doi.org/10.1051/e3sconf/20171901013

[11] HU, B., TURNER, J., AKEHURST, S. et al. Observations on and potential trends for mechanically supercharging a downsized passenger car engine: a review. *Proceedings of the Institution of Mechanical Engineers, Part D: Journal of Automobile Engineering*. 2016, **231**(4), 435-456. https://doi.org/10.1177/0954407016636971

[12] KUSZTELAN, A., YAO, Y.F., MARCHANT, D.R. A review of novel turbocharger concepts for enhancements in energy efficiency. *The International Journal of Thermal & Environmental Engineering*. 2011, **2**(2), 75-82. https://doi.org/10.5383/ijtee.02.02.003

[13] LEE, J., NELSON, D.J., LOHSE-BUSCH, H. Vehicle inertia impact on fuel consumption of conventional and hybrid electric vehicles using acceleration and coast driving strategy. *SAE Technical Paper* 2009-01-1322. 2009. https://doi.org/10.4271/2009-01-1322

[14] MELDOLESI, R., BADAIN, N. Scuderi split cycle engine: air hybrid vehicle powertrain simulation study. *SAE Technical Paper* 2012-01-1013. 2012. https://doi.org/10.4271/2012-01-1013

[15] MERKISZ, J., PIELECHA, J., RADZIMIRSKI, S. New Trends in Emission Control in the European Union. *Springer International Publishing*. Cham 2014. https://doi.org/10.1007/978-3-319-02705-0

[16] MYSŁOWSKI, J. Doładowanie silników [Supercharging of internal combustion engines]. *Wydawnictwa Komunikacji i Łączności*. Warszawa 2016.

[17] Nithesh, N. P. S, Effect of splitters in recirculation channels on performance of turbocharger compressors used in gasoline engines – a CFD study. *International Journal of Automotive and Mechanical Engineering*. 2019, **16**(1), 6214-6229. https://doi.org/10.15282/ijame.16.1.2019.10.0472

[18] SIVARAMAN, M., AAKASH, A., BHARATHIRAJA, B. et al. Design and performance analysis on E-Tronic turbocharger to eliminate turbo lag. *International Journal of Pure and Applied Mathematics*. 2018, **119**(12), 15687-15700. https://acadpubl.eu/hub/2018-119-12/articles/6/1452.pdf

[19] Turner, J.W.G. Popplewell, A. Marshall, D.J. et al. SuperGen on Ultraboost: Variable-Speed Centrifugal Supercharging as an Enabling Technology for Extreme Engine Downsizing. *SAE International Journal of Engines*. 2015, **8**(4), 1602-1615. https://doi.org/10.4271/2015-01-1282

[20] WILLIAMS, A., BAKER, A., GARNER, C. Turbo-discharging: predicted improvements in engine fuel economy and performance. *SAE Technical Paper* 2011-01-0371. 2011. https://doi.org/10.4271/2011-01-0371

[21] BOZZA, F., DE BELLIS, V., MARELLI, S. et al. 1D simulation and experimental analysis of a turbocharger compressor for automotive engines under unsteady flow conditions. *SAE International Journal of Engines*. 2011, **4**(1), 1365-1384. https://doi.org/10.4271/2011-01-1147

[22] KOŁODZIEJ, S., LIGUS, G., MAMALA, J. et al. Analysis of air flow velocity distribution in the intake system of an SI engine, *Combustion Engines*. 2017, **169**(2), 152-157. https://doi.org/10.19206/CE-2017-227

[23] BIENIEK, A., GRABA, M., HENNEK, K. et al. Analysis of fuel consumption of a spark ignition engine in the conditions of a variable load. *MATEC Web of Conferences*. 2017, **117**, 1-6. https://doi.org/10.1051/matecconf/201711800036

[24] MAMALA, J., BROL, S., JANTOS, J. The estimation of the engine power with use of an accelerometer. *SAE Technical Paper* 2010-01-0929. 2010. https://doi.org/10.4271/2010-01-0929

[25] KIM, E., CHOI, E. Estimates of critical values of aggressive acceleration from a viewpoint of fuel consumption and emissions. *Transportation Research Board 92nd Annual Meeting*. Washington 2013. https://trid.trb.org/view/1242034

[26] PIELECHA, I., PIELECHA, J. Simulation analysis of electric vehicles energy consumption in driving tests, *Eksploatacja i Niezawodnosc – Maintenance and Reliability*. 2020, **22**(1), 130-137. https://doi.org/10.17531/ein.2020.1.15

[27] Rover Jaguar Land, Direct injection of gas into a turbine volute, 2016. https://patents.google.com/patent/GB2552482

Prof. Jarosław Mamala, DSc., DEng. – Faculty of Mechanical Engineering, Opole University of Technology.
CEO, Science & Technology Park in Opole.
e-mail: *j.mamala@po.edu.pl*

Mariusz Graba, DEng. – Faculty of Mechanical Engineering, Opole University of Technology.
e-mail: *m.graba@po.edu.pl*

Andrzej Bieniek, DEng. – Faculty of Mechanical Engineering, Opole University of Technology.
e-mail: *a.bieniek@po.edu.pl*

Krzysztof Prażnowski, DEng. – Faculty of Mechanical Engineering, Opole University of Technology.
e-mail: *k.praznowski@po.edu.pl*

Krystian Hennek, MEng. – PhD student in the Faculty of Mechanical Engineering, Opole University of Technology.
e-mail: *k.hennek@po.edu.pl*

Szymon Kołodziej, DEng. – Faculty of Mechanical Engineering, Opole University of Technology.
e-mail: *s.kołodziej@po.edu.pl*

Bartosz Mazurek, MEng. – PhD student in the Faculty of Mechanical Engineering, Opole University of Technology.
R&D, Science & Technology Park in Opole.
e-mail: *b.mazurek@po.edu.pl*

Maciej Sproch, Eng. – student in the Faculty of Mechanical Engineering, Opole University of Technology.
R&D, Science & Technology Park in Opole.
e-mail: *m.sproch@po.edu.pl*

Article citation info:
ZEMLIK, M., DZIUBEK, M., PYKA, D. et al. Case study of accelerated wear of brake discs made of grey cast iron characterized by increased thermal stability. *Combustion Engines*. 2022, **190**(3), 45-49. https://doi.org/10.19206/CE-146698

Martyna ZEMLIK
Mateusz DZIUBEK
Dariusz PYKA
Łukasz KONAT
Dominika GRYGIER

Combustion Engines
Polish Scientific Society of Combustion Engines

Case study of accelerated wear of brake discs made of grey cast iron characterized by increased thermal stability

ARTICLE INFO

Received: 31 December 2021
Revised: 1 February 2022
Accepted: 14 February 2022
Available online: 5 March 2022

In this paper, the subject of the analysis is Rotinger High Performance brake disc, characterized by increased thermal resistance, which is a result of adequate design and material solutions. However, despite declared performance, the analyzed discs suffered accelerated wear over a period of about 20 months. The aim of this study was to assess the causes of the disc failure. As a result, it was showed that the applied material solution still does not differ from standard ones. According to the authors of this paper, an appropriate procedure to improve resistance to thermal fatigue is, among others, changing the shape of graphite precipitates from flake to spheroidal.

Key words: *brake discs, thermal fatigue, thermal cracks, gray cast iron*

1. Introduction

Brake discs used in passenger cars are usually made of grey cast iron, which ensures dimensional stability within a wide temperature range [2, 5]. Graphite, being the basic structural component, is characterized by high thermal conductivity, thus increasing its share in a material should ensure more intensive heat dissipation. Moreover, it also exhibits positive influence on vibration damping, sliding properties and improves features such as castability and machinability. As brake discs' temperature can be raised up to 600ºC during high-load braking and result in wear of friction pair, fading, brake disc coning and thermal fatigue, graphite plays crucial role in transferring heat and providing the overall system efficiency [11] and its shape may be also modified to provide higher thermal resistance [9]. The most advanced discs are made of ceramics and carbon composites, which make them resistant to temperatures of up to 1000°C. However, due to increased price, they are mainly used in racing cars and high performance vehicles. The selection of brake discs for a passenger car is based on many factors. Depending on the class of a car, its weight, intended use and price, the manufacturer equips it with a more or less advanced system.

Cast iron brake discs can be divided into monolithic, ventilated, ventilated slotted and/or drilled ones. The first of these are the least advanced. Being used in low-cost, lightweight cars, they are made of a solid piece of metal, whereby their primary drawback is tendency to heat up quickly, resulting in a drastically reduced braking force. Generally, discs are characterized by a certain heat capacity, and after reaching given temperature, the braking efficiency and heat absorption decrease significantly. Consequently, further operation in such conditions may cause irreversible damage. For this reason, new material solutions are developed [7] and discs designed for faster heat dissipation are used.

Ventilated discs have special channels in the centre of the disc that help them to transfer heat, whereby the heating time is much longer than in the case of monolithic ones [3] and they are suitable for urban roads as a result [6, 10]. Notched discs have grooves cut into the friction surface to prevent the loss of frictional force created by the accumulation of gases which block the pad from pressing properly against the disc. The grooves also evacuate dust, protect the pads from dirt and clean the surface from vitrification.

Drilled brake discs (Fig. 1) have numerous vent-holes, which continually expel the hot gases generated between disc and linings, eliminating the phenomenon of friction decay (fading). The risk of the entire braking system overheating is greatly reduced, as the hot air escapes from the surface faster. The likelihood of disc damage due to sudden temperature changes is also lowered, whereby they are used in high performance cars [1, 8]. Moreover, friction dust is channelled through the holes and then removed by centrifugal force.

Fig. 1. Ventilated and drilled brake disc

Brake discs are elements that wear out during operation and must be replaced if their dimensions exceed the limits. Cracks running across the entire width of the friction surface are also unacceptable. The most common causes of disc damage include thermal cracks [4], corrosion changes and wear of a friction surface e.g. through melting of brake linings. The objective of the performed materials science analysis was to evaluate the causes of accelerated wear of brake discs. According to the manufacturer's data, they were made of a material that belongs to the high carbon class and has enriched structure. As a result, the above-mentioned features should ensure higher thermal stability. However, the analysed discs were subject to accelerated wear over a period of about 20 months.

2. Materials and methods

A fragment of a worn Rotinger High Performance brake disc was used for tests. It was exploited for about 20 months, mainly in urban conditions (approximately 60%) and the rest accounts for motorway. The total mileage during that period equals to 16,800 km. The brake disc was cut out using a high-energy abrasive water-jet. Its basic geometric data are shown in Fig. 2. Moreover, additional worn out brake discs were taken for tests. Their working conditions are not specified, as they were taken from the garage to carry out comparative matallographic analysis.

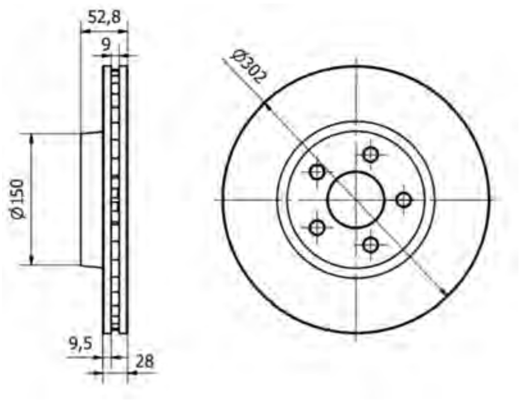

Fig. 2. Basic dimensions of the analyzed brake disc

Microscopic investigations were carried out using a Nikon AZ100 stereo microscope and a Nikon Eclipse MA200 light microscope, with magnifications ranging from 25–500×. Investigations were carried out on the material both in the non-etched state and after etching with HNO_3 solution (Nital). Image registration and analysis were performed using Nikon DS-Fi2 digital camera and Nikon NIS Elements software, respectively.

Chemical composition analyses were performed by means of a GDS500A glow discharge emission analyzer from the Leco company, using the following parameters: U = 1250 V, I = 45 mA, 99.999% argon. The results obtained were an arithmetic mean of five measurements.

The Hardness was measured using a Zwick/Roell ZHU 187.5 universal hardness tester. The Brinell method was applied, at a load of 187.5 kgf (1838.7469 N) and with a 2.5 mm diameter carbide ball, according to the quality standard PN-EN ISO 6506-1:2014-12.

3. Results

A macroscopic image of the brake disc is shown in Fig. 3. Its degree of degradation as a result of corrosion or tribological changes is relatively low, however there are characteristic radial cracks on the friction surface, whose main source are vent-holes (Fig. 4, 5). These types of cracks are formed when variable thermal loads occur during frequent and intensive braking, resulting in formation of internal stresses in the material. When the material is heated, its dimensions are increased as a result of thermal expansion caused by vibrations of atoms, simultaneously generating compressive stresses. Exceeding the yield point of the material due to excessive loading results in tensile stresses, which ultimately cause a break in the continuity of the material. This type of damage can cause the disc to fracture, reducing its stability and causing excessive pad wear.

Fig. 3. Macroscopic image of the analyzed brake disc; visible venting and gas removal system through notches and holes distributed in a characteristic radial-axial manner; unetched state

Fig. 4. Magnified section of the brake disc surface shown in Fig. 3; there can be observed radial cracks on the friction surface, which are initiated mainly at the vent-holes; unetched state

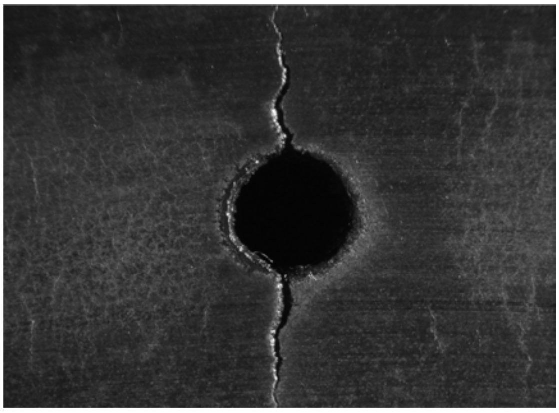

Fig. 5. Magnified section of the brake disc surface shown in Fig. 4 in the vent-hole area; visible cracks arranged in a radial way; unetched state

Macroscopic examination of the material in the unetched state (Fig. 6, 7) indicated the occurrence of unmodified flake graphite precipitates, corresponding to the standard no. I, according to PN-EN ISO 945-1:2019-09. The graphite distribution is consistent with the A standard and locally C, while the size of the precipitates lies in the range of 2–4, in compliance with the eight-stage scale. It should be noted here that this shape of precipitates is the most unfavorable one in terms of mechanical properties, since the sharp ends act as stress concentrators in the contact with metal matrix. This implies a significant deterioration of plastic and strength properties, including tensile strength R_m, flexural strength R_g and torsional strength R_s. In fact, flake graphite has a complex three-dimensional structure and its separations violate the continuity of the cast iron metal matrix to a great extent, while not transferring any stresses. Thus, the effective cross-sectional area of the disc structure is reduced. Moreover, the longer and thinner the flakes are, the more material's internal stresses are increased. What is more, cracks running along the entire cross-section can be also observed (Fig. 6).

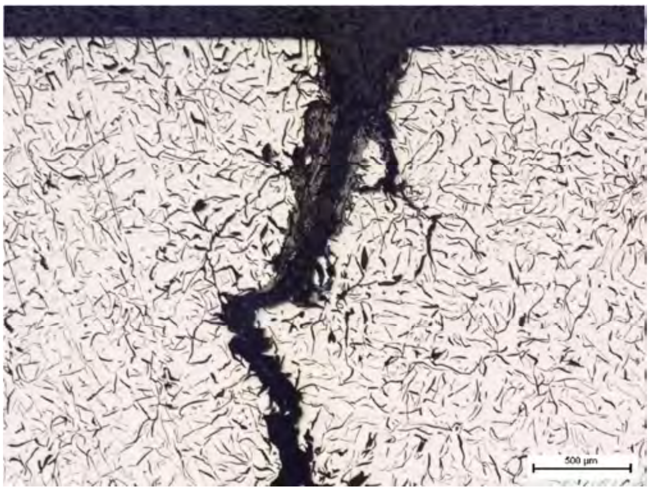

Fig. 6. Microscopic image of the analyzed brake disc. The visible crack spreads along the entire cross-section of the disc; unetched state, light microscopy

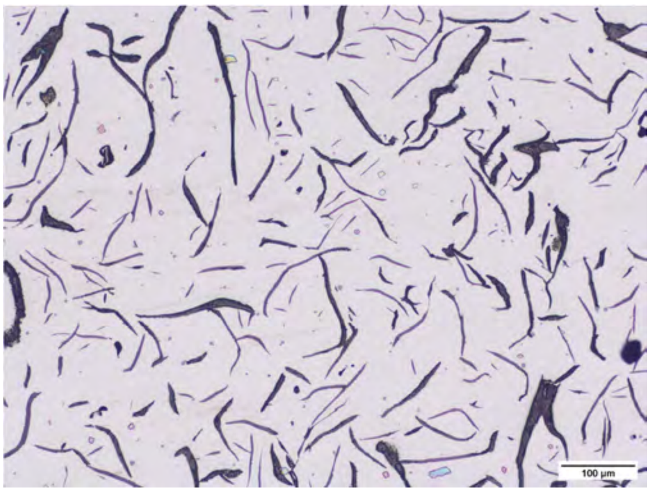

Fig. 7. Magnified image of the material structure of the analyzed brake disc shown in Fig. 6; visible flake inclusions of unmodified graphite; unetched state, light microscopy

Microscopic examination of the material in the as-etched state (Fig. 8, 9) indicated the presence of a perlite matrix. The theoretical strength of perlite is approximately R_m = 750 MPa and by binding in the matrix the highest possible content of carbon (C_{zw} = 0.77%), it provides relatively the highest tensile strength. At the same time, the ductile properties are reduced – for comparison, ferrite's elongation A = 40% and its KCU impact strength is 260 J/cm^2. In the case of pearlite, these values are A = 10% and KCU = 40 J/cm^2, respectively.

Fig. 8. Microstructure of the analyzed brake disc; visible flakes of graphite on the background of perlite matrix; precipitations of phosphite eutectic and manganese sulfides are also observed locally; light microscopy, etched with HNO_3

Phosphite eutectic precipitations are visible in Fig. 9. Their shape is limited by the concave surface of previously solidified austenitic matrix. When the percentage share of phosphorus is zero, ledeburite, being a mixture of austenite and cementite, begins to crystallize at 1147°C. As its content increases, the solidification temperature is lowered to about 950°C, and the resulting eutectic consists of cementite, iron phosphide, and austenite, which then desintegrates into pearlite at 745°C.

Fig. 9. Magnified image of the microstructure shown in Fig. 8; visible flakes of graphite on the background of perlite matrix; precipitations of phosphorus eutectic and manganese sulfides are also observed locally; light microscopy, etched with HNO_3

This structure is called steadite and its occurrence may be desirable. Steadite has hardness of over 500 HBW, so that its uniform distribution in the matrix provides an increase in wear resistance. In comparison, the hardness of perlite is approximately 200–250 HBW. Steadite appears already for the content of 0.1% P in the form of individual precipitates, and for the content above 0.7% P it forms a continuous lattice.

Furthermore, manganese sulfide inclusions are also observed locally, whereby manganese content in the cast iron varies between 0.4 and 1.4%. It is added in order to remove the disadvantageous effect of sulfur, which decreases the flowing power and thus deteriorates casting properties. The disbenefit of manganese is its strong affinity to carbon, and therefore it forms (Fe, Mn)$_3$C carbides that are more durable than cementite. As a result, it whitens gray cast iron.

Table 1 shows the chemical composition of the analyzed brake disc. The percentage share of carbon is equal to 3.22%, while in the case of silicon it is 1.71%. According to Maurer's diagram, such a ratio of carbon to silicon content ensures the occurrence of a perlite matrix for a casting with a wall thickness of 50 mm. Moreover, according to the Greiner-Klingenstein-Staub diagram, the total proportion of carbon and silicon equal to 4.93% results in the occurrence of a perlite matrix for wall thicknesses of 10–50 mm. Silicon is the primary graphitizing element, increasing the propensity for graphite formation during crystallization and eutectoid transformation. Furthermore, it also influences the nucleation of graphite, so that the graphite flakes are thinner and more uniformly distributed.

The phosphorus content on the level of 0.1% causes the occurrence of single precipitates of phosphite eutectic, whereas manganese in the amount of 0.57% effectively binds sulphur and does not cause whitening of gray cast iron. The addition of other elements is negligible.

The above analysis is confirmed by the results of hardness measurements performed after exploitation period (Table 2). The average value is 199 HBW, which corresponds to the hardness of perlite.

Table 1. Chemical composition of the analyzed brake disc

C	Mn	Si	P	S	Cr	Ni	Mo
Selected chemical element [% wt.]							
3.22	0.57	1.71	0.10	0.07	0.24	0.06	0.03

Table 2. Results of Brinell hardness tests

Number of measurement	Hardness [HBW]	Mean value [HBW]
1	197	199 ±29
2	203	
3	193	
4	202	
5	181	
6	207	
7	175	
8	201	
9	206	
10	228	

Comparative material testing of a set of monolithic ventilated brake discs showed that they were made of grey cast iron and their microstructure consisted of unmodified flake graphite precipitates and a perlite matrix. Slight microstructural differences were manifested only by the size of graphite precipitates. The discs were characterized by hardness in the range of 180–206 HBW. On this basis, it can be concluded that the applied material solution for the brake discs in question does not go beyond the generally applied (standard) construction and material solutions. Figure 10 and 11 presents macroscopic images of the analysed brake discs and their microstructure in the unetched state.

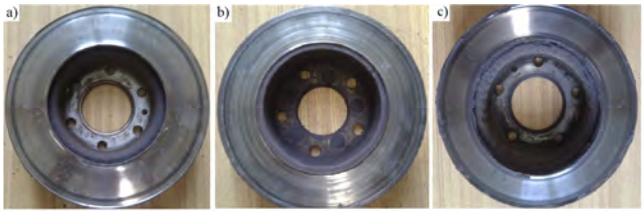

Fig. 10. Macroscopic images of comparative brake discs: a) numerous gouges occurring circumferentially on both friction surfaces, whose darker color indicates overheating; b) wear of the disc manifested by a decrease in thickness; c) wear of the disc due to corrosion changes

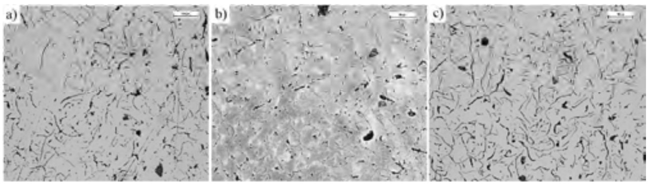

Fig. 11. Microscopic images of the analyzed brake discs shown in Fig. 10; in all cases flake precipitations of unmodified graphite are visible; they are characterized only by the variation of the size of the precipitates, and their shape and way of distribution are similar to each other; unetched state, light microscopy

4. Conclusions

The microstructure of the analyzed brake disc consists of flake graphite precipitates and perlite matrix, while the average hardness of the material is 199 HB. The above properties are typical for commercial brake discs. As it was declared by the manufacturer, an increased carbon content resulting in a higher proportion of graphite precipitates, was supposed to ensure stability for repeated heating and cooling. Despite the low level of wear, the disc was characterised – apart from standard tribological wear – by the occurrence of numerous cracks arranged in a radial manner. The material solution applied in the brake discs under consideration proved to be insufficient for the anticipated application in a motor vehicle. Additionally, it may be pointed out that the main source of cracks is the surface of vent-holes, where considerable corrosion changes are observed.

It should be noted that the perlite matrix, providing the highest possible strength despite the presence of graphite, at the same time shows an adverse effect on plastic and fatigue properties. According to the authors, the type and shape of graphite precipitates is also unfavorable. Flake graphite – even modified – always represents a structural notch and will act as stress concentrator. These conclusions were supported in [12], where ferritic matrix cast iron withstood 146 and 7146 thermal cycles for flake and spheroidal graphite, respectively. The presence of phosphorus eutectic precipitates in the matrix structure may also be of potential importance for crack propagation. During high loads, generating high temperature, the eutectic dissolves and the phenomenon of hot cracking occurs. Thereupon, further analysis should be focused primarily on the influence of graphite precipitates and phosphite eutectic on the thermal fatigue in brake discs.

Nomenclature

KCV	V-notch impact strength
A	percentage elenogation [%]
% wt.	mass fraction

Bibliography

[1] ATKINS, R.D., A century of high performance engine testing. *Combustion Engines.* 2005, **123**(4), 3-18. https://doi.org/10.19206/CE-117365

[2] BAGNOLI, F., DOLCE, F., BERNABEI, M. Thermal fatigue cracks of fire fighting vehicles gray iron brake discs. *Engineering Failure Analysis.* 2009, **16**(1), 152-163. https://doi.org/10.1016/j.engfailanal.2008.01.009

[3] BELHOCINE, A., BOUCHETARA, M. Thermal analysis of a solid brake disc. *Applied Thermal Engineering*. 2012, **32**, 59-67. https://doi.org/10.1016/j.applthermaleng.2011.08.029

[4] DUFRENOY, P., WEICHERT, D. A thermomechanical model for the analysis of disc brakes fracture mechanism. *Journal of Thermal Stresses.* 2003, **26**(8), 815-828. https://doi.org/10.1080/01495730390207622

[5] GOO, B.C., LIM, C.H. Thermal fatigue evaluation of cast iron discs for railway vehicles. *Procedia Engineering*. 2010, **2**(1), 679-685. https://doi.org/10.1016/j.proeng.2010.03.073

[6] KROPIWNICKI, B., FURMANEK, M. Analysis of the regenerative braking process for the urban traffic conditions. *Combustion Engines.* 2019, **178**(3), 203-207. https://doi.org/10.19206/CE-2019-335

[7] LI, W., YANG, X., WANG, S. et al. Comprehensive analysis on the performance and material of automobile brake discs. *Metals.* 2020, **10**(3), 377. https://doi.org/10.3390/met10030377

[8] MERKISZ. J., PIELECHA. I., MARKOWSKI. J. Operating parameters of high performance vehicle engines. *Combustion Engines.* 2007, **131**(4), 3-18. https://doi.org/10.19206/CE-117313

[9] SAWCZUK, W., JÜNGST, W., ULBRICH, D. et al. Modeling the depth of surface cracks in brake disc. *Materials.* 2021, **14**(14), 3890. https://doi.org/10.3390/ma14143890

[10] SZCZEPAŃSKI, T., SKARBEK-ŻABKIN, A. DZIEDZIAK, P. Impact of the road conditions on the amount of braking energy. *Combustion Engines.* 2017, **171**(4), 265-268. https://doi.org/10.19206/CE-2017-445

[11] YAN, H.B., FENG, S.S., YANG, X.H. et al. Role of cross-drilled holes in enhanced cooling of ventilated brake discs. *Applied Thermal Engineering.* 2015, **91**, 318-333. https://doi.org/10.1016/j.applthermaleng.2015.08.042

[12] ZYCH, J.S. Rola morfologii wydzieleń grafitu w kształtowaniu odporności na zmęczenie cieplne żeliwa. *Inżynieria Materiałowa.* 2015, **5**(207), 343-347. https://doi.org/10.15199/28.2015.5.30

Martyna Zemlik, MEng. – Faculty of Mechanical Engineering, Wroclaw University of Science and Technology.

e-mail: *martyna.zemlik@pwr.edu.pl*

Łukasz Konat, DEng. – Faculty of Mechanical Engineering, Wroclaw University of Science and Technology.

e-mail: *lukasz.konat@pwr.edu.pl*

Mateusz Dziubek, MEng. – Faculty of Mechanical Engineering, Wroclaw University of Science and Technology.

e-mail: *mateusz.dziubek@pwr.edu.pl*

Dominika Grygier, DSc., DEng. – Faculty of Mechanical Engineering, Wroclaw University of Science and Technology.

e-mail: *dominika.grygier@pwr.edu.pl*

Dariusz Pyka, DEng. – Faculty of Mechanical Engineering, Wroclaw University of Science and Technology.

e-mail: *dariusz.pyka@pwr.edu.pl*

Article citation info:
SIEDLECKI, M., MERKISZ, J., DOBRZYŃSKI, M. et al. Impact of the use of comfort devices on the exhaust toxic compounds from a modern PC car with spark ignition engine. *Combustion Engines*. 2022, **190**(3), 50-55. https://doi.org/10.19206/CE-142280

Maciej SIEDLECKI
Jerzy MERKISZ
Michał DOBRZYŃSKI
Kamil KUBIAK

Combustion Engines
Polish Scientific Society of Combustion Engines

Impact of the use of comfort devices on the exhaust toxic compounds from a modern PC car with spark ignition engine

ARTICLE INFO

Received: 13 August 2021
Revised: 30 August 2021
Accepted: 14 September 2021
Available online: 13 October 2021

The use of comfort systems, the number of which in vehicles is constantly increasing, has a direct impact on fuel consumption and engine load. As part of the article, the vehicle's drive in real operating conditions was analyzed in terms of the emission of toxic compounds. The tests were carried out without and with the systems turned on, using the PEMS apparatus, where road emissions of carbon dioxide, carbon monoxide, hydrocarbons, nitrogen oxides and solid particles were measured in terms of mass, number and size distribution of diameters. The track was driven four times with different setting of the powertrain of examined car. The differences concerned the number of comfort systems in the vehicle and the mode of operation of the combustion engine.

Key words: *exhaust emission, RDE, combustion engine, comfort devices*

1. Introduction

With the advancement in the automotive field, there is an increase in the number of amenities found in vehicles and affecting the comfort of passengers' travel. They are associated with increasing the weight of the vehicle, which translates into fuel consumption and the emission of toxic components. Mass directly influences the resistance to motion by increasing the inertia, and also, to a lesser degree, the rolling resistance [7, 9, 10, 13]. Air resistance may be influenced by external elements related to the stylistic versions, usually increasing the frontal area of the vehicle or increasing the frontal drag of the vehicle. The number of amenities is particularly high in luxury vehicles, often doubling the original purchase price. The assembled device needs electricity to power it, which increases the load on the internal combustion engine by taking power from the crankshaft and converting the mechanical work into the electric energy in the alternator [1, 5, 8]. It is often associated with the use of starter batteries with increased capacity or increasing their number. As part of the approval tests, their use is not measured for fuel consumption and the emission of toxic components into the atmosphere [11]. An example of a comfort system is the air conditioning system, which in most vehicles requires the engine to be running, preventing the start / stop system from working. Operation may also be limited with other systems turned on when the instantaneous power consumed by the vehicle is significant. When analyzing the equipment of vehicles, a transfer of technology to lower-class vehicles is observed, and currently, in the B segment, an optional 360-degree camera or active cruise control is observed [10].

Based on the work carried out in recent years, it was found that the qualitative and quantitative measurements of exhaust gases from internal combustion engines performed in laboratory conditions significantly differ from the actual emissivity of vehicles of a given category. It has been proved by various research institutions in Poland and abroad [3–6, 8, 9, 13, 14]. Therefore, continuous efforts are being made to develop detailed and universal methods of assessing pollutant emissions in road conditions, generally classified as RDE (Real Driving Emissions). The development and miniaturization of measuring equipment belonging to the PEMS group (Portable Emission Measurement System), which has been progressing in recent years, allows for more and more precise tests of the environmental performance of vehicles in real operating conditions. From the moment when the Euro 6c standard came into force in 2017, it became necessary to perform road measurements in the field of compliance control of PC class vehicles in operation [2, 4]. It is currently the best method of researching the real impact of vehicle operation on the surrounding environment.

As part of the article, a road test of the vehicle was carried out in various driving modes and with the comfort systems turned on and off. The tested vehicle was equipped with PEMS equipment connected to the exhaust system and the emission of toxic components and carbon dioxide was measured, which also allowed the measurement of fuel consumption.

2. Research methodology

2.1. Research objects

The tested vehicle was equipped with a petrol engine with a displacement of 1.984 dm^3, power of 185 kW and a maximum torque is 370 Nm (Table 1). The engine is a common unit in the VAG group with four cylinders and longitudinal position [10].

Table 1. Data of the tested vehicles engine [10]

Parameter	Value
Number and arrangement of cylinders and valves, engine type	4-cylinder, 4 valves per cylinder, spark ignition, inline cylinders
Fuel injection system	Direct injection
Displacement	1.984 dm^3
Maximum power	185 kW at 5000–6800 rpm
Maximum torque	370 Nm at 1500–4500 rpm
Compression Ratio	9.6:1
Aftertreatment systems	Double three way catalysts
Turbocharging	Turbocharger with VGT, inter-cooled

The tested vehicle had a curb weight of 1920 kg, during the tests it was loaded with the test equipment and two passengers, which translates into about 400 kg of additional weight (Fig. 1). Before the tests, the vehicle's mileage was 4,400 km. Before the tests, the technical condition of the vehicle was checked and showed no inaccuracies.

Fig. 1. The tested vehicle with PEMS apparatus

The comfort devices that were in the tested vehicle and that were turned on during passes 3 and 4 were: mirror heating, rear window heating, front and rear seat heating, front seat ventilation, sound system turned on at 80% of maximum power, air conditioning in auto mode set to a temperature of 21 degrees

2.2. Used apparatus

The equipment from the PEMS group was used for the measurements. It is a set of analyzers that analyze the exhaust gas sample taken from the exhaust system for the presence of harmful components in the form of: carbon dioxide and monoxide, nitrogen oxides, hydrocarbons and mass and number of emitted particles. For such a comprehensive assessment of the emissivity, 3 different SEMTECH DS analyzers were used (Fig. 2a). Particularly important in the case of modern petrol direct injection petrol engines is the assessment of particulate matter emissions. High-pressure fuel injection improves its atomization and facilitates the generation of a large amount of power from the same displacement volume, however, the lack of fuel evaporation associated with a shorter time that in the case of MPI (Multi Point Injection) systems it leads to weight reduction (PM), but increases the number of particles (PN). Therefore, the mass and particle size distribution tested by the EEPS instrument will also be analyzed (Fig. 2b and 2c). In this family of engines, emission is now reduced by a particulate filter in the exhaust system, while older designs used the second MPI injection system (the engine had 2 injectors per cylinder, direct and indirect) [10].

The technical data, where the range of tested parameters is listed, are listed in Table 2. The exhaust gas flow meter with a diameter of 2 inches was tightly connected to the exhaust system of the vehicle, which was adapted to the flow of exhaust gases from a turbocharged engine with a displacement volume of 1.5 to 2.5 dm^3. The information from the flow meter on the instantaneous flue gas mass flow allowed to determine the mass emission and the number of time periods during road tests

The route used for the study was located in the center of the city of Poznań (Fig. 3). It is characterized by different speed limits and well reflects the conditions of vehicles driving in the urban agglomeration. There are numerous infrastructure elements on it, such as several lanes and intersections with traffic lights. All tests, except for the cold start, were performed twice and the given result is the arithmetic mean of the obtained results. The length of the route was 11.04 km.

Fig. 2. View of the apparatus used in the research: a) SEMTECH DS analyzer, b) AVL MSS, c) EEPS TSI 3090 [12]

Table 2. Measurement range of used apparatus [12]

Central Unit		
Examined compound	Range	Accuracy [%]
THC [ppm]	0–40000	±2
CO [%]	0–8	±3
CO_2 [%]	0–20	
HC [ppm]	0–4000	
NO [ppm]	0–3000	±2
PM [mg/m^3]	0,005–50	±1
PN [nm]	5.6–560	±1
Exhaust flow meter		
Diameter	Flow measurement accuracy	Time response [s]
2 inch/51 mm	±2.5%	$T_{90} < 1$ s
Vehicle type	Protocols	
PC and LDV	SAE–J1850 PWM, SAE–J1850 VPW, ISO–9141–2, ISO–14230 (KWP–2000), ISO–15765 (CAN), ISO–11898 (CAN)	

The trip was planned in four configurations, i.e. test after a cold start, drive with a warmed-up engine vehicle, drive with a vehicle with switched on comfort receivers, drive with a warm engine and comfort systems in sport mode. Due to the lack of influence on the direct reproducibility of the tests, tests were carried out with all possible comfort systems as a reference from the assessment of their impact on the emissivity of the vehicle.

Fig. 3. View of the route used for testing [source: Google maps]

3. Results

Discussing the results at the beginning, the results concerning the test run in terms of speed, acceleration, rotational speed and load will be presented (Table 3).

Table 3. Parameters obtained during different cycles

Cycle/parameter	cold (1)	warm (2)	warm with devices (3)	sport with devices (4)
Average speed [km/h]	29.7	28.9	29.4	28.3
Average acceleration [m/s^2]	0.33	0.34	0.39	0.42
Average engine speed [rpm]	1223	1161	1231	1624
Average engine load [%]	23.7	19.0	20.3	24.8

All tracks were similar, which confirms the marginal impact of possible congestion on vehicle movement. The average speeds were very similar, as was the acceleration, which was the highest in the sport mode and was caused by an increased response to pressing the accelerator pedal. The differences are also visible in the engine speed. They are very similar for driving without and with comfort systems after warming up the engine. The obtained values were higher when the engine was cold and in sport mode, which also agrees with the theoretical assumptions. In these cycles, the engine speed and load were significantly increased. Similar parameters of the trip allow for the comparison of the emissivity of toxic compounds in the tested cycles.

The first component analyzed is carbon dioxide, which is directly related to the fuel consumption of the internal combustion engine. During the 1st cycle, when the engine is cold, fuel consumption is clearly higher than in cycle 2, where the engine is at operating temperature, and even more than in cycle 3, where comfort systems were used. The use of the sport mode greatly increased the fuel consumption (Fig. 4).

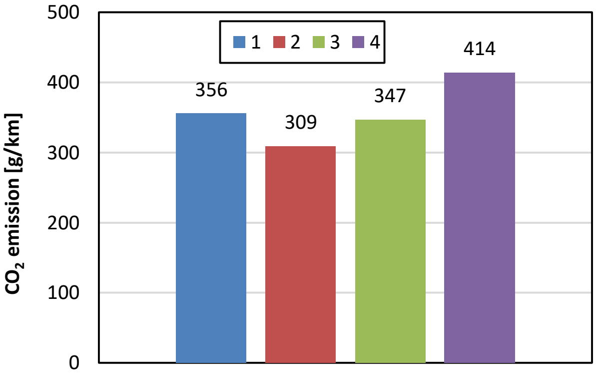

Fig. 4. CO$_2$ emissions during tests

The analysis of the emission of toxic compounds to gaseous compounds was started, the emission of carbon monoxide, i.e. a compound formed mainly as a result of local and global oxygen deficiency in the fuel-air mixture (Fig. 5). the obtained results will be referenced to the standard, but direct comparison will not be possible due to the different test conditions from the approval or cycle run in accordance with RDE. Limits were taken from the homologation of Euro 6c PC vehicles [4].

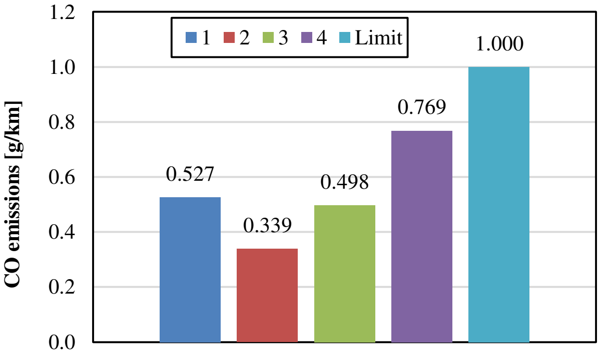

Fig. 5. CO emissions during tests

Increased CO emissions are typical for a cold engine, where the mixture is enriched and the lower temperature makes it difficult to evaporate the fuel. Warming up the engine significantly reduces carbon monoxide emissions (cycle 2), which remains below the cold engine value also for cycle 3. Sport mode significantly increases carbon monoxide emissions, most likely by increasing the torque and power output. None of the trips even comes close to the limit contained in the standards, which is confirmed by the authors' previous research in the study of carbon monoxide emissions [7, 8, 13]. The next analysis concerned the emission of hydrocarbons (Fig. 6).

The emission of hydrocarbons (in the case of the SEMTECH analyzer, calculated as the emission of propane) is very similar to that of carbon monoxide, which is also confirmed by theoretical assumptions. In this case, however, the highest value occurs for a cold start of the vehicle. The value is significantly reduced for the warm engine, but interestingly it is reduced by activating the comfort system, which was not the case with carbon monoxide. Switching on the sport mode, as in the first analyzed compound, significantly increases road emissions. Again, all results are below par, which also supports previous testing and proves the effectiveness of the aftertreatment systems and technologies used in modern SI engines. Another tested gas component was the emission of nitrogen oxides (Fig. 7).

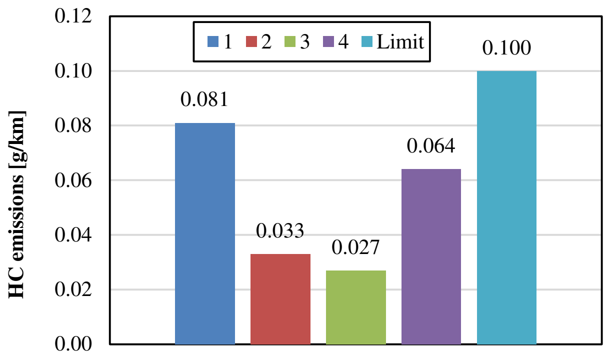

Fig. 6. HC emissions during tests

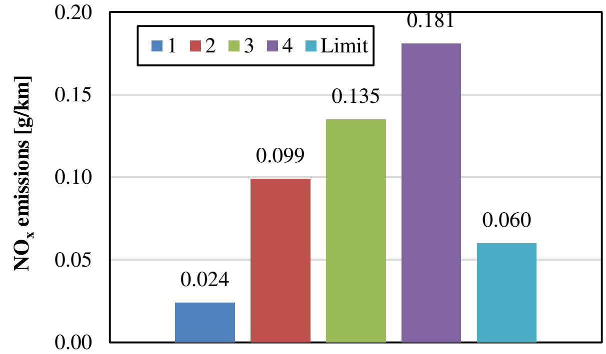

Fig. 7. NO$_x$ emissions during tests

The results of nitrogen oxides emission clearly match the theoretical assumptions, where their emission should increase in a hot engine and increase with increasing momentary loads. It is related to the increased temperature in the combustion chamber and the increased processes of combining oxygen with nitrogen contained in the air. The figure also shows the effect of the use of comfort modules on NO$_x$ emissions and the use of the sport mode. Comparing the mileage emission with the approval data, the obtained results are clearly greater for a warm engine. The discussed compounds concerned the gases contained in the exhaust gas. Further analysis will concern the emission of particulate matter (Fig. 8).

The first aspect considered was the mass of the particulates. It is the approximate mass of particles, mainly composed of soot, which is the cause of imperfections in the combustion process of the fuel in the chamber and the combustion of the engine oil. In this case, a cold engine, often running on a slightly enriched mixture and having, at least for part of the route, an underheated exhaust gas treatment system. The use of comfort systems almost triples their content, and the use of the sport mode increases it even more. It should be emphasized, however, that the obtained results are much lower than the approval limits and allow for conclusions about the environmental performance of the engine, which was not always found in other studies by the authors [2, 3]. Another analyzed index was the number of particles per kilometre (Fig. 9).

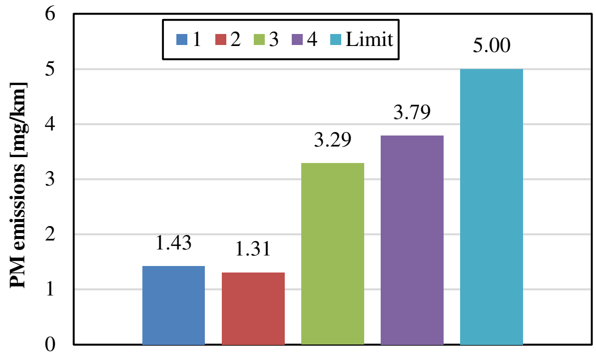

Fig. 8. PM emissions during tests

Particulate emissions in terms of numbers is an important aspect introduced in the limits for passenger vehicles in 2017 in the Euro 6c standard. Its introduction was related to the emission of nanoparticles caused by the use of direct gasoline injection. Nowadays, the advantages of this technology have practically dominated the market of engines in PC class vehicles [10]. The tests carried out as part of the test showed similar particle emissions in all test cycles. The lowest result was measured for the warm engine. The use of comfort systems increases their content by over 50%, and the use of the sport mode does not increase their content as clearly as for PM. Considering the results obtained in relation to the engine warmed up as a percentage, the use of the comfort systems and the sport mode increases the content of all compounds, except for hydrocarbons (Table 4).

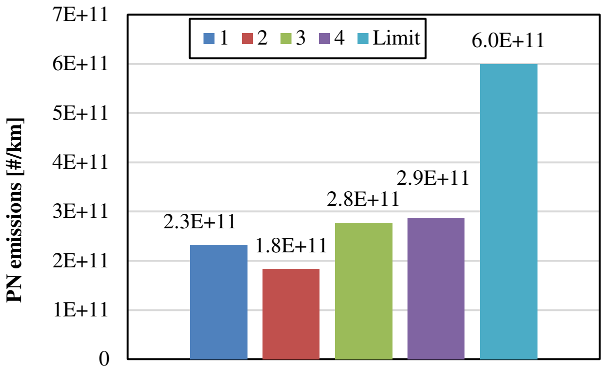

Fig. 9. PN emissions during tests

Taking the limit from the norm as 100% in the cycles obtained, lower values were obtained in all tested compounds, except for nitrogen oxides, where the increase was significant and exceeded three times the limits (Table 5).

Table 4. Relative emission in cycles 3 and 4 in comparison of cycle 2

Emission/cycle	CO	HC	NO_x	PM	PN
2	100%	100%	100%	100%	100%
3	147%	82%	183%	251%	151%
4	227%	194%	136%	290%	156%

Table 5. Relative emission in all cycles in comparison of limits (limit = 100%)

Compound/cycle	1	2	3	4
CO	53%	34%	50%	77%
HC	10%	17%	48%	41%
NO_x	40%	165%	225%	302%
PM	29%	26%	66%	76%
PN	39%	31%	47%	49%

The last aspect considered was the dimensional distribution of the diameters of the solid particles. It allows to consider the number not only quantitatively, but also allows to examine whether particles of a characteristic size are emitted from the engine, especially the smallest particles that are particularly dangerous to life. The results are shown in Figs 10–13. For ease of comparison, the range of values on the Y axis has been adjusted to the highest value obtained for cycle 3.

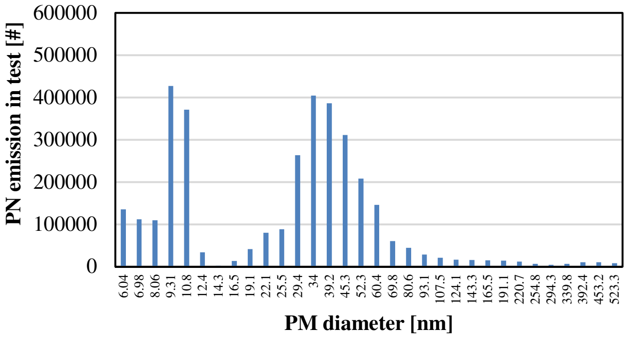

Fig. 10. PM diameter distribution during tests cycle no 1

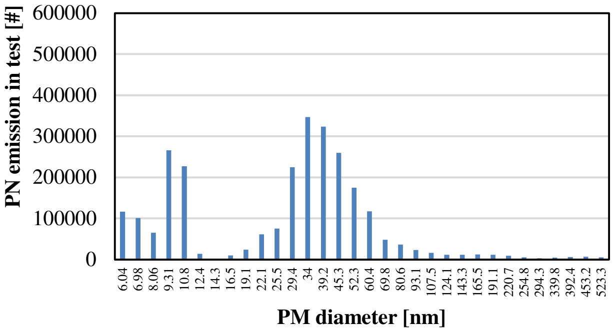

Fig. 11. PM diameter distribution during tests cycle no 2

In all the obtained cycles, very similar results were recorded for the distribution of diameters of 16 nm and larger. The obtained local maximum differs, which in all cases falls in the diameter of 34 nm. The value obtained is only lower for cycle 2, where the engine was warmed up and unloaded with the comfort systems. Much greater differences concern the emission of nanoparticles, i.e. the range of 6–12 nm. For cycles 1–3, the ratio of individual measured diameters seems to be very similar, it runs up for passes No. where the channel ratio of 9.31 and 6.04 is greater than in the other passes. Ruthlessly analyzing the obtained results, pass 3 and 4 do not differ much from each other, but 2 and 3 are very different. It points to an almost twice increase in the emission of nanoparticles after the use of comfort systems. The result for the cold engine is also greater than for cycle 2, but lower than for cycle 3 and 4. According to the authors, the increase in emissions measured in the exhaust manifold would be greater, but some of the particles are oxidized in the hot TWC.

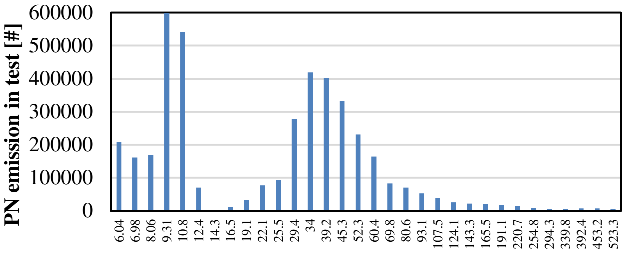

Fig. 12. PM diameter distribution during tests cycle no 3

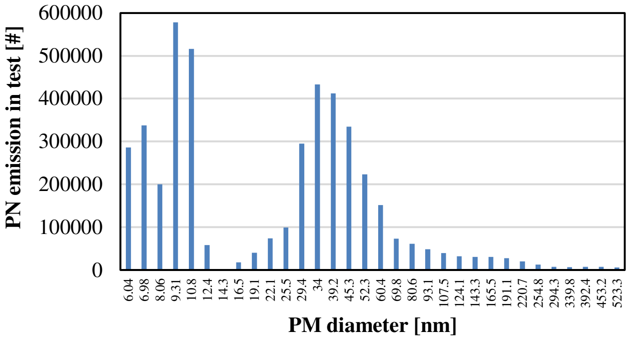

Fig. 13. PM diameter distribution during tests cycle no 4

The obtained results indicate an increase in the emissions of two compounds to reduce emissions, which are trying to be achieved by vehicle and engine manufacturers, i.e. nitrogen oxides and solid particles. The analysis also showed an increase in the emission of nanoparticles, the most dangerous for human life and health.

4. Conclusion

The article examines the emissions of a vehicle with a modern gasoline engine during real driving in the city center. The number of amenities in vehicles is constantly increasing, and the devices used are powered by the electricity generated by the engine, loading it. The impact of this load is not measured during approval tests, and such conditions occur in the actual operation of vehicles. The emission performance of gaseous components, apart from nitrogen oxides, is not significantly increased by the use of comfort systems. The increase took place in the field of nitrogen oxides and particulate matter, the emission of which is the biggest problem in currently produced vehicles with both spark ignition and compression ignition engines. The tested vehicle was characterized by relatively small dimensions and weight, in the future it is planned to extend the tests to higher segment vehicles.

Acknowledgements

The research was funded by European Union from European Regional Development Fund through the National Centre for Research and Development (Narodowe Centrum Badań i Rozwoju) – research project within the Smart Growth Programme (contract No. POIR.04.01.02-00-0002/18).

Nomenclature

DI	direct injection	PN	particle number
GPF	gasoline particulate filter	RDE	Real Driving Emissions
MPI	multi point injection	SI	spark ignition
PC	passenger cars	TWC	three way catalyst
PEMS	Portable Emissions Measurement System	VGT	variable geometry turbine
PM	particle mass		

Bibliography

[1] AIKAWA, K., JETTER, J.J. Impact of gasoline composition on particulate matter emissions from a direct-injection gasoline engine. Applicability of the particulate matter index. *International Journal of Engine Research*. 2014, **15**, 298-306. https://doi.org/10.1177/1468087413481216

[2] AOYAGI, Y. Measurement of flame temperature and soot amount for effective NO_x and PM reduction in a heavy duty diesel engine. *Combustion Engines*. 2019, **179**(4), 32-39. https://doi.org/10.19206/CE-2019-405

[3] BRZEŻAŃSKI, M., RODAK, Ł. Influence of the method of creating a hydrogen-air mixture on the emission of nitrogen oxides in a spark-ignition engine. *Combustion Engines*. 2019, **178**(3), 224-227. https://doi.org/10.19206/CE-2019-339

[4] GIECHASKIEL, B., LAHDE, T., SUAREZ-BERTOA, R. et al. Particle number measurements in the European legislation and future JRC activities. *Combustion Engines*. 2018, **174**(3), 3-16. https://doi.org/10.19206/CE-2018-301

[5] KURTYKA, K., PIELECHA, J. Cold start emissions from a gasoline engine in RDE tests at different ambient temperatures. *Combustion Engines*. 2020, **181**(2), 24-30. https://doi.org/10.19206/CE-2020-204

[6] LIJEWSKI, P., FUĆ, P., MARKIEWICZ, F. et al. Problems of exhaust emissions testing from machines and mobile devices in real operating conditions. *Combustion Engines*. 2019, **179**(4), 292-296. https://doi.org/10.19206/CE-2019-449

[7] MERKISZ, J., DOBRZYSKI, M., KUBIAK, K. An impact assessment of functional systems in vehicles on CO_2 emissions and fuel consumption, *MATEC Web of Conferences*. 2017, **118**, 00030. https://doi.org/10.1051/matecconf/ 201711800030

[8] MERKISZ, J., PIELECHA, J. Observations from PEMS testing of combustion engines of different applications. *Combustion Engines*. 2018, **174**(3), 40-55. https://doi.org/10.19206/CE-2018-305

[9] PIELECHA, J., KURTYKA, K., SKOBIEJ, K. The impact of vehicle dynamic parameters on the exhaust emissions in RDE tests. *Combustion Engines*. 2018, **175**(4), 26-34. https://doi.org/10.19206/CE-2018-404

[10] Porsche and Nissan materials.

[11] RYMANIAK, Ł., DASZKIEWICZ, P., MERKISZ, J. et al. Methods of evaluating the exhaust emissions from driving vehicles. *Combustion Engines*. 2019, **179**(4), 286-291. https://doi.org/10.19206/CE-2019-448

[12] Sensors Inc., AVL and TSI manuals.

[13] SIEDLECKI, M., MERKISZ, J., KUBIAK, K. et al. Impact of the use of comfort devices on the exhaust emission from a hybrid vehicle. *Combustion Engines*. 2019, **179**(4), 250-285. https://doi.org/10.19206/CE-2019-447

[14] WIŚNIOWSKI, P., GIS, M. Representativeness of emissions of toxic substances in bench tests reflecting the road traffic conditions of a vehicle. *Combustion Engines*. 2019, **177**(2), 88-90. https://doi.org/10.19206/CE-2019-215

Maciej Siedlecki, DEng. – Faculty of Civil and Transport Engineering, Poznan University of Technology.
e-mail: *maciej.siedlecki@put.poznan.pl*

Michał Dobrzyński, DEng. – Faculty of Civil and Transport Engineering, Poznan University of Technology.
e-mail: *michal.dobrzyński@put.poznan.pl*

Prof. Jerzy Merkisz, DSc., DEng. – Faculty of Civil and Transport Engineering, Poznan University of Technology.
e-mail: *jerzy.merkisz@put.poznan.pl*

Kamil Kubiak, MEng. – PhD student in the Faculty of Civil and Transport Engineering, Poznan University of Technology.
e-mail: *kamil.da.kubiak@doctorate.put.poznan.pl*

Article citation info:
LONGWIC, R., SANDER, P., TATARYNOW, D. Ecological aspects of using mixtures of canola oil with n-hexane in diesel engine. *Combustion Engines*. 2022, **190**(3), 56-60. https://doi.org/10.19206/CE-143245

Rafał LONGWIC
Przemysław SANDER
Dawid TATARYNOW

Combustion Engines
Polish Scientific Society of Combustion Engines

Ecological aspects of using mixtures of canola oil with n-hexane in diesel engine

ARTICLE INFO

Received: 25 August 2021
Revised: 9 September 2021
Accepted: 21 October 2021
Available online: 15 December 2021

The article discusses the results of research on the use of canola oil and canola oil with the addition of n-hexane in a compression-ignition engine. An engine with a Common Rail injection system was tested in real traffic conditions on the road and on a chassis dynamometer. The tested fuels were fed to the engine by an additional fuel supply system. An analysis of the effect of the addition of n-hexane on the emission of the main components of toxic exhaust gases was carried out. The proposed solution may contribute to extending the service life of currently used compression ignition engines due to the improvement of the ecological properties of this type of drive sources.

Key words: *Diesel engine, nitrogen oxides, hydrocarbons, carbon dioxide, combustion, canola oil, n-hexane, common rail*

1. Introduction

Today, thecombustion engine is widely used to drive means of transport [1]. The main problem of the use of means of transport is greenhouse gas emissions, which affect among others climate change observed in the world. It is believed that the main reason for this phenomenon is the use in vehicles of internal combustion engines powered by non-renewable petroleum-based fuels [2]. Therefore, it is particularly important to reduce carbon dioxide (CO_2) emissions into the atmosphere. Despite the increase in the number of electric vehicles used, there is still a significant number of vehicles with internal combustion engines in widespread use. The tightening of standards for the emission of toxic exhaust compounds forces work to be carried out in the field of searching for new types of fuels to power internal combustion engines. With regard to diesel engines, this work was carried out mainly in the field of obtaining fuels not from the refining of crude oil, the so-called alternative fuels (mainly biofuels) [3, 4]. The use of biofuel made from oilseeds (among others canola oil) brings significant benefits. It can be assumed that CO_2 emitted during the combustion of fuels of plant origin is quantitatively balanced by CO_2 taken up by plants in the process of photosynthesis during the period of plant growth (closed circuit CO_2) [5,6]. Despite the advantages of vegetable fuels, there are also problems associated with the use of canola oil (*Co*) as a fuel. The basic problems in the use of *Co* as a fuel include different physicochemical properties in relation to diesel fuel, such as density, viscosity, surface tension, cloud point, fractional composition. Canola oil also has a high temperature of blocking the cold fuel filter, approx. +12°C (CFPP – cold fuel plugging point). The use of vegetable oil can also lead to operational problems because it contains glycerine, which at high temperatures can change into acrolein (CH_2=CH–CHO). Acrolein can form carbon deposits (polymers, soot) in the engine and fuel lines [7–9]. The authors of the work dealing with this issue, conducted a number of studies on the engine dynamometer in static and dynamic conditions, during which the research diesel engine was powered by, among others, canola oil with various additives. The physicochemical properties of fuels have a direct impact on the course of the injection and combustion process, and indirectly on the ecological parameters of the exhaust gases [10–13]. Therefore, additives are being sought to change the physicochemical parameters of Co, so that they are close to the properties of diesel fuel. (Df). One of the proposed ways is to use a mixture of Co with n-hexane [14–18]. Due to the legal regulations on the level of emissions of toxic exhaust gas components, which force the control of emissions in dynamic conditions, measures have been taken to assess the ecological parameters of a diesel engine powered by mixtures of canola oil with n-hexane in these conditions. The article presents the results of diesel engine tests in real operating conditions reflected on the chassis dynamometer, as well as in road conditions.

2. Test stand and research methodology

The research was carried out at the Center for Innovation and Technology Transfer of the Lublin University of Technology, in the Laboratory ofthe Department of Motor Vehicles, equipped, among others, with a Dynorace chassis dynamometer, designed for vehicles with two-axle drive type DF4FS-HLS. The research stand is presented on Fig. 1. The engine of the test vehicle had a turbocharger with a discharge valve (without variable geometry), a common rail storage injection system, an EGR exhaust gas recirculation system and a DPF particulate filter. To measure ecological parameters in road driving conditions, the Herman HGA400 mobile exhaust gas analyzer was used, whose probe was located in the exhaust system, i.e., behind the diesel particulate filter (DPF). During the tests, CO_2 and O_2 as well as the main components of toxic exhaust gases (CO, HC, NO_x) were measured. The concentration of toxic compounds in the exhaust gases was also measured using the MAHA exhaust gas analyzer (in the conditions of movement on the chassis dynamometer, exhaust gas consumption before the catalyst). In addition, the engine of the test vehicle was identified using AVL's INDIMICRO 602 engine indication system. The signals recorded by the AVL system are the pressure waveform inside the cylinder, the signal of the position of the engine crankshaft, the injection pressure. To analyze the operating parameters of the engine controller, a diagnostic interface designed to work with the Bosch KTS system was used.

Fig. 1. Test stand consisting of: 1 – Fiat Qubo test car with 1.3 Multijet engine, 2 – computer with installed AVL Indicom V2.7 software, 3 – Indimicro 602 engine indicator system, 4 – DF4FS-HLS chassis dynamometer, 5 – additional fuel system tank, 6 – KTS Bosch – Diagnostic module, 7 – diagnostic exhaust gas analyzer and dymometer MET 6.3 by Maha, 8 – mobile exhaust gas analyzer Herman HGA400

Table 1. Basic physicochemical parameters of the tested fuels [12]

Fuel type	Density 20°C [kg/m^3]	Kinematic viscosity 20°C [mm^2/s]	Surface tension 20°C [mN/m]	Calorific value [MJ/kg]
Co	916.00	34.89	34.15	37.10
90%Co10%Hex	895.43	19.64	30.08	30.77
85%Co15%Fex	887.60	15.20	30.10	30.95
Df	840.00	2.70	29.15	43.84

Diesel fuel (Df) meeting the requirements of EN590, commercial canola oil (Co), non-reactive solvent n-hexane were used for testing. N-hexane (C_6H_{14}) is an organic chemical compound from the group of alkanos. N-hexane isomers are very little reactive and often used as solvents in organic reactions because they are highly non-polar. On the basis of canola oil (Co) two mixtures with n-hexane were made in proportions of 10% (90%Co10%Hex) and 15% (85%Co15%Hex). The main physicochemical properties of the tested fuels are presented in Table 1.

The tests were carried out under the driving conditions of the vehicle on the chassis dynamometer (case 1) and in real traffic, on the road (case 2), with the vehicle being loaded with rolling resistance and air resistance force. The researchwas carried out to determine the effect of the n-hexane additive on the operating parameters of the diesel engine and on the exhaust gas composition. The measurements were carried out in the fourth gear of the vehicle, at fixed engine speeds: 2000, 2500, 3000, 3500, 4000 rpm. The results obtained were related to the results achieved with diesel fuel. The studies concerned the exhaust gas composition of gases down the catalytic converter (this exhaust gas composition was measured in case 2) and before the catalytic converter (this exhaust gas composition was measured in case 1).

3. Research results

Figures 2 to 5 show the results of the obtained tests of ecological parameters of engine operation in selected conditions. Concentration of nitrogen oxides (NO_x), carbon monoxide (CO), carbon dioxide (CO_2), hydrocarbons (HC) and oxygen (O_2) were analysed. The studies carried out concerned two types of engine operating conditions (see cases 1 and 2).

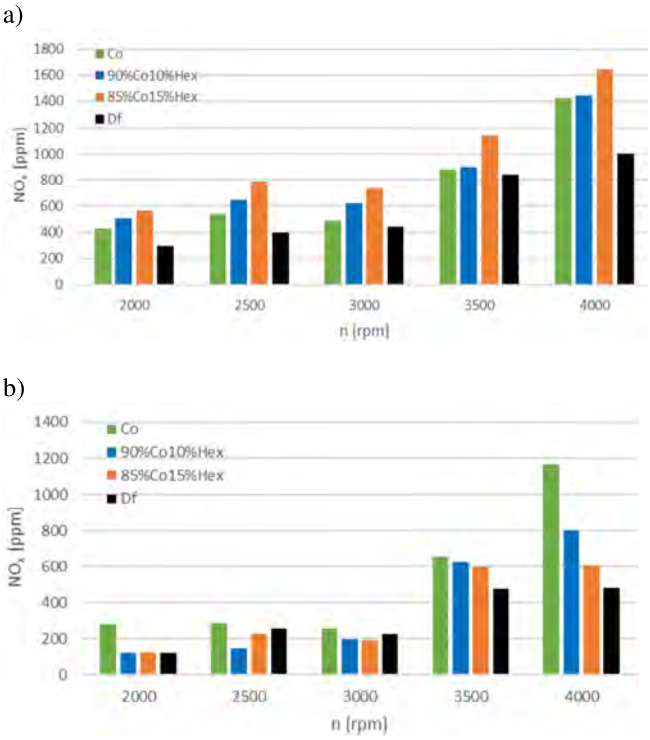

Fig. 2. The course of the concentration of nitrogen oxides (NO_x) in the exhaust gases depending on the rotational speed, for the operation of the Diesel engine powered by the tested fuels, a) case 1 (measurement before catalytic converter), b) case 2 (measurement after catalytic converter)

An analysis of the exhaust gas composition (before the exhaust after-treatment system) emitted during the operation of an engine running on vegetable fuels under the vehicle on the chassis dynamometer (Fig. 2a, case 1) showed that over the entire engine speed range, concentration of nitrogen oxides (NO_x) were higher than when using diesel (Df). The biggest relative difference occurred at a speed of

2500 rpm when powered by canola oil with the addition of 15% n-hexane (about 50%). For case 2 (Fig. 2b – driving the vehicle in real traffic, on the road), the differences in nitrogen oxides (NO_X) concentration when powered by canola oil with the addition of 15% n-hexane were no longer as large as for case 1. In the range of lower rotational speeds (2000–3500 rpm), the addition of n-hexane caused the no$_X$ concentration to be lower or at a comparable level to Df. The biggest relative difference when powered by canola oil with the addition of 10% n-hexane compared to diesel (Df) occurred at a speed of 2500 rpm (about 75%). As the rotational speed increased, the trend was reversed. The observed quantitative difference in NO_x concentration between the cases under consideration is mainly related to the operation of the exhaust aftertreatment system (catalytic converter, particulate filter).

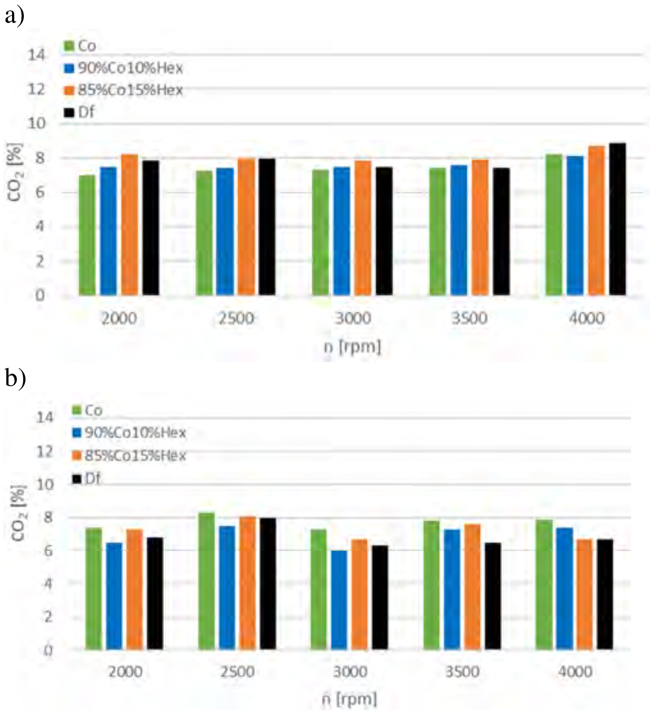

Fig. 3. The course of the concentration of carbon dioxide (CO_2) in the exhaust gas depending on the rotational speed, for the operation of the Diesel engine powered by the tested fuels, a) case 1 (measurement before catalytic converter), b) case 2 (measurement after the catalytic converter)

Figure 3 item A shows the results of the carbon dioxide (CO_2) concentration emitted during the operation of the engine running on the tested fuels (exhaust exhaust gas composition before the exhaust after-treatment system) under the chassis dynamometer (case 1).The analysis showed that over the entire speed range, CO_2 concentration were almost comparable to the use of diesel (Df). The differences were on the order of several percent. For case 2 (Fig. 3 item B – driving the vehicle in real traffic, on the road), the concentration of carbon dioxide (CO_2) when supplying the engine with canola oil over the entire speed range was higher compared to diesel (Df). The largest relative difference was 16% at 3500 rpm when powering the Co motor relative to Df. By supplying the engine with canola oil with the addition of n-hexane (10% and 15%), a lower CO_2 concentration was observed in relation to canola oil (Co) while in relation to diesel oil the largest relative difference was at a speed of 3500 rpm (about 14%) for 15% of the n-hexane additive.

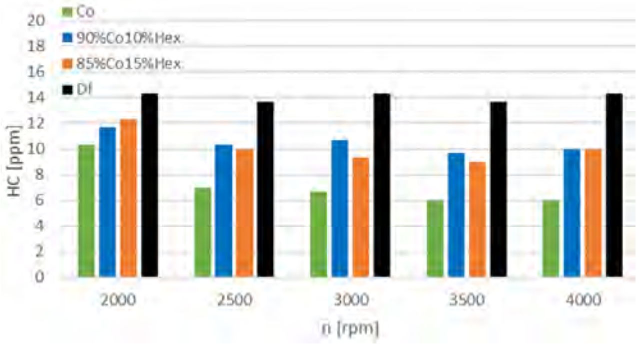

Fig. 4. The course of hydrocarbon concentration (HC) in the exhaust gas depending on the rotational speed, for the operation of the Diesel engine powered by the tested fuels (case 1)

The case studies carried out for case 2 (driving in real traffic, on the road) concerned the exhaust gas composition of gases behind the catalytic converter and the particulate filter. In this case, a trace amount of carbon monoxide (CO) and hydrocarbons (HC) in the exhaust gases was recorded. The operation of an engine powered by vegetable fuels (exhaust gas composition before the exhaust aftertreatment system) under the vehicle's driving conditions on the chassis dynamometer (Fig. 4 – case 1) showed higher HC concentration when powered Df relative to Co over the entire engine speed range.

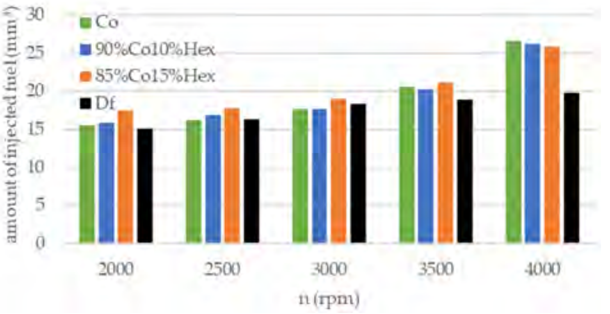

Fig. 5. Amount of fuel injected depending on the rotational speeds, for the operation of the Diesel engine powered by the tested fuels (case 1)

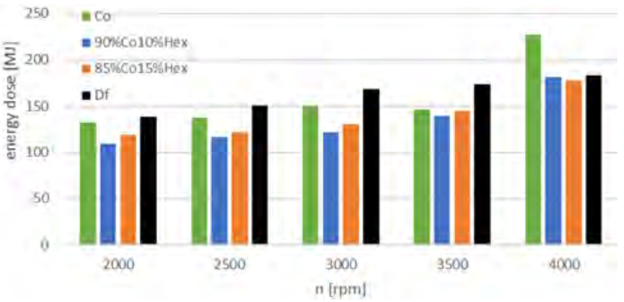

Fig. 6. Energy dose of the test fuels, depending on the rotational speeds, for the operation of the Diesel engine powered by the tested fuels (case 2)

Obtaining the same engine operating point determined by its rotational speed and load required the supply of a different volumetric dose of the tested fuels – as shown in

Fig 5. This was related to the different physicochemical properties of the fuels, which influenced the injection strategy implemented by the controller. At the same time, the tested fuels had different calorific values, which translated into the energy dose of injected fuels, which can be defined as the product of the calorific value of the fuel and the mass of the injected fuel (Fig 6). It seems that the above had a decisive impact on the observed ecological parameters obtained during the research.

4. Conclusions

Supplying a diesel engine with unprocessed canola oil is difficult due to its physicochemical properties, which are different from diesel fuel. This is especially true for viscosity and density, especially at low ambient temperatures. The high viscosity of canola oil is significantly reduced with the addition of n-hexane. Observation of the ecological parameters indicates that for pure canola oil (Co) and canola oil with the addition of n-hexane (10% and 15%), the level of NO_x concentration relative to diesel oil (Df) was higher for both cases (measurement before and after the catalytic converter), which is also confirmed by the conducted research described in the available literature [19–21]. The observed quantitative change between the investigated cases was mainly due to the operation of the haust gas cleaning system. When fueling the diesel engine with vegetable fuels, no significant differences were observed from Df in terms of carbon dioxide (CO_2) concentration. This leads to the conclusion that the use of canola oil with the addition of n-hexane may be a pro-ecological effect due to the absorption of carbon dioxide during plant growth. Therefore, it is possible to operate the tested engine when powered by canola oil and a mixture of canola oil with n-hexane in real vehicle traffic conditions. The only problem in terms of ecological conditions is the increased concentration of nitrogen oxides – further scientific considerations of the authors of the work will be devoted to limiting this phenomenon.

Nomenclature

CI	compression ignition
Co	canola oil
Df	diesel fuel
DI	direct injection
CR	common rail

Bibliography

[1] HO, R.J., YUSOFF, M.Z., PALANISAMY, K. Trend and future of diesel engine: development of high efficiency and low emission low temperature combustion diesel engine. *IOP Conference Series: Earth and Environmental Science.* 2013, **16**. https://doi.org/10.1088/1755-1315/16/1/012112

[2] YILDIZ, I., AÇIKKALP, E., CALISKAN, H. et al. Environmental pollution cost analyses of biodiesel and diesel fuels for a diesel engine. *Journal of Environmental Management.* 2019, **243**, 218-226. https://doi.org/10.1016/j.jenvman.2019.05.002.

[3] LABECKI, L., CAIRNS, A., XIA, J. et al. Combustion and emission of rapeseed oil blends in diesel engine. *Applied Energy.* 2012, **95**, 139-146. https://doi.org/10.1016/j.apenergy.2012.02.026.

[4] ZAHER, F. Vegetable oil as alternative fuel for diesel engines: a review. *Grasas y Aceites.* 1990, **41**, 82-91.

[5] AGARWAL, D., AGARWAL, A.K. Performance and emissions characteristics of Jatropha oil (preheated and blends) in a direct injection compression ignition engine. *Applied Thermal Engineering.* 2007, **27**, 2314-2323. https://doi.org/10.1016/j.applthermaleng.2007.01.009

[6] DE SOUZA, S.P., PACCA, S., DE ÁVILA, M.T. et al. Greenhouse gas emissions and energy balance of palm oil biofuel. *Renewable Energy.* 2010, **35**(11), 2552-2561. https://doi.org/10.1016/j.renene.2010.03.028

[7] BROCK, D., KODER, A., RABL, H.P. et al. New completely renewable biofuels: formulations and engine tests on an unmodified up-to-date diesel engine. *Green Chemistry.* 2018, **20**, 3308-3317. https://doi.org/10.1039/c8gc00606g

[8] LONGWIC, R., SANDER, P., NIEOCZYM, A. et al. Effect of some properties of hydrocarbon fuels on self-ignition delay. *Przemysł Chemiczny.* 2017, **5**. https://doi.org/10.15199/62.2017.5.30

[9] PARLAK, A. A study on performance and exhaust emissions of the steam injected DI diesel engine running with different diesel- conola oil methyl ester blends. *Journal of the Energy Institute.* 2019, **92**(3), 717-729. https://doi.org/10.1016/j.joei.2018.03.001

[10] ZDZIENNICKA, A., SZYMCZYK, K., JAŃCZUK, B. et al. Surface, volumetric, and wetting properties of oleic, linoleic, and linolenic acids with regards to application of canola oil in diesel engines. *Applied Sciences.* 2019, **9**(17), 3445. https://doi.org/10.3390/app9173445

[11] ZDZIENNICKA, A., SZYMCZYK, K., JAŃCZUK, B. et al. Adhesion of canola and diesel oils to some parts of diesel engine in the light of surface tension components and parameters of these substrates. *International Journal of Adhesion and Adhesives.* 2015, **60**, 23-30. https://doi.org/10.1016/j.ijadhadh.2015.03.001

[12] KRYSHTOPA, S., GÓRSKI, K., LONGWIC, R. et al. Increasing parameters of diesel engines by their transformation for methanol conversion products. *Energies.* 2021, **14**(6), 1710. https://doi.org/10.3390/en14061710

[13] GÓRSKI, K., SANDER, P., LONGWIC, R. The assessment of ecological parameters of diesel engine supplied with mixtures of canola oil with n-hexane. *IOP Conference Series: Materials Science and Engineering.* 2018, **421**, 042025. https://doi.org/10.1088/1757-899X/421/4/042025

[14] LONGWIC, R., SANDER, P. The course of combustion process under real conditions of work of a traction diesel engine supplied by mixtures of canola oil containing n-hexane. *IOP Conference Series: Materials Science and Engineering.* 2021, **14**(2), 123-138. https://doi.org/10.1088/1757-899X/421/4/042050

[15] LONGWIC, R., SANDER, P., ZDZIENNICKA, A. et al. Combustion process of canola oil and n-hexane mixtures in dynamic diesel engine operating conditions. *Applied Sciences.* 2020, **10**(1), 80. https://doi.org/10.3390/app10010080

[16] LONGWIC, R., SANDER, P., LOTKO, W. et al. Self-ignition of rapeseed and n-hexane mixtures in diesel engine. *Przemysł Chemiczny*. 2020, **99**, 206-210. https://doi.org/10.15199/62.2020.2.3

[17] LONGWIC, R., SANDER, P., JAŃCZUK, B. et al. Modification of canola oil physicochemical properties by hexane and ethanol with regards of its application in diesel engine. *Energies*. 2021, **14**(15), 4469. https://doi.org/10.3390/en14154469

[18] SANDER, P., LONGWIC, R., JAŃCZUK, B. et al. The use of canola oil, n-hexane, and ethanol mixtures in a Diesel engine. *SAE International Journal of Fuels and Lubricants*, 2021, **14**(2), https://doi.org/10.4271/04-14-02-0008

[19] ROY, M.M., WANG, W., BUJOLD, J. Biodiesel production and comparison of emissions of a DI diesel engine fueled by biodiesel-diesel and canola oil-diesel blends at high idling operations. *Applied Energy*. 2013, **106**, 198-208. https://doi.org/10.1016/j.apenergy.2013.01.057

[20] LI, Q., BACKES, F., WACHTMEISTER, G. Application of canola oil operation in a diesel engine with common rail system. *Fuel*. 2015, **159**, 141-149. https://doi.org/10.1016/j.fuel.2015.06.060

[21] TÜCCAR, G., TOSUN, E., ULUDAMAR, E. Investigations of effects of density and viscosity of diesel and biodiesel fuels on NO_x and other emission formations. *Academic Platform Journal of Engineering and Science*. 2018, **6**(2), 81-85. https://doi.org/10.21541/apjes.371015

Rafał Longwic, DSc., DEng. – Faculty of Mechanical Engineering, Lublin University of Technology.
e-mail: *r.longwic@pollub.pl*

Przemysław Sander, MEng. – Faculty of Mechanical Engineering, Lublin University of Technology.
e-mail: *p.sander@pollub.pl*

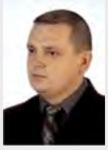

Dawid Tatarynow, MEng. – Faculty of Mechanical Engineering, Lublin University of Technology.
e-mail: *d.tatarynow@pollub.pl*

Article citation info:
GIS, M., GIS, W. The current state and prospects for hydrogenisation of motor transport in Northwestern Europe and Poland. *Combustion Engines*. 2022, **190**(3), 61-71. https://doi.org/10.19206/CE-144560

Maciej GIS
Wojciech GIS

Combustion Engines
Polish Scientific Society of Combustion Engines

The current state and prospects for hydrogenisation of motor transport in Northwestern Europe and Poland

ARTICLE INFO

Received: 18 September 2021
Revised: 5 October 2021
Accepted: 5 December 2021
Available online: 16 December 2021

The article presents the situation regarding the hydrogenisation of motor transport in Northwestern Europe, a region leading in this regard in Europe. The following countries were included in the analysis of national plans in this area, taking into account both technical issues – among others – concerning HRS and FCEV, their number, as well as economic issues (among other things relating to the costs of using hydrogen): Belgium, Denmark, France, Germany, the Netherlands, Norway and England. Reference was also made to the situation in Poland, where major fuel and energy companies (among others: Orlen, Lotos, PGNiG and ZE PAK Capital Group) are strongly interested in hydrogenisation of motor transport and manufacturers of vehicles – for example – Solaris or Autosan in producing vehicles equipped with fuel cells. Based on the analyses carried out at the Institute of Motor Transport, it was found that the good location of basic hydrogen refuelling stations is along the TEN-T corridors running across Poland. The order of their location is as follows: 1 – Poznan, 2 – Warsaw,3 – Bialystok, 4 – Szczecin, 5 – Łódź region, 6 – Tricity, 7 – Wroclaw, 8 – Katowice region, 9 – Kraków.

Key words: *motor transport, hydrogen, fuel cell*

1. Introduction

The European Union is the first in the world to introduce a restrictive law prohibiting the registration of new passenger cars equipped with internal combustion engines from 2035. This is the result of the adopted package of solutions [1], which sets out a reduction in greenhouse gas emissions by at least 55% by 2030 compared to the level of 1990 [2]. In 2050, the European Union is to become the first net zero-emission region in the world. At the same time, the European Union is proposing ambitious targets for reducing carbon dioxide emissions from new passenger cars and trucks: a 55% reduction in emissions from passenger cars by 2030 and a 50% reduction in emissions from trucks by 2030 [3].

In addition to the electrification of transport, which is still considered crucial, the simultaneous development of other zero-emission technologies is allowed. Among them is the hydrogenisation of transport. Hydrogen is the fuel of the future, the resources of which are practically inexhaustible. It is the most common chemical element in the universe and is one of the most common elements on Earth (mainly in the form of water and organic compounds). Thus, its use may constitute the future of many sectors of the economy, including transport.

The European Union also recognises the potential of hydrogen. In July 2020, the European Commission announced "A hydrogen strategy for a climate – neutral Europe" [4]. This is a strategic vision for the implementation in 2050 of "The European Green Deal" (European climate neutrality in 2050) [5–8].

In the wake of the COVID-19 pandemic, the European Union has decided to adopt an ambitious economic recovery plan. It has allocated EUR 750 billion for this purpose, including EUR 500 billion for grants and EUR 250 billion for loans to the Member States [6].

In the document mentioned above [6], the reconstruction process is divided into pillars. The first concerns support for the Member States for investment and reforms. The second pillar is kick-starting the EU economy by incentivising private investment. The third pillar is learning the lessons of the crisis. This is directly related to the cooperation of – among others – public authorities, industry and civil society – e.g. within the framework of the European Clean Hydrogen Alliance, based on the European Battery Alliance.

A gradual implementation of hydrogen has been announced. In the first phase, in 2020–2024, there are plans to install at least 6 GW of renewable hydrogen electrolysers in the EU (production of up to 1 million tonnes of renewable hydrogen). In the second phase (2025–2030), hydrogen will become an integral energy carrier in an integrated energy system in which at least 40 GW of renewable hydrogen electrolysers will have been installed by 2030 (production of 10 million tonnes of renewable hydrogen in the EU). In the third phase (2030–2050), technologies for effective decarbonisation will be used on a large scale [4, 9].

The potential in the hydrogen technology is recognized by Western European countries, including North-western European such as: Belgium, Denmark France, Germany, the Netherlands, Norway, and the United King-dom. Today, this region concentrates around 5% of global hydrogen demand and 60% of European demand [10].

According to Baseline scenario developed by International Energy Agency (IEA) – describes how demand for hydrogen could evolve considering energy- and climate-related policies already in place in the Northwestern European countries – hydrogen demand for transport (heavy-duty vehicles (HDV), medium-duty vehicles (MDV) buses, light-commercial vehicles (LCV), passenger light-duty vehicles (PLDV), shipping, rail and aviation) in the region would reach around 300 kt H_2 by 2030, driven by hydrogen use in fleets, such as buses and trucks, corresponding to close to 10% of the hydrogen demand in Northwestern Europe [10].

Urban transit buses represent a major opportunity. In particular, national targets for fuel cell bus deployment are deemed more feasible relative to PLDV, resulting in stock share of around 10% in the Netherlands [10].

The Accelerated scenario is based on enacting more ambitious energy- and climate-related policies and implementing supporting mechanisms that could facilitate adoption of hydrogen technologies [10].

In the Accelerated scenario, hydrogen use expands to light-commercial vehicles (LCV) and PLDV as well as shipping (mainly in the form of ammonia), resulting in an overall hydrogen demand of more than 1 Mt H_2 by 2030 (around 15% of the region's overall hydrogen demand). In PLDVs would reach over 1 million vehicles by 2030 and a share of around 1% of the stock. The stock number of HDVs by 2030, at 33,000, is much lower, but their typically higher annual mileage boosts hydrogen demand [10].

The realization of the Accelerated scenario would require expanding from the less than 200 HRS currently operating in the region to a range of 3000 to 4400 HRS [10].

In later chapters in case of FCEV (passenger cars and vans) mostly were passenger cars, whereas FCV mostly were FCEV.

2. Hydrogen Refueling Stations (HRS) Worldwide as of the end 2020, including HRS at Northwest Europe

At the end of 2020, 540 HRSs were in operation, including both public and private installations. Most HRSs are concentrated to Asia (278), followed by Europe (190) and North America (68). The country with the highest number of stations was Japan (137), Germany (90), China (85), the U.S. (63), ahead of South Korea (52) and France (38) [11]. In Northwest Europe (Belgium, Denmark, France, Germany, the Netherlands, Norway, and the United Kingdom) was 158 HRS in total at the end of 2020, it is about 83% HRS in Europe.

The growth in the number of HRS around the world over the 2017–2020 was as follows: 2017 (330), 2018 (381), 2019 (468), 2020 (540) [11]. The number of FCEVs per HRS in the six countries with the highest number of HRSs as of the end of 2020 was as follows: South Korea 194.1, U.S. 146.9, China 99.3, Japan 30.7, Germany 12.0, France 10.4. Most of the stations for passenger cars are operated at 700 bars, but for buses typically utilize was 350 bars [11]. Deployment status of HRS in Motor Transport as of end 2020 (2021 update) at Northwest Europe against the backdrop of the world is presented in Table 1 [11].

3. Fuel Cell Vehicles (all vehicle types) as of end 2020 (also in the case of Northwest Europe Countries)

An analysis indicates that 34,804 Fuel Cell Vehicles (FCV) of all types were in operation worldwide as of the end of 2020 (cars and vans; buses-with more than eight seats in addition to the driver's seat; light commercial vehicles-with a maximum mass not exceeding 3.5 tonnes; medium duty-trucks with a maximum mass exceeding 3.5 tonnes but not exceeding 12 tonnes; heavy duty trucks with a maximum mass exceeding 12 tonnes) [11]; (Table 2).

Table 1. Deployment status of HRS in Motor Transport as of the end 2020 at Northwest Europe against the backdrop of the world [11]

Country	Number of HRSs (public stations)	Notes
Asia	**278**	–
Japan	137(137)	700 bar
China	85(66)	–
South Korea	52(–)	–
India	2(–)	350 bar
Malaysia	1(–)	dual – 350/700 bar
Taiwan	1(–)	–
Australia	**1(1)**	**350 bar**
Europe	**190**	–
Germany*	**90(90)**	**700 bar (7 dual - 350/700 bar)**
France*	**38(28)**	**350–700 bar**
U.K.*	**13(10)**	**2x350 bar, 11x350/700 bar**
Austria	7(5)	both 350/700 bar available
Switzerland	6(–)	–
Denmark*	**6(6)**	**–**
Italy	5(1)	both 350/700 bar available
Spain	5(2)	4x350, 1x700 bar
Sweden	5(5)	mainly 700 bar, 2 dual (350/700 bar)$^{1/}$
Netherlands*	**5(3)**	**3 dual 350/700 bar, 1/2 – 350 bar**
Belgium*	**3(2)**	**1 dual 350/700 bar, 1–350 bar, 1–700 bar**
Norway*	**3(–)**	**2–700 bar, 1–350 bar**
Croatia	1(1)	1–30 bar (bicycles)
Czech Republic	1(1)	350 bar
Latvia	1(1)	350 bar
Iceland	1(–)	750 bar
North America	**68**	
U.S.	63(46)	350 bar and 700 bar
Canada	5(3)	700 bar
Central America	**1**	
Costa Rica	1(–)	350 bar
Middle East	**2**	
Saudi Arabia	1(–)	700 bar
United Arab Emirates	1(–)	700 bar
Worldwide	**540**	–
*Northwest Europe countries		

The vehicle mix is as follows: passenger cars (74.5%), buses (16.2%), and medium-duty trucks (9.1%), light commercial vehicles plus heavy-duty trucks (0.2%). Most passenger cars are in Asia (55%), followed by North America (36%) and Europe (9%). In the U.S. more than 99% fuel cell vehicle fleet is composed of passenger cars [11]; Table 2.

In Northwest Europe Countries fuel cell passenger cars and vans had at the end 2020 the following part in fleets of hydrogen vehicles: Germany 93.8%, France 94.7%, U.K. 87%, Denmark 97.5%, Netherlands 91.8%, Belgium 91.4%, Norway 97.0%. In total, these vehicles had 89.8% participation in FCV in Europe as of the end of 2020 (Table 2).

Table 2. Number of Fuel Cell Vehicles in Motor Transport as of the end 2020 at Northwest Europe against the backdrop of the world [11]

Country	**Number of Fuel Cell Vehicles (FCV) (all types in operation worldwide as of the end of 2020)**	**Notes Number of$^{1/}$**				
		Pass. cars and vans (FCEV)	**Buses (FCB)**	**LCV**	**MDT**	**HDT**
Asia	**22 746 (65%)**	**14141 (55%)**	**5452 (97%)**	–	–	–
Japan	4 200	4100	–	–	–	–
China	8 443	–	5290 (93.7%of the worldwide FCB fleet)	–	3153 (99.7% of the world-wide MDT fleet)	(50 were produced but had not registered by the end of 2020)
South Korea	10 093	10 041	–	–	–	–
India	10	–	–	–	–	–
Malaysia	–	–	–	–	–	–
Taiwan	–	–	–	–	–	–
Australia	**6**	–	–	–	–	–
Europe	**2 667(8%)**	**2465 (9%)**	**131 (2%)**	–	–	–
Germany*	**1 083**	**1016**	–	–	–	–
France*	**396**	**375**	–	–	–	–
U.K. *	**193**	**168**	–	–	–	–
Austria	47	45	–	–	–	–
Switzerland	115	93	–	–	–	–
Denmark*	**120**	**117**	–	–	–	–
Italy	34	22	–	–	–	–
Spain	17	17	–	–	–	–
Sweden	51	50	–	–	–	–
Nether-lands*	**342**	**314**	–	–	–	–
Belgium*	**70**	**64**	–	–	–	–
Norway*	**164**	**159**	–	–	–	–
Croatia	–	–	–	–	–	–
Czech Republic	1	1	–	–	–	–
Latvia	10	-	–	–	–	–
Luxemburg	2	2	–	–	–	–
Iceland	22	22	–	–	–	–
North America	**9380 (27%)**	**9316 (36%)**	**64 (1%)**	–	–	–
U.S.	9252	9188	–	–	–	–
Canada	128	128	–	–	–	–
South America	**1**	**1**	–	–	–	–
Brazil	1	–	–	–	–	–
Central America	**4**	4	–	–	–	–
Costa Rica	4	–	–	–	–	–
Middle East	–	–	–	–	–	–
Saudi Arabia	–	–	–	–	–	–
United Arab Emirates	–	–	–	–	–	–
Worldwide	**34 804 (100%)**	**25932$^{2/}$ (100%)**	**5 648$^{3/}$**	**49**	**3 161**	**14**

* Northwest Europe countries; 1/LCV – Light Commercial Vehicles; MDT – Medium-Duty Tracks; HDV – Heavy Duty Trucks; 2/including the rest of the world (5 pass. cars); 3/ including the rest of the world (1 – Fuel Cell Bus – FCB)

4. Motor transport hydrogenization in North-Western Europe courtiers

Belgium

Within the framework of the European HIT-2-Corridors project in December 2015 a proposal was developed - National Implementation Plan – Hydrogen Refuelling Infrastructure Belgium [9, 12, 13]. According to the said proposal, taking into account the average percentage of HRS stations in 2015–2020, 2020–2025, 2025–2030 in the total number of petrol stations in those years in respective countries, among others such as Germany, the UK, the Netherlands, France, Denmark, it was estimated in the said proposal that in the case of Belgium with about 3.200 petrol stations, the amount of HRS refers to 0.8% (2020) via 2.3% (2025) to 4.7% (2030). This is completely in line with the targets in other H2-Mobility countries. Thus, in years:

- 2015–2020 there should be 25 HRSs (20 in Flanders and 5 in Walloon region),
- 2020–2025 there should be 75 HRSs (50 in Flanders and 20 in Walloon region and 5 in Brussels),
- 2025–2030 there should be 150 HRSs (100 in Flanders and 40 in Walloon region and 10 in Brussels [9, 12, 13].

This results in overall CAPEX for HRS up to 2030 of about 170 million euros. For 2020 should be about 1000 FCEV in Belgium which is almost 0.02% of the total vehicle fleet. After 2020, during the early market introduction (2020–2025), the amount of FCEV's will grow to possibly 7500 FCEV's. This is almost 0.15% of the market. Finally, between 2025–2030, a ramp up could emerge which results in 30,000 FCEV (0.55% market penetration). For buses, the target is 50 buses in 2020, 250 in 2025 and 500 in 2030 [14, 15]. At the end of 2017 in Belgium there were, however, for example only 3 HRS (in Antwerp, Halle and Zaventem) and 21 FCEVs and several hydrogen buses [9, 16, 17].

According to European Alternative Fuel Observatory (EAFO) in Belgium were 2 refuelling points (HRS) and 64 FCEV at the end of 2020 [16]. In the case of the data from Forschungszentrum Jülich GmbH were 3 HRS (2 public stations) and 64 FCEV (70 Fuel Cell Vehicles (FCV) at the end of 2020 [11]. Summing up in Belgium:2017 (3 HRS, 21 FCEV); 2020 (3 HRS, 64 FCEV); 2025 (150 HRS, 7500 FCEV); 2028 (30,000 FCEV).

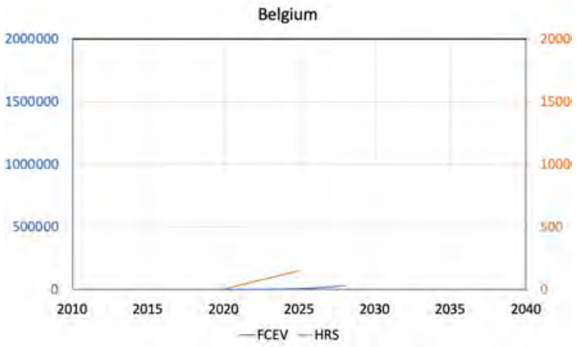

Fig. 1. The number of HRS and FCEVs in Belgium (2017-2028)

Denmark

The beginnings of the development of hydrogenisation of transport, including automotive transport in Denmark, practically started in 2001 by the creation of the "Danish Hydrogen and Fuel Cell Partnership", in which the Working Group "National FCH Transport Strategy Group" in 2008 prepared a national program "National R&D and demonstration strategy for FCH Transport". Between 2011 and 2014, several projects were implemented, co-financed by FCH-JU (The Fuel Cells and Hydrogen Joint Undertaking). In 2014, the “National Implementation Plan (NIP) for hydrogen refuelling infrastructure” was established. The first activities for FCEVs were undertaken in 2001 and for HRS – in 2006 [9, 19].

In March 2014, 17 FCEVs were in operation, mainly Hyundai iX35 cars and there were 3 HRS operating (in September 2014, the 4th was built). The focus was on supplying passenger cars with hydrogen at a pressure of 70 MPa. It was assumed that in 2025 electrical energy would be used, generated from hydrogen in 4.8 and in 2030 – 15.7% and 50% in 2050, replacing that derived from conventional fuels. Total electricity generation from renewable sources was expected in 2050. At the end of 2017, 10 HRSs (85 FCEV and several FCEB) were operated in Denmark [16]. According to EAFO in Denmark were 8 refuelling points (HRS) and 148 FCEV at the end of 2020 [18]. In the case of the data from Forschungszentrum Jülich GmbH were 6 HRS (6 public stations) and 117 FCEV (120 FCV) at the end of 2020 [9, 11].

The development scenarios of the FCEV fleet were made dependent on its dynamics. Thus, in the scenario assuming high development of the FCEV, it was assumed that in 2050 there would be 1.4 million vehicles (50% of the passenger car fleet). In the medium-sized development scenario of FCEV in the said year there were to be 1.1 million FCEVs (37.5% of the passenger car fleet), and 0.7 million FCEV (25% of the passenger car fleet) in the low development scenario of FCEVs in 2050. Those variants assumed respectively – in the high development scenario for FCEV the use of 100,000 FCEVs in 2015 (4% of the passenger cars fleet), in the medium-sized development in 2025 operation – 50,000 FCEVs (2% of the said fleet) and in the low development scenario operation in 2025 – 25,000 (1% of the said fleet) [9, 19].

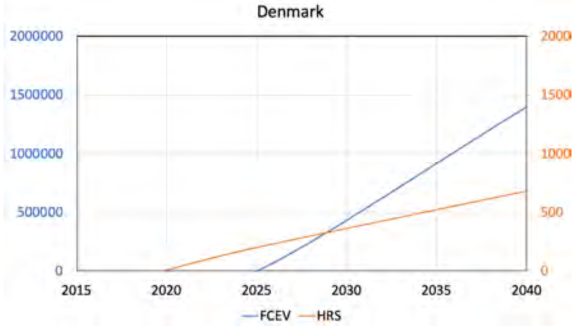

Fig. 2. The number of HRS and FCEVs in Denmark (2017–2050)

Whereas, in 2025, regarding HRS in the scenario assuming high development of FCEVs around 200 HRSs should be operated, roughly 1000 HRSs in 2050, and in the scenarios of low and medium development, in 2025 – approx. 100 HRSs and in 2050 – 500 HRSs. In Denmark analyses are made of the central, and local production of hydrogen. Electrolyser capacity in 2025, 2035, and 2050 is 88 MW, 579 MW and 1063 MW respectively, used in 85% [9, 19].

Summing up in Denmark: 2017 (10 HRS, 85 FCEV); 2020 (6 HRS, 117 FCEV); 2025 (100–200 HRS); 2050 (500–1000 HRS, 700,000–1,400,000 FCEV).

France

A hydrogenisation development plan in France, including motor transport, was prepared by the H2Mobilité France Consortium in 2013 and envisaged significant development of FCEV refuelling infrastructure from 96 HRS in 2022 to 602 HRS in 2030 (in 2026–2030 with a decreasing share of HRS with a hydrogen generation capacity of 212 kg/d in favour of HRS with a hydrogen production capacity of 420 kg/d) and the development of FCEVs from 23 thousand in 2022 to 773,000 in 2030, with hydrogen demand of up to 3,000 tonnes in 2022, to 89,000 tonnes in 2030 and electrical energy demand from 115 GWh p.a. in 2022 to 3,251 GWh p.a. in 2030 [9, 20].

According to the aforementioned development plan, in 2040 and 2050, the fleet of FCEV and light trucks will be 3.7 million vehicles and 7.3 million vehicles respectively, with a share of 9% and 17% in the total French market of passenger and light trucks [20]. With regard to reducing CO_2 emissions, the introduction of the said fleet of hydrogen vehicles would provide in a life cycle (with an average annual mileage of 15,600 km and mix hydrogen production – 75% using electrolysers) of 1.2 tCO_2 per year by vehicle in 2030, when the societal cost of CO_2 is evaluated at 105 euro per tonne [20]. At the end of 2017, there were 19 hydrogen refuelling stations and 263 vehicles served by them in France [16]. At the end of 2019, there were 26 HRSs operating and 34 planned in France. Most of the French HRS aim at refuelling of buses and delivery vehicle fleets [9, 21].

According to EAFO in France were refuelling points 36 (HRS) and 148 FCEV at the end of 2020 [18]. In the case of the data from Forschungszentrum Julich GmbH were 38 HRS (28 public stations) and 375 FCEV (396 FCV) at the end of 2020 [11]. However, according to International Partnership for Hydrogen and Fuel Cells in Economy (IPHE) were 41 HRS, 381 FC cars and 22 FC buses (updated July 2021) [22].

In 2018, presented was based on an in-depth “Hydrogen scaling up” study on the use of hydrogen in key areas of the world economy a plan for the development of hydrogenisation in France, including in motor transport [9, 23]. This plan assumes among others that:

- the number of HRS in 2023 will be 140 and 400 in 2028,
- the number of passenger cars and light trucks using fuel cells will be 10,000 in France in 2023 and 200,000 vehicles in 2028, and in 2050 18% of used passenger vehicles and light trucks will use hydrogen, as well as 25% of the registered bus fleet and 20% of the fleet of registered heavy trucks,
- investment expenditure – for example – for the implementation of 600 HRSs comes to 750 million euro.

The hydrogen distribution plan for the energy transition in 2018-2028 was presented by Minister for Ecological Transformation Nicolas Hulot on 01.06 2018 [9, 24]. According to that plan:

- in 2023 in France there should be 5000 light trucks, 200 buses and heavy-duty vehicles equipped with hydrogen fuel cells and 100 HRSs,
- in 2028 from 20,000 up to 50,000 light trucks, from 800 to 2000 buses and heavy-duty vehicles equipped with hydrogen fuel cells and from 400 to 1000 HRSs,
- in 2017 18.5% of electricity was derived from renewable sources and 40–60% of that energy should be stored,
- production of hydrogen by electrolysers is considered very important, for example Michelin plans to implement 15 electrolysers, 20 hydrogen refuelling stations and the purchase of 1000 vehicles equipped with hydrogen fuel cells (Zero Emission Valley project – Auvergne-Rhône-Alpes region),
- roughly 200 light hydrogen Hy-Kangoo trucks by symbioFC are used (price approx. 30 thousand euros). The price of 12 m of bus is about 450 thousand euro. Hydrogen buses are already in use in French cities.

Summing up in France: 2017 (19 HRS, 263 FCEV); 2019 (26 HRS+34HRS planned); 2020 (38 HRS, 375 FCEV); 2023 (100–140 HRS, 10,000 FCEV); 2028 (400–1000 HRS, 200,000 FCEV); 2030 (602 HRS, 773,000 FCEV).

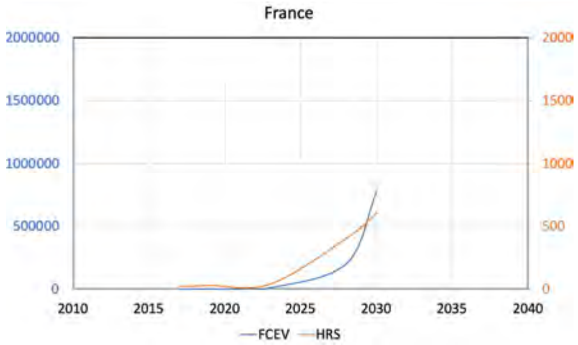

Fig. 3. The number of HRS and FCEVs in France (2017–2030)

Germany

A broader interest in the hydrogenization of motor transport in the Germany took place at the end of the 1990s. At that time, a several of works were carried out on the energy use of hydrogen in motor transport, its transport or distribution. An example could be the co-operation “Verkehrswirtschaftliche Energiestrategie” (VES, Transport Energy Strategy) between German politics and private companies which was founded in 1998. It was targeted at developing strategies to ensure a global leading role of the German car industry in alternative fuel technologies [9, 23].

Another example can be the CEP (Clean Energy Partnership, established in 2002) emerged from the VES as a joint political initiative, lead-managed by the German Ministry of Transport and Industry. While the VES took a more theoretical approach, the CEP puts the knowledge gained into practice. CEP has three phases: 2002–2008, 2008–2010 and 2011–2016 of different tasks. For instance, the second phase was committed to the qualification of applications in daily usage, e.g., improvement of vehicle efficiency and cold-start abilities as well as a cost reduction in vehicle and infrastructure technologies. In 2014, about 85 FCEV were operated within the framework of the CEP [9, 23].

Yet another example can be the H2-Mobility Initiative (2009), which originates from the VES. The Initiative, making it the centrepiece for the commercialization of FCEVs in Europe. The H2-Mobility initiative was transformed to a Joint Venture in 2012/13. The Initiative reviewed various options for building a Germany-wide H2-infrastructure assuming the serial production of FCEVs and public co-financing of further HRS and their development, in particular in large agglomerations. In 2012, it was expected that in 2020 there would be around 400 HRSs and approx. 150,000 FCEVs (in 2030 – 1000 HRSs and 1,800,000 FCEVs, respectively). It was also assumed that in 2023 there will be 500 HRSs operating, 500,000 FCEVs and 2 thousand FCEBs (Fuel Cell Electric Bus) [9, 23].

In 2012 Daimler, Linde, Air Products, Air Liquide and Total agreed to invest 20 M€ in a further 36 stations up to a total of 50 stations with the support of the Federal Government (NIP) by 2015 (due to the delayed market introduction of FCVs. It should be pointed out that the first public compressed hydrogen refuelling station was launched in Hamburg as early as in January 1999 and the world's first public liquid hydrogen station was launched at Munich Airport in May this year [24, 25]. However, at the end of December 2015, only 20 HRSs and 150 FCEVs were used [9, 26].

In the result of the undertaken efforts federal government, federal states, industry and science in 2006 “National Innovation Programme Hydrogen and Fuel Cell Technology” (NIP I) was adopted, functioning in years 2006–2016, which comprised a funding volume of 1.4 billion euros (in studies applied in the area of transport 471 projects were performed and 238 demonstrative projects). A governmental National Organization Hydrogen and Fuel Cell Technology – NOW was established in 2008 to manage the programme. It also operates in the area of electrical mobility. The above projects CEP and H2-Mobility Initiative have been included among others in NIP I. NOW organisation also operates the NIP II government programme for hydrogen and fuel cell technology for the period of 2016–2026. In this second phase, only the Federal Ministry of Transport and Digital Infrastructure (BMVI) was initially investing 250 million euros until 2019 to support hydrogen and fuel cell technology for the implementation of the programme [9, 27].

In the first stage of the development of the hydrogen refuelling infrastructure in the Germany by 2015, planned within the framework of H2 Mobility Initiative under the auspices of NIP I was the launch of 50 public HRS (vs. even 100 HRSs initially assumed). At the end of 2017, there were however 56 hydrogen refuelling stations in Germany, used by several hundred FCEVs (approx. 300). The construction of the aforesaid 50 HRS was completed in 2018 [28]. In the second phase of the development of this infrastructure by the end of 2020, with an investment of 350 million euro,100 hydrogen refuelling stations are planned to be launched and by the end of 2023 (initially by the end of 2025) 400 HRSs (10 HRSs each in the 6 largest metropolises, while ensuring a maxi-mum distance of 90 km between

HRS on motorways. In 2030 there should be 1000 HRS with full commercialisation [9, 29–32].

The main objective of the use of hydrogen in Germany in the case of motor transport is to reduce greenhouse gas emissions (mainly CO_2) and energy consumption by the said transport and to increase the share of renewable energy. The targets are as follows: a 40% reduction in greenhouse gas emissions in 2020 and 80–95% in 2050 vs 1990 for greenhouse gas emissions, and respectively a reduction by 10% and 40% in final energy consumption vs 2008, with an increase in the use of renewable energy up to – respectively – 18% and 60% in final energy consumption [32]. This involves the production of hydrogen based on electrolysers, the power of which is likely to be greater than 10 GW in 2030 [9, 33].

FCEVs currently have a long range of 400–700 km with a single refuelling, with refuelling time similar to that of conventional passenger cars, and investments in the refuelling infrastructure at 20 million FCEVs are equal to €40 billion (€51 billion for BEV – Battery Electric Vehicle), which gives FCEV an advantage over BEV [34,35]. In Germany, there were 87 hydrogen refuelling stations at the end of 2019 [36]. According to EAFO in Germany were 88 refuelling points (HRS) and 738 FCEV at the end of 2020 [18]. In the case of the data from Forschungszentrum Julich GmbH were 90 HRS (90 public stations) and 1016 FCEV (1083 FCV) at the end of 2020 [11]. However, according to IPHE were 97 HRS, 1195 FC cars, 79 FC buses and 2FC Trucks (updated July 2021) [22].

Summing up in Germany: 2015 (20 HRS, 150 FCEV); 2017 (56 HRS, 300 FCEV); 2019 (87 HRS); 2020 (90 HRS, 1016 FCEV); 2023 (400 HRS); 2030 (1000 HRS, 1,800,000 FCEV).

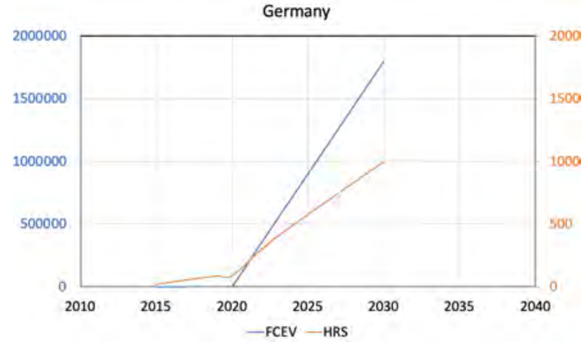

Fig. 4. The number of HRS and FCEVs in Germany (2015–2030)

The Netherlands

The Ministry of Infrastructure and Environment of the Netherlands at the end of 2011 initiated works on a programme on the hydrogenization of transport, and the resulting conclusions were presented in 2013. The program consisted of four phases:

- Phase 0 (2000–2012; research and development),
- Phase 1 (2012–2015; market preparation),
- Phase 2 (2015–2020; market introduction and yet market preparation),
- Phase 3 (after 2020; mass production and yet market preparation).

This programmed was concretized in the EU project – The Hydrogen Infrastructures for Transport (HIT), where 4 phases were also adopted. These were: Phase 1 (2014–2017; market preparation, 2–20 HRS, 1,500 hydrogen vehicles, access by 20% of the population), Phase 2 (2018–2023; early market introduction, 20–50 HRSs, 1500–15,000 hydrogen vehicles, access by 50% of the population), Phase 3 (2024–2030; full market introduction, 50–200 HRSs, 15,000–125,000 hydro- gen vehicles, access by 90% of the population), Phase 4 (after 2030; mass market, 1000–1400 HRSs, > 2.5 million hydrogen vehicles, access by 100% of the population). Development of the HRS network: initial network of 20 HRSs with 210 kg/day stations, upgrade of initial stations to 420 kg/day 5 years after installation, and installation additional 420 kg/day base on need for HRS capacity resulting from hydrogen demand and network utilization [9, 37, 38].

At the end of 2017 in the Netherlands functioning were only 3 hydrogen refueling stations and 34 hydrogen vehicles and several buses [16].

According to Dutch H2Platform (May 2018):

- by 2020 there should be: 20 HRS, 2000 FCEVs, 100 FCEBs, 500 vans, 20 trucks,
- whereas in 2030 there should be 216 HRSs, according to: Scenario Low 132,000 hydrogen vehicles, Scenario Mid 375 000 hydrogen vehicles, Scenario High 696 000 hydrogen vehicles, 300,000 FCEV, 65,000 LCVs (Light Commercial Vehicle), 7700 trucks and 1700 buses. Governmental Subsidies end 2026, total Capital expenditures (Capex) 2018–2030 = C725 million [9, 39, 40].

In July 2017, the Ministry of Economic Affairs and Climate Policy asked TKI Gas (gas network organization in the Netherlands) to manage the process to define the outlines of a roadmap for hydrogen [39]. The report was based on – among others – the findings of the "Hydrogen scaling-up" study, referring to the same areas of energy transition as those cited in this study, and assumed was a reduction in greenhouse gas emissions by 80–95% in 2050 vs 1990 [48]. The report addressed a wide range of issues related to its use. Attention was drawn to the need to develop ways of producing it based on renewable energy, distribution (refueling infrastructure) or use in heavy-duty vehicles [9, 41, 42].

This year a governmental document "Government Strategy on Hydrogen" has been published, stating that the National Climate Agreement includes an ambition to scale up electrolysis to approximately 500 MW of in-stalled capacity by 2025 and 3–4 GW of installed capacity by 2030. However, in order to support the targets, set out in the National Climate Agreement (50 HRS, 15,000 hydrogen vehicles and 3000 heavy-duty hydrogen vehicles by 2025; 300,000 hydrogen vehicles by 2030), a cooperation agreement with various stakeholders will be signed in this year. Electricity will be obtained for electrolysis from offshore wind farms and the gas network will also be used for hydrogen transmission [9, 43].

According to EAFO in Netherlands were X refueling points (HRS) and X FCEVs at the end of 2020 [18]. In the case of the data from Forschungszentrum Jülich GmbH were 5 HRS (3 public stations) and 314 FCEV (342 FCV) at the end of 2020 [11]. However, according to IPHE were 7 HRS, 390 FC cars, 12 FC buses and 11 FC Trucks (updated July 2021) [22].

Summing up in Netherland: 2017 (3 HRS, 34 FCEV); 2020 (5 HRS, 314 FCEV); 2025 (50 HRS, 15,000 FCEV); 2030 (216–1000 HRS, 300,000 FCEV).

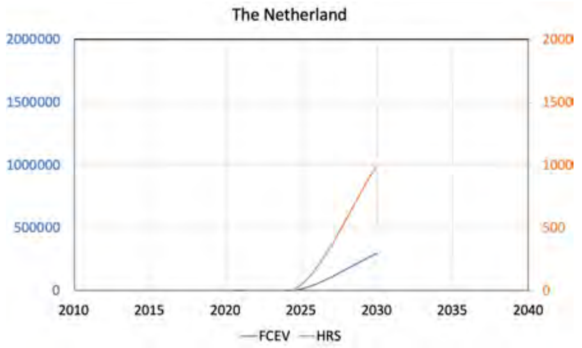

Fig. 5. The number of HRS and FCEVs in the Netherlands (2017–2030)

Norway

Norwegian greenhouse gas emissions were 52 million tonnes of CO_2 equivalents in 2018. Road traffic is responsible for 16.5 million tonnes CO_2 equivalents and 32% of total emissions. Hydrogen and other hydrogen-based systems have the potential to reduce emissions in the transport sector [44].

The Norwegian Hydrogen Council published in 2006 and 2012 two Actions Plans for the periods 2007–2010 and 2012–2015 respectively, plans in aspect use hydrogen. The Council's recommendations were not similarly embraced by the Government (the first National Norwegian Hydrogen Strategy in 2005) [45].

The HyNor-project (nationally supported project) started out as a hydrogen highway-project in Norway. It was initiated by large industrial companies such as Statoil and Norsk Hydro in 2003 with the goal of a market-realistic demonstration of hydrogen refuelling stations, as well as hydrogen vehicles. Several hydrogen refuelling stations were built along the 580-kilometer route from Oslo to Stavanger. Norway's first hydrogen fuelling station was opened in 2006 near Stavanger, the second in Porsgrunn in 2007, and two stations were opened in Oslo and Lier in 2009 [46].

The HyNor-project has tested several different hydrogen vehicles:

- 15 retrofitted Toyota Prius hydrogen internal combustion engine (ICE) vehicles (2007–2012)
- 4 Mazda RX-8 Hydrogen RE dual fuel hydrogen/gasoline ICE vehicles (2009–2012)
- 10 Mercedes-Benz B-class F-CELL (2011–2014)
- 5 Think City hydrogen cars
- 2 Hyundai ix35 FCEVs [46].

All new passenger cars and light vans sold in 2025 shall be zero-emission vehicles, and also new urban buses sold in 2025 shall be zero emitters or use biogas. By 2030, all new heavy-duty vehicles, 75% of new long- distance coaches and 50% of new trucks shall be zero emission vehicles [47].

At the end of 2017, were operational in Norway 9 HRS and 94 FCEV [16]. According to IPHE in March 2019, were only 6 HRS, 159 Fuel Cell Vehicles (includes Fuel Cell electric Vehicles with Range Extenders) and 5 Fuel Cell Buses [22]. By the end of 2019, 149 hydrogen cars, 1 light van, 5 hydrogen buses and 1 hydrogen truck had been registered in Norway. By comparison 260,581 electric cars, 7331 electric vans, 199 electric buses and 21 electric trucks had been registered by the end of 2019 [44]. According to EAFO in Norway were 3 refuelling points (HRS) and 195 FCEV at the end of 2020 [18]. In the case of data from Forschungszentrum Jülich GmbH were 3 HRS and 159 FCEV (164 FCV) at the end of 2020 [11]. Current status according to IPHE (updated July 2021): 6 HRS, 154 Fuel Cell Cars, 5 FC Buses and 4 Fuel Cell Trucks [22].

Current HRS network in Norway:

- Pursuing – H2 byproduct from chlorine production, 700 bar refueling
- Drammen – Trucked-in hydrogen, 700 bar refueling (shutdown in 2015 and moved to Oslo airport Gardermoen)
- Oslo – Trucked-in hydrogen, 700 bar refuelling
- Oslo – Gaustad – On-site electrolysis (10 Nm^3/h), 700 bar refuelling
- Oslo – Rosenholm – On-site electrolysis (2×60 Nm^3/h), 350 bar refueling (bus-only station)
- Lillestrom – H2 from biogas via Sorption Enhanced Steam Methane Reforming (SE-SMR) and solar electrolysis, 700 bar refuelling [46].

A study performed by LBST (Ludwig Bölkow Systemtechnik) for Statoil, analysing infrastructure build-up in the greater Oslo area indicates that in: “low scenario” 22,000 cars, “base scenario” 55,000 cars, and “high scenario” 110,000 cars will be in 2025, and also 30 HRS are to be built until 2025 [48].

In the fall of 2009, a Memorandum of Understanding (MoU) was signed by nine of the leading car manufacturers confirming that they will be ready to introduce hydrogen powered FCEV in the market from 2015. The Norwegian Klimakur2020 has based on this MoU created a scenario where the FCEV are introduced in Norway on a limited scale from 2016 [45]. In 2020 the market share is estimated at 1.5–2%, rising to 12% in 2030 with a total of 6 500 and 124 000 FCEVs in the fleet in 2020 and 2030 respectively [49].

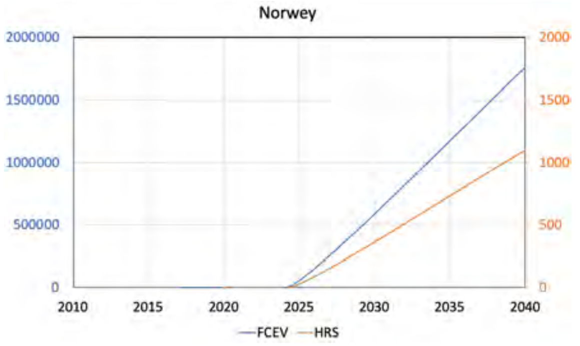

Fig. 6. The number of HRS and FCEVs in Norway (2017–2040)

The Norways study [50] conducted by NTNU (Norwegian University of Science and Technology, located in Trondheim), IFE (Institute for Energy Technology) and SINTEF (largest independent contract research organization in Scandinavia) in 2009, analyses hydrogen production, distribution and refuelling in Norway until 2050. The study concludes that complete national coverage of HRS is deemed attainable by 2040. Hydrogen would be available at 1100 of today's refuelling stations, each serving an average of 1600 vehicles, supplying hydrogen to a total of 1,760,000 vehicle [48].

Summing up in Norway: 2017 (9 HRS, 94 FCEV); 2019 (6 HRS, 149 FCEV); 2020 (3 HRS, 159 FCEV); 2025 (30 HRS, 55 000 FCEV; 2040 (1100 HRS, 1,760,000 FCEV).

United Kingdom

Within the UK H2 Mobility project determined that an initial minimum network of 65 HRS in 2015 in the right locations represents a good balance between consumer benefit and investment return. This network would cover major population centers, and connecting motorways, and roads to enable national mobility. It is based on having a minimum of two HRS per Local Authority District (LAD) in the targeted regions, with 8 km between HRS and within, a 10 minute drive. By 2025, 330 HRS was planned. In 2015–2020 in the UK H2 Mobility scenario amounting to 13,000 vehicles in the first five years, was limited by the cost of buying the vehicles. No subsidy for FCEV purchase or operation has been assumed in the roadmap [51].

At the end of 2017 in UK functioning were only 93 FC vehicles [16]. According to EAFO in UK were 12 refuelling points (HRS) 228 FCEV at the end of 2020 [18]. In the case of the data from Forsschungszentrum Jülich GmbH were 13 HRS (10 public stations) and 168 FCEV (193 FCV) at the end of 2020 [11]. According to IPHE were about 100 FCEV including FCEV with Range Extenders as of Dec. 2018 and 20 FC buses and 13 publically accessible HRS includes both 350 and 700 bar sites. Current status: 168 FC Cars and 1 FC Trucks (updated July 2021) [22].

In 2020, approximately 1000 fuel cell cars and > 30 HRS were expected to be operated in the UK. The expected status in 2025 is > 30,000 FC vehicles (practically, rather 10,000s of affordable FC vehicles on UK roads), > 150 HRS and 10's of OEM (Original Equipment Manufacturer) FCEV models available [52].

The UK H2 Mobility roadmap shows that by 2030:

- FCEVs will be at least cost-competitive with conventional vehicles.
- A network of 1,150 HRS can cover the whole country.
- 1.6 million FCEVs could be on UK roads. The HRS network is past its break-even point.
- Hydrogen production and retailing can be an attractive and profitable business leading to the natural growth of the HRS network as the FCEV fleet grows.
- CO_2 emissions (including fuel production) can be 75% lower for FCEVs than for equivalent diesel vehicles,
- and on a trajectory to zero CO_2 emissions by 2050.
- FCEVs will be on course to reach a 20–50% market share, in line with the Department of Energy and Climate
- Change (DECC) 2050 Pathway Analysis [51].

Hydrogen in United Kingdom is likely to be fundamental to achieving net zero in transport, potentially complementing electrification across modes of transport such as buses, trains and heavy goods vehicles (HGVs).

Transport is also a crucial early market for hydrogen, driving some of the earliest low carbon production in the UK. There are over 300 hydrogen vehicles on UK roads, mostly passenger cars and buses, and the government is supporting hydrogen use in transport with a £23 million Hydrogen for Transport Programme [53].

Approximately two per cent of England's local operator bus fleet is now zero emission – equipped with battery electric or hydrogen fuel cell. Will be implemented the National Bus Strategy and its vision of a green bus revolution, including setting an end date for the sale of new diesel buses and the Zero Emission Bus Regional Areas (ZEBRA) scheme. ZEBRA will provide up to £120 million in 2021/22 to begin delivery of 4,000 new zero emission buses, either hydrogen or battery electric, and the infrastructure needed to support them [53].

Hydrogen is a key strategic component to fully decarbonizing the UK's economy and the UK is well positioned to lead on the production of green hydrogen with significant technical expertise in electrolysers from world leading companies such as ITM Power, and the potential to generate significant quantities of renewable energy from offshore wind [53]. Summing up in United Kingdom: 2017 (18 HRS, 93 FCEV; 2020 (13 HRS, 168 FCEV; 2025 (150 HRS, 10,000 FCEV); 2030 (1150 HRS, 1,600,000 FCEV).

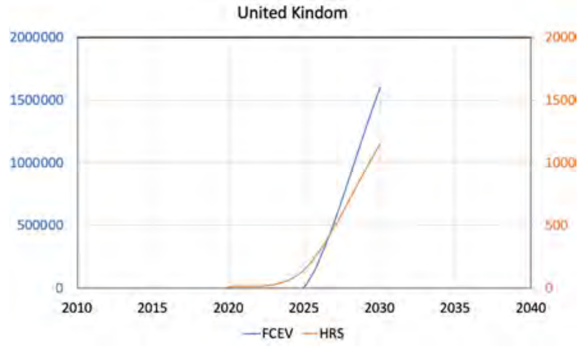

Fig. 7. The number of HRS and FCEVs in United Kindom (2017–2030)

5. Hydrogenization of motor transport in Poland

The territorial accessibility for hydrogen vehicles is determined by the availability of hydrogen refueling infrastructure, in the first place along with the TEN-T network [9, 55].

Within the European Project HIT-2-Corridors, as a result of the verification in Polish conditions, the original method developed for determining the initial location of the hydrogen refuelling station in Poland in the pre-commercial phase (2020–2030), the said location has been indicated along with the order of investment, taking into account above all the freedom to move around Poland of FC vehicles visiting Poland and transiting our country between other EU countries [9, 55].

The methodology developed is of a multi-stage character. Individual steps leading to the designation of the location of hydrogen refueling stations in Poland (as the methodology alone seems to be universal) are as follows:

Stage I: Method allowing to identify regions in which the hydrogen refueling stations should be located in the first place. The parameters considered include among others:

average GDP per capita, average population density (habitants per 100 km²), the number of people living in the largest cities in the region, out of the cities with more 250 thousand inhabitants, average traffic volume of passenger cars on the national roads of international significance running through the region (passenger cars/24 hours).

Stage II: Method allowing to identify urban centres, in which should be located the said stations. The parameters considered include among others: average distance of the cities, over 250 thousand inhabitants, from the place of hydrogen manufacture (acquisition), average distance of the cities, over 250 thousand inhabit-ants from the nearest hydrogen refueling station located outside Poland, number of taxies in the city, number of municipal transport buses.

Stage III: Method for determining the area of the station location [9, 55]. The parameters considered are: results of locating the stations in question obtained in stage I and II, and relying on the results of the measurement of average traffic volume of passenger cars on the roads leading to these cities or on selected road junctions located near these cities, traffic flow intensity of passenger cars was included on the roads leading to the cities listed below.

With the above criteria, the order in the construction of HRS in Poland is as follows: 1 – Poznan, 2 – Warsaw, 3 – Bialystok, 4 – Szczecin, 5 – the Lodz region, 6 – the Tri-City region, 7 – Wroclaw, 8 – the Katowice region, 9 – Krakow. The movement area of cars using fuel cells based on 9 base HRS (in total 30 HRS) situated in the national TEN-T road network by 2030, will cover the territory of Poland. Full commercialization of the hydrogen technology in Poland according to the analyses and studies: the years 2040–2050 respectively: 200–600 HRS, Assumptions: 600 thousand - 2 million cars, 500–-1000 buses, and 100–300 thousand cars transiting Poland annually [9, 55].

According to the e-mobility meter of the Polish Alternative Fuels Association (PSPA), the number of registrations of hydrogen passenger cars in Poland is 59; in the period January – August 2021, it was 58 units [56]. Polsat Group (Plus) alone has equipped itself with a fleet of hydrogen passenger cars (c.a. 50 passenger cars, including most likely 40 Toyota Mirai 2 and 10 Hyundai Nexo). A hydrogen refilling station was also established in Warsaw to supply them with hydrogen [57]. The hydrogen to power these cars will come from the Pątnów-Adamów-Konin Power Plant Complex (ZE PAK) belonging to the Polsat Group (Plus). This team decided to produce hydrogen using electricity obtained from biomass. It aims to produce hydrogen using electrolysers and use it to power buses. The first electrolyser will have a capacity of 2.5 MW, and together with the second, the capacity will increase to 5 MW. This gives 120 MWh of energy consumed per day to produce 2 tonnes of hydrogen or 60 kWh of energy for every kg of hydrogen produced. One electrolyser will generate hydrogen for powering 50 buses per day, and two will power 100 buses per day [58].

The draft Polish Hydrogen Strategy to 2030 with a perspective until 2040 assumes that 100 to 250 new hydrogen buses will be put into operation from 2025. And from 2030, 800 to 1000 new hydrogen buses, including those manufactured in Poland. The said project also assumes the construction of 32 new hydrogen refilling stations and the construction of at least five hydrogen valleys [59].

On May 18, 2021, a letter of intent was signed in Jesionka to create the Podkarpackie Hydrogen Valley [60]. During the Economic Forum in Karpacz this year, a letter of intent was signed regarding the creation of the Lower Silesian Hydrogen Valley [61]. In July this year, the creation of a hydrogen valley in Wielkopolska [62] was also announced. Planning to purchase buses are also Poznań (84 hydrogen buses) and Bielsko-Biała [63].

Hydrogen Eagle is an investment programme of the Orlen Group for the construction of an international network of hydrogen hubs (three in Poland, two in the Czech Republic, one in Slovakia) powered by electricity from renewable energy sources and innovative installations converting municipal waste into zero and low-emission hydrogen. Orlen wants to achieve a hydrogen generation capacity of approximately 50,000 tons per year by 2030. In Włocławek, Trzebinia and Płock, automotive-quality hydrogen production installations are being built, with a target total production capacity of over 1000 kg per hour. The company has launched a tender procedure for the construction of HRS stations located in Poznań and Katowice. Electrolysis installations producing zero-emission hydrogen will be powered by offshore and onshore wind energy and photovoltaics, 54 hydrogen refueling stations for individual, public and freight transport will be built in Poland, and 22 facilities will be built in the Czech Republic and 26 in Slovakia [64]. Orlen will form the Mazovian Hydrogen Valley [65].

At the end of 2018, representatives of Lotos Group announced that the first two hydrogen refueling points would be built in Gdańsk and Warsaw. Both HRS are part of the Pure H2 project, of which 20% is paid for from EU funds, and the entire investment is expected to cost 10 million euros. The Pure H2 project will create three main installations: a hydrogen purification plant to the purity of 99.999 H_2, hydrogen distribution plants, and two abovesaid refueling stations [66].

Last year, Lotos Group signed letters of intent regarding the supply of hydrogen and related refueling infra-structure for city buses with Gdynia, Wejherowo, Tczew and Rzeszów [67].

The most advanced project is Hydra Tank, comprising an experimental hydrogen refueling station. Polish Oil and Gas Company (PGNiG) has already signed a contract with a consortium of Polish- and UK-based companies to design and build the HRS. Slated for launch in 2021, the facility will be located at ul. Prądzyńskiego in the Wola District of Warsaw, in the vicinity of the existing CNG (compressed natural gas) filling station. PGNiG has start-ed investigating the possibility of storing and transmitting hydrogen using the natural gas network. A ‘green hydrogen’ production facility is to be built by the company’s branch in Odolanów under the InGrid – Power to Gas project. It is scheduled to come on stream in 2022. PGNiG intends to use electricity generated by photovoltaic panels for the purpose of the project [67].

6. Conclusions

For the development of FCVs it is necessary, first of all, to develop the HRS infrastructure for refueling them. It happens so in Germany (ranking second in the number of HRS at the end of 2020 in the world), in France (ranking second in Europe), as well as in UK (third place in Europe) but also in other smaller countries of Northwestern Europe i.e. Denmark, the Netherlands or Belgium, but also in Norway, as set out in this article. All these countries have plans for the use of hydrogen, the development of hydrogen vehicle refueling infrastructure and the related development of the hydrogen vehicle fleet. In Northwest Europe, considering the countries mentioned above, are 1 58 HRS in total at the end of 2020, i.e. about 83% HRS in Europe. In the above-mentioned countries of Northwestern Europe, there were also approx. 90% of FCEVs in Europe at the end of 2020. These countries dominate in the hydrogenisation of motor transport in Europe. There is only one HRS in Poland yet (during start-up) and 59 FCEV. Proposed locations of base HRS w Poland: 1 – Poznan, 2 – Warsaw, 3 – Bialystok, 4 – Szczecin, 5 – the Lodz region, 6 – the Tri-City region, 7 – Wroclaw, 8 – the Katowice region, 9 – Krakow, are justified, as indicated by the location plans in relation to HRS stations of the companies operating in the field of transport hydrogenisation.

The conducted analyses indicate that in aspect of the dynamics development of hydrogenisation of motor transport in Northwestern Europe, and in principle in Europe, Germany dominates. In Poland hydrogenisation of motor transport is only just developing. The most important thig is development of the refueling infrastructure for vehicles equipped with fuel cells. It should be developed first along the TEN-T road network running through Poland, as proposed in the article.

Nomenclature

CEP	Clean Energy Partnership
CO_2	Carbon dioxide
FCEV	Fuel Cell Electric Vehicles
FCV	Fuel Cell Vehicles
HDV	Heavy-Duty Vehicles
HRS	Hydrogen Refueling Stations
IEA	International Energy Agency
LCV	Light-Commercial Vehicles
MDV	Medium-Duty Vehicles
MW	Megawatts
PLDV	Passenger Light-Duty Vehicle

Bibliography

[1] Delivering the European Green Deal. European Commission. https://ec.europa.eu/info/strategy/priorities-2019-2024/european-green-deal/delivering-european-green-deal_en

[2] Communication from the Commission to the European Parliament, the Council, the European Economic and Social Committee and the Committee of the Regions. ‘Fit for 55’: delivering the EU’s 2030 Climate Target on the way to climate neutrality. COM (2021) 550 final Brussels, 14.7.2021.

[3] Proposal for a Regulation of the European Parliament and the Council amending regulation (EU) 2019/631 as regards strengthening the CO_2 emission performance standards for new passenger cars and new light commercial vehicles in line with the Union’s increased climate ambition. COM (2021) 556 final, 2021/0197 (COD). Brussels, 14.7.2021.

[4] Communication from the Commission to the European Parliament, the Council, the European Economic and Social Committee and the Committee of the Regions. A hydrogen strategy for a climate-neutral Europe. COM (2020) 301 final. Brussels, 8.7.2020.

[5] Communication from the Commission to the European Parliament, the European Council, the European Economic and Social Committee and the Committee of the Regions. The European Green Deal. COM (2019) 640 final. Brussels, 11 December 2019.

[6] Communication from the Commission to the European Parliament, the European Council, the European Economic and Social Committee and the Committee of the Regions. Europe’s moment: Repair and Prepare for the Next Generation. COM (2020) 456 final. Brussels, 27 May 2020.

[7] Europe's moment: Repair and prepare for the next generation. European Commission. https://ec.europa.eu

[8] Communication from the Commission to the European Parliament, the European Council, the European Economic and Social Committee and the Committee of the Regions. Powering a climate – neutral economy: An EU Strategy for Energy System Integration. COM (2020) 299 final. Brussels. 8.7.2020.

[9] GIS, W., GIS, M. Overview of the method and state of hydrogenization of road transport in the world and the resulting development prospects in Poland. *Open Engineering*. 2021, **11**(1), 570-583. https://doi.org/10.1515/eng-2021-0039

[10] Hydrogen in North-Western Europe. A vision towards 2030. IEA, April 2021.

[11] SAMSUN, R.C., LAURENT, A., REX, M. et al. Deployment status of fuel cell in road transport: 2021 Update. Jülich Forschungszentrum, 2021.

[12] VAN DER LAAK, W., MARTENS, A., NEIS, S. National Implementation Plan Hydrogen Refuelling Infrastrukture Belgium – H2 Mobility Belgium, WaterstofNet, December 2015.

[13] VAN DER LAAK, W. H2 Mobility Belgium. A plan for the development of a hydrogen refuelling infrastructure and implementation of fuel cell electric vehicles in Belgium. www.hyer.eu/wp-content/uploads/2016/04/7–Hydrogen-Road-Tour.pdf

[14] LEMKE, R. Market Introduction of Hydrogen Fuel, Berlin 2016.

[15] Wasserstoff – Spiegel, 1999, **1**.

[16] Closer look at the deployment of fuel cell EVs as of Dec. 2017. https://www.ieafuelcell.com/fileadmin/publications/AFC_TCP_survey_status_FCEV_2017.pdf.

[17] FRANÇOIS, I. National Policy Paper – Belgium. HyLAW Project, Dec. 2018.

[18] European Alternative Fuel Observatory, https://www.eafo/vehicles-and-fleet

[19] National Implementation Plan for Hydrogen Refueling Infrastructure, 3rd final edition, June 2014.

[20] H2Mobilité France, Study for a Fuel Cell Electric Vehicle national deployment plan, Mobilité Hydrogéne France, 2017.
[21] Press Release, 12th Annual assessment of H2 stations by Ludwig-Bölkow-Systemtechnik (LBST), February 19, 2020.
[22] International Partnership for Hydrogen and Fuel Cells in Economy (IPHE), https://www.iphe.net
[23] Développons l'Hydrogéne pour l'économie française, Étude prospective, Associacion française pour l'hydrogéne et les piles á combustible (AFHYPAC), Paris 2018.
[24] Plan de déploiement de l'hydrogéne pour la transition énergétique, Rapport de Ministére de la Transition Écologique et Solidaire, Paris 2018.
[25] Wasserstoff – Spiegel, 1999, **2**.
[26] Annual Report 2015 NOW GmbH.
[27] Annual Report 2018 NOW GmbH.
[28] BONHOF, K., THORSTEN, H., BUTSCH, H. 50 hydrogen refuelling stations in Germany. Within the frame of the National Innovation Programme Hydrogen and Fuel cell Technology, IFP/IEA/ITF Workshop, November 2012.
[29] BUTSCH, H. HRS Infrastructure in Germany and Europe – Current Activities, Washington, June 2014.
[30] Bundesministerium für Verkehr und digitale Infrastruktur: Nationaler Strategierahmen über den Aufbau der Infrastruktur für alternative Kraftstoffe, November 2016.
[31] THORSTEN, H. Deployment of Hydrogen and Fuel Cell Technology in Germany, EHEC, Spain 2018 NOW GmbH.
[32] NITSCH, J. Was dedeutet ein Klima- und was bedeutet ein Energieziel für den Verkehrsector? Zweites Fach-gespräch in Rahmen des Fachdialogs zur Mobilitäts- und Kraftstoff strategie des BMVBS, Berlin, 17 Juli 2012.
[33] BONHOF, K. The renewable and Clean Hydrogen Challenge of Mission Innovation. Hydrogen Ministerial Meeting 23th October, 2018 Tokyo, Japan.
[34] Hydrogen scaling up, A sustainable pathway for the global energy transition, Hydrogen Council, November 2017.
[35] ROBINIUS, M., LINSSEN, J., GRUBE, T. et al. Comparative analysis of infrastructures: hydrogen fueling and electric charging of vehicles, Jürlich Forschungzentrum, Energie & Umwelt/Energy&Environment, Band/Volume 408.
[36] Press Release, 12th Annual assessment of H2stations.org by LBST, 19 February 2020.
[37] WEEDA, M. NIP – NL, Version June 2014. ECN 2014.
[38] WEEDA, M. Economic analysis of HRS network build-up in the Netherlands, Petten, 3 July 2015, ECN-E–15-067.
[39] WEEDA, M. New impetus for hydrogen in the Netherlands, Information Day, Hydrogen Innovation Mission to the Netherlands, Embassy of the Kingdom of the Netherlands, Tokyo, 30 May 2018.
[40] DENCHER, R. Demand gathering & demand creation, Information Day, Hydrogen Innovation Mission to the Netherlands, Embassy of the Kingdom of the Netherlands, Tokyo, 30 May 2018.
[41] GIGLER, J., WEEDA, M. Outlines of a Hydrogen Roadmap. TKI NIEUW GAS, Topsector Energie, May 2018.
[42] VAN WIJK, A. et al. The Green Hydrogen Economy in the Northeern Netherlands, Groningen, the Netherlands October 2017.
[43] Government Strategy on Hydrogen, Ministry of Economic Affairs and Climate policy, 06.04.2020.
[44] The Norwegian Government's hydrogen strategy towards a low emission society. Norwegian Ministry of Petroleum, Norwegian Ministry of Climate and Environment.
[45] The Norwegian hydrogen Guide, https://hydrogen.no
[46] HyNor- project, https://en.wikipedia.org/wiki/HyNor
[47] National Transport Plan 2018-2029. Norwegian Ministry of Transport and Communications.
[48] PÜTZ, K., NØRBECH, T. Background paper for the IFP/IEA/ITF Workshop on "Developing infrastructure for alternative transport fuels and powertrains to 2020/2030/2050: A cross country assessment of early stages of implementation" OECD, 30 November 2012.
[49] Action Plan 2012–2015. Recommendation by the Norwegian Hydrogen Council according to the mandate given by the Ministry of Petroleum and Energy and the Ministry of Transport and Communications.
[50] NTNU, IFE, SINTEF (2009) Recommendations to the Norwegian Government for the implementation of hydrogen as transportation fuel in Norway, available at http://www.ntnu.no/ept/norways
[51] UK H2 Mobility.Phase1Results. April 2013.
[52] HART, D., HOWES, J., MADDEN, B. et al. Hydrogen and Fuel Cells: Opportunities for Growth. A Roadmap for the UK. E4tech and Elementary Energy. November 2016.
[53] UK hydrogen strategy.GOV.UK, 17 August 2021, https://www.gov.uk/government/publications/uk-hydrogen-strategy
[54] Decarbonising Transport. A Better, Greener Britain. Department for Transport, 2021.
[55] GIS, W., MENES, E., WAŚKIEWICZ, J. et al. Circumstances of the national plan for hydrogenization of road transport in Poland. ITS, Warsaw 2015.
[56] Licznik elektromobilności: rozbudowa infrastruktury ładowania w Polsce nabiera tempa, https://pspa.com.pl
[57] KIFER, Ł. Pierwsza stacja tankowania wodoru jest gotowa i prywatna. Telewizja wyprzedziła spółki energetyczne. Jun. 2021, https://moto.pl
[58] Zespół Elektrowni Pątnów-Adamów-Konin będzie wytwarzał wodór z biomasy: 60 kWh na 1 kg gazu. April 2020. https://elektrowoz.pl
[59] Polska Strategia Wodorowa do 2030 r. z perspektywą do 2040 r. – projekt, czerwiec 2021.
[60] Rzeszów sercem „Podkarpackiej Doliny Wodorowej", 18.05.2021, https://www.gov.pl
[61] Premier: Dolnośląska Dolina Wodorowa przyczyni się do rozwoju naszej gospodarki, 9.9.2021, https://www.gov.pl
[62] WOŹNIAK, A. Śląsk wykorzysta wodór dla odchodzenia od węgla. *Rzeczpospolita* 23.8.2021.
[63] WOŹNIAK, A. UE dofinansuje zielony wodór w Polsce. *Rzeczpospolita* 23.8.2021, 29.7.2021.
[64] Grupa Orlen z międzynarodowym programem wodorowym, https://www.orlen.pl
[65] Orlen będzie tworzył Mazowiecką Dolinę Wodorową, 10.9.2021, https://www.bankier.pl
[66] Wodór na stacjach Lotosu od 2021, https://www.lotos.pl
[67] PGNiG launches new hydrogen programm, 12.5.2020, http://en.pgnig.pl

Maciej Gis, DEng. – Environment Protection Centre in Motor Transport Institute.

e-mail: *maciej.gis@its.waw.pl*

Wojciech Gis, DSc., DEng., Prof. ITS – Motor Transport Institute.

e-mail: *wojciech.gis@its.waw.pl*

Article citation info:
SALA, R., KOŁEK, K., KONIOR, W. Methodology of diesel particulate filter testing on test bed for non-road engine application. *Combustion Engines*. 2022, **190**(3), 72-79. https://doi.org/10.19206/CE-142168

Rafał SALA
Kamil KOŁEK
Witold KONIOR

Combustion Engines
Polish Scientific Society of Combustion Engines

Methodology of diesel particulate filter testing on test bed for non-road engine application

ARTICLE INFO

Received: 18 August 2021
Revised: 31 August 2021
Accepted: 12 September 2021
Available online: 20 December 2021

This paper describes the methodology and test results of diesel particulate filter (DPF) functional testing performed on non-road compression ignition engine application installed on test bed. The scope of work included testing of various DPF regeneration strategies, backpressure and balance point tests and emission performance evaluation during a legislative test cycle. The aim of this study was to observe and investigate the influence of raw exhaust gas parameters on DPF functionality in terms of filtration efficiency, soot loading, type and duration of the regeneration and emission performance. Under investigation was the capability of soot burning rate and fuel penalty.

The DPF sample under test was part of the complete exhaust aftertreatment system (ATS) which consisted of: a diesel oxidation catalyst (DOC), a DPF and a selective catalytic reduction system (SCR) with urea dosing and ammonia slip catalyst (ASC). Testing was carried out on a heavy-duty diesel engine installed on a test stand with a dynamic dynamometer and equipped with an emission bench. The test program allowed to assess the engine matching to exhaust aftertreatment system with regard to emissions compliance, in-service operation and necessary engine control unit (ECU) calibration works. The results show the influence of the DPF regeneration strategy on its duration and on the soot mass burn rate. Passive DPF regeneration was a favorable mode of DPF cleaning, due to lack of fuel penalty and lower aging impact on the entire ATS. Optimization of soot flow rate, exhaust gas temperature and the chemistry of the DOC/DPF was further recommended to ensure the long-term durability of the entire system.

Key words: *exhaust aftertreatment, diesel particulate filter, soot oxidation, passive regeneration, emission*

1. Introduction

Registrations of new heavy duty vehicles with diesel engines remain dominant in terms of market share in EU in 2020 and amount to more than 96% [1]. The adverse effect of exhaust emissions on human health and the environment [2, 3] have forced EU institutions to act ever stricter towards the zero-emission, carbon neutral driveline solutions. Under the tightening regulatory framework, vehicle manufacturers introduce advanced and highly efficient exhaust aftertreatment techniques adapted to various diesel engine applications. The regular approach for NO_x reduction relies on utilization of high/low pressure exhaust gas recirculation (EGR) systems at the expense of increased emission of particulate matter, which is afterwards trapped and removed by a DPF filter. Different DPF configurations are available [4, 5], but wall-flow type filters are the most widely used. Wall-flow filters are honey-comb monoliths with parallel channels plugged alternately at each end to force the exhaust gas to pass through the porous filter wall, where soot is retained. Therefore, the exhaust backpressure increases in the exhaust line, penalizing fuel consumption, but the high filtering efficiency (in excess of 90%) makes DPF filters essential for complying with emission standards. Notably, the fuel economy penalty of DPF in heavy-duty vehicle can minimalized by the optimization of filter implementation. The experimental study of in-service operation of urban buses and intercity coaches reported as low fuel economy penalty as 0.6–1.8% [6]. When the soot accumulated reaches a threshold, fuel post-injections are commenced to increase periodically the exhaust gas temperature up to 650°C and to oxidize the soot collected inside the filter (active regeneration). DPF systems are designed to regenerate also continuously during the regular operation of the engine (passive regeneration), where the source of heat is the exhaust gas stream itself. This type of filter usually incorporates a form of catalysts to lower the soot oxidation temperature. Apart from temperature, other factors such as the exhaust gas (composition, flow rate) and the physicochemical properties of soot affect the regeneration process.

In the present work, a dedicated DPF sample was installed on a Euro VI diesel engine and tested on an engine dyno under transient and steady-state operating conditions. The test results obtained allowed evaluations of the filter functionality and its matching with a non-road engine application, under various work modes. The DPF was evaluated as part of the entire exhaust line, to ensure the required reliability, trouble free operation and compliance with emission standards.

2. Test method and facilities

2.1. Unit under test

The DPF under test was a part of complete ATS including a DOC (upstream DPF) and an SCR system with an ASC converter (downstream DPF). The filter substrate was of ceramic structure, coated with catalytic layer to enhance passive regeneration. The basic DPF parameters are shown in Table 1.

Table 1. Parameters of DPF under test

Parameter	Value
Volume	4.2 dm^3
Cell density	350 cpsi
Relative concentration of PGM	5 g/ft^3

For the test activities, a heavy duty diesel engine was used with the maximum power of 150 kW and peak torque of 650 Nm. The engine featured a common rail type, direct injection fuel system and was equipped with an open ECU and ETAS/INCA interface that allowed the ECU calibration to be modified for specific test purposes.

2.2. Test bed instrumentation

The engine with ATS were installed on an engine test bed equipped with AVL Fully Dynamic AC Dyno (APA 204/E) of max. power of 220 kW and max. torque of 934 Nm. The test bed automation system was the AVL Puma Open 1.5.3 with iGEM 1.5 package, capable of automatically executing the NRSC and NRTC legislative cycles and following the requirements of ECE Reg. 49 with corresponding EU, ISO and EPA directives.

Testing of various regeneration strategies required engine calibration adjustment; therefore, an external ECU interface ETAS and INCA 7.2 were used. Stable and repeatable DPF temperature at a given setpoint value was achieved by continuous adjustment of the ECU parameters, mainly the timing of fuel post injection and the fuel quantity expressed in mg/stroke.

Emission analysis was carried out by the raw/undiluted exhaust gas measurement method. The exhaust gas flow was calculated based on measurement from an air flow meter and a fuel meter. For the purposes of the study, three emission sampling points were installed on the exhaust line. The first sampling point was placed at the engine outlet; the second one was located downstream of the DOC and before the DPF; the third emission port was positioned downstream of the DPF, before the SCR catalyst.

Additionally, for analysis and monitoring purposes, temperature and pressure sensors were installed at each sampling point on the exhaust line.

An overview of engine and exhaust system layout on test bed is shown in Fig. 1.

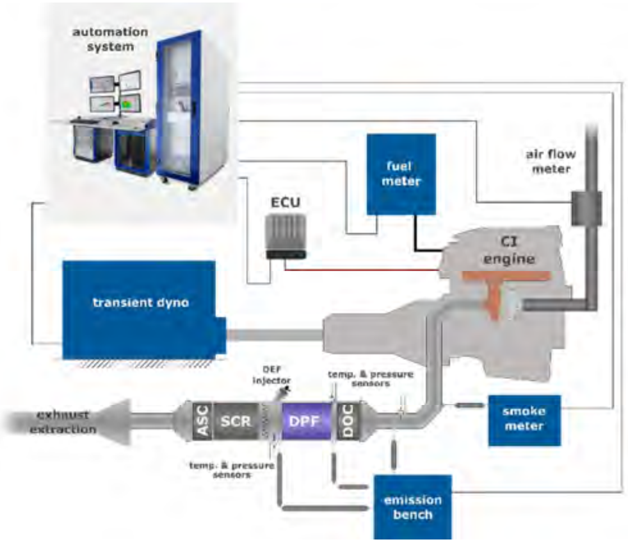

Fig. 1. Engine and exhaust system layout on test bed

The emission bench used was an AVL AMA i60 device equipped with a set of specific gas analyzers with the measuring ranges shown in Table 2. Additionally, for measurement of particulate, an AVL micro soot sensor and an AVL smoke meter were installed on the exhaust line.

Table 2. Emission analyzers ranges

Analyzer (principle of operation)	Range of measurement	
	Low	High
CO_2 (NDIR)	0–0.5%	0–20%
CO (NDIR)	0–50 ppm	0–5000 ppm
O_2 (PMD)	0–1%	0–25%
NO_x (CLD)	0–10 ppm	0–10000 ppm
NO (CLD)	0–10 ppm	0–10000 ppm
THC (FID)	0–300 ppm C1	0–60000 ppm C1
CH_4 (FID)	0–30 ppm C1	0–20000 ppm C1

2.3. Test method

The DPF functionality and characteristic were evaluated under the following test procedures:

- NRSC – Non Road Stationary Cycle,

is the name of ISO 8178 homologation stationary test cycle used for emission certification and/or type approval testing for non-road engine applications. The NRSC starts with hot engine conditions and represents a sequence of several steady-state modes with different weighting factors [7–10].

- NRTC – Non Road Transient Cycle is a transient driving cycle for mobile non-road diesel engines. The test is used internationally for emission certification and/or type approval process. The normalized engine speed and torque during the NRTC test are shown in Fig. 2.

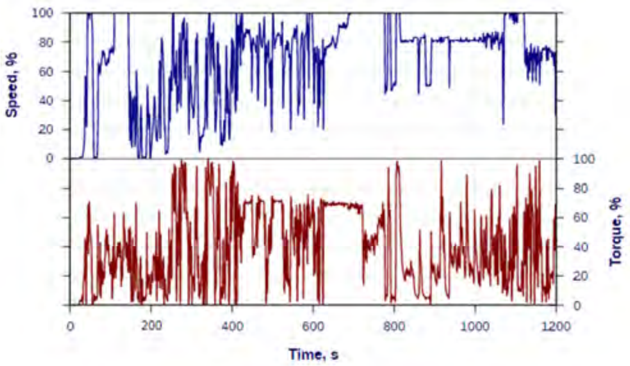

Fig. 2. Normalized speed and torque over NRTC cycle [10]

The NRTC is run twice, from a cold and a hot start, with a 20-minute soak period between the tests. The cold start weighting factors are 10% in the EU and 5% in the United States.

- Balance point test of the DOC–DPF system. The balance point test allows determination of the particle matter (PM) oxidation capability in the filter during normal engine operation – i.e., without fuel post injection used for active filter regeneration. This type of PM oxidation is referred to as passive filter regeneration. The balance point of a given DPF is understood as the lowest exhaust gas temperature at which the gas pressure drop across the filter remains constant over the time. This means that at the balance point conditions, the rate of passive regeneration of the filter is in equilibrium with the rate of PM inlet flow to the filter.

In the case of a steadily increasing DPF pressure drop, the filter is at an unfavorable operating point, as the exhaust temperature is too low for passive regeneration to occur efficiently and thus the soot loading in the DPF increases. Finally, the case of a steadily decreasing DPF pressure drop signifies that the temperature of the filter allows the soot to oxidize at a greater rate than that at which it continually accumulates in the filter. Passive filter regeneration at the lowest possible gas temperature is of key importance to reducing the number of active regeneration events, thus to limiting the fuel penalty, thermal stress and aging of the exhaust system and the dilution of lubrication oil. The last point occurs if fuel post injection is used during the exhaust stroke in order to heat up the exhaust.

The regeneration of diesel particulate filters involves the oxidation of solid particulates to gaseous products, preferably to carbon dioxide (CO_2). Depending on the DPF system design and on the engine operating conditions, the oxidation of carbon in diesel soot can occur via reactions with O_2 or nitrogen dioxide (NO_2). Oxygen is present in diesel exhaust at sufficient concentrations under nearly all operating conditions. However, relatively high temperatures are necessary to achieve sufficient regeneration rates with O_2.

The rate of soot oxidation can be increased, and the regeneration temperature decreased, if an oxidant more active than oxygen could be introduced to the particulate filter. It was found that nitrogen dioxide can oxidize diesel particulate at higher rates than oxygen [11]. Carbon in diesel soot is oxidized by oxygen with noticeable reaction rates at temperatures above 550°C. With NO_2, the process occurs at temperatures as low as 250°C, as illustrated in Fig. 3 [12].

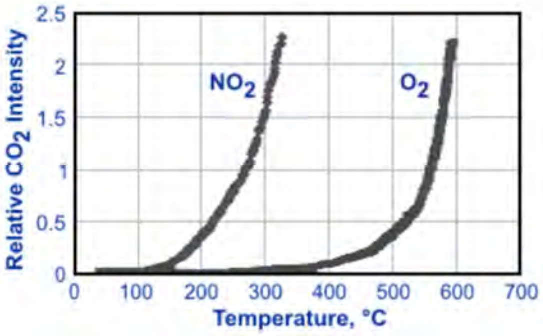

Fig. 3. Oxidation of PM by oxygen and nitrogen dioxide [13]

The presence of NO_2 in exhaust gas is essential for an efficient passive regeneration process therefore, the NO_2 concentration must be increased. The NO_2 formation is realized by catalytic oxidation of NO to NO_2 in the DOC placed upstream of the DPF. The DOC does not reduce the total NO_x concentration in the exhaust gas, but increases the NO_2/NO_x ratio. Oxidation of soot by NO_2 is the dominant mechanism of passive DPF regeneration.

- Filter pressure drop test

The test was run to determine the pressure drop curve and thus the exhaust flow resistance across the combined DOC and DPF converters. The pressure drop test was performed for the clean exhaust system condition, which was achieved by performing the active regeneration procedure and a preconditioning step at engine full load conditions. The test was composed of steady state engine running points with stepwise increased exhaust mass flow rate, recorded as a function of DOC–DPF system pressure drop. This type of test can be also used for comparison purposes between competitive systems' solutions.

- Filter loading and regeneration test

The test aimed at evaluation of filter regeneration efficiency and consisted of two phases: the filter soot loading and the regeneration phase. The filter loading method was elaborated to ensure sufficiently fast DPF loading with soot to reach the target amount. The optimal soot loading point was characterized by three features:

- high engine out soot emission,
- high exhaust gas flow,
- low exhaust gas temperature (to limit filter passive regeneration).

To set the optimal engine operating point, several trial measurements on various engine speed and load condition were carried out. Due to the fact that particulate matter deriving from the combustion process are composed mainly of elementary carbon (C), known as "black soot", the soot loading and C value on each measured point were calculated according to Equations 1 and 2 [14], respectively:

$$\text{Soot loading} = \frac{C}{\rho_{exh}} \cdot G_{exh}\ [\text{g/h}] \tag{1}$$

$$C = \frac{1}{0.405} \cdot 4.95 \cdot FSN \cdot e^{(0.38 \cdot FSN)}\ [\text{mg/m}^3] \tag{2}$$

where: G_{exh}– exhaust mass flow, ρ_{exh} – exhaust density, FSN – filter smoke number.

The composition of the PM from diesel combustion is shown schematically in Fig. 4.

Fig. 4. Composition of PM [15]

Each time before the soot loading phase commenced, the filter was cleaned up by passive regeneration with high gas temperature conditions. The filter was then weighed in its warm condition to establish the zero soot mass level. The duration of the soot loading phase depended on the desired soot level in the filter. The filter loading was followed by DPF weighing in its warm condition to define the actual amount of PM collected inside the filter.

The second phase was the filter regeneration with different strategies. Both active and passive regenerations were tested, with various combinations of exhaust gas temperature and regeneration durations.

After each regeneration during the second phase, the DPF was weighed in its warm condition to define the amount of oxidized PM.

3. Test results and discussion

3.1. NRSC test results

The purpose of NRSC test run to assess the overall emission performance of engine and exhaust system. Fig. 5 presents engine speed, torque profiles and regulated gaseous emissions measured at the DPF outlet. The CO and HC values remained at very low levels of up to 10 ppm, although single emission spikes were recorded. In contrast, the NO_x concentration ranged between 150–1400 ppm, but notably those values were measured upstream of the SCR system.

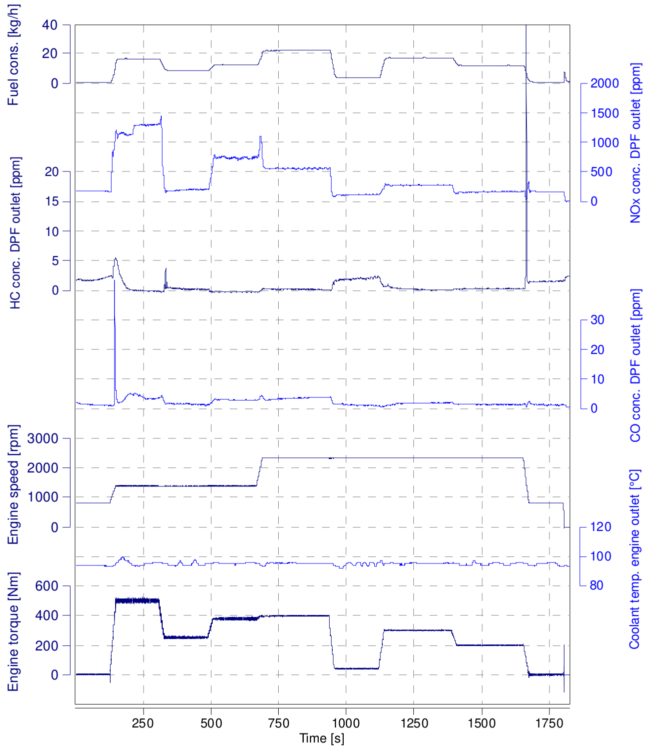

Fig. 5. NRSC test profile

The NRSC cycle lasted 1800s and consisted of 9 operating modes, calculated on the basis of a dynamic full load curve run on the engine. The operating modes cover a wide range of the in-field engine operation area at steady-state conditions.

3.2. NRTC test results

Subsequently, the emission behavior was evaluated for transient conditions under the cold/hot NRTC test. The cold NRTC phase of was started at an engine coolant temperature of 23°C; the test profile is illustrated in Fig. 6. Increased HC and CO concentration was measured over the first ca. 100 s, corresponding to the time period necessary for the DOC to achieve its light-off temperature. Until engine warm up to working temperature single spikes in CO concentrations were spotted. Similarly to the NRSC run, the NO_x measurement took place upstream of the SCR – and therefore the NO_x concentration remained high throughout the test.

Although the reduction rate of the total NO_x concentration in the DOC-DPF system was found to be negligible, it influenced the NO_x composition in terms of the NO_2 share. The NO_2 concentration at the engine outlet and DPF inlet locations are compared in Fig. 7.

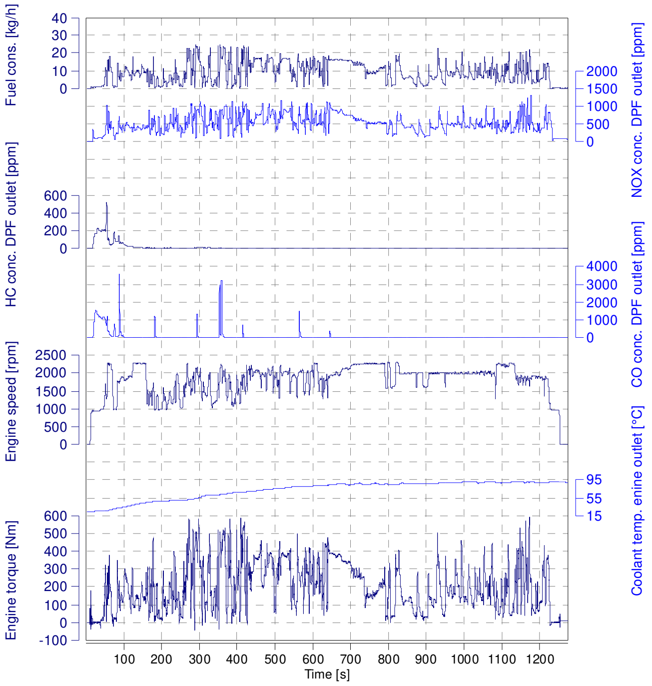

Fig. 6. NRTC test profile – cold phase

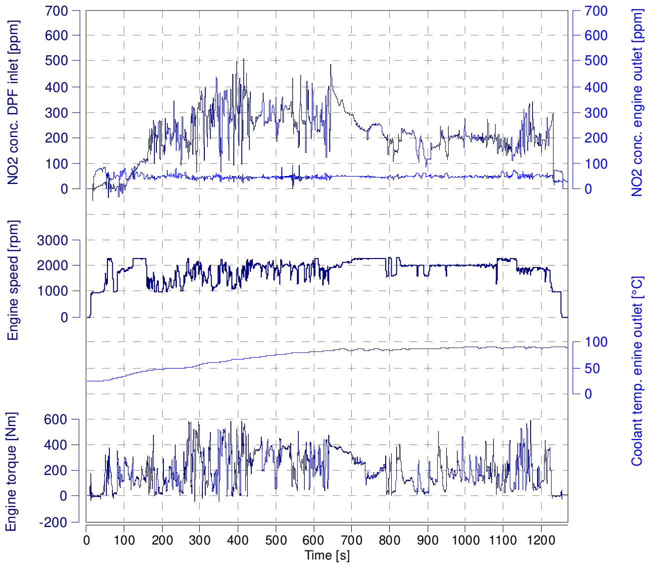

Fig. 7. NO_2 concentrations measured during the NRTC cold cycle

The engine outlet NO_2 values oscillated around 40–70 ppm, whereas downstream of the DOC (DPF inlet), the NO_2 reached a level of 100–500 ppm, depending on the engine operating point. An exception was noted during the first 130s of the test run, in which the engine outlet NO_2 level is greater than the DPF inlet one. Such behavior can be observed until the converter's light-off temperature is reached. The presence of NO_2 in exhaust gas is key for effective execution of passive regeneration. To assess the magnitude of DPF loading under transient operating conditions, continuous measurement of the soot concentration at the engine-out position was carried out.

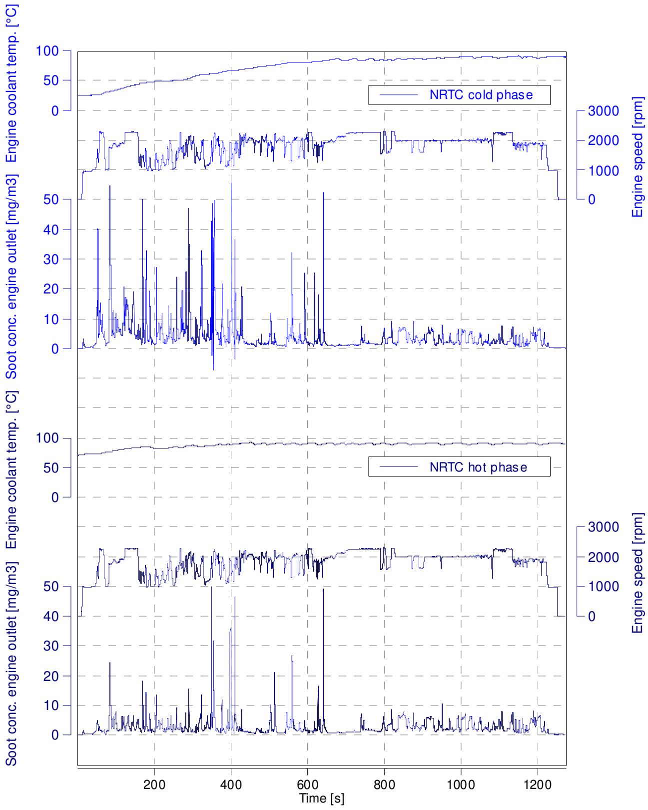

Fig. 8. Soot concentration measurement during the NRTC cold and hot cycles

Figure 8 shows the trace of soot concentration during the cold and hot phases of the NRTC test. An increased level of soot concentration was observed during the first 400 seconds of the cold NRTC phase. After the engine warm up to ca. 70°C coolant temperature, the soot concentration in both the cold and hot phases remained comparable.

3.3. Balance point test

The balance point test was performed on the DOC-DPF system only. The test consisted of 9 steady-state engine operating points, with each lasting approx. 20 minutes. The engine speed was fixed at one set value, while the engine load was varied so as to achieve a stepwise increase of gas temperature of 25–30°C for each successive test step.

The filter equilibrium between soot loading and soot oxidation was found at ca. 330°C, as marked by the cursor position in Fig. 9. This corresponded to a pressure drop across the DOC–DPF system of around 115 mbar, a value specific for that exhaust system layout.

The engine operation below an exhaust temperature of 330°C resulted in a steady increase in filter pressure drop, thus leading to the filter filling up with particulate and eventually clogging. To prevent such a situation during in-field operation, the active filter regeneration strategy needs to be implemented within the ECU.

On the other hand, in the case of exhaust gas temperatures greater than 330°C, the filter pressure drop decreased over time, thereby ensuring trouble-free operation considering steady-state operation.

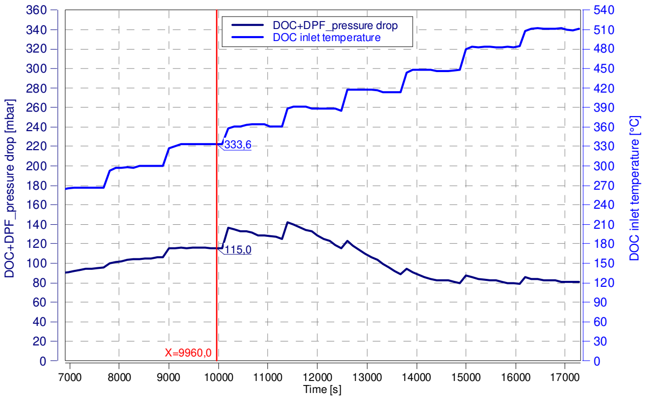

Fig. 9. DOC-DPF balance point test results

Short events of filter pressure drop increases were related to the transitions between test steps. Above a DOC inlet temperature of 360°C, the filter's capability for passive regeneration further increased, to levels significantly exceeding the rate of soot input into the filter. A strong decrease in filter pressure drop was observed until the DOC–DPF system had been completely cleaned up.

3.4. Pressure drop test

The DOC-DPF system was characterized by the measurement of the pressure drop curve that was plotted as a function of the exhaust mass flow rate. The pressure drop test lasted 15 minutes and aimed at evaluation of the gas flow resistance of the system. The test was run twice: at the beginning (SOT) and at the end (EOT) of the entire test program.

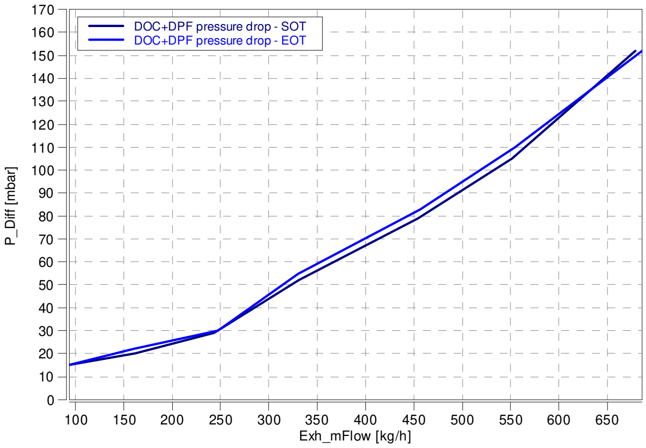

Fig. 10. DOC-DPF pressure drop test results

To determine the pressure drop curve, the test was started in the cleaned-up condition, after performing an active filter regeneration event. Measured test results are shown in Fig. 10. The maximum DOC–DPF delta pressure reached the value of ca. 150 mbar at the highest gas flow rate of 700 kg/h. The curve got steeper in shape after passing the point of 250 kg/h of gas flow.

Pressure drop tests run at SOT and EOT did not revealed any physical damages in the system that may occurred throughout the test program.

3.5. Filter loading and passive regeneration

3.5.1. Filter loading

The filter soot loading phase was performed in the steady-state conditions with limited the occurrence of passive regeneration. The filter inlet temperature was set to not exceed the 290°C, so below the balance point temperature.

The target amount of soot to be collected inside the DPF was 20 g and the length of loading time was calculated on the basis of the smoke value and Equations 1 and 2. The real mass of the soot accumulated inside the DPF was determined by periodical filter deinstallation from the exhaust line and weighing on a balance under defined (hot) conditions. Figure 11 presents the DPF delta pressure curve during the test.

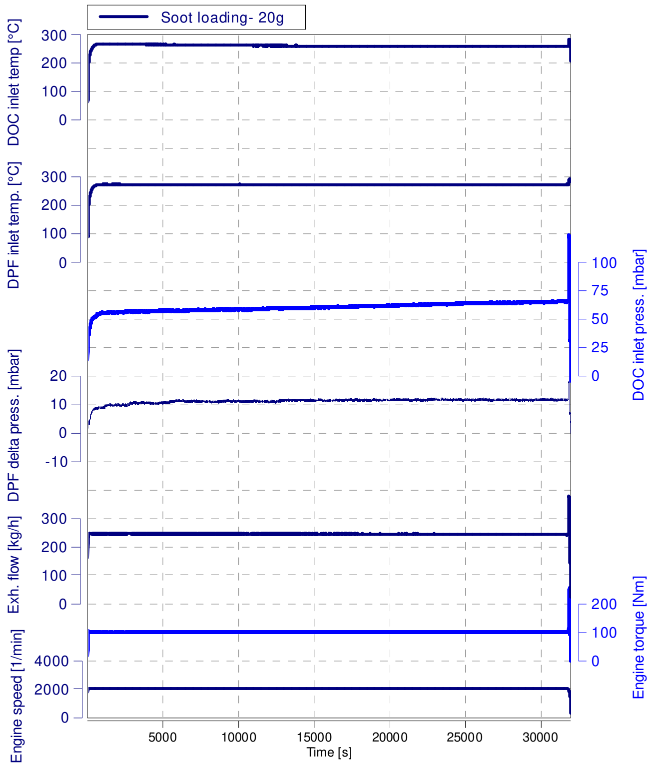

Fig. 11. Filter loading phase for passive regeneration

The test parameters related to engine operation, such as engine speed, torque and outlet gas temperature remained stable over time.

3.5.2. Passive filter regeneration

Following the filter loading phase to reach the target soot mass, passive filter regeneration was initialized. The engine operating point was changed to run at high output in order to achieve a gas temperature of 400°C (measured at the DPF inlet). The fuel post injection was not activated in this scenario. Figure12 illustrates the tendency of decreasing DOC inlet gas pressure and, at the same time, only a slight impact of passive regeneration on the DPF pressure drop.

The passive regeneration lasted until the amount of soot mass accumulated in the loading phase was completely burned out. Subsequently, the DPF was weighed and the soot burning efficiency was assessed.

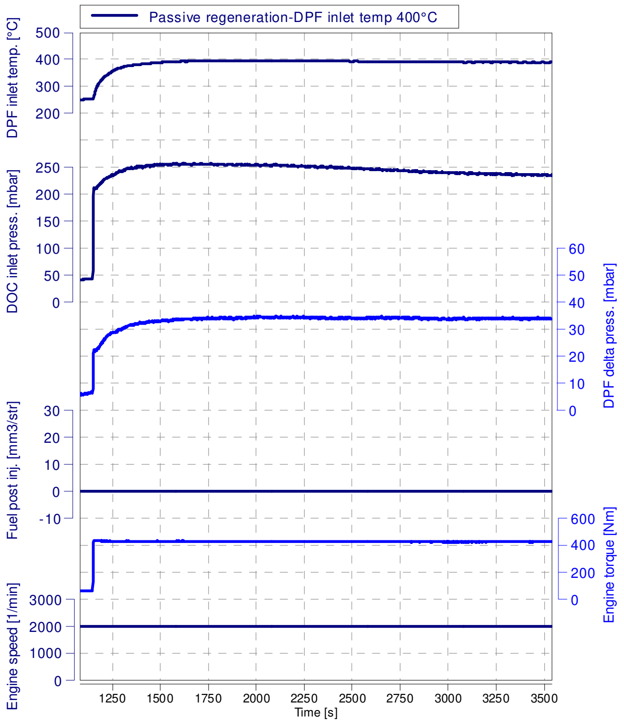

Fig. 12. Passive regeneration of the filter

3.6. Filter loading and active regeneration

3.6.1. Filter loading

The filter loading for the active regeneration event was performed in a similar way as for the passive one. The only difference in the loading procedure was that the target soot mass was increased to 40 g. This greater level of soot accumulation was achieved by extending the duration of loading phase. The inlet DOC and delta DPF pressure curves are shown in Fig. 13.

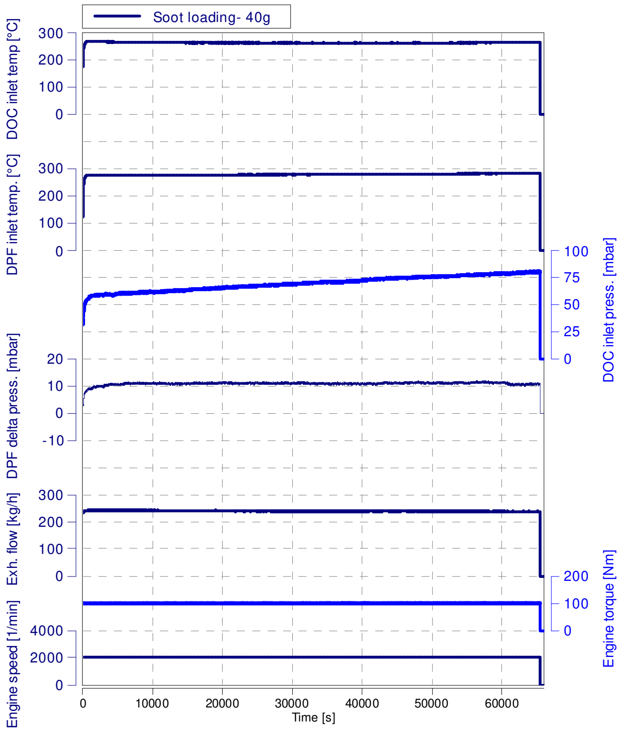

Fig. 13. Filter loading phase for active regeneration

3.6.2. Active filter regeneration

The active filter regeneration was run at 600°C gas temperature (measured at the DPF inlet; Fig. 14).

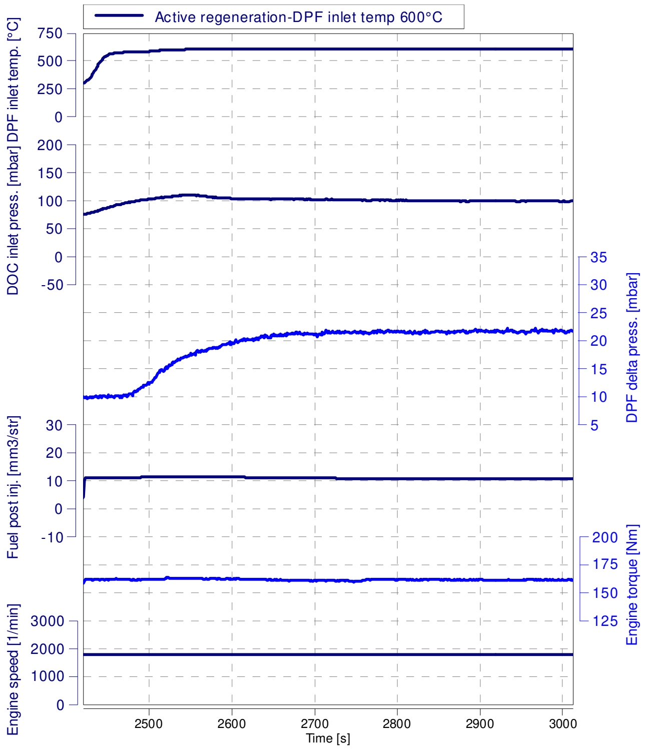

Fig. 14. Active filter regeneration

Elevated gas temperature was achieved by fuel post injection, with the quantity controlled by the ECU via ETAS/INCA interface. The regeneration event lasted ca. 600 s, which was found to be sufficient to fully oxidase the accumulated soot. Subsequently, the DPF was weighed and the soot burning efficiency was assessed.

4. Conclusion

This paper presents a methodology for diesel particulate filter testing performed on an engine dynamometer. The research work conducted provided background information on filter performance in terms of soot loading characteristics and the capabilities of soot oxidation under passive or active regeneration events. The filter was coupled with DOC converter installed in the upstream position. As a DOC–DPF system, it was characterized for emission performance including NO_2 formation, gas flow resistance and the equilibrium gas temperature that allowed safe engine operation without the necessity of triggering active filter regeneration.

For the overall engine and aftertreatment system evaluation, the NRTC and NRSC legislative cycles were performed.

The examples of filter soot loading and regeneration process were presented for engine testing laboratory conditions.

Close analysis of the exhaust system parameters under operation on a test bench is necessary to understand and predict the system behavior during in-field operation of the vehicle or machinery. It allowed to control the system functionality in an effective way, avoiding any malfunctions caused by gas temperature exceedances or filter clogging.

Nomenclature

ASC	ammonia slip catalyst
ATS	aftertreatment system
CI	compression ignition
CLD	chemiluminescence detector
CO	carbon oxide
CPSI	cells per square inch
DI	direct injection
DOC	diesel oxidation catalyst
DPF	diesel particulate filter
ECU	engine control unit
HC	hydrocarbons
FID	flame ionization detector
FSN	filter smoke number
ISO	International Organization for Standardization
NDIR	nondispersive infrared
NO_x	nitrogen oxides
NO	nitrogen oxide
NO_2	nitrogen dioxide
NRSC	Non-Road Stationary Cycle
NRTC	Non-Road Transient Cycle
PGM	Platinum Group Metals
PM	particulate matter
PMD	paramagnetic detection
ppm	parts per million
SCR	Selective Catalytic Reduction

Bibliography

[1] EUROPEAN AUTOMOBILE MANUFACTURERS ASSOCIATION, ACEA. Medium and heavy trucks over 3.5 t new registrations by fuel type in the European Union. 2020:https://www.acea.auto/files/ACEA_trucks_by_fuel_type_full-year-2020.pdf (accessed on 06.2021).

[2] GOYAL, P., JAISWAL, N., KUMAR, A. et al. Air quality impact assessment of NO_x and PM due to diesel vehicles in Delhi. *Transportation Research Part D: Transport and Environment*. 2010, **15**(5), 298-303. https://doi.org/10.1016/j.trd.2010.03.002

[3] POURAZAR, J., FREW, A.J., BLOMBERG, A. et al. Diesel exhaust exposure enhances the expression of IL-13 in the bronchial epithelium of healthy subjects. *Respiratory Medicine*. 2004, **98**(9), 821-825. https://doi.org/10.1016/j.rmed.2004.02.025

[4] NEEFT, J.P.A., MAKKEE, M., MOULIJN, J.A. Diesel particulate emission control. *Fuel Processing Technology.* 1996, **47**(1), 1-69. https://doi.org/10.1016/0378-3820(96)01002-8

[5] FINO, D., SPECCHIA, V. Open issues in oxidative catalysis for diesel particulate abatement. *Powder Technology*. 2008, **180**(1-2), 64-73. https://doi.org/10.1016/j.powtec.2007.03.021

[6] FLEISCHMAN, R., AMIEL, R., CZERWINSKI, J. et al. Buses retrofitting with diesel particle filters: Real-world fuel economy and roadworthiness test considerations. *Journal of Environmental Sciences*. 2018, **67**, 273-286, https://doi.org/10.1016/j.jes.2017.09.011

[7] ISO 8178. Reciprocating Internal Combustion Engines. Exhaust Emission Measurement.

[8] KOTUS, M., PEXA, M., KUBÍN, K. Modelling of non-road transient cycle – comparison of three tractors. *Journal of Central European Agriculture*. 2013, **14**(4), 1281-1294. https://doi.org/10.5513/JCEA01/14.4.1344

[9] WORLDWIDE EMISSIONS STANDARDS. On and off-highway commercial vehicles. Delphi Technologies. 2018/2019.

[10] DIESELNET. https://dieselnet.com (accessed on 08.2021).

[11] COOPER, B.J., THOSS J.E. Role of NO in diesel particulate emission control. *SAE Technical Paper* 890404. 1989. https://doi.org/10.4271/890404

[12] ALLANSSON, R., BLAKEMAN, P.G., COOPER, B.J. et al. Optimising the low temperature performance and regeneration efficiency of the continuously regenerating diesel particulate filter (CR-DPF) system. *SAE Technical Paper* 2002-01-0428. 2002. https://doi.org/10.4271/2002-01-0428

[13] MAJEWSKI, W.A. Diesel filter regeneration. https://dieselnet.com (accessed on 08.2021).

[14] NORTHROP, W.F., BOHAC, S.V., CHIN, J-Y. et al. Comparison of filter smoke number and elemental carbon mass from partially premixed low temperature combustion in a direct-injection diesel engine. *Journal of Engineering for Gas Turbines and Power*. 2011, **133**(10), 102804. https://doi.org/10.1115/1.4002918

[15] Smoke value measurement with the filter-paper-method. *AVL Application Notes*. 2005, AT1007E, Rev. 02.

Rafał Sala, DEng. – Engine Research Department, BOSMAL Automotive Research and Development Institute Ltd, Poland.

e-mail: *rafal.sala@bosmal.com.pl*

Witold Konior – Engine Research Department, BOSMAL Automotive Research and Development Institute Ltd, Poland.

e-mail: *witold.konior@bosmal.com.pl*

Kamil Kołek – Engine Research Department, BOSMAL Automotive Research and Development Institute Ltd, Poland.

e-mail: *kamil.kolek@bosmal.com.pl*

Article citation info:
FAR, M., GALLAS, D., URBAŃSKI , P. et al. Modern combustion-electric PowerPack drive system design solutions for a hybrid two-unit rail vehicle. *Combustion Engines*. 2022, **190**(3), 80-87. https://doi.org/10.19206/CE-144724

Mariusz FAR
Dawid GALLAS
Patryk URBAŃSKI
Aleksandra WOCH
Kuba MIEŻOWIEC

Combustion Engines
Polish Scientific Society of Combustion Engines

Modern combustion-electric PowerPack drive system design solutions for a hybrid two-unit rail vehicle

ARTICLE INFO

Received: 29 October 2021
Revised: 24 November 2021
Accepted: 9 December 2021
Available online: 27 December 2021

The article presents an innovative solution of a two-unit rail vehicle system for passanger transport with a dual-drive, diesel engine and electric motor. The vehicle was designed as a combination of two units, one dedicated to each of the two drive systems, where one unit provides electric drive while the other a combustion engine. The selection of engine and drive components was presented along with the aftertreatment systems used in the design. The provided solution was created in response to the dynamic needs of rail vehicle operators in the European Union who aim to reduce exhaust emissions without compomising the reach of the existing rail networks.

Key words: *rail vehicles, combustion-electric drive, PowerPack, hybrid drive, dual-drive railbus*

1. Introduction

The ongoing global efforts to reduce the emissions of toxic and harmful compounds to the atmosphere resulted in a push towards new and innovative transport solutions. Transport as a branch of industry in 2016 contributed 30% of the total emissions of CO_2 in the EU. Of which as much as 72% was generated by road vehicles, with rail vehicles contributing merely 0.5% [9]. This, however, means that out of the total 4432 million tons of CO_2 equivalent emitted, in that year the transport sector contributed 1330 million tons, with road transport adding 957 million tons and rail transport adding about 6.65 million tons. Due to the clear dominance of road transport new and increasingly more strict regulations on exhaust emissions from road vehicles have been continuously introduced throughout the EU. These efforts culminated in new measurement methods and very stringent requirements to be met by all newly produced engines. This, however, resulted in many other forms of transport being left behind, and not receiving much legislative pressure to increase efficiency and innovate. Hence the development of new drive and propulsion technologies for rail vehicles has been slow, only recently resulting in some significant technological innovations, even though those are not yet ready for full commercial use.

One of the main aspects impacting rail vehicle operations, emissions, and applicability is the rail infrastructure. The simplest available solution to reduce exhaust emissions of CO_2 from rail transport is switching to electric vehicles. This, however, is only possible for lines and routes that are fully electrified on all sections. Since the costs of electrification and maintenance of rail infrastructure are relatively high, levels of rail lines electrification in the EU vary greatly between member countries. While Switzerland has electrified all of its railway lines the EU-28 average in 2018 was only 54%, where Poland was slightly above that average at 64%. Due to the limited levels of railway lines electrification rail vehicles and locomotives with combustion engines remain necessary [1, 19]. This, however, might change, as new technologies and drive system solutions become more prevalent.

Aside from the newest technologies in rail propulsion systems, such as hydrogen fuel cells [7], most working solutions that can avoid the problems resulting from non-electrified railways, while still reducing CO_2 emissions, include some form of drive hybridization [5, 10]. This means combining a conventional diesel engine system with an electric drive system [3], preferably along with some energy storage and recovery capabilities [4]. Hybrid drives are a proven solution with a long history of use, especially in road vehicles, and clear advantages. Their use in rail vehicles is sometimes made difficult due to the space limitations. The article presents a new solution two-unit hybrid drive solution for passenger rail vehicles, designed by the Łukasiewicz Research Network's Rail Vehicles Institute "TABOR" as a modern solution to the problem of insufficient railway electrification. A design using two opposing combustion engines with generators was discussed and presented along with the drive system components and subcomponents, including the exhaust emissions aftertreatment systems for the equipped combustion engines.

2. Internal combustion vehicle standards

2.1. European standards

The source of energy in modular drive systems is an internal combustion engine in most cases, which, due to its nature of operation, emits harmful substances into the atmosphere resulting from the fuel combustion process [6, 15, 16, 21, 22]. In order to reduce the environmental impact of vehicles equipped with internal combustion engines, exhaust emission limits were introduced. Currently, these standards are becoming increasingly more restrictive, forcing producers to use advanced technologies that reduce the engine emissions. The permissible values along with the measurement methods and procedures were defined that varied depending on the vehicle type, its technical parameters, and the country for which it was being approved.

European regulations apply in the European Union and the European Economic Area. The Euro exhaust emission standards (labeled from 1 to 6) introduce limits for PC (*Passenger Car*) and LDV (*Light Duty Vehicle*) vehicle types and distinguish between two types of ignition, i.e. spark-ignition and compression-ignition, as well as the type of fuel used. Normative documents relating to compression ignition engines have more restrictive limit values for carbon monoxide CO and nitrogen oxides NO_x compared to spark ignition engines, which is dictated by the nature of their operation. In addition, compression ignition engines from Euro 1 require compliance with the particulate matter exhaust emission limits (for spark ignition engines this was added along with the Euro 5 standards). The latest regulations also enforce a control test of the particle number generated in operation. From Euro 6c, exhaust emissions are tested on the basis of the WLTC (*Worldwide Harmonized Light Vehicles Test Cycle*) test, replacing the previous NEDC (*New European Driving Cycle*) test. Currently, laboratory tests are supplemented by tests in real operating conditions (*Real Driving Emissions* – RDE) performed with the use of portable measuring equipment belonging to the PEMS (*Portable Emissions Measurement System*) category (Fig. 1).

Fig. 1. Example of a PEMS device – SEMTECH DS [17]

European regulations for HDVs (*Heavy Duty Vehicles*) are included in Euro I-VI standards. The Euro VI standard introduced an emission measurement procedure carried out using the WHSC (*World Harmonized Stationary Cycle)* and WHTC (*World Harmonized Transient Cycle)* tests. These tests are standardized test procedures for the European Union, the United States, Japan and Australia. The last normative document (Euro VI) also changed the regulations regarding the control of conformity in operation. Also in the case of heavy vehicles, tests are currently required in real road conditions measured using PEMS type equipment.

The exhaust emission standards also apply to combustion engines used in off-road applications, in the standard defined as Stage I-V. Over time these limits gradually became more and more restrictive (Fig. 2). Exhaust emission limit values for rail traction engines were being introduced from Stage III onwards, split into the Stage IIIA and Stage IIIB standards. They contain a separate category for diesel engines used in locomotives (category R, RL, RH) and in railcars (category RC). The applicable test procedure for testing in accordance with the Stage I-IIIA is the NRSC (*Non-Road Stationary Cycle*). From Stage IIIB and IV onwards, it is also necessary to meet the emission limits in the NRTC (*Non-Road Transient Cycle*) test (Fig. 3).

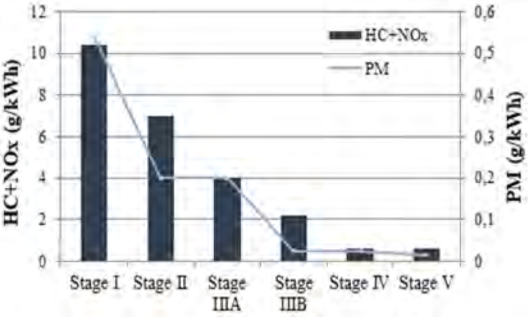

Fig. 2. Stage I-V emission limits for NRMM vehicles (130 kW ≤ P ≤ 560 kW) [18]

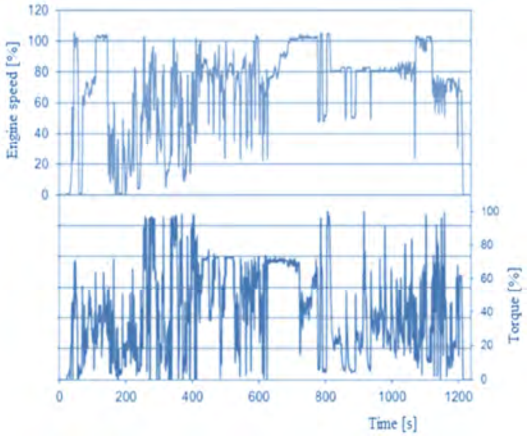

Fig. 3. The NRTC test procedure parameters [18]

2.2. American and Japanese standards

The exhaust emission standards for locomotives in the US take into account newly manufactured and modernized locomotives. There is a division into engines running on diesel and other fuels. The regulations are specified in the documents called Tier 0-4. In 2008, the previously set values in the Tier 0-2 standards were tightened. In addition, new requirements included in Tier 3 and Tier 4 were also introduced. For the test procedure the pollutant emission is measured during a 10-phase static test, which differs in the proportion of individual phases depending on the vehicle category, i.e. shunting and linear locomotives.

In Japan, the emission limits for internal combustion engines used in off-road vehicles and machines apply to the 19 to 560 kW power range. The vehicles are split into two groups, i.e. registered vehicles and unregistered vehicles. The exhaust emission standards for both categories are identical, but have been introduced by separate legal acts. The limit values for 2006-2008 were developed based on the US Tier standards, while in 2008 a tightening of the limits was ordered based on the provisions of Tier 4 Interim/Stage IIIB (in 2011-2013) and Tier 4/Stage IV (in 2015-2016). Emission measurements are performed in accordance with the JIS B 8001-1 8-phase test. For standards introduced in 2008, there is also an additional requirement to perform an NRTC test. Figure 4 shows the emission standards applicable in individual countries around the world.

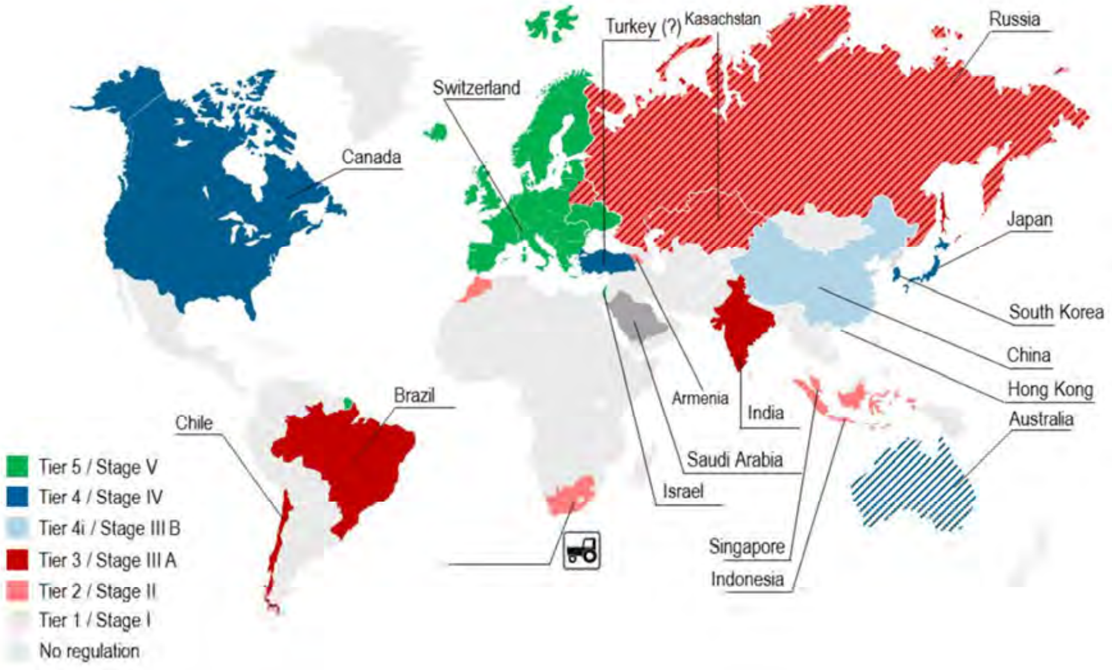

Fig. 4. Emission standards in individual countries [8]

3. Powerpack drive systems

A PowerPack is defined as a group of systems that are a part of an easily replaceable module that connects the engine (most often an internal combustion engine, but other types of drive units, e.g. electric motors, are becoming increasingly popular), along with a gearbox and other mechanisms necessary for the vehicle drive system to function properly. This system is used in many types of industrial equipment designs, as well as in various means of transport. The most common application is the use of this type of solution in the military industry (Fig. 5), i.e. armored vehicles, varying from tanks to armored infantry vehicles [10, 23].

Fig. 5. Removal of the Powerpack system from the M75 APC infantry transport vehicle [11]

Taking into account the many advantages that characterize PowerPack systems, it is expected that in the future manufacturers of leading industries and transport sectors will increase their use of such solutions. Many internal combustion vehicles, due to their high degree of wear and tear, undergo or will undergo thorough modernization, which also includes a modernization of their drive systems. Replacing the drive unit with a modular one, and the easier access for maintenance service that comes with it, makes this type of a solution more popular. Recently, modernization projects have been developed for the T-72 and PT-91 tanks. These projects use Renk's PowerPack systems with the designation 350S [12] (Fig. 6).

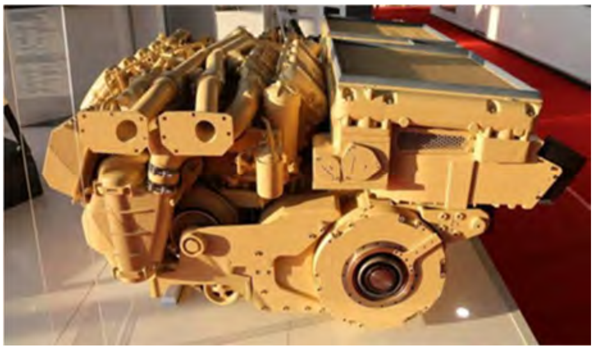

Fig. 6. Renk's PowerPack systems with the designation 350S [12]

The Powerpack system is also used in other branches of the industry, where such systems are often used as stationary energy generators. This solution has also been widely adopted in marine transport, where modular drive systems are used in seaworthy vessels such as yachts and ferries (Fig. 7). The power provided by such a Powerpack module can reach even up to 8000 kW, as shown by the example offered by MTU solutions [14, 20].

Modular drive systems are also becoming a standard element when designing new rail vehicles (Fig. 8). Hybrid solutions such as diesel-electric, meaning an internal combustion engine with a mechanical drive or with a hydraulic drive, are growing in popularity in this branch of transport. PowerPacks designed for rail transport are distinguished by a relatively flat, compact structure suitable for installation under the floor or on the roof of an existing vehicle [20].

The company that has significantly developed this technology and its applications for rail transport is MTU. The manufacturer offers systems capable of generating power of up to 700 kW in the case of the MTU PowerPack Series 1600 (Fig. 9).

The main advantages of using a PowerPack module include:

- modularity, it distinguishes the drive system from other types of drives,
- configuration that resembles Plug & Play which enables quick and easy installation as well as disassembly for maintenance or replacement with another module unit.

Fig. 7. MTU series 890 PowerPack [20]

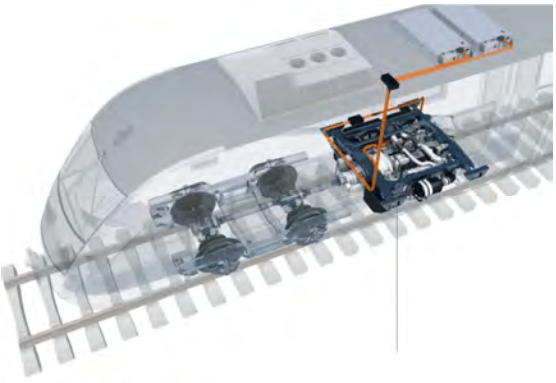

Fig. 8. Powerpack from the MTU company designed for railbus applications [20]

As a result the operating time loss during maintenance or replacement is minimized and the running costs of the vehicle decrease,

- compact arrangement of drive system elements significantly reduces the weight of the whole module,
- real-time monitoring and regulation of operation using the electronic engine management system,
- hybrid systems are characterized by an environmentally friendly drive solution with proven technology and an optimized combustion process,
- PowerPack modules are equipped with aftertreatment and other technologies that enable the reduction of toxic compounds generated in the combustion process [2, 13].

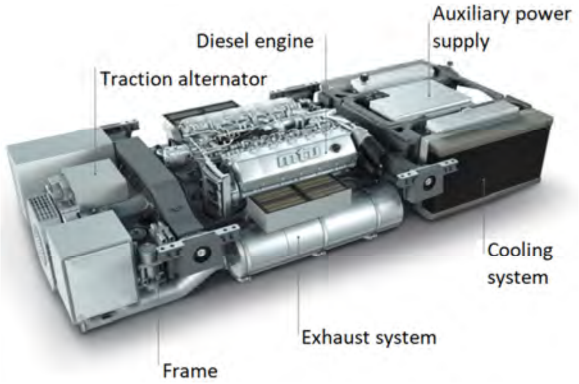

Fig. 9. MTU series 1600 PowerPack [20]

4. 227M railcar powerpack drive systems

4.1. 227M railcar

Due to the requirements for meeting stringent exhaust emission standards and modern design solutions, the railway industry used a solution resulting from these two factors.

One of the vehicles in which the Powerpack solution was used is the 227M railcar. In September 2021, FPS H. Cegielski presented a new rail vehicle from the Plus platform for the first time. It is a hybrid vehicle equipped with the EPS PowerPack system that focuses on ecology and technological development. Modular drive solutions are increasingly more often used in public and freight transport. As an example, a railbus for regional passenger transport was designed by Łukasiewicz Research Network – Rail Vehicles Institute "TABOR". The two-unit vehicle is innovative due to the use of two different propulsion sources (Fig. 10). One of the vehicle units is driven using an electric motor. When driving in electric mode, energy is drawn from the electric traction via the pantograph. In the event of a breakdown of the overhead line or its absence, the vehicle can switch to the diesel mode thanks to the installation of two internal combustion engines with power generators in the other unit. This means that the described vehicle can travel on both electrified and non-electrified routes.

The vehicle rests on four bogies. Two of them are trolleys that are located at the fronts of the two units. The other two are motor bogies which are located close to the consist connection points on the units back. Electric motors are mounted on the motorized bogies, which are powered using the electric traction when driving in electric mode or from a generator set when in the diesel driving mode. The generator set was installed in the Diesel unit between the driver's compartment and the passenger compartment (Fig. 11).

Fig. 10. Diesel and Electric modules of the type 227M rail vehicle

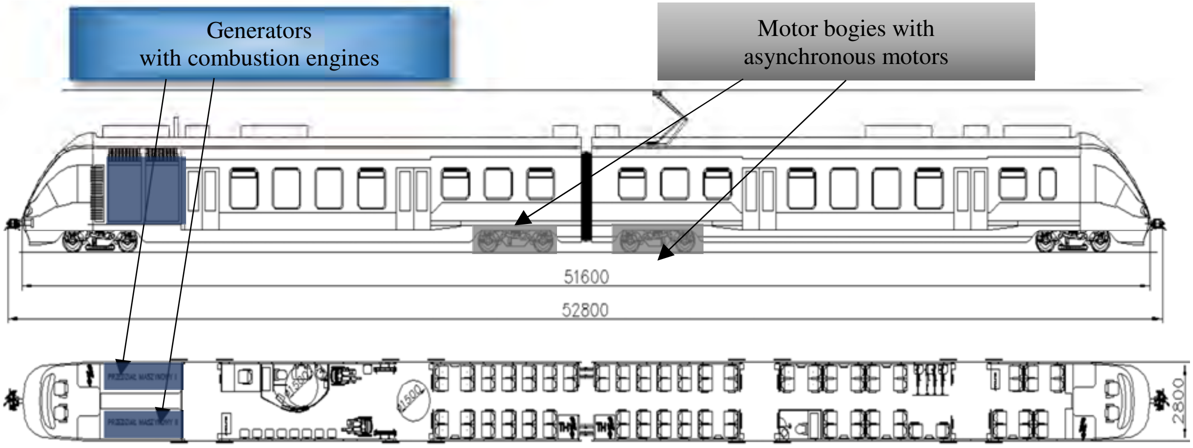

Fig. 11. Location of generating sets and motor bogies

4.2. Engine unit

The machinery space consists of two generating sets installed on the sides of the vehicle and is separated by a corridor leading to the driver's cab. In the case of driving using the diesel drive mode, the drive is powered using two TCD 12.0 L6 diesel engines by Deutz with a power of 400 kW (Fig. 12). Table 1 shows the data relating to the drive unit and on Fig. 13 presents dimensions of the engine.

Table 1. Data sheet for the Deutz TCD 12.0 L6 engine unit

Engine data	**TCD 12.0 L6**	**Unit**
Engine type	Compression-ignition four-stroke engine	[–]
Turbocharging	Turbocharger with charge air cooling	[–]
Cooling type	water cooled	[–]
Cylinder layout	In-line	[–]
Cylinder number	6	[–]
Piston diameter/stroke	130/150	[mm]
Total engine displacement	11946	[cm^3]
Supply system	Common Rail	[–]
Exhaust gas aftertreatment system (EU Category V)	Diesel Oxidation Catalyst (DOC) + Selective Catalytic Reduction (SCR) + Diesel Particulate Filter (DPF)	[–]
Number of valves per cylinder	4	[–]
Valve clearance: inlet/outlet	0.3 $^{\pm0.05}$/0.4 $^{\pm0.05}$	[mm]
Order of ignition	1–5–3–6–2–4	[–]
Direction of rotation looking at the flywheel	left	[–]
Engine power according to ISO 9249	400@1900 rpm	[kW]
Max torque	2500@1200 rpm	[Nm]
Coolant quantity (only engine without radiator/hoses and pipes)	≈ 24	[dm^3]
Allowable permanent coolant temperature	max 110	[°C]
Quantity of oil during oil change (with filter)	≈ 41.5	[dm^3]
Oil sump temperature, maximum	130	[°C]
Oil pressure minimum (low idle, warm engine)	170/1.7	[kPa/bar]
Maximum permissible air temperature downstream of the boosted air cooler	60	[°C]
Weight without cooling system according to DIN 70020-A	≈ 1005 ±3.5%	[kg]

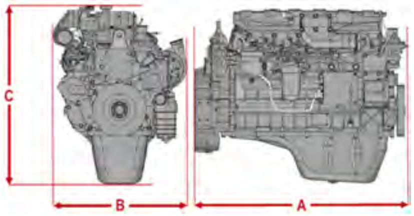

Fig. 12. Deutz TCD 12.0 L6 engine unit dimensions: A – 1335 mm, B – 853 mm, C – 1156 mm [8]

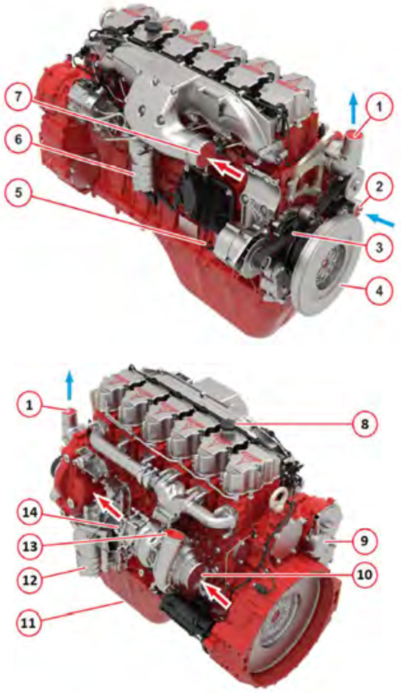

Fig. 13. Engine structure: 1 – coolant outlet, 2 – coolant inlet, 3 – v-rib belt, 4 – torsional vibration damper, 5 – oil dipstick, 6 – fuel filter, 7 – boost air intake, 8 – oil inlet, 9 – engine block ventilation, 10 – air inlet, 11 – oil drain plug, 12 –lubricating oil filter, 13 –boost air outlet, 14 – exhaust [8]

4.3. Generator

While driving in the combustion engine mode, the diesel engines drive the Emit GTds500S4A generator with a rated apparent power of 460 kVA. There are two devices of this type on the vehicle, which supply electricity to four traction electric motors installed on the vehicle bogies. Specifications for the GTds500S4A generator were shown in Table 2.

Table 2. Technical specifications of the GTds500S4A generator

Data	**Value**	**Unit**
Engine type	GTds500S4A	[–]
Rated power	460	[kW]
Rated speed	1800	[rpm]
Rated voltage	3000 ±5%	[V]
Rated frequency	60 ±2%	[Hz]
Rated current	88.5	[A]
Efficiency	93	[%]
Mass	1850	[kg]
Operating temperature	From –30 to +40	[°C]
Stator winding connection	Star	[–]
Insulation class	H (VPI)	[–]

The space behind the driver's cabin in the Diesel Unit is provided for the installation of the combustion engine with the traction generator and the exhaust gas aftertreatment system. Because the engine can only be accessed from the side, it was necessary to invert the entire engine-generator system (Fig. 14).

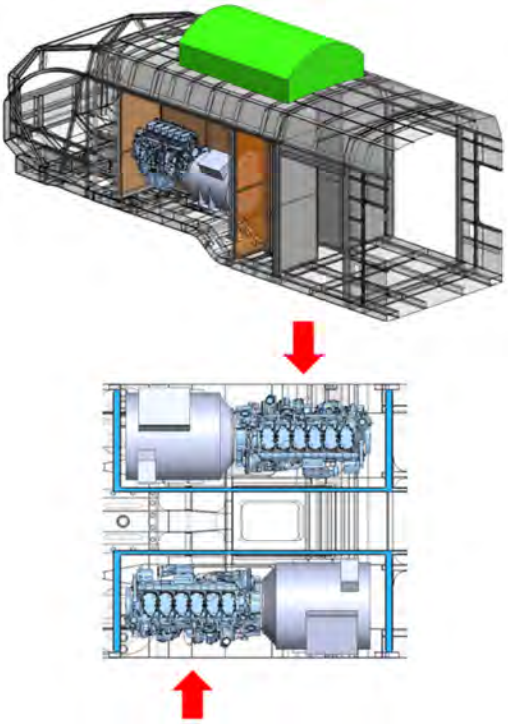

Fig. 14. Location of machine room spaces; red arrows indicate the direction from which it will be possible to access and service the engine and the traction generator (top view)

4.4. Exhaust aftertreatment system

The combustion drive system met the Stage V exhaust emission standard. In order to achieve this level of exhaust emission reduction, it was necessary to use a sophisticated exhaust aftertreatment system. The exhaust system consisted of: Selective Catalytic Reduction (SCR), Diesel Particulate Filter (DPF), and Diesel Oxidation Catalyst (DOC). The complete exhaust aftertreatment system was shown in Fig. 15.

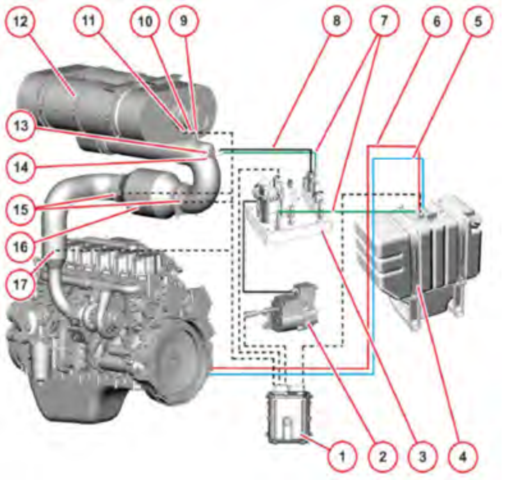

Fig. 15. Exhaust aftertreatment system: 1 – engine control module, 2 – SCR compressor, 3 – SCR pump, 4 – SCR tank, 5 – coolant line, dispenser, 6 – pre-heating line, SCR tank, 7 – SCR line, 8 – AdBlue® injection air supply line, 9 – NH_3 sensor, 10 – NO_x sensor, 11 – temperature sensor, 12 – SCR catalyst with a particulate filter (DPF), 13 – air access connection points, 14 – SCR injector, 15 – temperature sensor, 16 – Diesel Oxidation Catalyst (DOC), 17 – NO_x sensor [8]

4.5. Machine room

The combustion drive system powerpack is mounted on the 227M vehicle and is the source of electricity for the traction motors. Thanks to this solution, the rail vehicle is able to reach a travel speed of 120 km/h while operating using the internal combustion engine. The generators can be accessed by removing the side panel from the outside of the vehicle. Figures 16 shows machine room and components of the combustion generator. Figure 17 shows the powerpack and its location in the real vehicle.

5. Summary

The limited electrification of railways in Poland and many other EU member states necessitates employment of a mixed rolling stock, including both combustion engine drive systems as well as electric drive systems supplied by overhead power lines. This solution ceases to be viable when pressure is put on the reduction of the size of rolling stock powered by combustion engines. This, however, has become the reality for most operators as continued legislative efforts by the European Union and the EU Parliament require a steady reduction in the amounts of CO_2 emitted into the atmosphere to combat global warming. Additionally reduced limit values for the emission of toxic exhaust components demand innovation, both in the field of drive systems and exhaust aftertreatment solutions. Thus, as a response to the growing market needs, various rolling stock producers offer new solutions that are to satisfy the changing landscape of rail vehicles. One of such solutions, discussed in this article, was the 227M railbus. It is a two-unit hybrid solution, utilizing a dual-drive system separated between the two units. The combustion unit is equipped with two diesel engine-generator sets and each unit has one motor bogie with asynchronous motors for electric propulsion. The combined drive systems allow the vehicle to travel through rail lines that have only partial electrification, as well as enable options of better energy management during driving thanks to the addition of the electric drive.

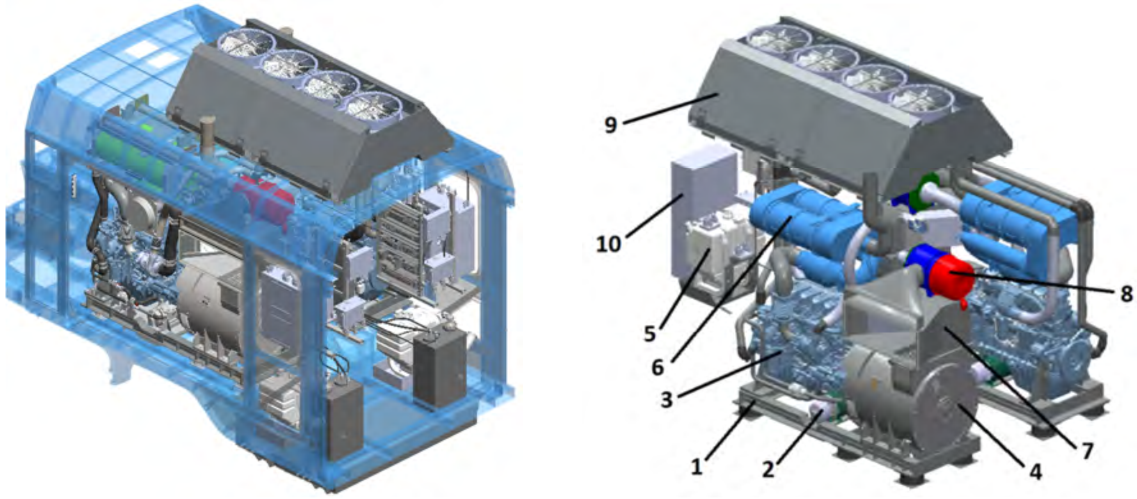

Fig. 16. Left: Machine room. On the right: components of the combustion generator: 1 – generator frame, 2 – heater, 3 – combustion engine, 4 – traction generator, 5 – AdBlue tank, 6 – exhaust aftertreatment system with mufflers, 7 – ventilation duct of the traction generator, 8 – intake air filter with a duct, 9 – cooling system for two engines, 10 – engine control module space

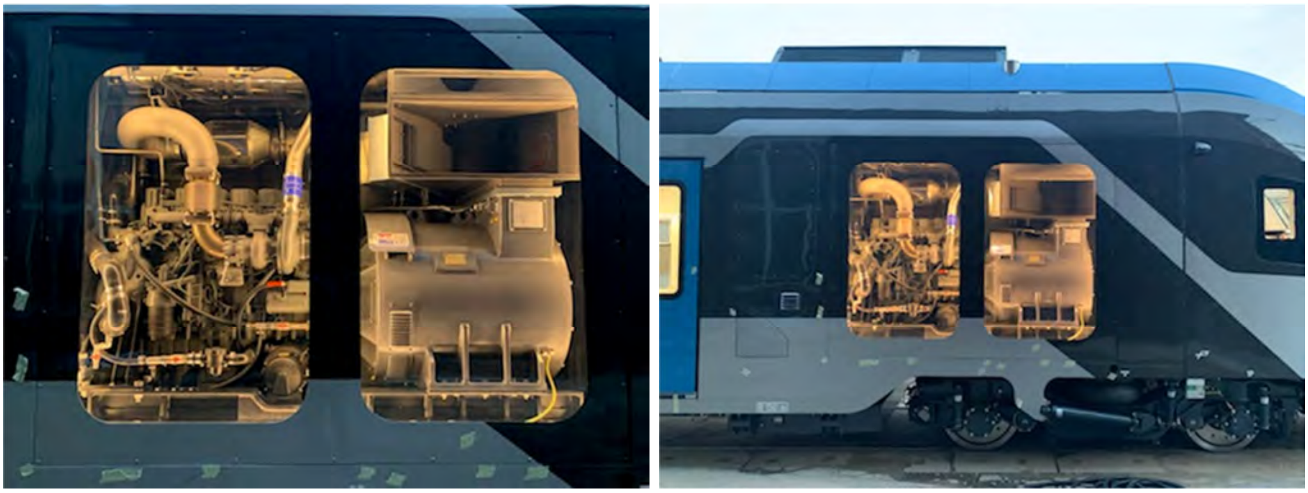

Fig. 17. Engine-generator unit of 227M railcar and 227M rail vehicle with drive unit

Acknowledgements

This work was supported by the Applied Research Program No. PBS3/B6/26/2015 entitled: "Light rail bus for regional traffic" and co-financed by the National Centre for Research and Development.

Nomenclature

DOC	Diesel Oxidation Catalyst
DPF	Diesel Particulate Filter
EU	European Union
HDV	Heavy Duty Vehicles
LDV	Light Duty Vehicle
NEDC	New European Driving Cycle
NRSC	Non-Road Stationary Cycle
NRTC	Non-Road Transient Cycle
PC	Passenger Car
PEMS	Portable Emissions Measurement System
RDE	Real Driving Emissions
SCR	Selective Catalytic Reduction
US	United States of America
WHSC	World Harmonized Stationary Cycle
WHTC	World Harmonized Transient Cycle
WLTC	Worldwide Harmonized Light Vehicles Test Cycles

Bibliography

[1] ANDRZEJEWSKI, M., DASZKIEWICZ, P., URBAŃSKI, P. et al. Impact of a locomotive engine modernization on fuel consumption. *MATEC Web of Conferences. EDP Sciences.* 2021, **338**, 01001. https://doi.org/10.1051/matecconf/202133801001

[2] Biuro Handlowe RUDA Sp. z o.o. Sp. k. materials

[3] BARBOSA, F.C. Hybrid rail technology review: an intermediate pathway for electrifying the freight and commuter rail sector-a technical and operational assessment. *ASME/IEEE Joint Rail Conference. American Society of Mechanical Engineers.* 2021, V001T07A001. https://doi.org/10.1115/JRC2021-58271

[4] CIPEK, M., PAVKOVIĆ, D., KLJAIĆ, Z. et al. Assessment of battery-hybrid diesel-electric locomotive fuel savings and emission reduction potentials based on a realistic mountainous rail route. *Energy*. 2019, **173**, 1154-1171. https://doi.org/10.1016/j.energy.2019.02.144

[5] DASZKIEWICZ, P., ANDRZEJEWSKI, M., MEDWID, M. et al. Analysis of the selection of chosen technical parameters of the powertrain system for a diesel-electric rail-road tractor. *Combustion Engines*. 2021, **186**(3), 64-71. https://doi.org/10.19206/CE-140723

[6] DASZKIEWICZ, P., ANDRZEJEWSKI, M., URBAŃSKI, P. et al. Analysis of the exhaust emissions of toxic compounds from a special purpose rail machine PŁT-500 during profiling the ballast cess. *Journal of Ecological Engineering*. 2021, **22**(7), 80-88. https://doi.org/10.12911/22998993/139214

[7] DASZKIEWICZ, P., KURC, B., PIGŁOWSKA, M. et al. Fuel cells based on natural polysaccharides for rail vehicle application. *Energies*. 2021, **14**(4), 1144. https://doi.org/10.3390/en14041144

[8] Deutz company materials

[9] European Parliament Infographics https://www.europarl.europa.eu

[10] HERWARTZ, S., PAGENKOPF, J., STREULING, C. Sector coupling potential of wind-based hydrogen production and fuel cell train operation in regional rail transport in Berlin and Brandenburg. *International Journal of Hydrogen Energy*. 2021, **46**(57), 29597-29615. https://doi.org/10.1016/j.ijhydene.2020.11.242

[11] HUNNICUTT, R.P. Pershing: a history of the medium tank T20 series. *Feist Publications*. Berkeley, California 1971.

[12] Defence24. https://www.defence24.pl

[13] Flickr. https://www.flickr.com

[14] K&W DRIVE SYSTEMS. https://www.kwds.at

[15] KAMIŃSKA, M., RYMANIAK, Ł., LIJEWSKI, P. et al. Investigations of exhaust emissions from rail machinery during track maintenance operations. *Energies*. 2021, **14**(11), 3141. https://doi.org/10.3390/en14113141

[16] LIJEWSKI, P., MERKISZ, J., FUC, P. et al. Air pollution by the exhaust emissions from construction machinery under actual operating conditions. *Applied Mechanics and Materials*. 2013, **390**, 313-319. https://doi.org/10.4028/www.scientific.net/AMM.390.313

[17] MERKISZ, J., LIJEWSKI, P., FUĆ, P. The comparison of the emissions and fuel consumption in vehicles fitted with different powertrain under real operating conditions. *Silniki Spalinowe*. 2011, **50**.

[18] MERKISZ, J., LIJEWSKI, P., FUĆ, P. et al. Development of the methodology of exhaust emissions measurement under RDE (Real Driving Emissions) conditions for non-road mobile machinery (NRMM) vehicles. *IOP Conference Series: Materials Science and Engineering*. 2016, **148**, 012077. https://doi.org/10.1088/1757-899X/148/1/012077

[19] MICHALAK, P., MERKISZ, J., STAWECKI, W. et al. The selection of the engine unit – main engine generator during the modernization of the 19D/TEM2 locomotive. *Combustion Engines*. 2020, **182**(3), 38-46. https://doi.org/10.19206/CE-2020-307

[20] MTU company materials

[21] RYMANIAK, L., SIEDLECKI, M., SOKOLNICKA, B. et al. Comparative test of an internal combustion engine ecological indicators in real operating conditions and on a dynamic engine dynamometer. *IOP Conference Series: Materials Science and Engineering*. 2018, **421**(4), 042069. https://doi.org/10.1088/1757-899X/421/4/042069

[22] SZYMLET, N., LIJEWSKI, P., FUĆ, P. et al. Comparative analysis of passenger car and non-road machinery specific emission in real operating conditions. *2018 International Interdisciplinary PhD Workshop (IIPhDW). IEEE.* 2018, 226-230. https://doi.org/10.1109/IIPHDW.2018.8388362

[23] WALENTYNOWICZ, J. Propulsion motors for combat vehicles. *Journal of KONES Powertrain and Transport*. 2006, **13**(4), 129-140. https://kones.eu/ep2006_4.html

Mariusz Far, DEng. – Łukasiewicz Research Network – Rail Vehicle Institute "TABOR", Poland.

e-mail: *mariusz.far@tabor.lukasiewicz.gov.pl*

Patryk Urbański, MEng. – Łukasiewicz Research Network – Rail Vehicle Institute "TABOR", Poland.

e-mail: *patryk.urbanski@tabor.lukasiewicz.gov.pl*

Dawid Gallas, MSc. – Łukasiewicz Research Network – Rail Vehicle Institute "TABOR", Poland.

e-mail: *dawid.gallas@tabor.lukasiewicz.gov.pl*

Aleksandra Woch, MEng. – Łukasiewicz Research Network – Rail Vehicle Institute "TABOR", Poland.

e-mail: *aleksandra.woch@tabor.lukasiewicz.gov.pl*

Kuba Mieżowiec, Eng. – Łukasiewicz Research Network – Rail Vehicle Institute "TABOR", Poland.

e-mail: *kuba.miezowiec@tabor.lukasiewicz.gov.pl*

Article citation info:
WOLFF, A., KOSZAŁKA, G. Influence of engine load on piston ring pack operation of an automotive IC engine. *Combustion Engines*. 2022, **190**(3), 88-94. https://doi.org/10.19206/CE-141737

Andrzej WOLFF
Grzegorz KOSZAŁKA

Combustion Engines
Polish Scientific Society of Combustion Engines

Influence of engine load on piston ring pack operation of an automotive IC engine

ARTICLE INFO

Received: 6 September 2021
Revised: 3 November 2021
Accepted: 20 December 2021
Available online: 14 February 2022

A piston-rings-cylinder (PRC) assembly determines the blowby, engine oil consumption, and friction and wear processes accompanying the system's operation. Thus, it is crucial for the whole IC engine efficiency and lifetime. A lot of research effort is put into increasing the performance of this complex and highly dynamic system. Advanced, comprehensive models play an important role in understanding and improving the PRC system.

In the presented work, the effect of load on the operation of the ring pack of an automotive gasoline engine is analyzed. A comprehensive model that covers the gas flow through the crevices of the PRC system, ring displacements in the groove, and ring lubrication was used for this analysis. The results of the simulations show that the local thickness of the oil film, especially near the piston top dead center is compared to the height of the combined surface roughness of a cylinder liner and piston rings, and friction-related asperity contact strongly increases as the engine load increases. The simulations also show that the engine load affects the axial displacements of the rings in the grooves but practically does not affect the thickness of the oil film left by the ring pack on the cylinder liner.

Key words: *automotive IC engine, piston rings, blowby, ring dynamics, hydrodynamic lubrication, mixed friction*

1. Introduction

A piston-rings-cylinder (PRC) system is an important part of an internal combustion engine and strongly affects its efficiency and lifetime. The system decides about the combustion chamber airtightness, engine oil consumption, and friction and wear processes accompanying the operation of the system. Mechanical losses related to the friction in the system are usually the major contributor to the total mechanical losses of the engine [5, 6, 8]. Research to improve the system are crucial and widely conducted. Nowadays, the biggest effort in this field is focused on reducing friction losses while maintaining oil consumption and component life.

Because of the influences of many factors and the highly dynamic way of operation, the determination of the effect of a particular factor on the performance of the whole system is usually extremely difficult based only on empirical tests. Appropriate mathematical models help to evaluate the effects of both design and operational factors on the performance of the PRC system and thus improve system design [4, 9, 14, 17].

The engine oils of lower viscosity are used to reduce fluid friction. However, this makes the oil film thickness between the rings and the cylinder liner comparable to the surface roughness [1, 14, 21]. That means that not only fluid but also mixed lubrication should be taken into account while modelling the ring pack operation of a modern engine.

Numerical simulations of the operation of the gasoline engine ring pack with the use of the PRC system model considering mixed lubrication are presented. The results of simulations under the conditions of maximum engine power have been most often discussed in the literature. On the contrary, the results of calculations for partial engine loads, i.e., those in which car engines operate most often, are presented in this article.

2. Modelling of piston ring pack operation

2.1. Developed sub-models

The developed PRC system model consists of two main models: a) model of gas flow through the crevices existing between parts creating the system, and b) model of oil flow in the lubrication gap between the rings and cylinder liner. Furthermore, it consists of the following sub-models: model of contact of rough surfaces, model of axial movement of rings within piston grooves, and model of elastic torsional deformation of piston rings. All these models and sub-models are coupled (Fig. 1).

The particular models and sub-models are briefly described below. All models and sub-models have been described in detail in previous publications [15-21].

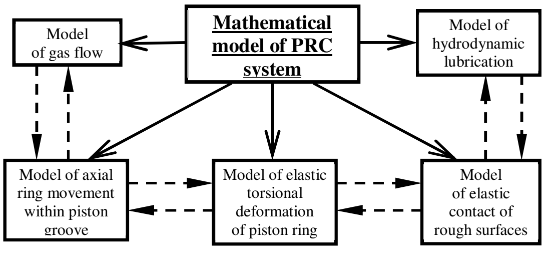

Fig. 1. A developed comprehensive model of the system: piston-rings-cylinder (PRC) [21]

2.2. Model of gas flow through the labyrinth seal of piston rings

The gas flow model [10, 11, 17] consists of several volume regions V_1, V_2, …, V_5, which are connected by orifices with cross-section areas A_1, A_2, …, A_6 (Fig. 2). The volumes V_3, V_5, correspond to volumes between the piston rings, while volumes V_2, V_4 correspond to groove volumes behind rings. Orifices with cross-section areas A_1, A_4 correspond to the ring end gaps, whereas orifices with cross-sections A_2, A_3, A_5, A_6 correspond to ring-side crevices [10, 11].

It was also assumed that the gas flow through orifices is isentropic (depending on pressure ratio – subsonic or sonic). The heat transfer between gas in the particular regions and surrounding walls was taken into account.

Leaks between piston rings and cylinder liner were defined by flow areas of ring end gaps, which depend on the position of the piston in the cylinder.

In addition, the mathematical description takes into account changes in the volume of gas in the regions and cross-section areas between the rings and the piston grooves due to axial movement of the rings [5, 7, 8, 11, 14].

In the mathematical model of these phenomena, equations of the following physical laws are utilized (here given for a gas volume region number *k*):

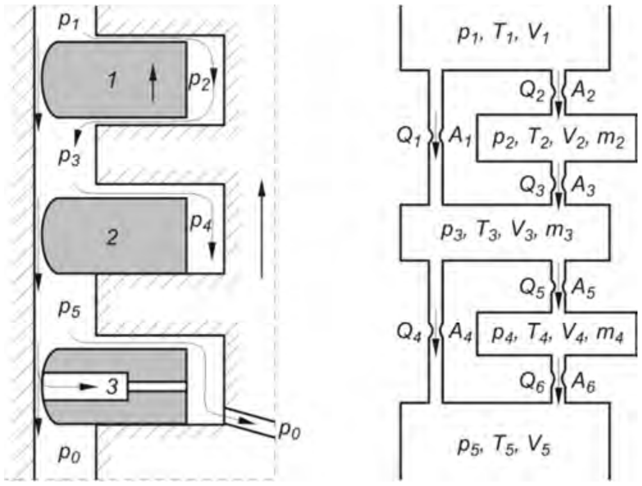

Fig. 2. Scheme of gas flow through the labyrinth seal: piston–rings–cylinder system and applied physical model for the ring pack of three piston rings [21]

equation of mass balance:

$$\mathrm{dm_k} = \sum\nolimits_i \mathrm{dm_{In_i}} - \sum\nolimits_j \mathrm{dm_{Out_j}} \tag{1}$$

equation of energy balance:

$$\sum_i \mathrm{dm_{In_i}} \cdot \mathrm{h_{In_i}} - \sum_j \mathrm{dm_{Out_j}} \cdot \mathrm{h_{Out_j}} - \delta \mathrm{Q_{Wall}} - \delta \mathrm{E_{fri}} = \mathrm{d(m_k \cdot u_k)} + \mathrm{p_k} \cdot \mathrm{dV_k} \tag{2}$$

gas state equation in differential form:

$$\mathrm{dT_k} = \mathrm{T_k} \cdot \left(\frac{\mathrm{dp_k}}{\mathrm{p_k}} + \frac{\mathrm{dV_k}}{\mathrm{V_k}} - \frac{\mathrm{dm_k}}{\mathrm{m_k}}\right) \tag{3}$$

where: m – gas mass, p – gas pressure, T – gas temperature, u – internal gas energy, h – gas enthalpy, Q – heat transferred through cylinder walls, E – friction loss energy; Indexes: In – gas inflow, Out – gas outflow, i – number of inflow channel, j – outflow channel number, k – analysed gas volume.

The pressure variation over the top ring was determined by pressure measurements inside the cylinder during a cycle of its operation. The pressure between all the piston rings was calculated using the above-presented gas flow model. For this purpose, a computer program *GASFLOW* was developed and applied [15–21].

2.3. Model of mixed lubrication

Two main cases of oil flow in the PRC system are presented in Fig. 3.

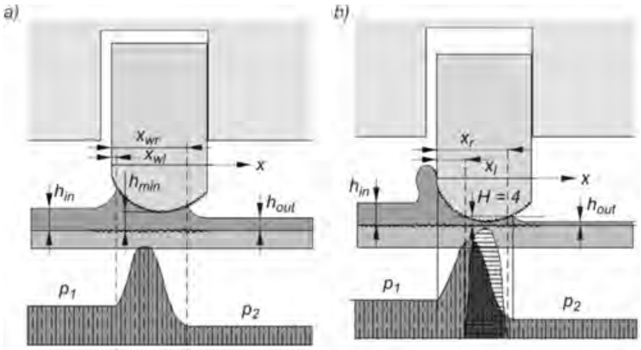

Fig. 3. Scheme of gap between the ring face and cylinder liner in the case of: a) fluid and b) mixed friction [21]

A one-dimensional form of the modified Reynolds equation developed by Patir and Cheng [12, 13] has been used to calculate hydrodynamic forces in the case of rough gap surfaces. This equation is applicable to any general roughness structure and takes the following form that contains sliding and squeeze motion:

$$\frac{\partial}{\partial x}\left(\varphi_x \frac{h^3}{12\mu} \frac{d\bar{p}}{dx}\right) = \frac{U}{2}\frac{d\bar{h}_T}{dx} + \frac{U}{2}\sigma\frac{d\varphi_S}{dx} + \frac{d\bar{h}_T}{dt} \tag{4}$$

where: t – time; x – coordinate along with the cylinder liner; h – nominal oil film thickness; h_T – the average gap between the ring and cylinder; p – hydrodynamic pressure; U – axial ring velocity; μ – dynamic oil viscosity; $v = \partial h_T/\partial t$ – radial ring velocity, σ – composite root mean square roughness of sliding surfaces.

To preserve the solution of equation (4), it is necessary to describe the boundary conditions concerning oil flow. The upstream boundary condition states that the hydrodynamic pressure is equal to the gas pressure p_1 (see Fig. 3a):

$$\mathrm{p(x_{wl})} = \mathrm{p_1} \tag{5}$$

The downstream boundary condition states that the oil pressure is equal to the gas pressure $\boldsymbol{p_2}$ and the pressure gradient is equal to zero, which corresponds to the so-called "Reynolds assumption":

$$\mathrm{p(x_{wr})} = \mathrm{p_2} \quad \text{and} \quad \left.\frac{\partial \mathrm{p}}{\partial \mathrm{x}}\right|_{\mathrm{x_{wr}}} = 0 \tag{6}$$

The hydrodynamic force (per unit circumference) F_h [N/m] can be calculated by integration of the hydrodynamic pressure distribution as follows:

$$\mathrm{F_h} = \int_{\mathrm{x_{wl}}}^{\mathrm{x_{wr}}} \mathrm{p(x)dx} \tag{7}$$

Then the hydrodynamic friction force F_{fri} [N/m] can be obtained:

$$\mathrm{F_{fri}} = \int_{\mathrm{x_{wl}}}^{\mathrm{x_{wr}}} \left(\frac{\mathrm{h}}{2}\frac{\partial \mathrm{p}}{\partial \mathrm{x}} - \frac{\mu \mathrm{U}}{\mathrm{h}}\right)\mathrm{dx} \tag{8}$$

In addition, the power loss P_{fri} [W/m] can be calculated as follows:

$$\mathrm{P_{fri}} = |\mathrm{F_{fri}} \cdot \mathrm{U}| + \left|\mathrm{F_h} \cdot \frac{\partial \mathrm{h}}{\partial \mathrm{t}}\right| \tag{9}$$

The significance and mathematical description of empirical coefficients ϕ_x, ϕ_S concerning the equation (4) are presented in works [12, 13].

The effects of interacting asperities of piston ring and cylinder liner surfaces were modelled using the mathematical model developed by Greenwood and Tripp [3], which was described in detail in publication [17].

The numerical solution of the Patir&Cheng equation (4) is based on the implicit finite difference scheme. For this purpose, the computer program *RINGAS* has been developed and applied [15–21].

2.4. Model of ring torsional deformation and ring axial movement in the piston groove

A scheme of forces acting on a piston ring, action lines, and distances between these forces and the centre of gravity S of the ring cross-section are shown in Fig. 4. All the forces are referenced to the unit of the ring circumference c_{imc} (unit forces [N/m]).

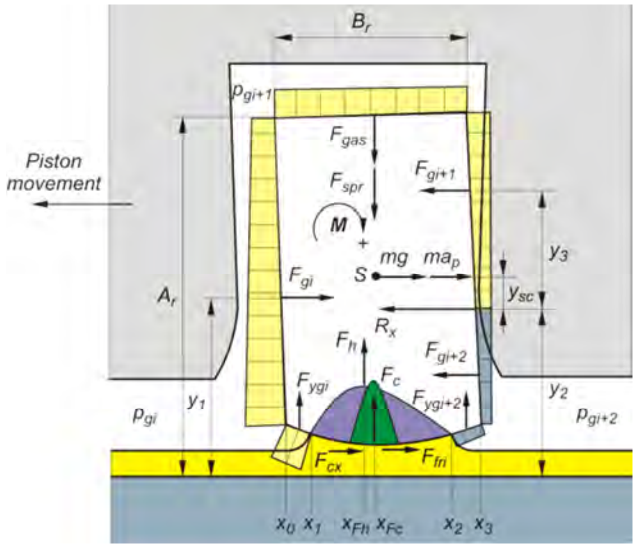

Fig. 4. Scheme and definitions of forces acting on a piston ring. Nomenclature: F_h – hydrodynamic normal force, F_c – contact normal force, F_{spr} – ring spring force, F_{gas} – back ring gas force, F_{ygi} – leading edge gas force, F_{ygi+1} – trailing edge gas force, R_x – groove reaction force, F_{fri} – viscous friction force, F_{cx} – contact friction force, F_{gi} – leading side gas force, F_{gi+1}, F_{gi+2} – trailing side gas forces, m – ring mass, g – gravitational acceleration, a_p – piston acceleration [21]

A typical set of equations for the single lip piston ring has the following form (see Fig. 4):

a) in the radial direction

$$\Sigma F_r = F_h + F_c + F_{yg\,i} + F_{yg\,i+2} - F_{spr} - F_{gas} = 0 \quad (10)$$

b) in the axial direction

$$\Sigma F_x = R_x - F_{fri} - F_{cx} + F_{g_{i+1}} + F_{g_{i+2}} - F_{g_i} - \frac{m}{c_{imc}}(g + a_p) = 0 \quad (11)$$

Using these equations, the reaction force R_x between the ring and piston groove in every time step can be calculated. If the sign of this force changes, the axial movement of the ring in the piston groove begins. At this point, the value of the reaction force $R_x = 0$ and the axial movement of the ring relative to the piston groove can be described by the following differential equation:

$$\frac{m}{c_{imc}}\frac{d^2x_r}{dt^2} = -F_{fri} - F_{cx} + F_{g_{i+1}} + F_{g_{i+2}} - F_{g_i} - \frac{mg}{c_{imc}} \quad (12)$$

The ring movement x_r completes when the ring reaches the opposite side of the piston groove.

Similarly, like in articles of Dowson [2] and Tian et al. [14], the twist around the centre of gravity of the ring cross-section (point S in Fig. 4) can be described by the following equation of equilibrium of acting moments:

$$\Sigma M_S = F_h\left(x_S - x_{F_h}\right) + F_c\left(x_S - x_{F_c}\right) - (F_{fri} + F_{cx})\frac{A_r}{2} - F_{g_i}(y_2 + y_{sc} - y_1) - F_{g_{i+1}}(y_3 - y_{sc}) + F_{g_{i+2}}\left(\frac{y_2}{2} + y_{sc}\right) + R_x \cdot y_{sc} - K \cdot \theta = 0 \quad (13)$$

Estimating the ring torsional stiffness K and using the equation (13) of moment equilibrium, the ring twist angle θ can be calculated. All the piston grooves are assumed to have curved surfaces in the radial direction (Fig. 4) due to their typical wear profiles. However this time, the effect of ring twist has not been taken into account.

3. Experimental verification of developed models

The model has been verified for a two-stroke marine Diesel engine [15–17]. The experimental verification of the model of gas flow through the labyrinth seal of piston rings was carried out using measurements of unsteady gas pressure: in the cylinder, between the piston rings, and under piston performed by piezoelectric sensors mounted in the piston. A satisfactory qualitative and quantitative compatibility of the analyzed pressure variations has been achieved. The maximal relative differences between measured and calculated pressures have not exceeded 15% [15, 17].

On the other hand, the experimental verification of the hydrodynamic model of piston rings involved measurement of scraped oil volumes by a gland-box of a two-stroke marine engine. Examination of scraped oil volumes by the ring pack (of the gland-box of a marine IC engine) proves a satisfactory quantitative agreement between numerical and experimental results. The maximal relative differences between measured and calculated values have not exceeded 10% [15, 17]. Unfortunately, similar measurements for piston ring packs of tested engines have not been carried out.

4. Computational results

4.1. Main data of the tested engine

The simulations have been done for a four-stroke spark-ignition engine of a middle-class passenger car operating at low, medium, and high load at a constant rotational speed of 2000 rpm. The main data of the engine is presented in Table 1.

Table 1. Engine specification

Cylinder bore [mm]	84
Piston stroke [mm]	90
Number of cylinders	4

The type of ring set considered is common in car engines. It consists of three rings: a compression ring, a scraper ring, and a two-lip oil ring. The main dimensions of piston rings are presented in Table 2. All the rings have conventional straight ring end gaps.

Table 2. Main parameters of piston rings

Parameter	Ring 1	Ring 2	Ring 3
Total axial width [mm]	1.20	1.50	4.0
Axial width (upper land) [mm]	–	–	1.0
Axial width (lower land) [mm]	–	–	1.0
Radius of parabolic sliding surface [mm]	180	180	244
Offset of parabolic sliding surface [mm]	0.30	1.12	2.0
Radial thickness [mm]	3.8	3.8	3.8
Nominal ring end gap [mm]	0.20	0.30	0.30
Mass [g]	12.5	16.7	25
Elastic tension force (per unit of circumference) [N/m]	375	350	1545

The surface geometry of the piston ring package, with vertical dimensions magnified by a factor of 1000 relative to the horizontal ones, is depicted in Fig. 5. All the rings are barrel-shaped.

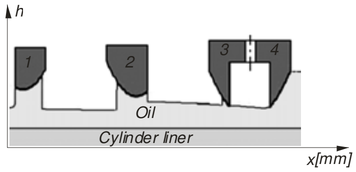

Fig. 5. Ring pack geometry under consideration (1– compression ring, 2 – scraper ring, 3 – the upper lip of the oil ring, and 4 – the lower lip of the oil ring)

The lubrication parameters of the PRC system can be seen in Table 3. The main parameters of the rough structure of the liner and ring surface are presented in Table 4.

Table 3. Lubrication parameters of the analyzed PRC system [19]

Oil type	Multigrade SAE 10W/50
Oil density	$\rho = 900$ kg/m^3
Growth velocity of the oil film thickness due to oil fog condensation on the cylinder liner under the ring pack	$v_{fog} = 800$ μm/s
Decrease velocity of the oil film thickness in the combustion chamber due to evaporation	$v_{evap} = 10$ μm/s

Table 4. Surface roughness parameters [19]

Surface data parameters	Cylinder liner	Piston rings
RMS roughness	$\sigma_1 = 0.22$ μm	$\sigma_2 = 0.044$ μm
Elastic modulus	$E_1 = 1.13 \cdot 10^{11}$ N/m^2	$E_2 = 1.5 \cdot 10^{11}$ N/m^2
Poisson's ratio	$\nu_{P1} = 0.26$	$\nu_{P2} = 0.25$
Combined parameters	Cylinder liner and piston rings	
RMS roughness	$\sigma = 0.224$ μm	
Asperity density	$\eta = 1.114 \cdot 10^{12}$ m^{-2}	
Asperity radius/ curvature	$\beta = 0.2 \cdot$μm	

4.2. Calculation results

During experimental measurements, the pressure variations in the first cylinder were measured for three engine loads, i.e., small (engine torque of M = 10 Nm), medium (100 Nm), and high (140 Nm) at a constant rotational speed of 2000 rpm. The following maximum gas pressure values in the cylinder can be seen (Fig. 6): 1.66 MPa at low load, 4.95 MPa at medium load, and 4.48 MPa at high load. Although the peak gas pressure in the cylinder at high load is lower than at medium load, the mean indicated pressures increase with the engine load (Table 5).

Table 5. Load parameters of an automotive engine under consideration at the rotational speed of 2000 rpm

Engine load parameters	Engine load (at 2000 rpm)		
	Low	Medium	High
Engine torque M [Nm]	10	100	140
Mean indicated pressure [MPa]	0.150	0.703	0.954

The pressure variation over the top ring was assumed to be equal to the pressure measured inside the cylinder during a cycle of its operation.

Typically, the figures that will follow show variations of some physical parameters as functions of the crankshaft rotation angle, beginning from the piston bottom dead centre (BDC) of the four-stroke engine operation (0°). In this case, the end of the compression phase is at 180° of the crankshaft rotation (piston top dead centre – TDC).

The higher the gas pressure, the stronger the radial gas force acting to increase the ring diameter. It means that the radial gas force can be many times greater than the natural force due to ring stiffness acting in the same direction. First of all, the top ring is strongly pressed against the cylinder liner surface. For this reason, the comparisons of computational results concerning different engine loads are presented for the top piston ring (Fig. 7–9).

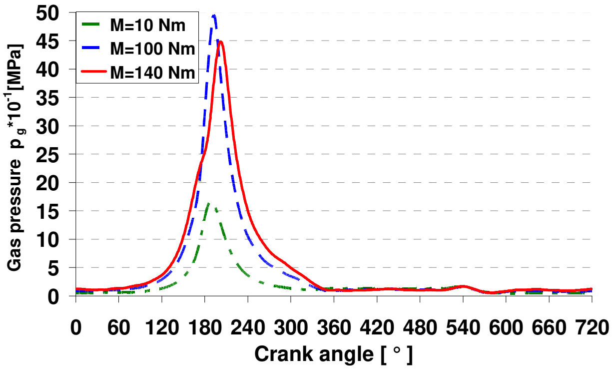

Fig. 6. Gas pressure variations in cylinder versus crank angle for low, medium, and high engine load operation at a rotational speed of 2000 rpm

In Fig. 7, axial lifts of the top ring in the piston groove as a function of crank angle for three analysed engine loads are shown. Due to significant changes in gas pressure the axial movements of the ring within its piston groove can be observed. This phenomenon takes place twice during the whole cycle (0–720°) of the four-stroke engine in case of the low load, i.e., in crank angle ranges 240–350° and 556° up to 128° of the new engine operation cycle. Quick gas pressure variations in the crank angle range 258–351° are followed by five oscillations of axial movement of the top ring in cases of medium and high loads. In addition, longer ring lifts take place: one in the crank angle range 495–720° at medium engine load and two in crank angle ranges 493–545° and 556–640° at high engine load.

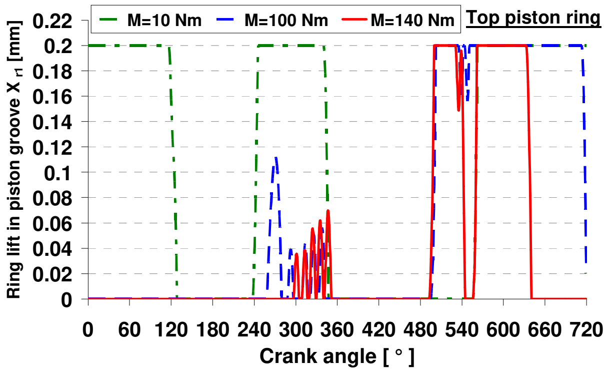

Fig. 7. Variations of the top ring lift X_{r1} in the groove versus crank angle for three engine loads

The nominal axial clearance of the top ring in piston grooves equals 0.20 mm and for the second and third piston ring – 0.30 mm. Each short-lasting ring movement in the piston groove is followed by a change of the acting point of the reaction force R_x to the other flank of the piston groove and also a sign change of this force (Fig. 4). Obviously, $R_x = 0$ during the ring movement between the two piston groove flanks.

The total radial force acting on a piston ring compensates the gas force F_{gas}, hydrodynamic force F_h, elastic contact force due to surface roughness F_c, and spring force F_{spr} (see Fig. 4 and equation (5)). In Fig. 8, variations of total radial forces of the top piston ring for different engine loads versus crank angle are presented.

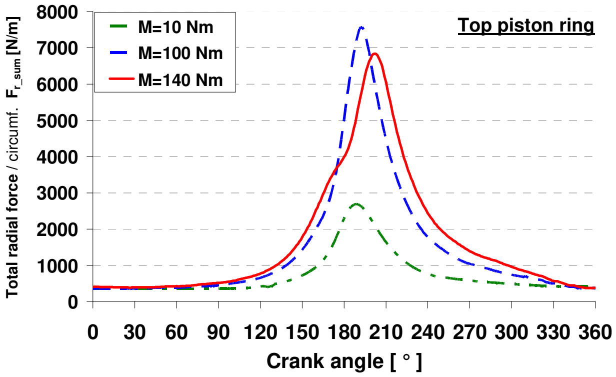

Fig. 8. Variation of total radial unit force (hydrodynamic and elastic contact) F_r for the top piston ring versus crank angle

Variations of the total radial force look similar to the variations of gas pressures in the cylinder (Fig. 6). The top piston ring's maximum radial forces (per unit of piston ring circumference) can be seen: 2680 N/m at low load, 7570 N/m at medium load, and 6830 N/m at high load.

The total friction forces acting on piston rings consist of two tangential components: hydrodynamic and elastic contact forces due to surface roughness. Variations of total friction forces for the top ring as functions of crank angle are presented in Fig. 9.

Maximum values of hydrodynamic components of friction forces are much lower than components of elastic contact forces – at high engine load, these components are equal to17 N/m) and 425 N/m, correspondingly. The mixed friction forces are particularly noticed near the top dead centre (at the beginning of the expansion phase), where the highest gas pressure and oil temperature are reached. The sign change of these forces at TDC results from the change in the direction of piston movement. The higher engine load, the bigger value of total friction force acting on the sliding surface of the top ring can be observed. The following maximum total friction forces (per unit of piston ring circumference) of the top ring can be seen: 111 N/m at low load, 246 N/m at medium load, and 440 N/m at high load.

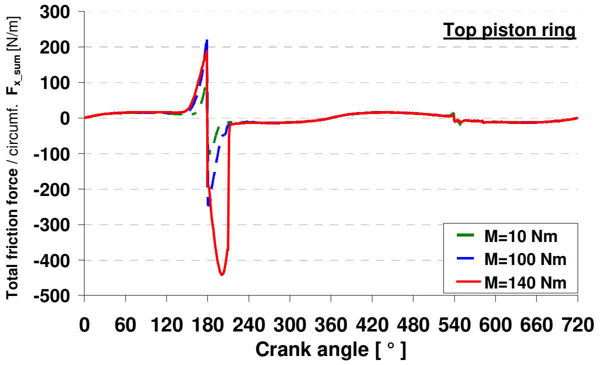

Fig. 9. Variation of total friction unit force F_x for the top piston ring versus crank angle

Maximum values of hydrodynamic components of friction forces are much lower than components of elastic contact forces – at high engine load, these components are equal to17 N/m) and 425 N/m, correspondingly. The mixed friction forces are particularly noticed near the top dead centre (at the beginning of the expansion phase), where the highest gas pressure and oil temperature are reached. The sign change of these forces at TDC results from the change in the direction of piston movement. The higher engine load, the bigger value of total friction force acting on the sliding surface of the top ring can be observed. The following maximum total friction forces (per unit of piston ring circumference) of the top ring can be seen: 111 N/m at low load, 246 N/m at medium load, and 440 N/m at high load.

The total power losses related to the top ring motion versus crank angle are presented in Fig 10. These power losses significantly depend on instantaneous piston velocity. For this reason, their highest values of 90 W are mostly noticed at crank angles of 90°, 270°, 450° and 630°, where the maximum piston velocity is reached, and they drop almost to zero at piston reverse points. Although the piston velocity is equal to zero at the reverse points, the total power loss can be different from zero because of the ring squeezing velocity $\partial h/\partial t$ (see Eq. (8)). The total power losses significantly depend on the engine load (Fig. 10). This is primarily due to asperity contact – hydrodynamic friction only slightly depends on the engine load, while the elastic contact forces due to surface roughness depend very strongly, primarily at the beginning of the expansion stroke.

In Fig. 11 the variations of the minimum oil film thickness in the gap of the top piston ring versus crank angle for three chosen engine loads are shown. It should be explained that hydrodynamic forces generated in the gap between liner and ring lip are proportional to the ring axial velocity.

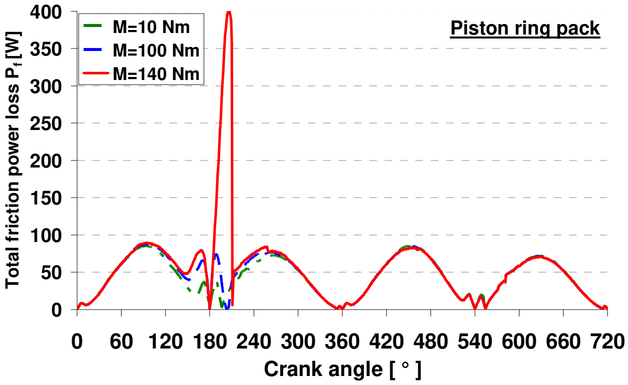

Fig. 10. Variations of total friction power loss P_f versus crank angle

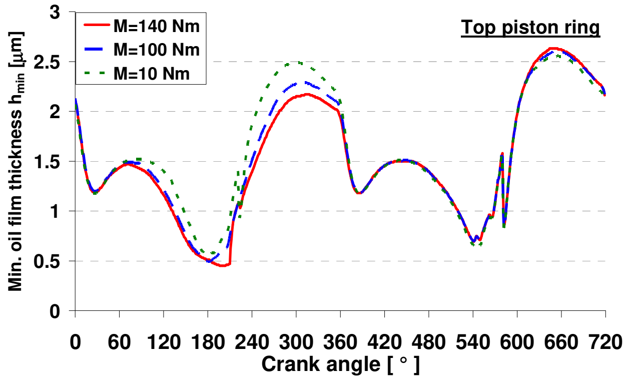

Fig. 11. Variations of the minimum oil film thickess in the gap of the top piston ring versus crank angle for three engine loads

During a cycle, the axial velocity tends to zero near the turning points (TDC and BDC). In these areas, the oil film thickness is strongly reduced, because the only force acting against the gas and ring stiffness forces is the hydrodynamic force generated by the squeeze velocity.

The higher engine load, the lower oil film thickness of the top ring can be observed, especially in compression and expansion strokes. In other two strokes a negligible influence of the engine load on the minimum oil film thickness is noticed.

The motion of the ring pack scrapes and distributes the oil on the cylinder liner leaving the oil film profiles shown in Fig. 12. An uneven oil film distribution along the cylinder liner can be clearly seen.

Low film thickness near the piston top dead centre (TDC) and peaks of accumulated oil near the leading ring lips should be noticed. The minimum oil film thickness at TDC is about 0.35 μm and can be compared with the RMS roughness of the cylinder liner that equals 0.22 μm. The very low local values of oil film thickness near TDC can be explained by the high pressure of gas and high temperature in this area during the compression and working phases of engine operation. Due to high gas forces, piston rings are strongly pressed against the cylinder surface. On the other hand, the high temperature reduces the oil viscosity. The calculation results presented in Fig. 12 show a negligible influence of the engine load on the distribution of the oil film thickness on the cylinder surface.

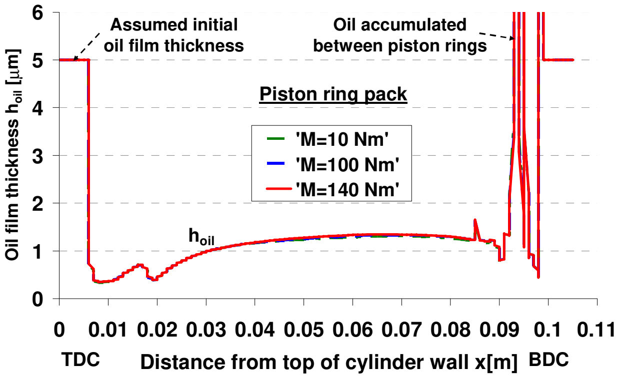

Fig. 11. Variations of the oil film thickness h_{oil} left by the ring pack along cylinder wall

All the computational results of the PRC system have been carefully analyzed using a developed computer animation program called *ANIMATE* [15–21].

5. Conclusions

The major conclusions that may be drawn from the results are as follows:

1. The developed mathematical model and simulation program gives a lot of practical information that would be more complicated and expensive to obtain using experimental methods.
2. In order to use the simulation program, a number of essential input data are needed. They include dimensions of PRC system and pressure in the combustion chamber.
3. Simulations for automotive SI engine showed that:
   - engine load affects the axial movements of the rings in the grooves,
   - engine load strongly affects the elastic contact of the ring and cylinder surface asperities, and so the total power losses due to the ring friction,
   - engine load practically does not affect the thickness of the oil film left by the ring pack on the cylinder liner.

Acknowledgments

The first author expresses his gratitude to *Wärtsilä's R&D* engine centre (nowadays: *Winterthur Gas & Diesel Ltd.*) in Winterthur (Switzerland) for having the opportunity to work on projects concerning mathematical modelling and numerical simulation of tribological systems of piston rings during several research periods at this company.

Nomenclature

PRC	piston-ring-cylinder
TDC	top dead center
BDC	bottom dead center
RMS	root mean square

Bibliography

[1] BOLANDER, N.W., STEENWYK, B.D., SADEGHI, F. et al. Lubrication regime transitions at the piston ring – cylinder liner interface. *Proceedings of the Institution of Mechanical Engineers, Part J: Journal of Engineering Tribology.* 2005, **219**, 19-31. https://doi.org/10.1243/135065005X9664

[2] DOWSON, D. Piston assemblies: background and lubrication analysis. *Engine Tribology*. Elsevier, Amsterdam 1993. https://doi.org/10.1016/S0167-8922(08)70013-0

[3] GREENWOOD, J., TRIPP, J.H. The contact of two nominally flat rough surfaces. *Proceedings of the Institution of Mechanical Engineers*. 1971, **185**, 625-633. https://doi.org/10.1243/PIME_PROC_1970_185_069_02

[4] GULWADI, S.D. Analysis of tribological performance of a piston ring pack. *Tribology Transactions.* 2000, **43**(2), 151-162. https://doi.org/10.1080/10402000008982325

[5] HEYWOOD, J.B. Internal combustion engine fundamentals. *McGraw-Hill Inc*. 1988.

[6] HOLMBERG, K., ERDEMIR, A. The impact of tribology on energy use and CO_2 emission globally and in combustion engine and electric cars. *Tribology International*. 2019, **135**, 389-396. https://doi.org/10.1016/j.triboint.2019.03.024

[7] KNOLL, G., PEEKEN, H., LECHTAPE-GRÜTER, R. et al. Computer-aided simulation of piston and piston ring dynamics. *Journal of Engineering for Gas Turbines and Power.* 1996, **118**, 880-886. https://doi.org/10.1115/1.2817009

[8] KOSZAŁKA, G., HUNICZ, J. Comparative study of energy losses related to the ring pack operation in homogeneous charge compression ignition and spark ignition combustion. *Energy*. 2021, **235**, 121388. https://doi.org/10.1016/j.energy.2021.121388

[9] KOSZAŁKA, G., NIEWCZAS, A., GUZIK, M. Predicted and actual effect of cylinder liner wear on the blowby in a truck diesel engine. *SAE Technical Paper* 2008-01-1717. 2008. https://doi.org/10.4271/2008-01-1717

[10] KOSZAŁKA, G. Application of the piston-rings-cylinder kit model in the evaluation of operational changes in blowby flow rate. *Eksploatacja i Niezawodność – Maintenance and Reliability*. 2010, **4**, 72-81.

[11] KOSZAŁKA, G., GUZIK, M. Mathematical model of piston ring sealing in combustion engine. *Polish Maritime Research*. 2014, **4**(84), 66-78. https://doi.org/10.2478/pomr-2014-0043

[12] PATIR, N., CHENG, H.S. An average flow model for determining effects of three-dimensional roughness on partial hydrodynamic lubrication. *Journal of Tribology.* 1978, **100**(1), 12-17. https://doi.org/10.1115/1.3453103

[13] PATIR, N., CHENG, H.S. Application of average flow model to lubrication between rough sliding surfaces. *Journal of Tribology.* 1979, **101**(2), 220-229. https://doi.org/10.1115/1.3453329

[14] TIAN, T. Dynamic behaviors of piston rings and their practical impact-part ii: oil transport, friction, and wear of ring/liner interface and the effects of piston and ring dynamics. *Proceedings of the Institution of Mechanical Engineers, Part J: Journal of Engineering Tribology.* 2002, **216**, 229-247. https://doi.org/10.1243/135065002760199970

[15] WOLFF, A. Experimental verification of the model of piston ring pack operation of an internal combustion engine. *The Archive of Mechanical Engineering*. 2009, **56**(1), 73-90. https://doi.org/10.24425/ame.2009.132089

[16] WOLFF, A. Influence of engine load on piston ring pack operation of a marine two-stroke engine. *Journal of KONES Powertrain and Transport*. 2012, **19**(2), 557-569. https://doi.org/10.5604/12314005.1138276

[17] WOLFF, A. Simulation based study of the system piston-ring-cylinder of a marine two-stroke engine. *Tribology Transactions.* 2014, **57**(4), 653-667. https://doi.org/10.1080/10402004.2014.895886

[18] WOLFF, A. Influence of sliding surface roughness and oil temperature on piston ring pack operation of an automotive IC engine. *IOP Conference Series: Materials Science and Engineering*. 2016, **148**, 1-10. https://doi.org/10.1088/1757-899X/148/1/012090

[19] WOLFF, A. Numerical analysis of gas flow through the labyrinth seal of piston rings of an automotive IC engine. *IOP Conference Series: Materials Science and Engineering*. 2018, **421**, 1-11. https://doi.org/10.1088/1757-899X/421/4/042082

[20] WOLFF, A. Influence of piston ring profiles and oil temperature distribution on cylinder liner lubrication of a marine two-stroke engine. *Combustion Engines*. 2019, **178**(3), 257-263. https://doi.org/10.19206/CE-2019-345

[21] WOLFF, A. Numerical analysis of the system piston-ring-cylinder of an automotive IC engine. *SAE Technical Paper* 2020-01-2160, 2020. https://doi.org/10.4271/2020-01-2160

Andrzej Wolff, DSc., DEng. – Faculty of Transport of Warsaw University of Technology.

e-mail: *wolff@wt.pw.edu.pl*

Prof. Grzegorz Koszałka, DSc., DEng. – Faculty of Mechanical Engineering, Lublin University of Technology.

e-mail: *g.koszalka@pollub.pl*

Article citation info:
AUGUSTYNOWICZ, A. Tendencies in development of energy assistance systems in an electric car. *Combustion Engines*. 2022, **190**(3), 95-103. https://doi.org/10.19206/CE-145714

Andrzej AUGUSTYNOWICZ

Combustion Engines
Polish Scientific Society of Combustion Engines

Tendencies in development of energy assistance systems in an electric car

ARTICLE INFO

Received: 2 December 2021
Revised: 6 January 2022
Accepted: 11 January 2022
Available online: 14 February 2022

As awareness regarding ecology increases among drivers, some characteristics of electric vehicles mean that they attract a greater interest. The basic factors determining the demand for electric cars include their pricing, access to charging stations and the cost per 1 kWh. Considering the above, the aim of this paper is to review the current areas of research into renewable energy sources, such as wind and solar energy and energy derived from vertical displacements of the car body associated with road roughness. The use of such solutions will allow the battery to be charged while the vehicle is in motion and extend the time of travel without stopping the vehicle for charging. The publication forms an overview of findings in the area and the scope of the research reported here relate to the most recent research. For this purpose, reviews of academic and industrial literature were carried out.

Key words: *electric cars, renewable energy, wind turbine, photovoltaic systems, regenerative shock absorber*

1. Introduction

Nowadays in the world, where carbon dioxide emissions and pollution form a major concern, electric cars are becoming more and more attractive. In comparison with cars running on petroleum-derived fuels, electric vehicles generate little or no greenhouse gases and air pollutants. As a result of the advances in the automotive technology, we have faced considerable progress in electric car design in recent years. Almost every major car maker in the world is now starting to develop fully electric models. In addition, due to incentives and campaigns customers are also attracted by the idea of using an electric car.

The Allied Market Research (AMR) [1] report, which provides a thorough analysis of the automotive market, reveals an exponentially growing demand for fuel-efficient, high-performance, low-emission vehicles. The report also contains a statement that the growth in this demand can be encouraged by restrictive government emissions regulations in many countries. On the other hand, technological advances and proactive government initiatives are providing the automotive market with exponential growth (Fig. 1). Allied Market Research is the market research and business consultation division of Allied Analytics LLP. AMR provides global enterprises as well as medium and small businesses with reports on market research and Business Intelligence solutions. Its role includes advice and support to their clients in making strategic business decisions in relevant market areas. In a report by this company [1], we can read that the global electric vehicle market is segmented by vehicle type, type and class, and region. By type, it is divided into Battery Electric Vehicle (BEV), Hybrid Electric Vehicle (HEV) and Plug-in Hybrid Vehicle (PHEV). According to vehicle type, it is classified into two-wheelers, passenger cars and commercial vehicles. Due to the class of the vehicle, it is divided into the mid-price and luxury class. By region, the market is analyzed in North America (United States, Canada and Mexico), Europe (Germany, France, UK, Netherlands, Norway and the rest of Europe), Asia-Pacific (China, Japan, Singapore, South Korea and the rest of Asia Pacific) and LAMEA (Latin America, Middle East and Africa).The key players in the electric vehicle market include Tesla, BMW Group, Nissan Motor Corporation, Toyota Motor Corporation, Volkswagen AG, General Motors, Daimler AG, Energica Motor Company SpA, BYD Company Motors and Ford Motor Company.

The authors of the report indicate some of the advantages of electric cars that can play a decisive role on their attractiveness compared to cars with classic engines:

1. Electric vehicles are characterized by lower operating costs compared to traditional cars. Although the mechanical parts in an electric vehicle are expensive, the number of parts is smaller. This also reduces the risk of mechanical failure. In addition, regular maintenance required on conventional cars, including oil changes, fluid supplement and the supply of other consumables, is not required in electric vehicles. Although the need to replace the battery is the only big expense in electric vehicles, such cars offer sufficient mileage prior to the need to do so.
2. Electric vehicles are characterized by smaller pollutions than traditional cars as they do not emit exhaust gases. In addition, electric vehicles can be charged using renewable energy, sources which can further reduce greenhouse gas emissions. On the other hand, manufacturers are also taking initiatives for more environmentally friendly methods in manufacturing electric vehicles. Several companies use recycled and bio-based materials to produce electric vehicles.
3. Electric cars have a lower center of gravity which reduces the likelihood of a vehicle rolling over. The risk of fires and explosions is also reduced. Moreover, it is much quieter than a traditional car and more dynamic in city traffic due to the better torque characteristics of the electric motor.

Electric cars use batteries as their primary power source. However, an important disadvantage of electric cars is related to the significantly shorter range compared to the vehicles with classic ICEs. In city class cars, the range ranges from 100 to 120 km, and in the case of top-of-the-range cars, it is around 500 km. Manufacturers try to solve this problem place in electric cars as large batteries as possible for the purpose of and possible additional energy generation and storage units [2]. Fortunately, intensive research is underway to develop batteries that will make electric cars more attractive [3]. China appears to be the first region to undertake a transition from conventional to electric vehicles, but its perspective in time is still uncertain. Europe is likely to be next, due to legal regulations and determination to fight climate change [4].

Electric cars (EVs) currently provide the best performance in terms of energy-efficiency (Fig. 2). Their efficiency ranges from 60% to 66% in the urban driving cycle. However, if this balance was to include the energy recovery from regenerative braking (converted after reuse), we find out that the efficiency of electric cars ranges from 86% to 94%. For comparison, in a car with a conventional combustion engine (ICE) in urban driving conditions only 12–25% of the energy derived from fuel is used to drive the car. Most of the energy is lost by the internal combustion engine in the form of heat, frictional losses and ineffective combustion. In the urban driving cycle, hybrid cars have at their disposal 21–40% of energy derived from fuel and electrochemical battery [5, 6].

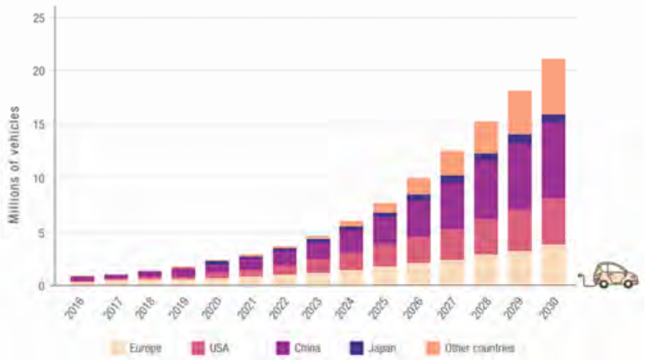

Fig. 1. Global growth of the electric vehicle market (Bloomberg New Energy Finance (BNEF))

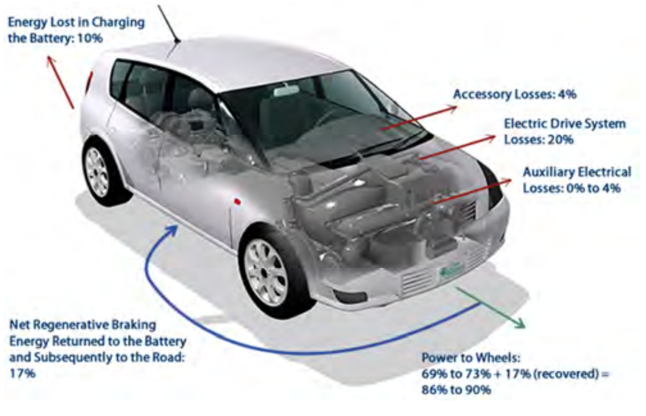

Fig. 2 Electric car energy requirements for combined City/Highway driving [5]

In an electric car, energy is employed for a variety of purposes. Most of the energy is used as the source of power to the wheels (as the energy of motion). A significant amount of energy is also delivered to power the auxiliary devices (lights, drive assistance systems, sound system, etc.). There are cooling and heating systems necessary to ensure proper operation of the powertrain system (electric motor, batteries).

We can assume that for most lithium-ion cells, the permissible operating temperature is in the range of 15–50°C. Below this range, the battery is already operating with limited efficiency. However, when this temperature range is exceeded, the cell can be damaged. For this reason, producers of electric cars choose a cooling system that is appropriate to a given type of cell and the maximum current intensity associated with it [7].

In addition, heating as well as air conditioning of the interior of the passenger compartment also requires considerable amounts of energy. It has been shown that, depending on the ambient temperature conditions, the use of the air conditioning system may reduce the accessible range by around 18–37% [8, 9].

2. Current requirements for electric vehicles

The development of electric cars is mainly relative to the capacity of energy storage equipment. Batteries form the leading element. The lithium-ion battery is one of the promising battery technologies and, therefore, it plays the dominant role in new electric cars (Fig. 3). Arguments such as life cycle, high energy density, high efficiency, low self-discharge as well as low maintenance costs are usually provided as the main reasons for the use of lithium-ion batteries in electric cars [10, 11]. However, a rather complex temperature monitoring system [12] as well as charging and discharging cycles [13] are assumed in such conditions.

Even for the case when batteries have high energy density, they generally have a low power density, making them an element with a low efficiency for rapid energy transformations [14]. Therefore, it is beneficial to combine the batteries with another storage element with complementary properties, such as an ultracapacitor (UC), which provides high power density combined with low energy density [15]. Moreover, the degradation of batteries is accelerated when they are subjected to discontinuous or rapidly changing current profiles (e.g. as a result of abrupt acceleration and braking cycles) [16]. However, the use of an ultracapacitor (UC) leads to the slowing of the battery degradation process.

One of the main factors that can limit the popularity of electric cars is related to the limited driving range. An effective solution to this problem is associated with maximization of the energy efficiency of electric vehicles in order to increase their driving range. As regenerative braking forms a key technology for electric vehicles, this area is of constant interest to researchers (Fig. 4) [17, 18].

A system based on single-pedal electric vehicle control was developed in order to further improve conventional regenerative braking systems and their energy recovery capacity. The brake pedal is only employed for emergency braking [19].

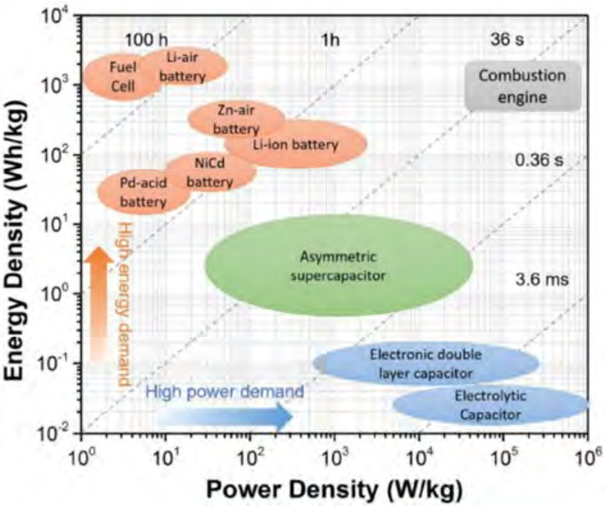

Fig. 3. Ragone plot illustrating the performance of specific power vs specific energy for different electrical energy-storage technologies [11] (times shown in the plot represent discharge times, obtained by dividing the energy density by the power density)

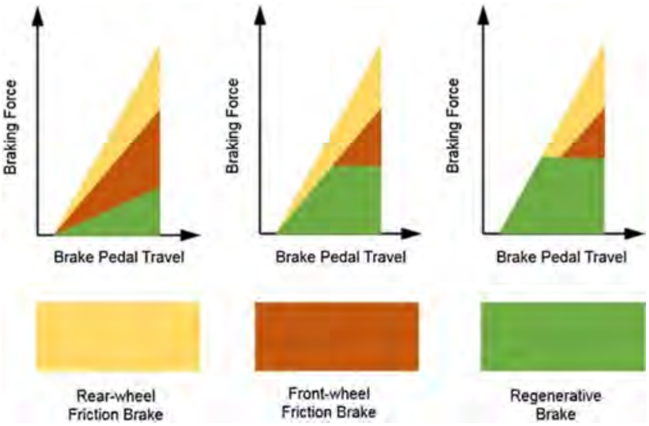

Fig. 4. Three different control strategies applied in regenerative braking process [17]

The simulation results demonstrated that the car deceleration control by one pedal has met the requirements for vehicle braking, and the braking distance complied with safety regulations. The simulated NEDC urban driving cycle performed on a mid-range passenger car showed an energy recovery of 26.12%. Verification of the NEDC cycle on a chassis dynamometer showed a similar level of energy recovery, lower by 0.48% [20].

3. Power management systems

Energy management systems in electric cars form one of the most important and popular areas of research at present. Over the past few decades, several types of energy management strategies have been developed for hybrid cars. These strategies can be classified according to two main categories: one is based on the heuristic concept; the second is based on the theory of optimal control. The first one mainly includes algorithms based on learning rules and fuzzy logic [21, 22]. Initially, energy management strategies were dominated by such algorithms due to their simplicity in implementation. However, such strategies cannot guarantee optimal power distribution between energy sources and consumers. In addition, fuzzy rules and logic require expert knowledge. To solve this problem, the theory of optimal control was originally proposed, including both dynamic programming, developed by R.E. Bellman [23] and the Pontryagin minimum principle (PMP) [24–26]. Over time, mainly due to the fact that the computation time was too long, the real-time control had to be modified. Some researchers have proposed stochastic dynamic programming (SDP) [27] to overcome this problem.

4. Current directions of research into development of electric vehicles

The useful parameters of electric vehicles are related to their primary source of energy, that is, batteries. The travel range expected by drivers requires high-capacity batteries. Current lithium-ion batteries are characterized by the quick discharge cycle and thus require frequent recharging. Due to this disadvantage, people are discouraged from electric vehicles.

In order for the batteries to easily meet the requirements presented above, ultracapacitors with excellent parameters, in particular at low temperatures, are installed in cars. Managing the operation of an ultracapacitor with a lithium-ion battery requires the use of a hybrid energy storage system (HESS) with a properly developed management strategy [28].

Regardless of the above, attempts are made to implement solutions, systems that can charge the battery while the vehicle is in motion and extend the driving range without the need to stop for recharging.

Considering the above, the aim of the publication is to review the research carried out using renewable energy sources, such as wind and solar energy, and energy derived from vertical displacement of a car driving on road roughness.

4.1. Wind energy

A wind turbine with a vertical axis can be used to utilize wind energy in a car [29]. If such a turbine was installed inside the front grille of a vehicle, the turbine could be applied for generating power. As the vehicle drives, air flows through the vehicle's grille and drives the turbine. There will be variations in the flow rate of air entering the vehicle depending on the vehicle speed. If the vehicle is traveling at a higher speed, the airflow will be greater. The research carried out by Niranjana [30] found that when the vehicle is traveling at a speed of 90 km/h, the wind turbine is capable of generating 1000 W of power. Altab Hossain et al. [31], tested a similar turbine for a wind speed of 90 km/h and obtained power output of 709 W, and at 72 km/h, the output would be equal to 567 W.

The study by Niranjana found that the efficiency of a turbine can be increased by modifying its size and blade design. A similar conclusion was also offered by Nikam and Kherde [32] who additionally analyzed wind turbines with a horizontal axis. In turn, Gulve and Barve [33] comparing wind turbines found that those with the vertical axis provide a greater efficiency. On the other hand, Awal et alia [34], examined horizontal axis wind turbines to demonstrate the effect of the use of a diffuser on the volume of power that is generated.

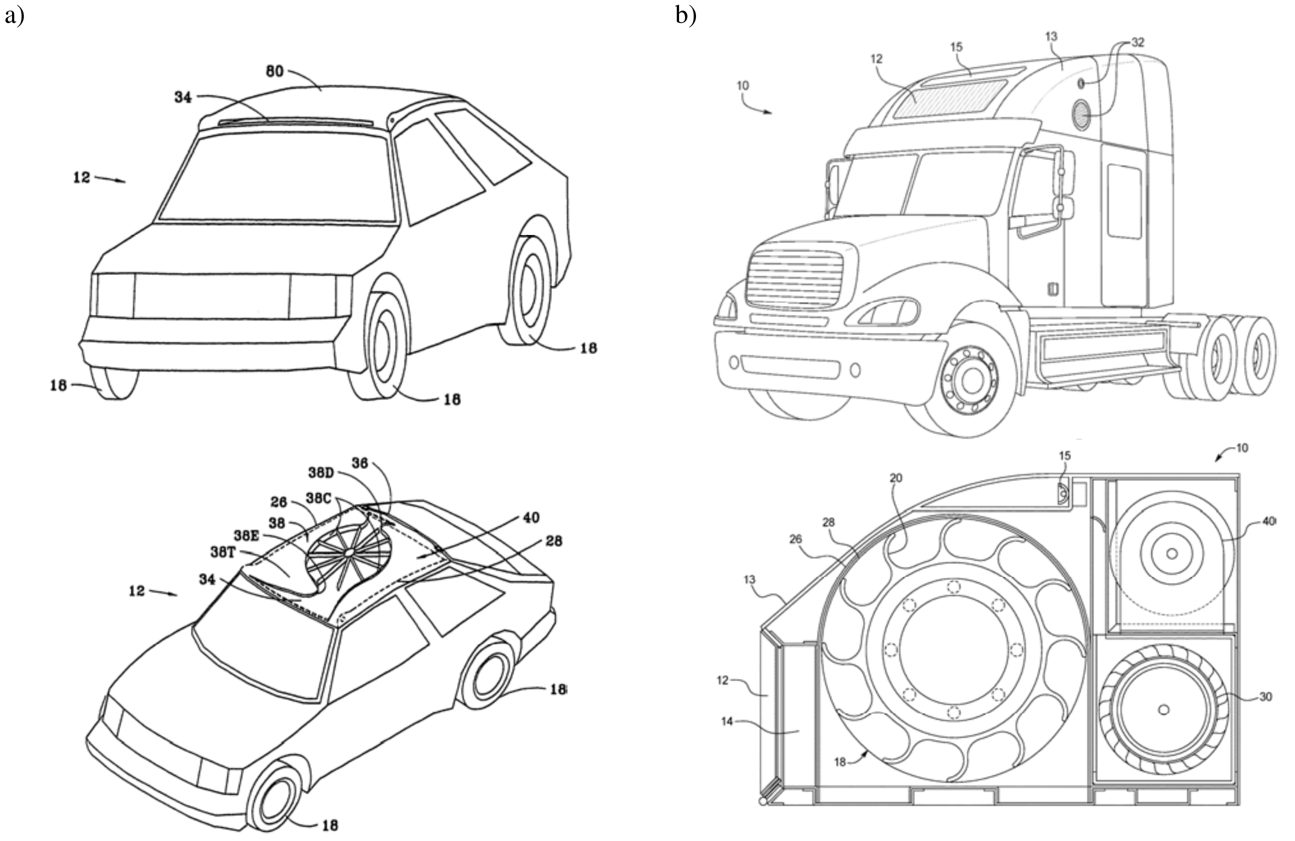

Fig. 5. Systems for harnessing wind energy: a) US Patent 10358038B1 [35], b) US Patent 10655604B1 [36]

A variety of ideas for electricity storage systems using a wind-powered turbine have been presented in the form of patents for many years. The most up-to-date is the system of using wind energy to charge the vehicle's electric battery, regardless of whether the vehicle is parked or in motion. It was presented in the result of research and patent by Peter W. Ripley (Fig. 5a) [35]. In this study, a roof-mounted double vertical wind turbine was proposed that is connected to an electric generator, which could use wind energy both when the vehicle is in motion and when it does not move.

Another current invention of James R. Parker (Fig. 5b) [36] involves a generator and an electrical energy storage system using a wind turbine assisted by the exhaust air system. The vehicle-mounted energy generator and energy storage system includes: an air intake with a shield facing the front of the vehicle through which air enters when the vehicle drives. A cylindrical air rotor assembly including one or more integrated blades positioned such that air flowing through the air inlet applies a positive pressure to the one or more rotor blades that drive one or more generators. One or more batteries are applied to store the energy generated by the rotor assembly.

4.2. Solar energy

Despite spectacular results in competitions such as the World Solar Challenge, vehicles that are powered exclusively by the sun do not offer a practical alternative to conventional cars due to significant limitations in maximum power and range. On the other hand, photovoltaics can be an effective and clean additional source of energy for electric vehicles (Fig. 6) [37].

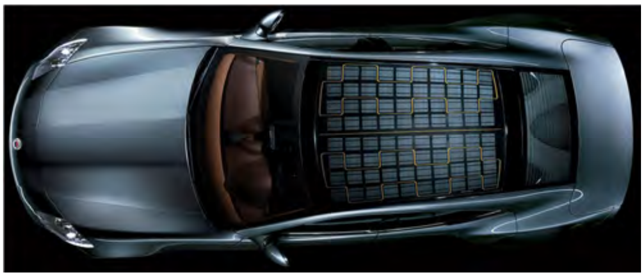

Fig. 6. Solar roof of the KARMA Revero [37]

A power supply system applicable for the cooling of the interior of the vehicle cabin provides a practical idea including simplest form of a solar panel, proposed and tested by Yan, Tseng and Leong [38]. This solution offers the removal of hot air from the car interior that can be replaced with cool fresh air from the outside environment. The assembly consists of a solar cell panel with a capacity of 27 W, four fans and a battery with a capacity of 850 mAh. This kit for self-assembly (KIT) weighs less than 1500 g. It has been found that a fully charged battery is capable of driving the fans for approximately 45 minutes. The time obtained may seem very short. However, we should remember that cloudy skies also mean low sun exposure and therefore the need for removing hot air from the cabin is reduced.

The space available for solar panels in cars is quite limited for stationary applications. It is therefore mandatory to maximize their performance and accurately forecast useful energy production [39]. A quantitative assessment of the contribution of solar energy is needed when carrying out a cost-benefit analysis of the design of a solar powered vehicle. The research carried out in this matter [40] demonstrated that the roof panel of the FIAT Punto passenger car (Fig. 7) reached a maximum output of 165 W on a sunny summer day, while the panel on the front hood reached a total power of 75 W (Fig. 8). The efficiency of the modules is influenced by temperature, which reduces the efficiency of the roof panel to 18% and of the hood panel to 19.8%.

Fig. 7. Hybrid Solar Vehicle prototype [40]

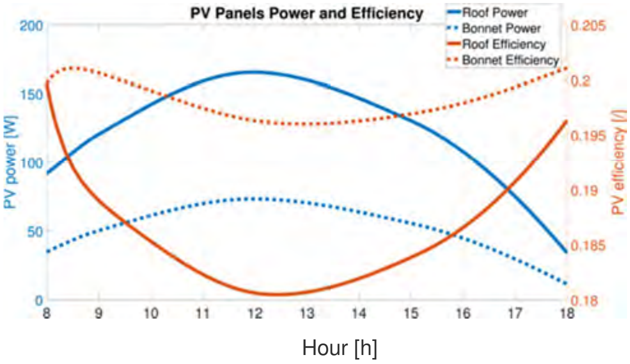

Fig. 8 Power and efficiency of the PV panels during parking on August 5th [40]

The potential benefits of solar energy are clearly visible indeed: it is free and plentiful but there are also limitations such as weather conditions and last but not least is the solar flux density. If solar panels are to be properly designed and utilized, they can generate a part of the total energy needed by a car in particular in the conditions of city driving. Moreover, their economic feasibility in automotive applications appears to be increasingly encouraging, due to the spectacular cost reductions that we have faced in recent decades [41]. In fact, in recent years, more and more attention has been paid to integrating photovoltaics, especially in electric cars [42, 43]. The energy gain of the photovoltaic system integrated in the vehicle differs from the designs applied in the standard photovoltaics.

This is mainly due to the difference in the intensity of solar radiation on the car roof and the body due to its variable orientation in relation to the sun, as well as its curved shape. Car manufacturers forecast that photovoltaic panels that will have a curved shape to fit the car's bodywork. In the publication [42], a method of assessing the efficiency of photovoltaic panels was developed and a correction factor was proposed that takes into account the curvature of the car body and the irregular distribution of sunlight and shade on the curved surface of car panels. The publication [43] estimated that replacing all classic passenger cars in Japan with hybrid vehicles comprising a photovoltaic module with a rated power of 800 W, that is capable of generating a mean power of 1.8 kWh/day, would reduce CO_2 emissions by 63%. To confirm the reliability of this statement, photovoltaic modules were installed on a Toyota Prius test car (Fig. 9) on all possible body surfaces with a total area of 6.8 m^2, achieving an average output of 2.1 kWh/day.

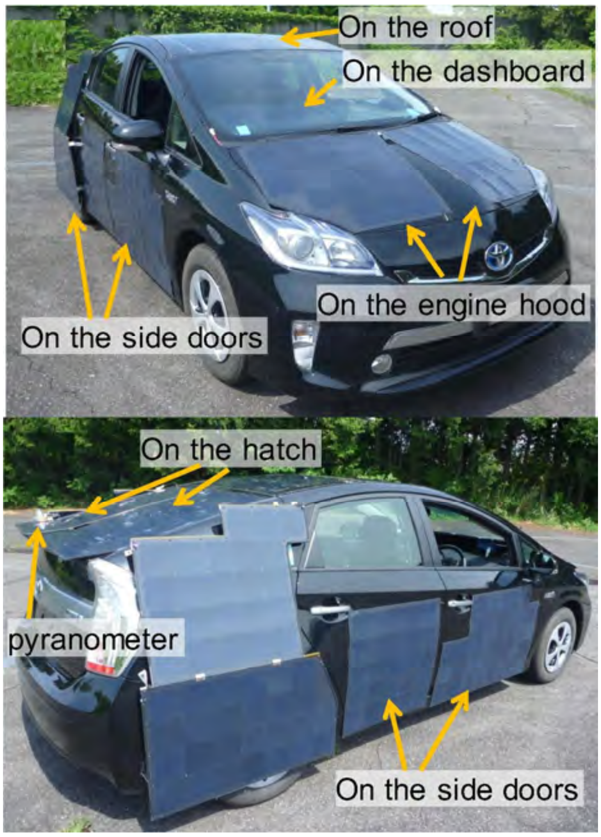

Fig . 9 Test vehicle Toyota Prius [43]

The study reported in [44] indicates that a typical roof area (1.7–2.0 m²) of a medium-class car, comprising a photovoltaic panels with a power (340–500 W), can yield an additional driving range per year in the range from 1900 up to 3,400 km (Table 1). Fig. 10 shows the range of the potential offered by the photovoltaics used on selected cars. The presented data does not take into account the conditions when the battery is fully charged when solar energy is not available.

Table 1. Investigated types of electric vehicles and selected parameters corresponding to them [44]

Vehicle	Consumption [kWh/100 km]	Battery capacity [kWh]	Range [km]	Roof area [m^2]	Potential solar power [W]	Yearly energy yield [kWh]	Yearly solar driving range [km]
Audi e-tron	24,0	95	436	2,3	460	495	2063
BYD e6	21,5	80	400	2,2	440	473	2200
Chevrolet Bolt EV	16,0	60	380	2,0	400	430	2688
Hyundai Ioniq Electric	13,8	38,2	311	2,2	440	473	3428
Daimler EQC	23,5	80	390	2,1	420	452	1923
Nissan Leaf	20,0	40	270	1,8	360	387	1935
Tesla Model 3	16,0	75	560	2,5	500	538	3363
Volkswagen ID3	14,0	77	550	1,9	380	409	2921
BMW i3	13,1	37,9	359	1,9	380	409	3122
Renault ZOE	17,7	52	386	1,7	340	366	2068

The latest development takes the form of Lightyear One (Fig. 11), solar powered car with a range of 725 km. A photovoltaic module with an area of 5 m^2 and rated power of 1075 W was installed on the vehicle [45]. The range of the vehicle is influenced by its energy consumption, which results from the low drag coefficient equal to 0.2, lightweight construction, including the battery, and the innovative Turanza Eco tires developed by Bridgestone [46] with very low rolling resistance (Fig. 12).

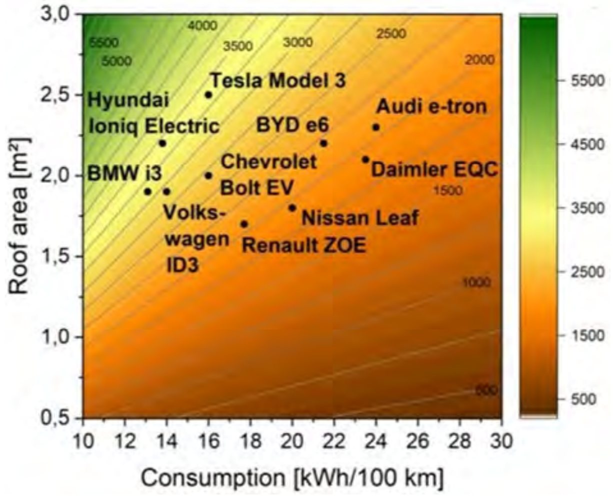

Fig. 10. Potential solar range for different electric vehicles depending on available horizontal roof area and consumption [44]

Fig. 11. Lightyear One – Solar Electric Powered Car [45]

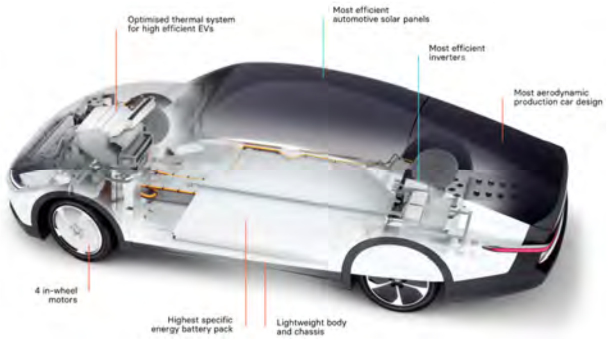

Fig. 12. Lightyear One – main components [45]

4.3. Energy of damper vibration

Nearly all cars apply dampers to absorb vibrations from road roughness. Energy in conventional shock absorbers is dissipated in the form of heat and is not utilized in any way. The energy recovery system not only recovers vibration energy, but also converts it into electrical energy that can be stored in batteries as a source of power. Since the idea of energy recovery was intensified in the last century, energy efficiency has gained in importance in the automotive industry, the research of suspensions with energy recovery systems was revived to [47].

The publication [48] contains an outline of a suspension system with energy recovery with an energy efficiency of 55% found while driving on the road with a intermediate-class surface quality, at a speed of 60 km/h. In selected passenger cars, off-road vehicles and trucks, power was obtained with the following values: 105.2 W, 384 W and 1152 W, respectively.

The publication [49] presents a system with the mean efficiency of 40%, and the maximum 52%. The power recorded in the system was 270 W.

A similar effect in terms of the amount of power recovered by a vehicle in urban traffic can be found in the publication [50]. The obtained power ranges from 71.3–387 W. Simulation and bench tests carried out in 2019-2020, on the basis of available technologies and control techniques, did not demonstrate a significant improvement in the efficiency of the suspension with energy recovery [51–54]. For vehicles driving on the road, the surface quality of the middle class ranges from 100 W to 400 W.

There is agreement in the above-mentioned tests that the damping characteristics and the level of energy regeneration in the suspension system with energy recovery are mainly influenced by the damping force, road roughness, vehicle speed, suspension stiffness, tire stiffness, wheels and wheel mass.

The up-to-date active suspension systems require energy for the power supply and control the actuator assembly. Thus, one of the most interesting goals to be achieved by the researchers [55, 56] involved the achievement of such efficiency of the energy recuperation of suspension vibrations that did not only meet the demand for energy consumption by the active suspension but also offered some excess.

5. Conclusion

Electric cars will be the future of automotive industry. We can note that car manufacturers now add more and more electric vehicles to their range of vehicles. Everyone works on electric vehicles, from reputable manufacturers to the ones that create new brands. The era of modern electric vehicles has only just begun. New electric vehicles have greater capacities, cheaper, safer and more reliable.

In Poland, in recent years, many stations have been built, but they are not well equipped. Only a small number of stations have chargers for quick charging. This is important, especially for high-powered cars. Then the charging time using the DC charger is significantly longer. Such situation has a negative impact on the increased sales of electric cars in Poland [57].

We are facing conditions in which electric vehicles that offer a range exceeding 200 km on a single charge start to become common, with a note that the latest Tesla Model S Long Range Plus claims to offer a maximum range of 550 km. Electric car makers are eagerly awaiting a battery breakthrough that will improve vehicle range as well as the battery life itself. The start-up company Innolith was developing a high-density lithium-ion battery (1000 Wh/kg) that could solve both of these problems [58].

The latest patents in terms of weight reduction and battery performance include the developments of lithium-sulfur cells. These are fully compostable biodegradable organic batteries that will not only offer an adequate environmental option but will also charge them very quickly. They are also significantly lighter. The newest lithium-sulfur (Li-S) battery offered on the market offers an energy density of 2567 Wh/kg, reflecting up to a three to fivefold increase in performance over current Lithium-Ion (Li-Ion) design counterparts [59, 60].

Electric vehicles design involving lightweight materials and the use of composites will undoubtedly play their part. However, this can be a much greater role than simply reducing vehicle weight, but also improving safety in case of accidents, driving dynamics and overall vehicle strength. Particular proposals in terms of weight reduction include increasingly lighter composite materials used in battery housings. Additionally, they play an important role as insulation, as they perform better than classic materials, maintaining the batteries at their operating temperature (thermal equilibrium state) [61].

The use of renewable energy sources such as wind and solar energy forms some of the issues that are frequently considered by research centers with the purpose of improving the energy balance of electric cars. The proposed solution offers measurable benefits and is only a matter of assessing the rationale and economic justification of their use by a specific manufacturer of electric cars.

The same question applies to the use of energy derived from vertical displacements of a vehicle in motion due to road roughness. However, it should be remembered that the amount of energy that can be recovered depends on the degree of roughness of the road surface and the speed of the car. If we assume that the road infrastructure will be characterized by better quality of road surfaces over time, the use of a depreciation system with energy recovery may turn out to be ineffective.

Bibliography

[1] Electric vehicle market – global opportunity analysis and industry forecast, 2020-2027, 2020.

[2] SKOURAS, T., GKONIS, P., ILIAS, C. et al. Electrical vehicles: current state of the art, future challenges, and perspectives. *Clean Technologies*. 2019, **2**(1), 1-16. https://doi.org/10.3390/cleantechnol2010001

[3] SHARMA, S., PANWAR, A.K., TRIPATHI, M.M. Storage technologies for electric vehicles. *Journal of Traffic and Transportation Engineering (English Edition)*. 2020, **7**(3), 340-361. https://doi.org/10.1016/j.jtte.2020.04.004

[4] BARKENBUS, J.N. Prospects for electric vehicles. *Sustainability*. 2020, **12**(14), 5813. https://doi.org/10.3390/su12145813

[5] Where The Energy Goes: Electric Cars, 2020.

[6] THOMAS, J. Drive cycle powertrain efficiencies and trends derived from EPA vehicle dynamometer results. *SAE International Journal of Passenger Cars – Mechanical Systems*. 2014, **7**(4), 1374-1384. https://doi.org/10.4271/2014-01-2562

[7] LECHOWICZ, A., AUGUSTYNOWICZ, A. Problems of electricity and thermal management of an exemplary electric vehicle. *Maszyny Elektryczne – Zeszyty Problemowe*. 2018, **3**(119), 43-47

[8] XIE, Y., ZHAOMING, L., KUINING, L. et al. An improved intelligent model predictive controller for cooling system of electric vehicle. *Applied Thermal Engineering*. 2021, **182**, 116084. https://doi.org/10.1016/j.applthermaleng.2020.116084

[9] PAN, L., LIU, C., ZHANG, Z. et al. Energy-saving effect of utilizing recirculated air in electric vehicle air conditioning system. *International Journal of Refrigeration*. 2019, **102**, 122-129. https://doi.org/10.1016/j.ijrefrig.2019.03.018

[10] MIAO, Y., HYNAN, P., VON JOUANNE, A. et al. Current Li-Ion battery technologies in electric vehicles and opportunities for advancements. *Energies*. 2019, **12**(6), 1074. https://doi.org/10.3390/en12061074

[11] SHAO, Y., EL-KADY, M.F., SUN, J. et al. Design and mechanisms of asymmetric supercapacitors. *Chemical Reviews*. 2018, **118**(18), 9233-9280. https://doi.org/10.1021/acs.chemrev.8b00252

[12] WU, S., XIONG, R., LI, H. et al. The state of the art on preheating lithium-ion batteries in cold weather. *Journal of*

Energy Storage. 2020, **27**, 101059. https://doi.org/10.1016/j.est.2019.101059

[13] SHEN, S., SADOUGHI, M., CHEN, X. et al. A deep learning method for online capacity estimation of lithium-ion batteries. *Journal of Energy Storage*. 2019, **25**, 100817. https://doi.org/10.1016/j.est.2019.100817

[14] SARLIOGLU, B., MORRIS, C.T., HAN, D. et al. Driving toward accessibility: a review of technological improvements for electric machines, power electronics, and batteries for electric and hybrid vehicles. *IEEE Industry Applications Magazine*. 2017, **23**(1), 14-25. https://doi.org/10.1109/MIAS.2016.2600739

[15] SATPATHY, S., DAS, S., BHATTACHARYYA, B.K. How and where to use super-capacitors effectively, an integration of review of past and new characterization works on super-capacitors. *Journal of Energy Storage*. 2020, **27**, 101044. https://doi.org/10.1016/j.est.2019.101044

[16] JAFARI, M., GAUCHIA, A., ZHAO, S. et al. Electric vehicle battery cycle aging evaluation in real-world daily driving and vehicle-to-grid services. *IEEE Transaction Transportation Electrification*. 2017, **4**(1), 122-134. https://doi.org/10.1109/TTE.2017.2764320

[17] QIU, C., WANG, G. New evaluation methodology of regenerative braking contribution to energy efficiency improvement of electric vehicles. *Energy Conversion Management*. 2016, **119**, 389-398. https://doi.org/10.1016/j.enconman.2016.04.044

[18] KROPIWNICKI, J., FURMANEK, M. Analysis of the regenerative braking process for the urban traffic conditions. *Combustion Engines*. 2019, **178**(3), 203-207. https://doi.org/10.19206/CE-2019-335

[19] HONGWEN, H., CHEN, W., HUI, J. A single-pedal regenerative braking control strategy of accelerator pedal for electric vehicles based on adaptive fuzzy control algorithm. *Energy Procedia*. 2018, **152**, 624-629. https://doi.org/10.1016/j.egypro.2018.09.221

[20] LIU, W., QI, H., LIU, X. et al. Evaluation of regenerative braking based on single-pedal control for electric vehicles. *Frontiers of Mechanical Engineering*. 2020, **15**, 166-179. https://doi.org/10.1007/s11465-019-0546-x

[21] LI, Q., CHEN, W., LI, Y. et al. Energy management strategy for fuel cell/battery/ultracapacitor hybrid vehicle based on fuzzy logic. *International Journal of Electrical Power and Energy Systems*. 2012, **43**(1), 514-525. https://doi.org/10.1016/j.ijepes.2012.06.026

[22] LI, D., XU, B., TIAN, J. et al. Energy management strategy for fuel cell and battery hybrid vehicle based on fuzzy logic. *Processes*. 2020, **8**(8), 882. https://doi.org/10.3390/PR8080882

[23] LIN, C.C., PENG, H., GRIZZLE, J.W. et al. Power management strategy for a parallel hybrid electric truck. *IEEE Transactions on Control Systems Technology*. 2003, **11**(6), 839-849. https://doi.org/10.1109/TCST.2003.815606

[24] SERRAO, L., RIZZONI, G. Optimal control of power split for a hybrid electric refuse vehicle. *Proceedings of the American Control Conference*. 2008, 4498-4503. https://doi.org/10.1109/ACC.2008.4587204

[25] CHASSE, A., SCIARRETTA, A. Supervisory control of hybrid powertrains: An experimental benchmark of offline optimization and online energy management. *Control Engineering Practice*. 2011, **19**(11), 1253-1265. https://doi.org/10.1016/j.conengprac.2011.04.008

[26] KIM, N., CHA, S.W., PENG, H. Optimal equivalent fuel consumption for hybrid electric vehicles. *IEEE Transactions on Control Systems Technology*. 2012, **20**(3), 817-825. https://doi.org/10.1109/TCST.2011.2123099

[27] LIN, C.C., PENG, H., GRIZZLE, J.W. A stochastic control strategy for hybrid electric vehicles. *Proceedings of the 2004 American Control Conference*. 2004, **5**, 4710-4715. https://doi.org/10.23919/acc.2004.1384056

[28] XIONG, R., DUAN, Y., CAO, J. et al. Battery and ultracapacitor in-the-loop approach to validate a real-time power management method for an all-climate electric vehicle. *Applied Energy*. 2018, **217**, 153-165. https://doi.org/10.1016/j.apenergy.2018.02.128

[29] SUN, X., CHEN, Y., CAO, Y. et al. Research on the aerodynamic characteristics of a lift drag hybrid vertical axis wind turbine. *Advances in Mechanical Engineering*. 2016, **8**(1), 1-11. https://doi.org/10.1177/1687814016629349

[30] NIRANJANA, S.J. Power generation by vertical axis wind turbine. *International Journal of Emerging Research Management &Technology*. 2015, **4**(7), 1-7. http://matjournals.in/index.php/JoADD/article/view/1304

[31] HOSSAIN, A., IQBAL, A.K.M.P., RAHMAN, A. et al. Design and development of A 1/3 scale vertical axis wind turbine for electrical power generation. *Journal of Urban and Environmental Engineering*. 2007, **1**(2), 53-60. https://doi.org/10.4090/juee.2007.v1n2.053060.

[32] NIKAM, D.A., KHERDE, S.M. Literature review on design and development of vertical axis wind turbine blade. *International Journal of Engineering Research and Applications.* 2015. https://www.ijera.com/special_issue/NCERT-Nov-2015/156161.pdf

[33] GULVE, P., BARVE, S.B. Design and construction of vertical axis wind turbine. *International Journal of Mechanical Engineering and Technology*. 2014, **5**(10), 148-155.

[34] AWAL, M.R., JUSOH, M., SAKIB, M.N. et al. Design and implementation of vehicle mounted wind turbine. *ARPN Journal of Engineering and Applied Sciences*. 2015, **10**(19), 8699-8706. http://www.arpnjournals.com

[35] RIPLEY, P. Wind Turbine for Electric Car, US 10358038B1, July 2019.

[36] PARKER, J. Power evacuated, barrel impellered, pneumatic electric generating and storage system and methods (PEBI system), US10655604B1, May 2020.

[37] a2-solar Advanced and Automotive Solar Systems GmbH, 2021. www.a2-solar.com

[38] YAN, Y.-A., TSENG, C.-Y., LEONG, J.C. Feasibility of solar powered cooling device for electric car. *Energy Procedia*. 2012, **14**, 887-892, https://doi.org/10.1016/j.egypro.2011.12.1028

[39] ARAKI, K., JI, L., KELLY, G. et al. To do list for research and development and international standardization to achieve the goal of running a majority of electric vehicles on solar energy. *Coatings*. 2018, **8**(7), 251. https://doi.org/10.3390/coatings8070251

[40] TIANO, F.A., RIZZO, G., MARINO, M. et al. Evaluation of the potential of solar photovoltaic panels installed on vehicle body including temperature effect on efficiency. *eTransportation*. 2020, **5**, 100067. https://doi.org/10.1016/j.etran.2020.100067

[41] Renewable power generation costs in 2019, International Renewable Energy Agency, Abu Dhabi 2020. https://www.irena.org/

[42] ARAKI, K., OTA, Y., YAMAGUCHI, M. Measurement and modeling of 3D solar irradiance for vehicle-integrated photovoltaic. *Applied Sciences*. 2020, **10**(3), 872, https://doi.org/10.3390/app10030872

[43] MASUDA, T., ARAKI, K., OKUMURA, K. et al. Static concentrator photovoltaics for automotive applications. *Solar Energy*. 2017, **146**, 523-531. https://doi.org/10.1016/j.solener.2017.03.028

[44] HEINRICH, M., KUTTER, C., BASLER, F. Potential and

challenges of vehicle integrated photovoltaics for passenger cars. *37th European Photovoltaic Solar Energy Conference and Exhibition*. 2020, 1695-1700. https://doi.org/10.4229/EUPVSEC20202020-6DO.11.1

[45] BILLINGTON, J. Bridgestone creates special ‘EV eco tires’ for solar-powered electric car with 725km range. *Electric & hybrid vehicle technology international*. April 23, 2021. https://www.electrichybridvehicletechnology.com/

[46] Bridgestone and lightyear combine forces for the world’s first long-range solar electric powered car. *BridgestoneAmericas.com*. April 22, 2021. https://www.bridgestoneamericas.com/

[47] LV, X., JI, Y., ZHAO, H. et al. Research review of a vehicle energy-regenerative suspension system. *Energies*. 2020, **13**(2), 441. https://doi.org/10.3390/en13020441

[48] ZHANG, Y., GUO, K., WANG, D. et al. Energy conversion mechanism and regenerative potential of vehicle suspensions. *Energy*. 2017, **119**, 961-970. https://doi.org/10.1016/j.energy.2016.11.045

[49] SALMAN, W., QI, L., ZHU, X. et al. A high-efficiency energy regenerative shock absorber using helical gears for powering low-wattage electrical device of electric vehicles. *Energy*. 2018, **159**, 361-372. https://doi.org/10.1016/j.energy.2018.06.152

[50] SHI, D., PISU, P., CHEN, L. et al. Control design and fuel economy investigation of power split HEV with energy regeneration of suspension. *Applied Energy*. 2016, **182**, 576-589. https://doi.org/10.1016/j.apenergy.2016.08.034

[51] BOWEN, L., VINOLAS, J., OLAZAGOITIA, J.L. Design and potential power recovery of two types of energy harvesting shock absorbers. *Energies*. 2019, **12**(24), 4710. https://doi.org/10.3390/en12244710

[52] LI, S., XU, J., PU, X. et al. A novel design of a damping failure free energy-harvesting shock absorber system. *Mechanical Systems Signal Processing*. 2019, **132**, 640-653. https://doi.org/10.1016/j.ymssp.2019.07.004

[53] LONG, G., DING, F., ZHANG, N. et al. Regenerative active suspension system with residual energy for in-wheel motor driven electric vehicle. *Applied Energy*. 2020, **260**, 114180. https://doi.org/10.1016/j.apenergy.2019.114180

[54] ZHANG, R., ZHAO, L., QIU, X. et al. A comprehensive comparison of the vehicle vibration energy harvesting abilities of the regenerative shock absorbers predicted by the quarter, half and full vehicle suspension system models. *Applied Energy*. 2020, **272**, 115180. https://doi.org/10.1016/j.apenergy.2020.115180

[55] LIU, J., LI, X., ZHANG, X. et al. Modeling and simulation of energy-regenerative active suspension based on BP neural network PID control. *Shock and Vibration*. 2019, **2019**, 8. https://doi.org/10.1155/2019/4609754

[56] IQBAL, M.Y., WU, Z., TIE, W. et al. High-efficiency energy harvesting by using hydraulic electromagnetic regenerative shock absorber. *Mechanisms and Machine Science*. 2021, **105**, 276-294. https://doi.org/10.1007/978-3-030-75793-9_28

[57] MACIEJEWSKA, M., FUĆ, P., KARDACH, M. Analysis of electric motor vehicles market. *Combustion Engines*. 2019, **179**(4), 169-175. https://doi.org/10.19206/ce-2019-428.

[58] AGRAWAL, M., RAJAPATEL, M.S. Global perspective on electric vehicle 2020. *International Journal of Engineering Research & Technology*. 2020, **9**(1), 8-11. https://doi.org/10.17577/IJERTV9IS010005

[59] HONG, H., MOHAMAD, N.A.R.C., CHAE, K. et al. The lithium metal anode in Li-S batteries: challenges and recent progress. *Journal of Materials Chemistry A*. 2021, **9**(16), 10012-10038. https://doi.org/10.1039/d1ta01091c

[60] LI, Y., GUO, S. Material design and structure optimization for rechargeable lithium-sulfur batteries. *Matter*. 2021, **4**(4), 1142-1188. https://doi.org/10.1016/j.matt.2021.01.012

[61] RAMASWAMY, K., O’HIGGINS, R.M., LYONS, J. et al. An evaluation of the influence of manufacturing methods on interlocked aluminium-thermoplastic composite joint performance. *Composites Part A: Applied Science and Manufacturing*. 2021, **143**, 106281. https://doi.org/10.1016/j.compositesa.2021.106281

Andrzej Augustynowicz, DSc., DEng. – Opole University of Technology.

e-mail: *A.Augustynowicz@po.opole.pl*

Article citation info:
CHWIST, M. Comparative analysis of heat release in a reciprocating engine powered by a regular fuel with pyrolysis oil addition. *Combustion Engines*. 2022, **190**(3), 104-112. https://doi.org/10.19206/CE-146694

Mariusz CHWIST

Combustion Engines
Polish Scientific Society of Combustion Engines

Comparative analysis of heat release in a reciprocating engine powered by a regular fuel with pyrolysis oil addition

ARTICLE INFO

Received: 8 December 2021
Revised: 30 December 2021
Accepted: 14 February 2022
Available online: 5 March 2022

The article presents a comparative analysis of heat release rate in a spark-ignition engine powered by various fuels as follows: butanol, gasoline, a mixture of butanol with tire pyrolysis oil (TPO), and mixtures of butanol with oil from biomass pyrolysis (BPO). Selected combustion phases were analyzed. Additionally, ignition delay calculations were performed in the ANSYS Chemkin Pro program for the surrogates of the tested fuels. Popular surrogates quoted in numerous publications were used as substitute fuels. The paper presents an original surrogate of oil from tire pyrolysis.

Key words: *pyrolysis oil, butanol, ignition delay, surrogate, Ansys Chemkin-Pro*

1. Introduction

Pyrolysis is a thermochemical process in a reactor in an oxygen-free atmosphere at a temperature of 300˚C to 2000˚C. As a result of the temperature, the input material is decomposed into simpler chemical compounds. The pyrolysis process can be divided into 3 stages. The first is drying, the temperature of the material does not exceed 100˚C. The second step is to separate the volatile matter from the material. The last phase is the breakdown of long chains of hydrocarbon compounds into shorter ones. Secondary reactions between the pyrolysis products take place in this stage [1, 3].

Pyrolysis can be a process that converts waste into a high-calorific liquid, in addition to producing gas and a carbon-containing solid. The oil produced has many uses, one of which is to power a reciprocating internal combustion engine. All kinds of materials of organic origin can be used as input materials for the pyrolysis process: biomass waste, municipal waste, polymer waste, etc [7, 9].

Depending on the raw material used for the pyrolysis process, an oil with different physical-chemical properties and compositions is obtained. Other factors which influence the compositions of the obtained oil are as follows: type of pyrolysis reactor, process conditions, additional catalytic compounds [1, 9, 19].

In recent years, extensive research has been carried out on the pyrolysis process. The number of publications on this topic is gradually growing from year to year. In the SCOPUS database, 9,737 articles were published in 2021, compared to 2015, when the number of articles with this keyword was 5,560. In addition, pyrolysis is used on an industrial scale to process waste. The largest global companies research the use of pyrolysis products, by name ChemCycling^{TM} project, including BASF, New Energy, Quantafuel, Remondis [10].

The main novelty in the article is a comparative analysis of the thermodynamic cycle, taking into account the course of heat release in a reciprocating internal combustion engine powered by a mixture of pyrolysis oil with butanol and selected reference fuels.

2. Materials

At the first stage of the research, it was necessary to find a solvent that can mix and make blends with the two oils taken for analysis. The first one was the tire pyrolysis oil (TPO) and the second one: the biomass pyrolysis oil (BPO). Gasoline was not taken as the reference fuel due to solubility problems [3, 4]. BPO was not miscible with gasoline, as shown in Fig. 1b. To achieve a stable mixture, n-butyl alcohol was used as the reference fuel and solvent. Both pyrolysis oils formed a stable and premixed blend as shown in Fig. 1a.

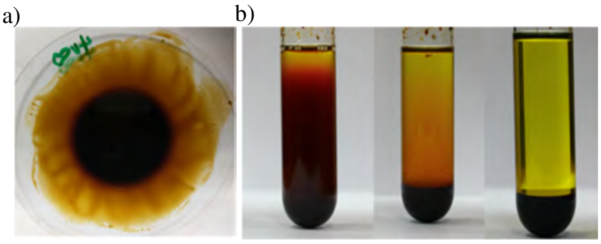

Fig. 1. On the left, a mixture of tire pyrolysis oil with butanol, on the right, a mixture of biomass pyrolysis oil and gasoline

Table 1 compares the properties of a typical tire pyrolysis oil and unleaded Eurosuper 95 gasoline. What distinguishes TPO compared to gasoline is its high oil density, high kinematic viscosity, and high flash point. The calorific value and elemental composition are similar to that of gasoline [2,6].

Table 1. Comparison of the properties of tire pyrolysis oil and gasoline

Property	Tire pyrolysis oil	Gasoline Eurosuper 95
Density [g/cm^3]	0.943–0.935	0.742
Kinematic viscosity [cSt]	4.62–5.68	0.5–0.75
Flash point [ºC]	< 30–53	–40
LHV [MJ/kg]	41.6–43.5	42.8
Composition (%wt) C	87.57–81.0	86
H	10.35–6.6	14
N	< 1–0.6	0

Tire pyrolysis oil is a mixture that contains a large number of compounds. As reviewed from the literature one can find results of the GC-MS analyzes that showed over 100 chemical compounds in a typical pyrolysis oil. An exemplary analysis is presented in Table 2, in which the substances of their highest content are depicted [1, 20].

Table 2. GC-MS composition of tire pyrolysis oil [20]

Name	Formula	Peak area [%]
Ethylbenzene	C_8H_{10}	12.16
Toluene	C_7C_8	10.55
Styrene	C_8H_8	8.94
1,1′-(1,3-Propanediyl)bis-benzene	$C_{15}H_{16}$	2.53
2,4′-Dimethyl-1,1′-biphenyl	$C_{14}H_{14}$	2.5
Isopropylbenzene	C_9H_{12}	2.39
Terphenyl	$C_{18}H_{14}$	2.28
Propylbenzene	C_9H_{12}	2.07
α-Methylstyrene	C_9H_{10}	1.76
1-Methyl-2-isopropylbenzene	$C_{10}H_{14}$	1.55
p-Xylene	C_8H_{10}	1.36
4-Methylpyridine	C_6H_7N	1.34
2-Methyl-1,3-butadiene	C_5H_8	1.12
1-(1-Cyclopenten-1,1-cyclopenten-1-yl)naphthalene	$C_{15}H_{14}$	1.12
Benzene	C_6H_6	1.1
Total		52.77

The second tested oil, obtained from biomass pyrolysis, has different properties than TPO. Table 3 shows its typical properties. Compared to BPO to gasoline Eurosuper 95, BPO has a lower calorific value, higher water content, higher density, and higher kinematic viscosity. The elemental composition of BPO is characterized by a small proportion of carbon which is replaced by a large proportion of oxygen [11].

Table 3. The properties of biomass pyrolysis oil [7, 9, 15]

Property	Unit	Typical range	Test methods
HHV	MJ/kg	14–19	DIN51900, ASTM D240
LHV	MJ/kg	13–18	DIN51900
Water	wt%	20–30	ASTM E203
pH	–	2–3	ASTM E70
Total Acid Number	mg KOH/g	70–100	ASTM D664, ASTM D3339
Kinematic viscosity at 40°C	mm^2/s	15–40	EN ISO 3104, ASTM D445
Density at 15°C	kg/dm^3	1.11–1.30	EN ISO 12185, ASTM D4052
Pour point	°C	9–36	EN ISO 3016, ASTM D97
Carbon	wt% on d.b.	50–60	ASTM D5291
Hydrogen	wt% on d.b.	7–8	ASTM D5291
Nitrogen	wt% on d.b.	< 0.5	ASTM D5291
Suplhur	wt% on d.b.	< 0.05	EN ISO 20846, ASTM D 5453-09
Oxygen	wt% on d.b.	35–40	–
Solids	wt%	< 1	ASTM D7579
Ash	wt%	< 0.3	EN ISO 6245
Flash point	°C	40–110	EN ISO 2719, ASTM D93B

Tests and the analysis of the properties of oils from biomass pyrolysis and tire pyrolysis are the reference points for the results of the simulations carried out later in the work. In the ANSYS Chemkin Pro program, the ignition delay was calculated for the tested fuels.

3. Heat release equation

To determine the heat release rate, equation (1) was used, which results directly from the first law of thermodynamics:

$$\delta Q_{ch} = dU_s + \delta Q_{st} + \delta W + \sum h_i \cdot dm_i \qquad (1)$$

where: δQ_{ch} – heat release from combustion, dU_s – internal energy of the fluid filling the engine cylinder, δQ_{ht} – heat transferred to the engine walls, dW – work done by the fluid to the environment, $\sum h_i \cdot dm_i$ – crevices losses in energy.

The following simplifications were used in the analysis: heat release to the cylinder walls is ignored, therefore the determined heat is net heat, and the gap losses are also ignored. The quotient $\gamma = c_p/c_v$ can be calculated as the polytrophic index of compression before ignition. The final form of the equation for the heat release rate is defined with equation 2 [5]:

$$\frac{dQ_{net}}{d\varphi} \cong \left(\frac{1}{\gamma - 1}\right) p \frac{dV}{d\varphi} + \left(\frac{\gamma}{\gamma - 1}\right) V \frac{dp}{d\varphi} \qquad (2)$$

where: γ – the ratio of the specific heats (c_p/c_v) at constant pressure and constant volume, respectively, p – in-cylinder combustion pressure, V – in-cylinder volume, φ – crank angle (CA) deg, Q_{net} – net heat release during combustion.

The quotient c_p/c_v was determined as depicted in Fig. 2 by equation (3). Where p_0 and v_0 are the pressure and volume of the combustion chamber just before the spark timing, and p_1 and v_1 are the pressure and volume of the combustion chamber 5 CA deg ahead of point 0 (Fig. 2) [5].

$$\gamma = \frac{\log \frac{p_0}{p_1}}{\log \frac{V_1}{V_0}} \qquad (3)$$

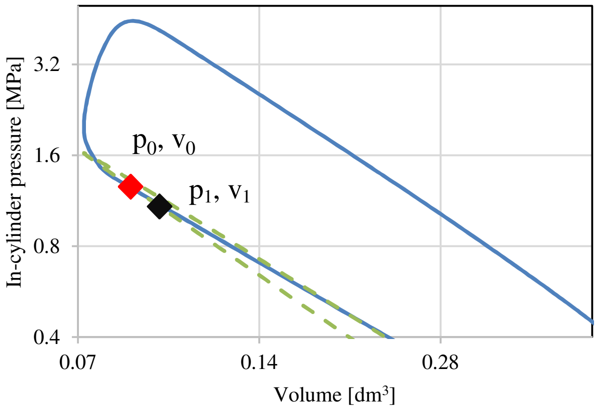

Fig. 2. Points used to calculate the polytrophic index

To calculate the total heat release, equation (2) should be integrated. Additionally, the heat release charts were recalculated to the normalized range of 0–1. An exemplary course of cumulative heat release consistent with equation (4) is shown in Fig. 3.

$$Q_{net} = \int dQ_{net} \tag{4}$$

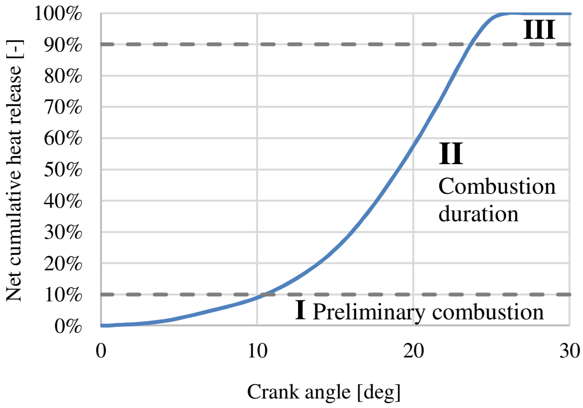

Fig. 3. The course of heat release as a result of butanol combustion in the UIT-85 engine

The presented curve of net heat release can be divided into 3 combustion phases [5]:

- Phase I can be managed as the preliminary combustion-this is the time that elapses from the spark discharge to the release of 10% of the cumulative heat release.
- Phase II is a developed course of combustion – it defines the time in which the production of 80% of heat takes place, i.e combustion duration.
- Phase III is the burning of fuel residues in the cylinder surrounded by a large amount of exhaust gases.

The exact determination of the end of combustion (100% NCHR) is difficult, therefore the first two phases of combustion are of interest in further analysis.

4. Experimental conditions

During the experimental tests, the test stand with the UIT-85 engine was used, presented in Fig. 4. The test stand consists of a spark-ignition engine, which is equipped with an encoder built on the camshaft, an air flow meter is installed in the intake manifold to measure the intake air flow rate. The sensor for indicating the engine was built into the spark plug. The engine load was realized with the aid of an electric asynchronous motor powered by a frequency converter and connected to the electric grid. Fuel injection was into the engine's intake manifold. Table 3 shows the technical parameters of the engine.

Fig. 4. View of the test stand with the UIT-85 engine

Table 3. Technical data of the engine UIT-85 [8]

UIT-85	Four-stroke, spark-ignited, naturally-aspirated, OHV
Number of cylinders	1
Number of valves	2
Cylinder bore	85 mm
Piston stroke	115 mm
Connecting rod	266 mm
Engine displacement	652 cm^3
Compression ratio	7–13
Crankshaft speed	600-850 rpm
Cooling	water cooling system

During the experiment, the engine was running at 600 rpm. The compression ratio, CR, was set to 10. The amount of fuel injection was determined based on the excess air ratio. The engine was fed with a stoichiometric mixture.

The ignition timings that generated the highest value of IMEP were selected for the analysis of heat release curves. The list of spark timings for the tested fuels is presented in Table 3.

Table 3. Spark discharge angle for tested fuels

Fuel name	Symbol	Spark timing [CA after TDC]	The pressure at the moment the spark timing [MPa]
Unleaded Eurosuper 95	Pb95	–8	1.48
n-butanol	Butanol	–10	1.32
Mixture: 75% n-butanol and 25% TPO	Butanol + 25% TPO	–12	1.27
Mixture: 50% n-butanol and 50% TPO	Butanol + 50% TPO	–12	1.31

The most delay spark timing was set for gasoline, which was 8 CA before TDC. Spark angle of 10 CA before TDC was set for pure butanol. 12 CA spark timing was set for butanol mixtures with the addition of tire pyrolysis oil. Figure 5 shows the pressure curves for the tested fuels vs. crankshaft angle.

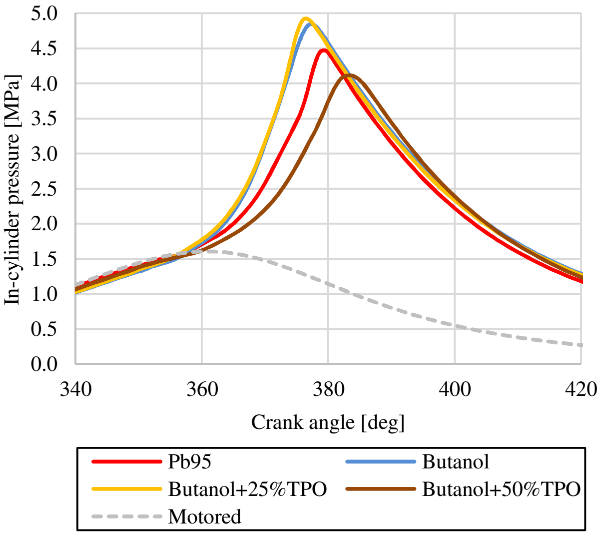

Fig. 5. In-cylinder pressure vs. crank angle

Based on the recorded in-cylinder pressure curves, the heat release rate was calculated by equation (2).

5. Experimental results

The calculated heat release rate for all tested fuels is shown in Fig. 6. For easy comparison of the curves, it was assumed that the spark timing was 0 CA for all these tests. In Figure 6, it can be seen that butanol burns the fastest. However, the maximum NHRR value is the lowest. The rate of heat release has the highest value for gasoline. Butanol + 50% TPO burns the longest. After integrating the waveforms from Fig. 6, a cumulative heat release profile for the tested fuels was obtained and is presented in Fig. 7.

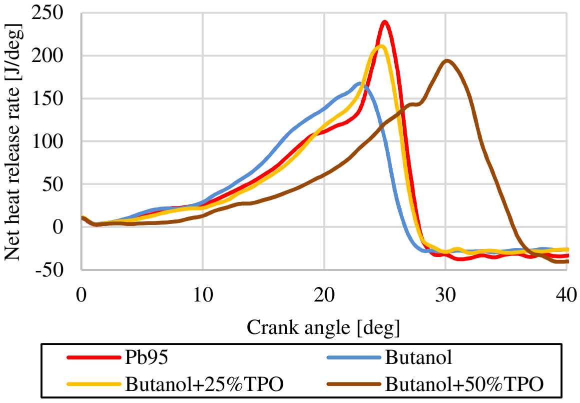

Fig. 6. The net heat release rate for various fuel

The net cumulative heat release was used to analyze the individual combustion phases. Based on diagram 7, the duration of the preliminary combustion (0–10% NCHR) and the duration of the main combustion phase (10–90% NCHR) were calculated.

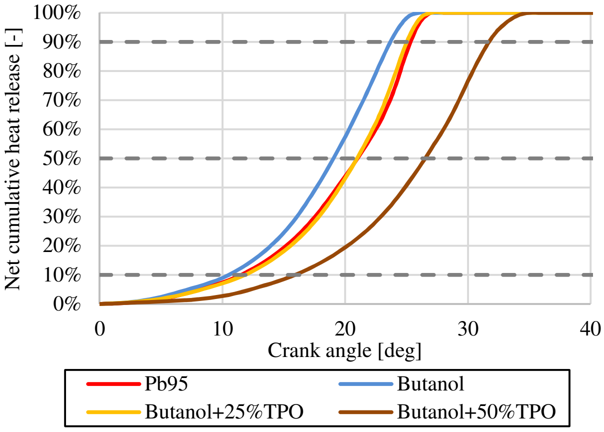

Fig. 7. Net cumulative heat release for various fuel

The shortest preliminary combustion was for butanol and amounted to 10.5 CA deg (Fig. 8), and converted into time units, this delay is 2.8 ms (Fig. 9). Gasoline (11.5 CA = 3.1 ms) and Butanol + 25% TPO (11.8 CA = 3.2 ms) had a slightly longer preliminary combustion. The fuel Butanol + 50% TPO had the longest preliminary combustion, which was 15 CA deg, and converted into time units, this delay is 4 ms.

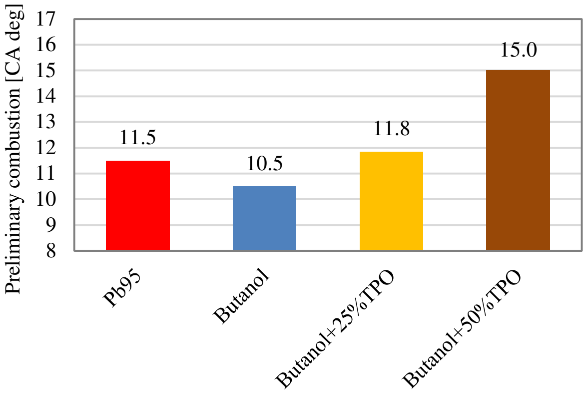

Fig. 8. Preliminary combustion for various fuel in [CA deg]

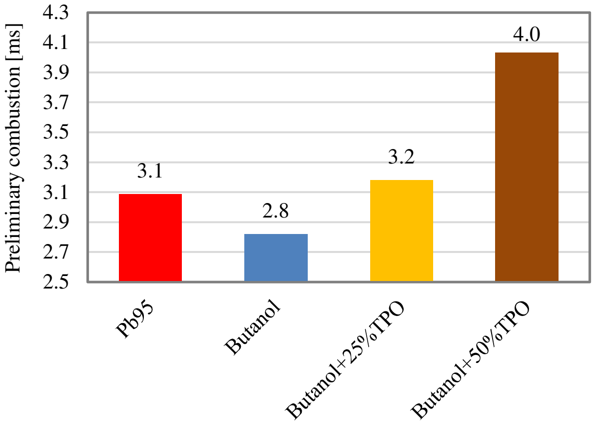

Fig. 9. Preliminary combustion for various fuel in [ms]

The combustion duration phase was the shortest and almost identical for butanol and Butanol + 25%TPO. It amounts to 13.2 CA deg, which in milliseconds gives the result of 3.55 ms. Gasoline had a longer combustion duration phase by 0.7 CA deg, which in terms of time units gives the result of 3.73 ms. The combustion duration of the mixture Butanol + 50%TPO was the longest. This process lasted 15.1 CA deg what corresponds to the time of 4.06 ms (Fig. 10 and 11).

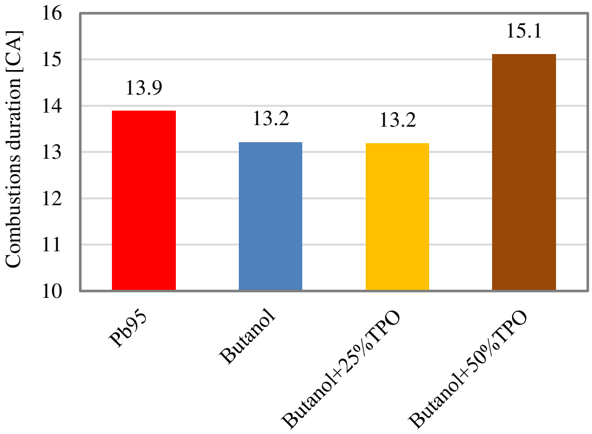

Fig. 10. Combustions duration for various fuels in [CA]

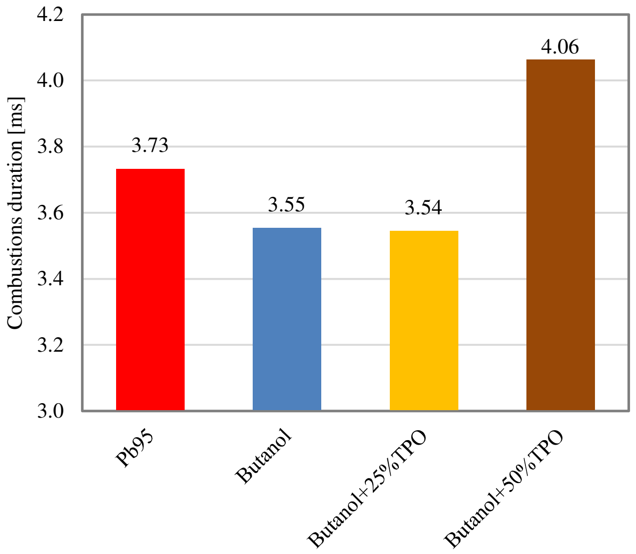

Fig. 11. Combustions duration for various fuels in [ms]

Based on the analysis of the two combustion phases, the following conclusions can be drawn. Pure butanol burns up the fastest. Gasoline and Butanol + 25% TPO have very similar heat release patterns. Butanol + 50% TPO has the longest preliminary combustion and the longest duration of the main combustion phase.

In the second phase of the experiment, the analysis included butanol as the reference fuel and the mixture designated as Butanol + 20% BPO, which consists of butanol of 80% and 20% oil from biomass pyrolysis by volume. For the comparative analysis, it was established that the spark timing will be constant for both fuels and will be 15 CA before TDC. For such ignition timing, the highest mean indicated engine pressure was calculated. The IMEP chart for the tested fuels is shown in Fig. 12.

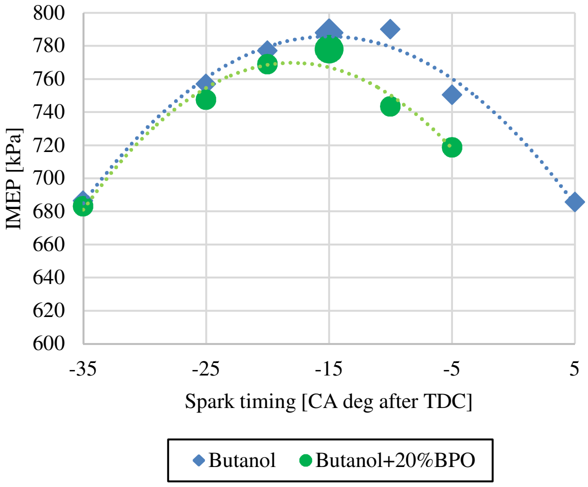

Fig. 12. IMEP for butanol and Butanol + 20% BPO

Based on the data collected from the engine tests (shown in Fig. 13, 14) and using equation 2, the NHRR was calculated. The polytrophic index was calculated as in the first part of the experiment according to equation 3.

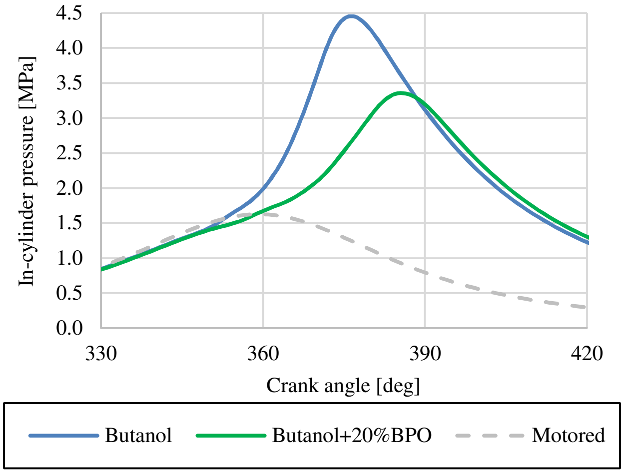

Fig. 13. In-cylinder pressure vs. crank angle

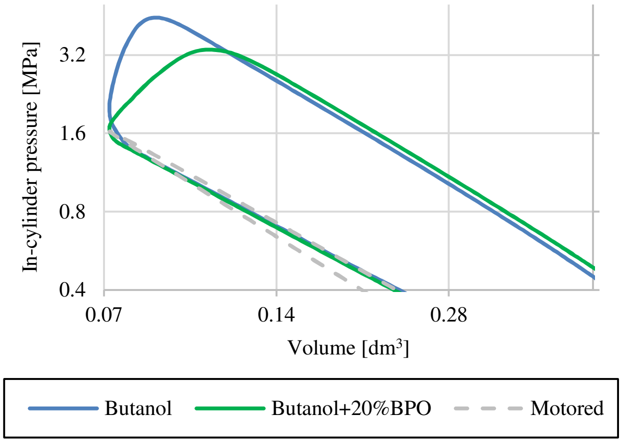

Fig. 14. In-cylinder pressure vs. volume

The p-V diagram shows a lower pressure peak for Butanol + 20% BPO. The maximum pressure recorded during the indication for this fuel was 3.35 MPa. For pure butanol, the maximum pressure was 4.45 MPa. The maximum value for butanol occurred noticeably earlier, which indicates faster ignition of the fuel, and confirms the NHRR course presented in Fig. 15.

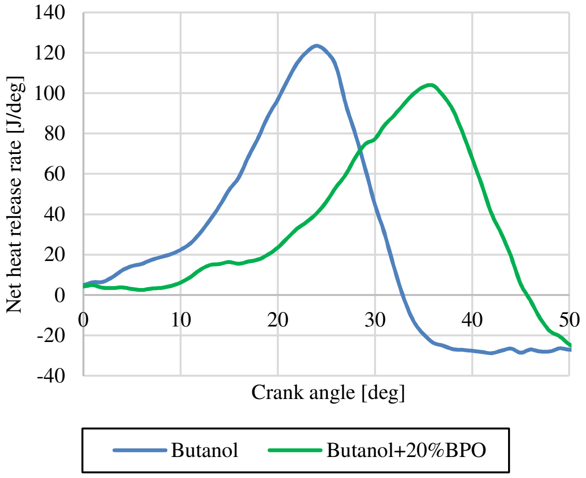

Fig. 15. The net heat release rate for butanol and Butanol + 20% BPO

The curve of NHRR after integration gives the result in the form of cumulative net heat release, which is presented in Fig. 16.

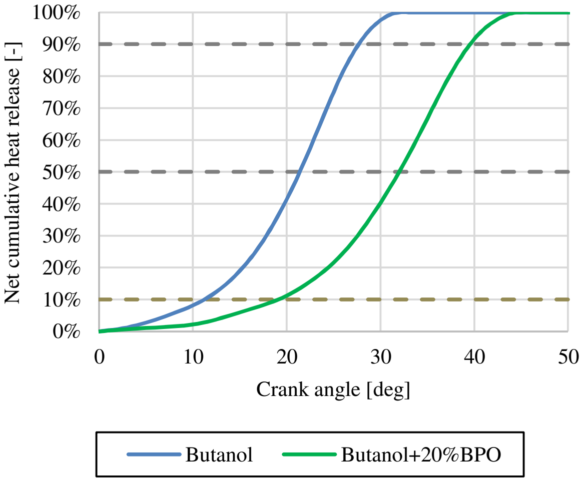

Fig. 16. Net cumulative heat release

The selected combustion phases are marked in the NCHR diagram (Fig. 16). The preliminary combustion for butanol was 2.2 ms. Adding 20% BPO to the reference fuel increased the preliminary combustion by 1.6 ms. The duration of the main combustion phase was also longer for the Butanol + 20% BPO mixture. It was 4 ms. Butanol burned shorter by 0.8 ms. Additionally, the combustion duration phase is divided in half. It has been checked which half lasts longer. For both tested fuels, it was registered that the combustion of the second part of the combustion duration takes place faster than the first one. The individual values are presented in Fig. 17.

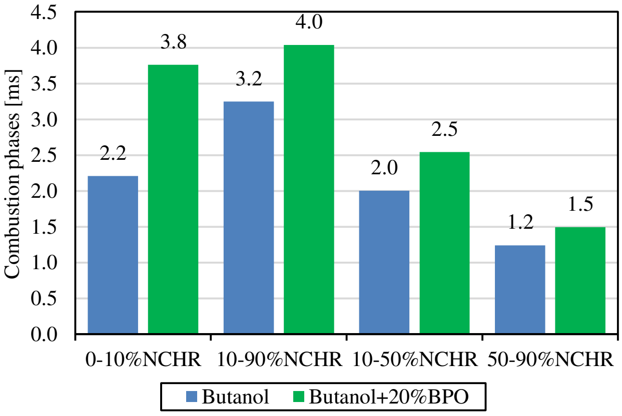

Fig. 17. Combustion phases

7. Combustion modeling in ANSYS Chemkin-Pro

In the next part of the research, simulations were carried out in the ANSYS Chemkin-Pro program to calculate the ignition delay of the tested fuel surrogates [18]. The simulations were carried out in the Closed Homogenous Reactor in which conditions similar to those prevailing in a spark-ignition engine were assumed. In the program, the ignition was autoignition but in the experiment, the ignition was forced by a spark. A stoichiometric mixture was burned in the reactor. The combustion kinematics mechanism developed by scientists from the CRECK Modeling group at the Milan University of Technology was used for the calculations. The kinetic combustion mechanism consisted of 402 chemicals and 16118 reactions [16]. The ignition delay in the performed simulations was defined as the time from the start of the simulation to the moment of the maximum VHPR value. An exemplary course of heat release from the simulation is shown in Fig. 18.

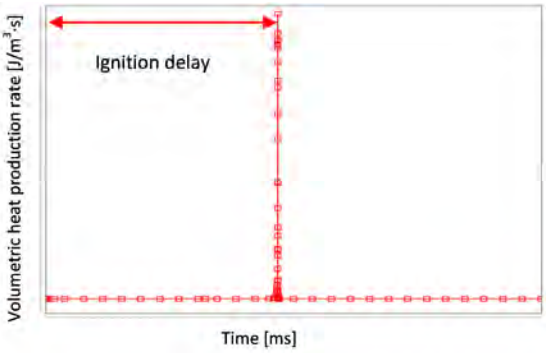

Fig. 18. Ignition delay determined in ANSYS Chemkin-Pro

To perform the simulation in the reactor, the reactants had to be declared. From the literature data, the used fuel surrogates for modeling the combustion of real fuels were taken. The list of selected surrogates and their composition is presented in Table 4.

Table 4. Composition of surrogate of fuel [12, 14]

Name	Formula	[wt. %]	Description
Iso-Butanol	IC_4H_9OH	1	Reference fuel
PRF	IC_8H_{18} NC_7H_{16}	0.95 0.05	A gasoline surrogate with an octane number of 95 corresponding to the Eurosuper 95 lead-free gasoline used in the experiment.
TRF-E	C_2H_5OH C_7H_8 IC_8H_{18} NC_7H_{16}	0.05 0.41 0.40 0.14	Unleaded gasoline surrogate containing an alcohol additive in the form of 5% by weight. Ethanol is a bio component of the popular Eurosuper 95 gasoline.
BPO	$C_6H_{10}O_5$ CH_2OHCH_2OH CH_2OHCHO CH_3CO_2H DMF H_2O MEOLE VANILLIN	0.30 0.07 0.07 0.05 0.06 0.24 0.03 0.18	Surrogate of pyrolysis oil obtained from biomass (biomass pyrolysis oil-BPO). The composition took from the research report of the Residue2heat project. Surrogate mixed with butanol in various proportions [15].
TPO	$C_{10}H_{16}$ $C_6H_5C_2H_5$ C_7H_8 XYLENE	0.15 0.45 0.25 0.15	The proposed composition of tire pyrolysis oil surrogate.

Butanol was the reference fuel in both the simulation and the tests. Butanol is one compound from the IC_4H_9OH database. In the case of gasoline, two alternative surrogate fuels were selected that reflected the properties of the real gasoline. The first, designated PRF, is a mixture of isooctane and n-heptane. The second, more complex, surrogate is a 4-component mixture containing ethanol, toluene, isooctane, and n-heptane, designated as TRF-E. A surrogate developed by the research team as part of the Residue2Heat research was used to model the combustion of oil from biomass pyrolysis. The last modeled fuel was a tire pyrolysis oil surrogate. No surrogate for oil from tire pyrolysis has been found in the literature, therefore an attempt was made to compose an own surrogate that would reflect the properties consistent with those of the tire pyrolysis oil.

The proposed tire pyrolysis oil surrogate consisted of four substances: Limonene, Ethylbenzene, Toluene, Xylene. These are compounds selected from the analyzed GC-MS reports of tire pyrolysis oils. The compounds that had the largest share in the composition were selected. The properties of the individual components of the TPO surrogate are presented in Table 5.

Table 5. Properties of compound of tire pyrolysis oil [13, 17]

Property	Unit	Limonen	Etylobenzen	Toluen	Xylen
Mass fraction	[%]	15	45	25	15
Formula	–	$C_{10}H_{16}$	C_8H_{10}	C_7H_8	C_8H_{10}
Carbon content	[wt %]	0.88	0.91	0.91	0.91
Hydrogen content	[wt %]	0.12	0.09	0.09	0.09
Density	[kg/m^3]	841	866	867	874
Viscosity	[mPas]	–	678	587	
LHV	[MJ/kg]	–	40.9	40.24	40.9
Pour point	[°C]	–74.35	–94.9	–95	–48
Boiling point	[°C]	176	136.2	110.6	139
Flash point	[°C]	51	15	4	29
Autoignition temperature	[°C]	245	432	480	525
Cetane Number	–	19	4/6	3/0/–5	8
Octane number	–	73	98	112	124

Ignition delay was calculated for all fuel surrogates for 3 temperatures: 900 K, 1000 K, 1100 K and 1200 K. Additionally, simulations were carried out for various pressures: 10 bar, 15 bar and 20 bar. Figure 19 shows the ignition delay for PRF and TRF-E.

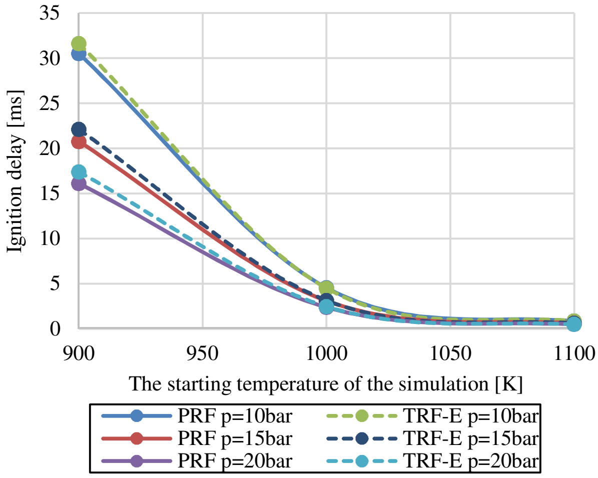

Fig. 19. Ignition delay for PRF and TRF-E

The diagram shows that the initial temperature of the simulation has a great influence on the ignition delay. The starting pressure has a slight influence on the ignition delay. As the pressure increases the ignition delay decreases. The most important conclusion from the presented comparison of both surrogates, however, is that both alternative fuels have almost the same ignition delay. In the range of lower temperatures, TRF-E has a slightly longer delay compared to PRF.

In Figure 20 the ignition delay for all tested surrogates is presented. The initial pressure was set the same for all simulations and amounted to 15 bar. The graph shows that TPO had the longest delay in the entire tested temperature range. In the middle of the graphs, 3 waveforms overlap namely: butanol, PRF, and TRF-E which have a very similar ignition delay. BPO had the shortest ignition delay from the simulations.

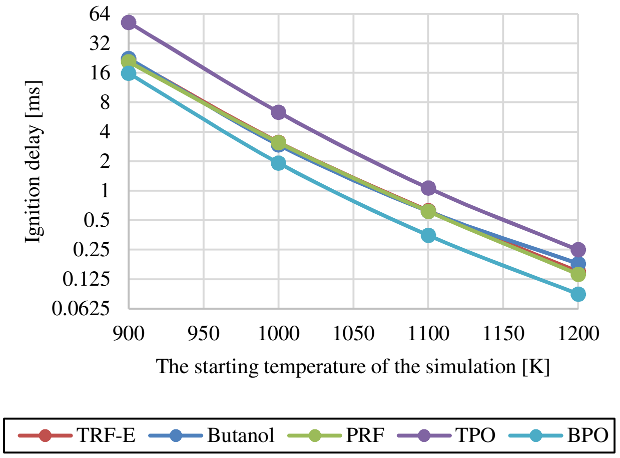

Fig. 20. Ignition delays for research surrogates

Comparing the calculated ignition delay with the experiment, conclude is that all surrogates except BPO have a delay consistent with the results of the experiment. Oil from biomass pyrolysis should have a longer ignition delay than that of butanol and gasoline supplements, but the simulation results did not confirm this. In an attempt to find the cause of this discrepancy, the ignition delay calculations were performed for the individual components of the BPO surrogate. The simulation results are presented in Fig. 21.

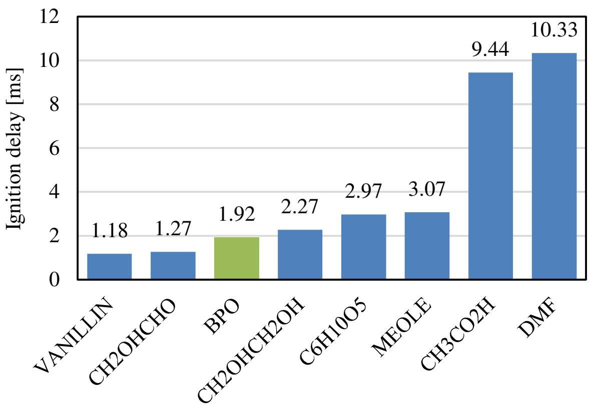

Fig. 21. Ignition delays all compounds of BPO surrogate

The calculated ignition delay of the individual components revealed that the mixture consists of two groups of compounds. The first group of substances had a short ignition delay of less than 3.1 ms, and two compounds with a long ignition delay of more than 9 ms. Compounds with long ignition delay accounted for only 11% by weight.

Figure 22 shows the ignition delay for all tested surrogates, for a pressure of 15 bar and a temperature of 1000 K.

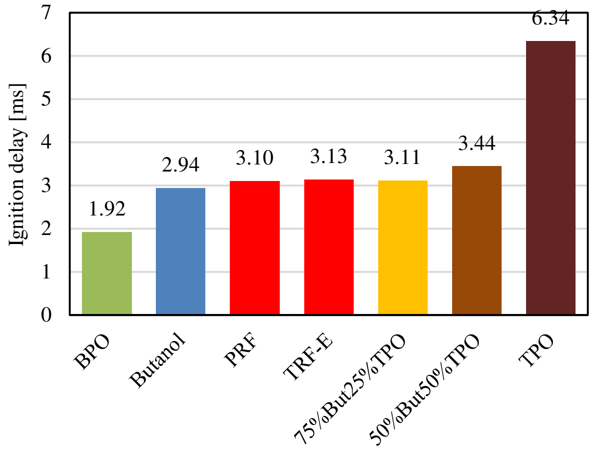

Fig. 22. Ignition delay of all research surrogates

Figure 22 show that with the increase in the share of the proposed oil surrogate from tire pyrolysis, the ignition delay increases. Which is in line with the trend observed during the experiment. The influence of TPO on the ignition delay is shown in Fig. 23.

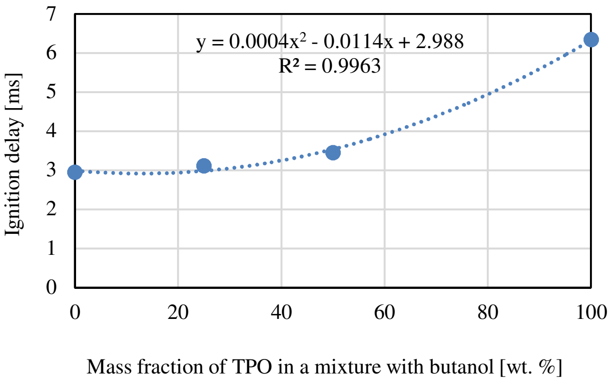

Fig. 23. Influence of TPO surrogate for ignition delay

The proposed tire pyrolysis oil surrogate consists of 4 chemical compounds. To investigate how a given component influences the ignition delay, calculations of the ignition delay were performed separately for all components of the supplement. The obtained results are presented in Fig. 24.

The proposed composition of the TPO surrogate contains two groups of compounds. The first two, limonene, and ethylbenzene, had a shorter ignition delay compared to the value for the mixture, while the other two components. i.e. xylene, and toluene had a longer ignition delay than the obtained value for the surrogate.

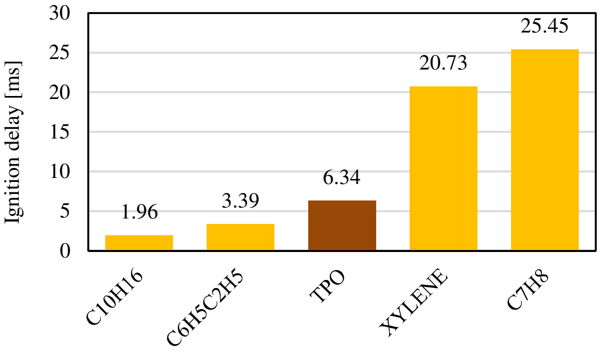

Fig. 24. Ignition delay of all compounds of TPO surrogates

8. Summary

Butanol can be considered a universal solvent for biomass pyrolysis oil (BPO) and tire pyrolysis oil (TPO), unlike Eurosuper 95 gasoline with which BPO cannot be mixed. Butanol burns the fastest but has the lowest maximum heat release and the shortest fuel preliminary combustion.

Eurosuper 95 gasoline and Butanol + 25% TPO have similar heat release profiles for each stage of fuel combustion.

A mixture of Butanol + 50% TPO burns the longest and has the longest preliminary combustion.

Oil from biomass pyrolysis (BPO) increases the preliminary combustion phase compared to the reference fuel – butanol and also extends the main combustion phase.

For all tested fuels, the combustion phase of 10–50% lasts longer than the combustion duration 50–90%.

The ANSYS Chemkin Pro software was used to model the combustion of a homogeneous stoichiometric mixture of butanol and for fuel surrogates in a closed and insulated reactor as a reference.

The gasoline was modeled using two surrogates. For the temperature of 900 K, a bigger delay in ignition of the TRF-E surrogate can be observed compared to the PRF. For higher temperatures, latency was almost identical for both surrogates.

The composition of the oil surrogate from biomass pyrolysis proposed in the report on the Residue2Heat project does not correctly reflect the fuel ignition delay for the assumed conditions. 5 out of 7 components of the proposed surrogate have a shorter ignition delay time than the value for the mixture. The surrogate has a much shorter ignition delay than butanol, which is inconsistent with the experiment.

To model the combustion of oil from tire pyrolysis, a four-component surrogate consisting of toluene, ethylbenzene, xylene, and limonene was developed and proposed based on the literature. The influence of the proposed TPO surrogate on the ignition delay is correct with the experiment.

There is a correlation in trends between the experiment and simulations calculated using the Chemkin program for all tested fuels, except for the oil surrogate from biomass pyrolysis (BPO).

Nomenclature

BPO	biomass pyrolysis oil	NCHR	net cumulative heat release
CA	crank angle	NHRR	net heat release rate
CR	compression ratio	OHV	overhead valve
GC-MC	gas chromatography mass spectrometry	TDC	top dead center
HHV	higher heating value	TPO	tire pyrolysis oil
IMEP	indicated mean effective pressure	VHPR	volumetric heat production rate
LHV	lower heating value		

Bibliography

[1] ALKHATIB, R. Development of an alternative fuel from waste of used tires by pyrolysis. *Environmental Engineering*. 2014. Ecole des Mines de Nantes.

[2] BOGARRA-MACIAS, M., DOUSTDAR, O., FAYAD, M.A. et al. Performance of a drop-in biofuel emulsion on a single-cylinder research diesel engine. *Combustion Engines*. 2016, **166**(3), 9-16. http://doi.org/10.19206/CE-2016-324

[3] CHWIST, M., PYRC, M., GRUCA, M. et al. By-products from thermal processing of rubber waste as fuel for the internal combustion piston engine. *Combustion Engines*. 2020, **181**(2), 11-18. https://doi.org/10.19206/CE-2020-202

[4] CHWIST, M., SZWAJA, S., GRAB-ROGALIŃSKI, K. et al. Bio-oil blended butanol as a fuel to the spark ignition internal combustion reciprocating engine. *Combustion Engines*. 2017, **169**(2), 93-96. https://doi.org/10.19206/CE-2017-216

[5] HEYWOOD, J.B. Internal Combustion Engine Fundamentals. *Mcgraw-Hill College*. 1988.

[6] JUMA, M., KORENOVA, Z., MARKOS, J. et al. Pyrolysis and combustion of Scrap tire. *Petroleum & Coal*. 2006, **48**(1), 15-26.

[7] KARDAŚ, D., KLUSKA, J., KLEIN, M. et al. Modelowe kompleksy agroenergetyczne: Teoretyczne i eksperymentalne aspekty pirolizy drewna i odpadów. *Wydawnictwo UWM*. 2014.

[8] KOLODZIEJ, C.P., WALLNER, T. Combustion characteristics of various fuels during research octane number testing on an instrumented CFR F1/F2 engine. *Combustion Engines*. 2017, **171**(4), 164-169. https://doi.org/10.19206/CE-2017-427

[9] KOMENDA, P. Analiza procesu termicznej przeróbki biomasy. 2019. Monografie nr **154**. *Wydawnictwo PAN. Komitet Inżynierii Środowiska*. Warszawa.

[10] KRUGER, C. Evaluation of pyrolysis with LCA 3 – case studies, *BASF SE*, 31.07.2021.

[11] LEHTO, J., OASMAA, A., SOLANTAUSTA, Y. et al. Fuel oil quality and combustion of fast pyrolysis bio-oils. *VTT Technology*. 2013. **87**, 79.

[12] MAURO, S., SENER, R., GÜL, Z.M. et al. Internal combustion engine heat release calculation using single-zone and CFD 3D numerical models. *International Journal of Energy and Environmental Engineering*. 2018, **9**, 215-226. http://doi.org/10.1007/s40095-018-0265-9

[13] MIKULSKI, M., AMBROSEWICZ-WALACIK, M., HUNICZ, J. et al. Combustion engine applications of waste tire pyrolytic oil. *Progress in Energy and Combustion Science*. 2021, **85**, 100915. https://doi.org/10.1016/j.pecs.2021.100915

[14] MORGAN, N., SMALLBONE, A., BHAVE, A. et al. Mapping surrogate gasoline compositions into RON/MON space. *Combustion and Flame*. 2010, **157**, 6. https://doi.org/10.1016/j.combustflame.2010.02.003

[15] OASMAA, A., OHRA-AHO, T., LINDFORS, C. Physicochemical properties of FPBO. **D3.3**. *Renewable residential heating with fast pyrolysis bio-oil report*, VTT, 2017.

[16] RANZI, E., FRASSOLDATI, A., STAGNI, A. et al. Reduced kinetic schemes of complex reaction systems. Fossil and biomass-derived transportation fuels. *International Journal of Chemical Kinetics*. 2014, **46**(9), 512-542. https://doi.org/10.1002/kin.20867

[17] SAJDAK, M., MUZYKA, R. Use of plastic waste as a fuel in the co-pyrolysis of biomass. Part I. The effect of the addition of plastic waste on the process and products. *Journal of Analytical and Applied Pyrolysis*. 2014, **107**, 267-275. https://doi.org/10.1016/j.jaap.2014.03.011

[18] SIERADZKA, M., RAJCA, P., ZAJEMSKA, M. et al. Prediction of gaseous products from refuse derived fuel pyrolysis using chemical modelling software – Ansys Chemkin-Pro. *Journal of Cleaner Production*. 2020, **248**, 119277. https://doi.org/10.1016/j.jclepro.2019.119277

[19] SZWAJA, M., CHWIST, M., SZWAJA, S. et al. Impact of pyrolysis oil addition to ethanol on combustion in the internal combustion spark ignition engine. *Clean Technologies*. 2021, **3**(2), 450-461. https://doi.org/10.3390/cleantechnol3020026

[20] UCAR, S., KARAGOZ, S., OZKAN, A.R. et al. Evaluation of two different scrap tires as hydrocarbon source by pyrolysis. *Fuel*. 2005, **84**, 1884-1892. https://doi.org/10.1016/j.fuel.2005.04.002

Mariusz Chwist, MEng. – PhD student in Faculty of Mechanical Engineering and Computer Science, Czestochowa University of Technology.

e-mail: *mariusz.chwist@pcz.pl*

PTNSS

Wrocław University
of Science and Technology

X INTERNATIONAL
CONGRESS ON COMBUSTION ENGINES

POLISH SCIENTIFIC SOCIETY
OF COMBUSTION ENGINES

18th-20th June 2023

congress.ptnss.pl

Wroclaw University of Science and Technology
Faculty of Mechanical Engineering
Wyb. St. Wyspianskiego 27, 50-370 Wroclaw, Poland

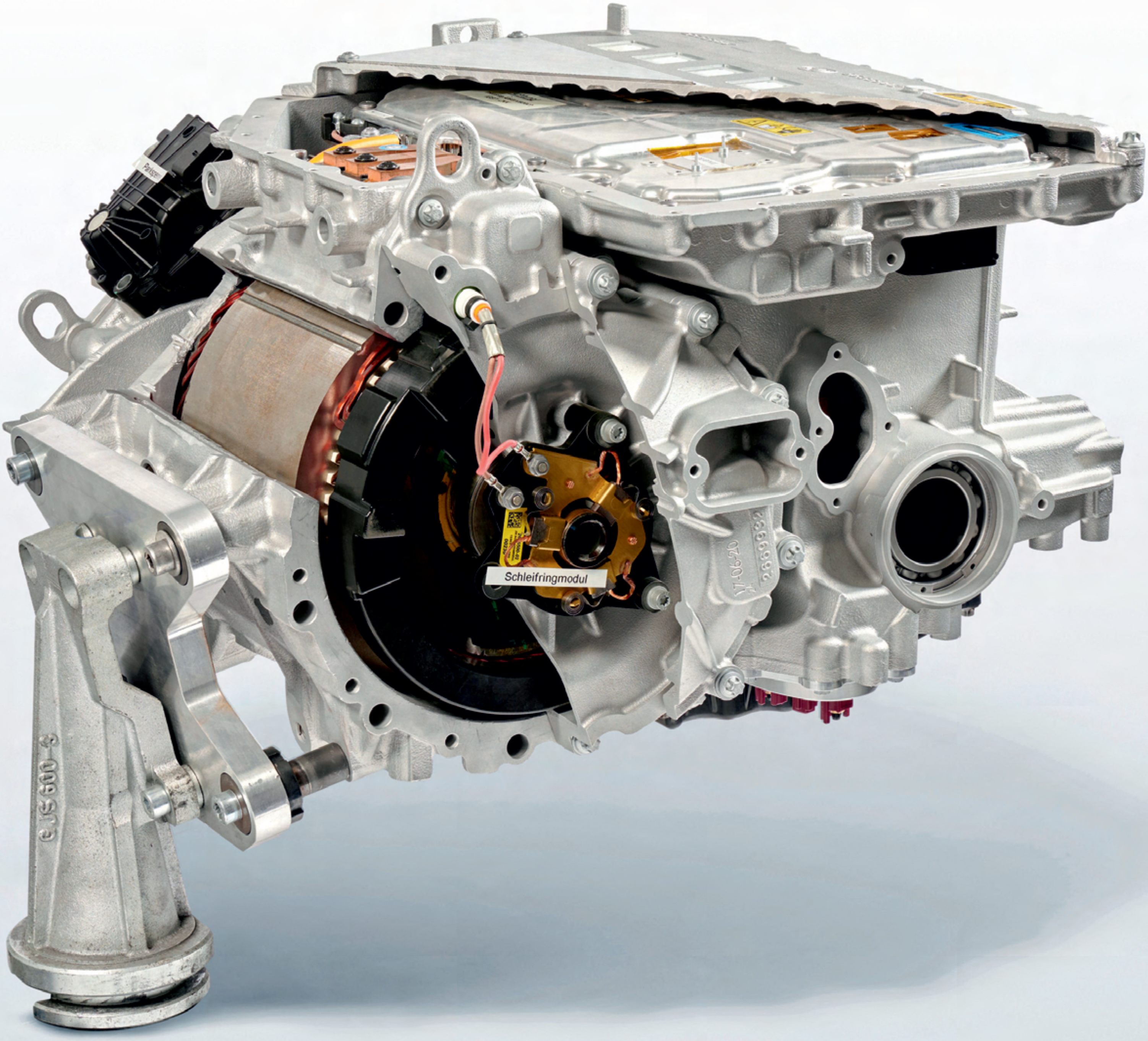

Publisher:

Polish Scientific Society of Combustion Engines

9 772300 989002

ISSN: 2300-9896
eISSN: 2658-1442

Combustion Engines

Polskie Towarzystwo Naukowe Silników Spalinowych

www.combustion-engines.eu